Semen Quality Detection Using Acoustic Wave Sensors

A thesis submitted in partial fulfilment of the requirements of the Nottingham Trent University for the degree of Doctor of Philosophy

Shaun Atherton

February 2011

A million million spermatozoa

All of them alive;

Out of their cataclysm but one poor Noah

Dare hope to survive.

And among that billion minus one

Might have chanced to be

Shakespeare, another Newton, a new Donne--

But the One was Me.

Shame to have ousted your betters thus,

Taking ark while the others remained outside!

Better for all of us, froward Homunculus,

If you'd quietly died!

- Aldous Huxley

Stand back, I'm going to try science.

- Randall Munroe

I have not failed. I've just found 10,000 ways that won't work.

- Thomas A. Edison

Onwards and upwards.

- Michael Newton

Acknowledgments

I would like to thank my supervisors. Dr Mike Newton and Prof Glen Mchale, your time, suport, knowledge and advice proved invaluable. Thank you for having faith that I'd see my PhD through to the end, even when I had none. Dr David Hughes, thank you for your insights into the biological side of the project and for being the one person who didn't smirk at the mention of sperm.

My thanks to Paul Roach, Christophe Trabi, Nicola Doy, Gary Wells, Carl Evans, Rob Morris, Neil Shirtcliffe and Simon Stanley for their help, friendship and coffee breaks. I couldn't have hoped for better lab mates.

Thanks also to Dave Parker and Stephen Elliott for their technical suport. I apologise if there is anything I haven't returned.

I am indebted to my family, my parents Linda and David, and my siblings Dean, Dawn and Jade. They took pride in my achievements and thought a PhD sounded incredibly clever. Their love and suport made all this possible.

Lastly my love and thanks to Bernie Bailey, I feel privileged to have met you. You gave me the drive and determination to finish when I needed it the most. Hugs :-*

Contents

Abstract

Artificial insemination (AI) is a widely used part of the modern agricultural industry, with the number of animals inseminated globally being measured in the millions per anum. Crucial to the success of AI is that the sperm sample used is of a high Quality. Two factors which determine the quality of the sample are the number of sperm present and their motility. There are numerous methods used to analyse the quality of a sperm sample, but these are generally laboratory based, expensive and in need of a skilled operator to perform the analysis. It would, therefore be useful to have a simple and inexpensive system which could be used outside the laboratory, immediately prior to the insemination of the animal.

Presented in this thesis is work developing a time of flight (ToF) technique which makes use of a quartz crystal microbalance (QCM), operating at 5 MHz, as the sensing element. Data is shown developing a device where a 50 µl sample of boar sperm is added to a liquid filled swim channel, which the sperm are allowed to self-propel down and attach to the surface of a QCM at the end. The attachment of the sperm to the surface causes a measurable frequency decrease in the QCM, aproximately 50 Hz. An average effective mass measurement was made using a QCM and gave a value of 8 ± 5 pg per sperm, which was used in conjunction with the frequency change to determine the number rate of sperm reaching the QCM. Additional data is presented to investigate the effect of environmental temperature on the ToF of the sperm, showing a decrease in ToF between 23 ^{0}C to 37 ^{0}C. The system was also used to investigate increasing the swim speed of the sperm by chemical means. A range of 20 µmol to 100 µmol of progesterone was added to the swim medium and the ToF was shown to decrease as a result.

To further develop the system, large commercial electronics were replaced by smaller circuits built in-house. An oscillator circuit based on a Pierce oscillator was used to drive the QCM and a frequency counter circuit making use of a universal frequency to digital converter (UFDC-1) was used to measure the frequency of the QCM. ToF experiments were performed which showed these pieces of equipment to be effective for performing the analysis of sperm samples. The swim cell itself was also refined, resulting in a compact, modular design.

Work was performed developing layer-guided, single-port acoustic resonators to replace the QCM as the sensing element in the sperm analysis device. A maximum mass sensitivity of 1110 Hzµg^{-1}cm^{-2} was found for devices on a $LiTaO_3$ substrate with a 6 µm guiding layer. While viscosity-density sensing experiments found a maximum sensitivity of 488 KHz Pa$^{-1/2}$ kg$^{1/2}$ for a 4 µm guiding layer.

1. Introduction

1.1 Motivation

There are more than 100 million artificial inseminations (AI) performed on cattle globally each year [1], with a further 40 million performed on pigs, 3.3 million on sheep and 0.5 million on goats [2]. This makes AI a well-established and routine part of modern agriculture. For this reason, a method of accurately and precisely determining the viability of a sperm sample prior to insemination is a hugely import issue for the agricultural industry. It is possible in most cases to freeze sperm and thaw out as needed, however, this is not always possible and the sperm of some species react badly to the freezing process [3]. Consequently there is a limited window of oportunity to analyse the sperm sample between the collection of the sperm and insemination taking place, usually no more than a few days with the use of sperm extenders.

Current methods of sperm analysis are often subjective processes that require specialist equipment, a skilled operator and a laboratory to perform the analysis in. Typically, the techniques used look at the concentration of sperm in a sample and their motility. Optical techniques such as haemocytometers and counting chambers [4], computer assisted analysis [5] or a combination of fluorescent staining and flow cytometry [6] are the methods typically used.

There is a clear need for a portable, fieldable tool for the in situ (onfarm) analysis that would allow a sperm sample to be tested immediately prior to insemination. The conditions on a farm would require a device which is robust, needs no complex sample preparation techniques and provides a simple "yes" or "no" answer, rather than requiring complicated interpretation of results. That is not to say that such a system couldn't be used for more detailed analysis if needed.

Newton *et al* [7] showed that a simple "time of flight" (ToF) technique, measuring the time of swim of sperm between two points, could be employed to analyse the motility of sperm samples. This process involved using a quartz crystal microbalance (QCM), as a mass sensor to detect arrival time, and provided a real time screening technique which monitored the motility of the sperm in the sample. This preliminary work provided little detailed information about the sample, such as number of sperm reaching the sensor, neither did it take into account factors such as the effect of temperature or swim medium composition of the motility of the sperm. Further, this preliminary work used a bulky oscillator and frequency counter. A fieldable device for the pre-insemination test of a sperm sample would require significant miniaturisation and cost reduction of the system.

Surface Acoustic Wave (SAW) devices are one form of acoustic sensors [8] which offer a number of advantages over QCMs . The main advantage is improved sensitivity. There is a practical limit on how

thin a QCM can be made due to concerns over its fragility. The sensitivity of a QCM is related to its frequency, the higher the frequency the more sensitive the device, which increases as the crystal thickness decreases. So a practical limit on the crystal thickness also limits the sensitivity of the device.Due to the use of interdigital transducers (IDT) to excite a wave in a SAW device, the frequency is independent of substrate thickness and is instead inversely proportional to the width of the IDTs. While there is a practical limit on the IDT size, the frequency far exceeds that of QCMs and so results in a more sensitive device.

The most sensitive types of SAW device employ guiding layers. Originally, Love wave devices filled this role [9]. More recently, guiding layers have been aplied to shear horizontal acoustic plate mode (SH-APM) [10] and shear horizontal surface acoustic wave (SH-SAW) devices [11]. A useful technique would be to extend the use of guiding layers to improving the sensitivity of single-port acoustic resonators. Single-port devices have a single set of IDTs acting as both the input and output of the device. Single-ports offer a compromise between the relative electronic simplicity of a two terminal QCM and the high sensitivity allowed by an IDT based device.

In addition to the sensitivity of the device, there are a number of other factors to consider when making a sensor. The sensor should show reproducibility, meaning the response of the sensor should be consistent for each sample analysed under the same parameters. Also, if any part is to be reused it should not alter the outcome. There should, ideally, be no drift in the sensor over the course of analysing a sample. More specifically, for this project, the sensor should be part of a portable system. So the sensor and related equipment should be robust, easy to handle and self-contained.

1.2 Project overview

Initial work in this project involved a continuation of the work performed by Newton *et al* [7]. The same system was employed to take a more in depth look at the sperm analysis. Work was carried out to use the detector as an analytical tool for measuring the number of sperm in a sample, rather than just their ToF. This was done by calculating the average effective mass of a sperm cell and using the frequency data from the QCM to determine how many sperm reached the detector. Samples were also optically analysed to verify the number of sperm present on the crystal within the sample cell. Work was also carried out to investigate some of the operating parameters of the system, for example, the environmental temperature, and the use of progesterone to try to hyperactivate the sperm. This is detailed in chapter 3.

Chapter 4 deals with an investigation into single port SAW resonators as a possible alternative to the QCM as the sensing element of the sperm analysis system. The desire to use single-ports is due to their higher sensitivity thanks to their high operating frequency. Single-port resonators were fabricated on quartz and $LiTaO_3$ substrates. S1813photoresist guiding layers were aplied to the surface and their effect on the frequency of the device measured. The optimum layer thickness was investigated by measuring the change in frequency of the devices to both an aplied mass and the viscosity of a liquid in contact with the surface. Sputter coating successive gold layers onto the surface of the sensors was used to investigate the sensor response to mass loading, while the liquid used for the density-viscosity experiments was a range of water glycerol solutions.

In chapter 5, work continuing the QCM based experiments is discussed. The majority of the system was miniaturised. The quartz crystal was replaced with a smaller one, 14 mm in diameter. The swim cell was made smaller and the path length reduced. The commercial oscillator previously used was replaced by a circuit designed and built in house. The frequency counter was also replaced with a system built in house. Experiments were performed to test the viability of the new aparatus and compare it to the commercial equivalents.

Chapter 6 reports a series of conclusions, detailing the achievements and main points of interest of this thesis. Additionally, a series of suggestions for further work are included. These cover further developments of the sperm analysis system and aplications beyond screening for AI purposes.

2. Literature Review

And Theory

2.1 Acoustic wave sensors

2.1.1Thickness shear mode resonators

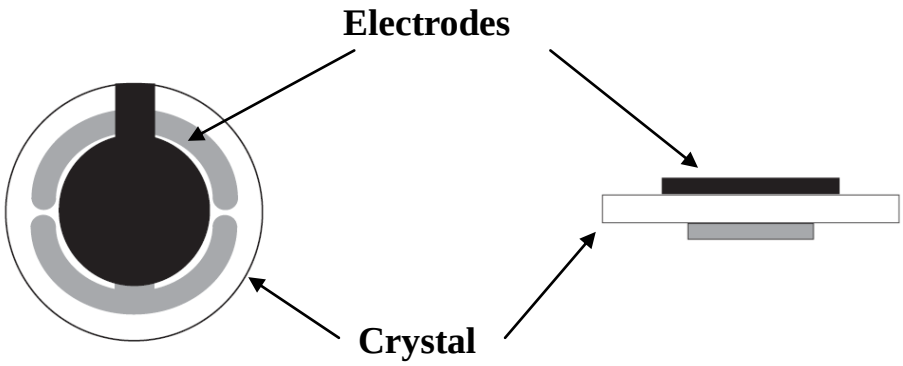

Figure 2.1: Diagram of a quartz crystal microbalance.

A classic acoustic wave device is the thickness shear mode resonator (TSM). The TSM resonator typically consists of a disk of piezoelectric quartz with circular electrodes on oposite faces of the crystal, as shown in Figure 2.1. If an AC voltage is aplied to these electrodes the electric field will, due to the piezoelectric effect, cause shear deformation of the quartz that creates an acoustic standing wave between the two faces.

In 1880 Pierre and Jacques Currie had demonstrated the piezoelectric effect [12]. They showed that in certain materials a mechanical deformation would result in an electrical charge being produced. In 1881 Gabriel Lipmann deduced from fundamental principles that the converse effect should be possible [13], something which the Curies had failed to predict. They were, however, responsible for confirming the existence of the converse effect.

Originally the piezoelectric effect was little more than a laboratory curiosity. There didn't exist, at the time, equipment to amplify the small electrical signals produced by the crystals. In 1921 Cady used a quartz crystal to regulate the frequency of an oscillator circuit [14], making the first quartz crystal resonator. Then in 1923 Pierce developed a number of quartz oscillators [15]. In the 1940s amplifiers were invented which allowed the electricity produced by the piezoelectric effect to be more closely investigated and led to a greater commercialisation of the phenomenon. The 1950s then saw the development of a larger number of products making use of it.

2.1.2 Sauerbrey and mass sensing

The displacement associated with the wave in a TSM resonator is maximum at the surface of the crystal, causing the device to be sensitive to surface interactions. The wavelength of this wave is determined by the thickness of the crystal, given in equation 2.1

$$\lambda_q = 2t_q \tag{2.1}$$

where λ_q is the wavelength in the quartz crystal and t_q is the thickness of the crystal. Given that $v=f_0\lambda$, λ_q can be replaced to give equation 2.2.

$$f_0 = \frac{v_q}{2t_q} \tag{2.2}$$

Here, f_0 is the fundamental frequency of the crystal and v_q is the speed of the wave. It then becomes clear that the resonant frequency of the TSM resonator is a function of the thickness of the crystal. So in order to make higher fundamental frequency devices, the thickness of the crystal must be reduced. This places a practical uper limit on the frequency at which a TSM resonator can operate. If the crystal becomes too thin then the fragility of it causes problems for both the manufacture and the handling of the device. As a result, TSM resonators typically operate at frequencies below 30MHz.

In the late-1950s the work of a physics PhD student in Germany called Gunter Sauerbrey recognised that adding rigid mass to the surface of a TSM resonator would effectively increase the thickness of the crystal and result in a frequency change [16]. This was the first report of a TSM resonator being used for sensing mass deposition, and led to TSM resonator being more commonly referred to as quartz crystal microbalances (QCM). With a QCM, the sensitivity can be defined as follows [17]

$$S_m = \frac{1}{\Delta m}\left(\frac{\Delta f}{f_0}\right) \tag{2.3}$$

where S_m is the mass sensitivity, Δm is the change in mass, Δf is the change in frequency and f_0 is the resonant frequency of the device. Since mass sensitivity is related to frequency and frequency is related to crystal thickness, the practical limit on thickness also limits the sensitivity of any device which uses a QCM as a sensing element.

The QCM's ability to sense mass is due to mass loading on the surface having the effect of changing the thickness of the crystal. By considering it this way, a change in mass can be related to a change in frequency. The extra thickness of the mass can be expressed as equation 2.4

$$t_l = \frac{M}{A\rho_l} \tag{2.4}$$

Here t_l is the added thickness of the mass layer, M is the mass of this layer, A is the surface area of the layer and ρ_l is the density of the material. The density of the crystal ρ_q, along with the shear modulus μ_q, determines the speed of the wave in the QCM. This is shown in equation 2.5

$$v = \sqrt{\frac{\mu_q}{\rho_q}} \tag{2.5}$$

Equation 2.2 can be modified to give an expression relating a change in thickness to a change in frequency.

$$\frac{\Delta f}{\Delta t_l} = -\frac{v}{2t_q^2} \tag{2.6}$$

Rearranging equation 2.2 into $v = 2 f_0 t_q$ and substituting into equation 2.6 gives

$$\frac{\Delta f}{f_0} = -\frac{\Delta t_l}{t_q} \tag{2.7}$$

Taking equations 2.4, 2.5 and 2.6 and substituting them into equation 2.7 results in the Sauerbrey equation

$$\Delta f_0 = -\frac{2\Delta m f_0^2}{A\sqrt{\mu_q \rho_q}} \tag{2.8}$$

Here f_0 is the fundamental frequency and Δf is the change in frequency caused by the added mass, Δm, A is the surface area of the QCM and μ_q and ρ_q are the shear modulus and density of the crystal respectively. The Sauerbrey equation can be used to relate frequency decreases to the addition of mass to the surface. If the crystal is operated at a harmonic frequency, mass loading causes a frequency shift of Δf_n given that

$$\Delta f_n = n\Delta f_0 \tag{2.9}$$

2.1.3 Kanazawa and Gordon

The main limitation of the Sauerbrey equation is that it only accounts for rigid mass on the surface of a crystal. For many aplications, a QCM needs to be able to sense the properties of liquids. When immersed in a liquid, the frequency of the crystal is dependent on the density, viscosity and conductivity of the liquid [18]. If, however, the liquid is free of electrolytes then the frequency of the crystal is only affected by the viscosity and density of the liquid [19].

Due to the liquid having a damping effect, the wave only penetrates a small distance into the liquid. This is known as the penetration depth.

$$\delta = \sqrt{\frac{2\eta}{\rho\omega}} \tag{2.10}$$

Where δ is the penetration depth and $\omega=2\pi f$ is the resonant angular frequency. The first physical models of a QCM operating in a liquid were reported in 1985 [20, 21]. In their calculations, Kanazawa and Gordon treated the QCM as a loss-less elastic solid and the liquid as a purely viscous, Newtonian fluid. The change in frequency can then be attributed to the coupling of the oscillation of the crystal with a dampened shear wave in the liquid. The Kanazawa and Gordon equation relates the change in frequency of the crystal to the viscosity-density product of the liquid

$$\Delta f = -nf_0^{\frac{3}{2}}\left(\frac{\eta_l \rho_l}{\pi \mu_q \rho_q}\right)^{\frac{1}{2}} \tag{2.11}$$

Here η_l and ρ_l are the viscosity and density of the liquid respectively and μ_q and ρ_q are the shear modulus and density of the crystal respectively. There is also an *n* term in the equation, this denotes the harmonic number.

Between the Sauerbrey and the Kanazawa and Gordon equations, the frequency change when the crystal is used either to sense rigid mass or a viscous fluid, or even rigid mass whilst the crystal is immersed in a fluid, can be described. It is also possible to use a QCM to measure other changes in a liquid, such as the electrical conductivity [22].

QCMs have been used for a wide variety of applications [23]. A QCM can be given a selective coating causing specific molecular species to bind to the surface, such as molecularly imprinted polymers [24]. The mass binding to the surface causes a frequency decrease, as described by the Sauerbrey equation, and the selective coating means the frequency change is only caused by the analyte being measured. In this way a QCM can be used as a selective sensor for vapours, for example in bomb detection [25] or in the food industry [26].

QCMs with selective coatings are also used as biosensors. Hong *et al* used a QCM as a DNA sensor, testing a range of immobilisation techniques [27]. QCMs were used by Chen *et al* and Zhang *et al* to sense proteins [28, 29]. While Reddy *et al* have used QCMs as a glucose biosensor [30]. All of these cases take advantage of the high sensitivity of the QCM and the versatility a QCM offers due to the range of selective coatings which can be added to the surface. They also show that QCMs can offer quick and simple alternatives to established techniques, also demonstrated by Newton *et al* in the construction of their simple sperm quality detection device [7].

2.1.4 Equivalent circuit model

One method of modelling a QCM is with an equivalent circuit. There are a number of such circuits [31], one of which is the lumped–element model [32, 33] also known as the Butterworth-Van Dyke (BVD) model. Here the QCM is modelled as an LCR circuit, shown in Figure 2.2. The two electrodes on either

side of the QCM cause a static capacitance (C_0) and electromechanical coupling cause parallel contributions of inductance (L_1), resistance (R_1) and capacitance (C_1). Figure 2.2 shows a circuit diagram illustrating this. Also shown are the extra inductance (L_2) and resistance (R_2) contributions when the crystal is in a liquid and the additional inductance (L_3) caused by mass loading.

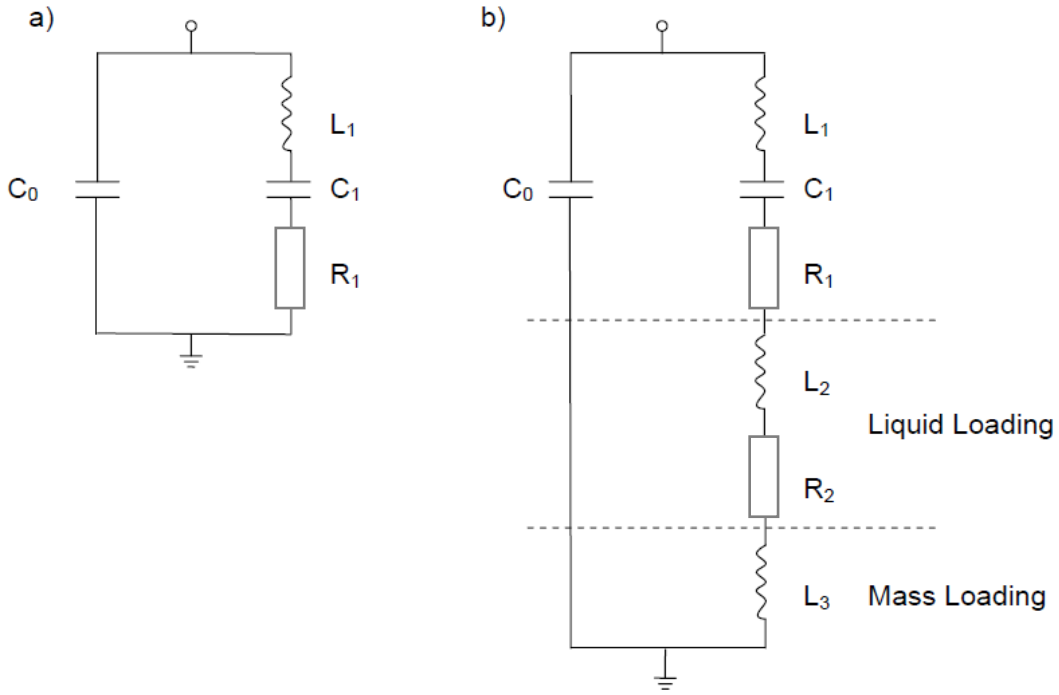

Figure 2.2: Butterworth-Van Dyke equivalent circuit model of a QCM

By using impedance analysis to measure the frequency and bandwidth of the crystal, the properties of a liquid can be determined. The bandwidth is found by measuring the loss in reflected power over a range of frequencies either side of the resonant peak. The damping of the oscillations of the crystals by the liquid is related to the bandwidth. In the case of a Newtonian liquid, the increase in bandwidth is proportional to the square root of the viscosity-density product of the liquid, as is a corresponding decrease in frequency. Figure 2.3 illustrates this effect by plotting the reflected power of a QCM against its frequency, for both a liquid loaded and unloaded crystal. The change in bandwidth is another variable which can be measured in addition to the change in frequency. If the change in bandwidth is defined as ΔB, then equation 2.12 shows how it relates to the physical properties of the crystal and the liquid and resonant frequency [34].

$$\Delta B = 2 f_0^{\frac{3}{2}} \left(\frac{\eta_l \rho_l}{\pi \mu_q \rho_q} \right)^{\frac{1}{2}} \tag{2.12}$$

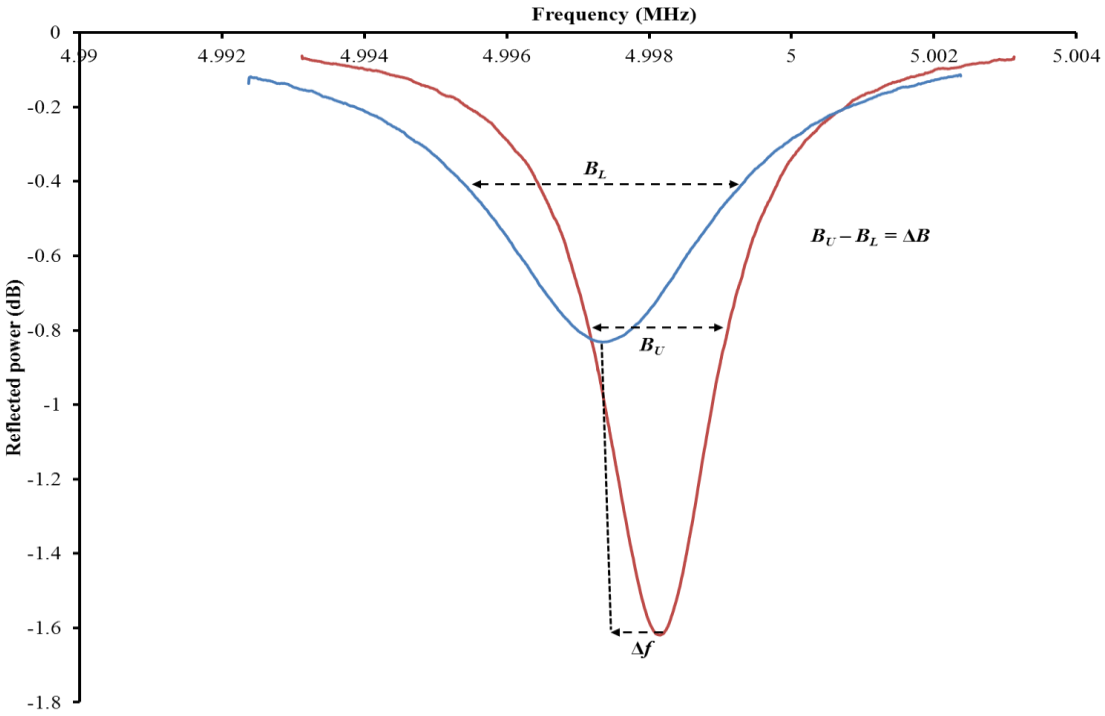

Figure 2.3: Graph showing the change in frequency and band width for a loaded (blue line) and an unloaded crystal (red line).

2.1.5 QCM oscillator circuits

A high stability oscillator can be used to drive a quartz crystal for liquid sensing aplications. The design of such a device, and the goal of making it low cost, is not easy. Arnau recently gave a detailed review of this area [35] as well as doing work improving electronic interfaces for QCMs [36]. An oscillator circuit essentially takes the form of an amplifier with positive feedback. The presence of a quartz crystal causes the circuit to lock onto the resonant frequency of the crystal.

Nimal *et al* investigated the use of a Pierce oscillator circuit for a two port acoustic wave device [37]. Eichelbaum *et al* compared three different methods of driving a crystal, impulse excitation, network analysis and oscillators [38]. Each was found to have its advantages and disadvantages. An oscillator circuit provides an analogue signal, which allows for easy digital processing, and can be constructed from low cost components. It is necessary to ensure a high stability of both the phase and the circuit itself.

2.1.6 Surface normal compressional waves in liquids

The transverse wave excited in the QCM has little effect on a liquid in contact with the surface. Beyond a small amount of liquid entrainment within the penetration depth, typically less than a few microns, the liquid remains largely unperturbed parallel to the crystal. However, studies have shown that a QCM may cause a surface normal compressional wave in a liquid [39].

These waves are capable of long range propagation into the liquid. They are even capable of being reflected from the liquid boundary, such as an air liquid interface. The reflected waves can cause the creation of cyclic compressional wave resonances. This can then affect the resonant frequency of the crystal due to the compressional waves affecting the complex electrical impedance of the QCM. The compressional wave resonance is dependent on the distance between the crystal and the liquid surface, when the distance is allows a standing wave between the crystal and the liquid boundary. So if the liquid is allowed to evaporate then this distance will reduce and move through several depths where a standing wave can be suported, Figure 2.4. Reddy *et al* showed the distance required to move through a resonance cycle in water is only 70μm, which can be achieved relatively quickly due to evaporation in an open cell.

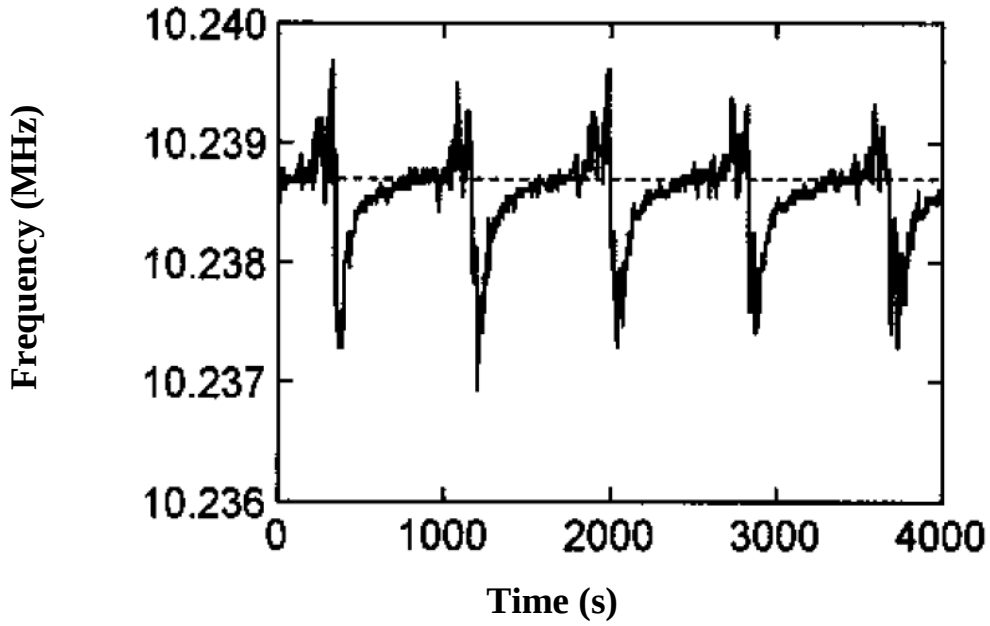

Figure 2.4: Change in QCM frequency over time as the liquid depth changes [43]

The cause of these waves is generally considered to be the non-uniform motion of the crystal surface [40-42]. An ideal model of the QCM deals with a crystal of infinite size and considers a uniform wave motion on the surface of the crystal, resulting in just the transverse wave being excited. However, a real QCM is relatively small in the lateral direction and so the wave motion across the surface is non-uniform. This non-uniformity takes on a Gaussian profile and so causes the compressional wave in the entrained liquid. Another factor to the compressional wave are flexural vibrations in the crystal [43]. These flexural vibrations couple with the shear vibrations and so contribute to the surface normal compressional wave. It is possible to use the compressional waves, in addition to the shear waves, in sensing aplications [44].

2.1.7 Operating at harmonics

As mentioned previously, the main limitation of the QCM is the relatively low frequency and the effect this has on the sensitivity. One method of overcoming this is to drive the crystal at one its harmonics. QCMs will oscillate at odd numbered harmonics, 3rd, 5th, 7th etc. While this doesn't quite compare to using a higher fundamental frequency, this method does allow for a QCM to be used at a higher frequency and so become more sensitive. Given that the Sauerbrey equation shows an f_0^2 dependence, where f_0 is the fundamental frequency, and also has an *n* term for the harmonic number, there is an important distinction between using a higher harmonic and a higher fundamental frequency. For example, a QCM with a fundamental frequency of 5MHz would have an f_0^2 of 25×10^{12}. If this was driven at the 3rd harmonic, 15MHz, the f_0^2 term would be multiplied by 3 to get 75×10^{12}. Compared to a QCM with a fundamental of 15MHz, where f_0^2 would be 225×10^{12}, it can be seen that increasing the fundamental has a significantly higher impact than operating at a harmonic. Similarly, the Kanazawa and Gordon equation has a dependence on $f_0^{3/2}$. Again, increasing the fundamental frequency has a bigger impact than using a higher harmonic.

2.2 Surface Acoustic Wave devices

2.2.1 Wave propagation modes

It was Rayleigh who, in 1885, first discovered the existence of a wave that propagated through a solid at the surface-air boundary [45]. For example, the destructive force in an earth quake is carried by just such a wave. The name Rayleigh Wave refers to a wave that exhibits a surface normal, reverse elliptical motion that propagates through the material at 90% of the speed of sound. The surface normal nature of this wave means that it becomes damped when immersed in a liquid. For this reason Rayleigh wave sensors are used in other phases, such as the gas phase [46 - 50].

Rayleigh waves were the first type of acoustic wave discovered. Later studies would discover waves with different properties, some of which are shown in Figure 2.5, but all conforming to the acoustic speed of the material through which they propagate.

Other modes include

- **Shear Horizontal Surface Acoustic Wave (SH-SAW)** – If the apropriate cut and rotation of the crystal is used then a wave with a shear horizontal component will be excited [51]. With this wave there is negligible surface normal component, rather the crystal undergoes a shearing motion normal to the surface. The result is a wave that does not suffer large energy losses when used in a liquid [17]. This makes them useful for liquid sensing [52] and as bio sensors [53, 54]
- **Surface Skimming Bulk Wave (SSBW)** – This is a shear horizontal wave, but the angle of propagation takes the wave into the bulk of the substrate. SSBW devices have also been used in bio sensing aplications [55].
- **Surface Transverse Waves (STW)** – An STW is achieved by altering the surface properties of the substrate with a periodic metal grating. The grating has a smaller periodicity than the IDTs and so causes regeneration of the wave with a smaller wavelength. The effect of this is to slow the wave at the surface and prevent it from radiating into the bulk. This creates a purely transverse wave with no surface normal component. Without a surface normal component the STW are useful for liquid sensing, but can still be used in other areas such as gas sensing [56].
- **Flexural Plate Wave (FPW)** – An FPW makes use of a thin membrane like substrate. By using a sufficiently thin substrate the wave will perturb both sides of the device. Another property is the ability to operate the device at a lower phase speed than the speed of sound in many liquids,

eliminating compressional waves. The main down side to the FPW is that due to the substrate being so thin, the device becomes very fragile. FPW devices have been used for liquid sensing [57], biosensing [58, 59] and vapour sensing [60, 61].

- **Love Waves** – By adding a guiding layer to an SH-SAW a Love wave device is made. The layer should be a material with a low acoustic speed and be thin when compared to the substrate. The layer serves to confine wave energy to the surface or the device and thus increase the sensitivity.
- **Shear Horizontal Acoustic Plate Mode (SH-APM)** – The two faces of an SH-APM device act as wave guides, keeping the wave confined to the bulk of the device. Like the QCM, the SH-APM sensitivity is related to the thickness of the substrate. More importantly, both faces of the device are involved in the motion of the wave. This allows either side of the SH-APM device to be used for sensing. SH-APMs have been used for a wide variety of aplications, including bio [62, 63] and liquid [64-66] and work has been done to investigate their mass sensitivity [67, 68].

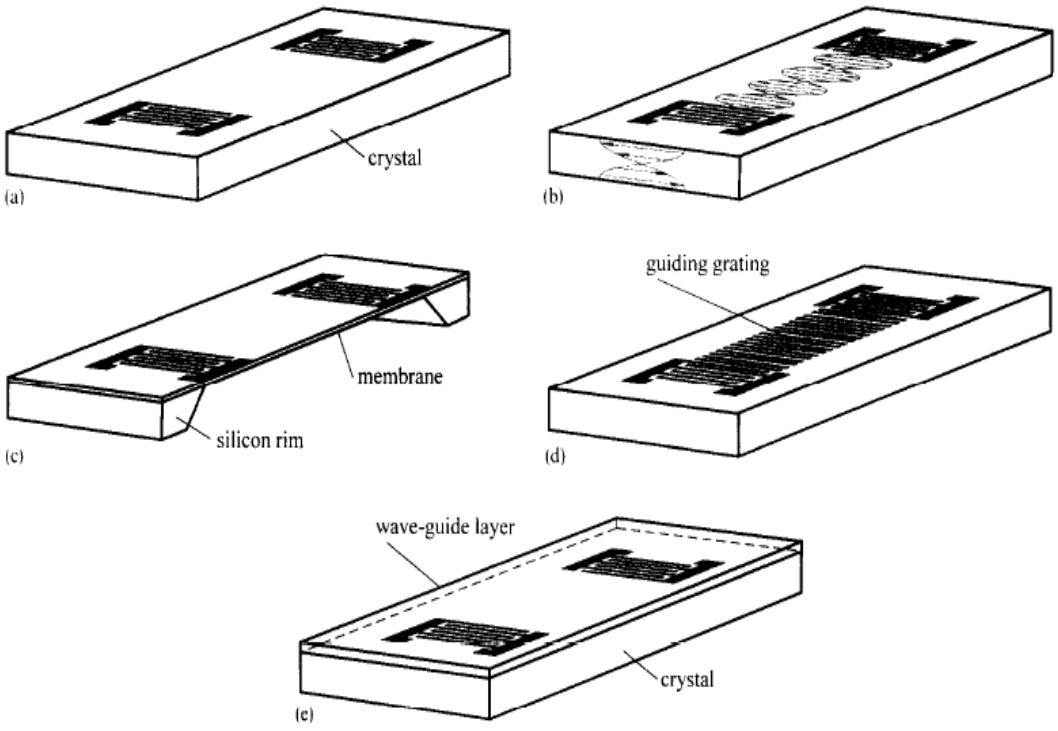

Figure 2.5: a) Rayleigh wave b) acoustic plate mode c) flexural plate mode d) surface transverse wave e) Love wave [69]

2.2.2 Interdigital transducers

In 1965 White and Voltmer developed the interdigital transducer (IDT) [8]. This was a great step forward in the field of acoustic wave technology. They would come to be key to designing higher frequency devices making use of the various wave modes. An IDT consists of a set of interlocking metallised fingers on the surface of a substrate. These fingers can be made in a variety of configurations, the most common of which is the single-single IDT. However, other designs are possible, some of which are shown in figure 2.6

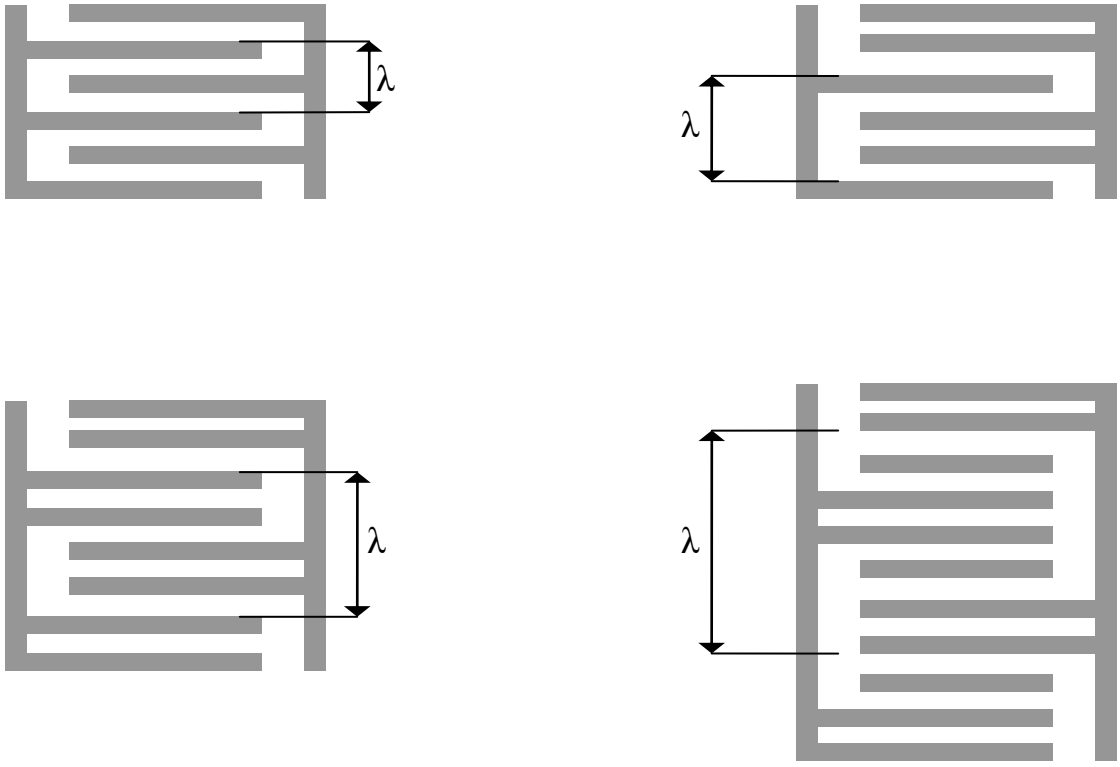

Figure 2.6: Single-single IDTs (top-left), single-double (top-right), double-double IDTs (bottom-left) and six finger (bottom right).

By aplying an alternating current to the IDTs the two sets have become alternatively charged. Due to the piezoelectric effect, a substrate undergoes a mechanical deformation as a result of the electric field. The IDTs cause this deformation to take the form of a wave, Figure 2.7.

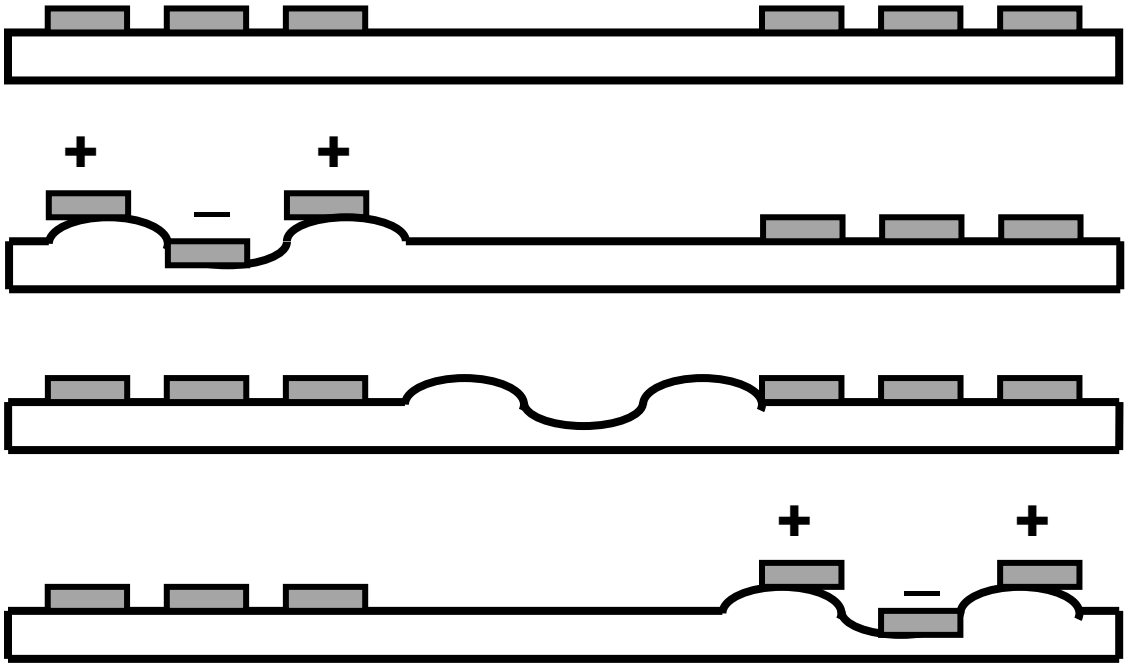

Figure 2.7: As the IDTs become alternately charged the piezoelectric substrate undergoes a mechanical deformation. Due to the periodicity of the IDTs this deformation takes the form of a wave. The second set of IDTs then picks up the electrical signal caused by this wave.

The wave length of this wave is determined by the spacing of the IDT fingers. In a standard IDT design with single electrodes separated by a whole wavelength, this dependence can be expressed as

$$\lambda = 4d \tag{2.13}$$

where d is the width of each IDT finger. In the case of a double-double IDT, the wave length is doubled. The frequency of the wave can be selected by choosing the width of the IDT fingers, provided the acoustic speed in the substrate is known. This is due to the relationship between speed, frequency and wavelength

$$f = \frac{v}{\lambda} \tag{2.14}$$

Given the acoustic speeds in piezoelectric materials and the ability to design IDTs to be as small as a few microns, acoustic wave devices typically operate in the region of 10's of MHz up to several GHz. This is the key advantage that IDT based devices have over QCMs, the ability to operate at much higher frequencies and so be significantly more sensitive. There are practical limits on the IDT size and so their

frequency. If the fingers are too small then standard photolithographic techniques are no longer adequate for fabricating the devices, placing a typical uper limit of aproximately 3 GHz which is considerably higher than the uper frequency limit of a QCM.

In addition to being able to generate an acoustic wave, IDTs can also be used to detect them. A typical arrangement is the delay-line configuration. Here there are two sets of IDTs spaced some distance apart on the surface of the substrate. One of them is used as the input and a wave propagates towards the second set of IDTs. The deformation of the crystal due to the wave cause an electrical charge. As the wave passes under the second set of IDTs the electrodes pick up this charge and, due to the periodic nature of the wave and the IDTs, a voltage can be measured. In this way the frequency of the wave at the output can be measured. By monitoring any changes to the wave when it reaches the output IDTs, the area between the two can be used as a sensing area. Since the wave speed remains constant and the wavelength is determined by the size of the IDTs, it is the frequency of the wave which changes. This configuration is known as a delay-line.

Due to the nature of a standard, single finger IDT, the wave they generate propagates in both directions causing them to be bi-directional radiators. This means that only half of the energy that produces the wave never reaches the output IDT. As a result there is an inherent 6dB loss when using simple, SAW, delay-line devices. In addition to this are various other effects, such as coupling efficiency, resistive loss and impedance mismatch, which cause most SAW devices to have an insertion loss of 15 – 30 dB.

2.2.3 Piezoelectric substrates

The three most common materials used to generate piezoelectricity are quartz (SiO_2), lithium niobate ($LiNbO_3$) and lithium tantalate ($LiTaO_3$). Each substrate has its own advantages and disadvantages and each can be used to generate different types of acoustic waves depending on the method of generation and the orientation of the crystal [70]. Quartz, for example, can be cut at such an angle so as to select the temperature dependence of the resulting device. In this way, first order temperature effects can be minimized. $LiNbO_3$ and $LiTaO_3$ do not share this property and will always have a temperature dependence no matter what cut angle is used. Other, less commonly used, piezoelectric materials include gallium arsenide (GaAs), silicon carbide (SiC), langasite (LGS), zinc oxide (ZnO), aluminium nitride (AlN), lead zirconium titanate (PZT), and polyvinylidene fluoride (PVdF).

2.2.4 SAW resonators

The use of SAW resonant cavities can be used to make up for the 6dB loss due to the bi-directionality of a SAW device. Either two port or one port devices can be used. The principle of the resonant cavity is the use of two acoustic mirrors to reflect the propagating wave and so form a standing wave between the two mirrors. There are four ways of reflecting an acoustic wave [71]. These are:

- **Mechanical/Mass loading (ML) -** This is caused by a change in the mass density and elastic properties in the path of the wave. For example, the difference between the path being metallized or not metallized.
- **Piezoelectric shorting (PS) -** If the metal fingers of the IDT or grating locally short the electric field generated by the SAW, then this can be a cause of reflections. This method is best utilised in substrates with a large mechanical coupling constant, K^2, like $LiNbO_3$ or $LiTaO_3$.
- **Electrical regeneration (ER) -** This is due to the SAW generating an electric potential (due to induced charge on metal strips) between metallized strips which are not shorted together. The effect of this electric potential is the generation of another wave. This new wave is in addition to a wave that is reflected from the strips due to piezoelectric shorting.
- **Geometric discontinuity (GD) -** GD is caused by a change in the topography of the substrate. The physical properties remain the same though. This is generally achieved by etching a groove into the surface of the substrate.

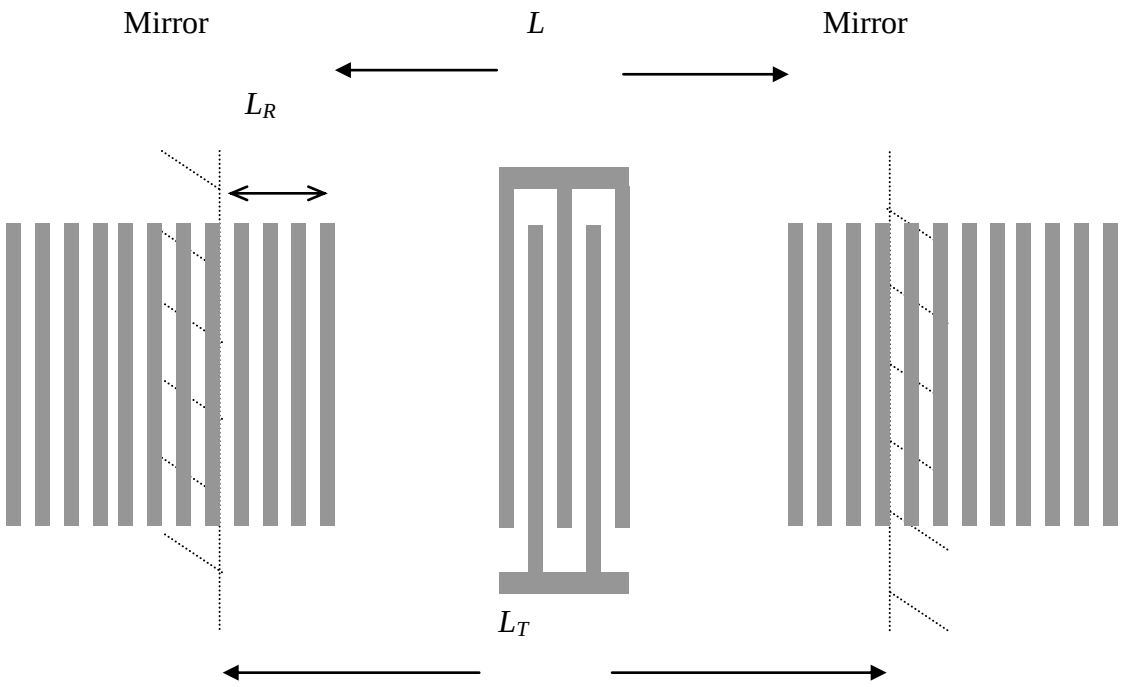

Figure 2.8: Reflection gratings act an acoustic mirror where the actual point of reflection is some distance into the grating.

Typically, the mirror will be a reflector grating. A reflector grating consists of a number of reflecting strips, each with a small reflectivity. The number of strips should then be high enough that the sum reflectivity is close to unity, Figure 2.8.

If the reflection grating is simple parallel metal strips on a strong piezoelectric substrate, then both PS and ER result. By having the strips connected the ER is different and so too is the reflectivity. This is largely dependent on the manner in which the grating is connected. The grating can be a simple closed circuit grating, or it can be some more elaborate configuration like a positive/negative reflector (PNR) grating. The PNR type has a larger reflection coefficient than either the open or closed styles. Figure 2.9 shows the three different styles of reflection grating.

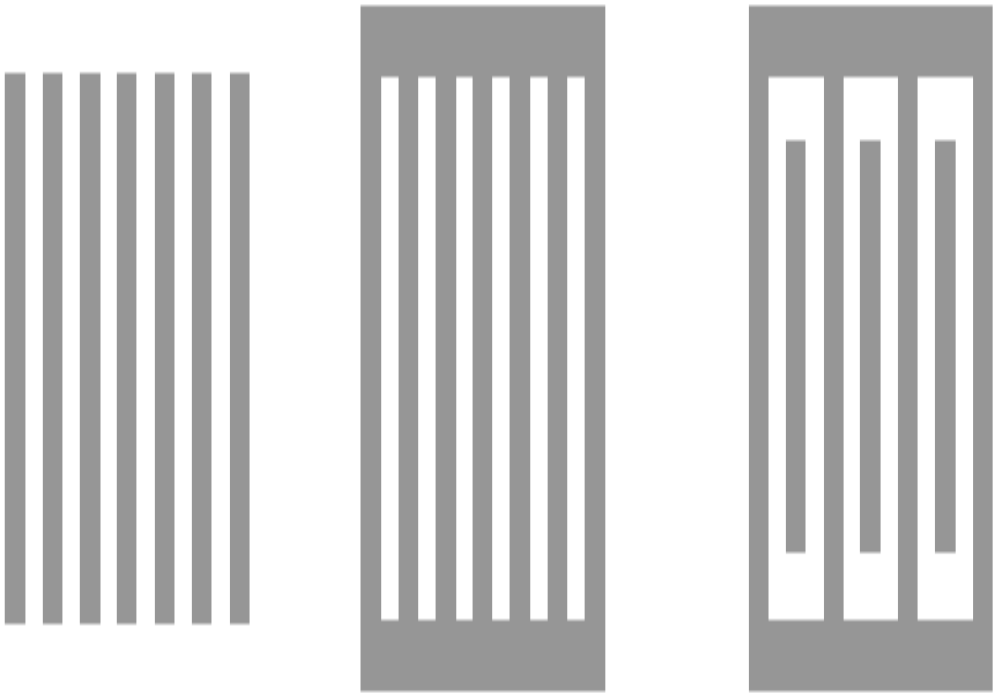

Figure 2.9: Open circuit reflector grating (left), closed circuit reflector grating (middle), PNR reflector grating (right).

2.2.5 Single-port SAW resonators

One port SAW resonators have been used in liquid sensing aplications by Nomura *et al* [72]. A single-port resonator was fabricated on a $LiTaO_3$ substrate and used for liquid sensing. Figure 2.10 shows a diagram of the device used and a graph showing the frequency response to changes in viscosity of the loaded liquid.

The sensor had a thin photoresist layer aplied to the surface. This was purely for insulating purposes and the thickness was not varied to investigate the effect on the device sensitivity. Single-ports have also been used for gas sensing [73].

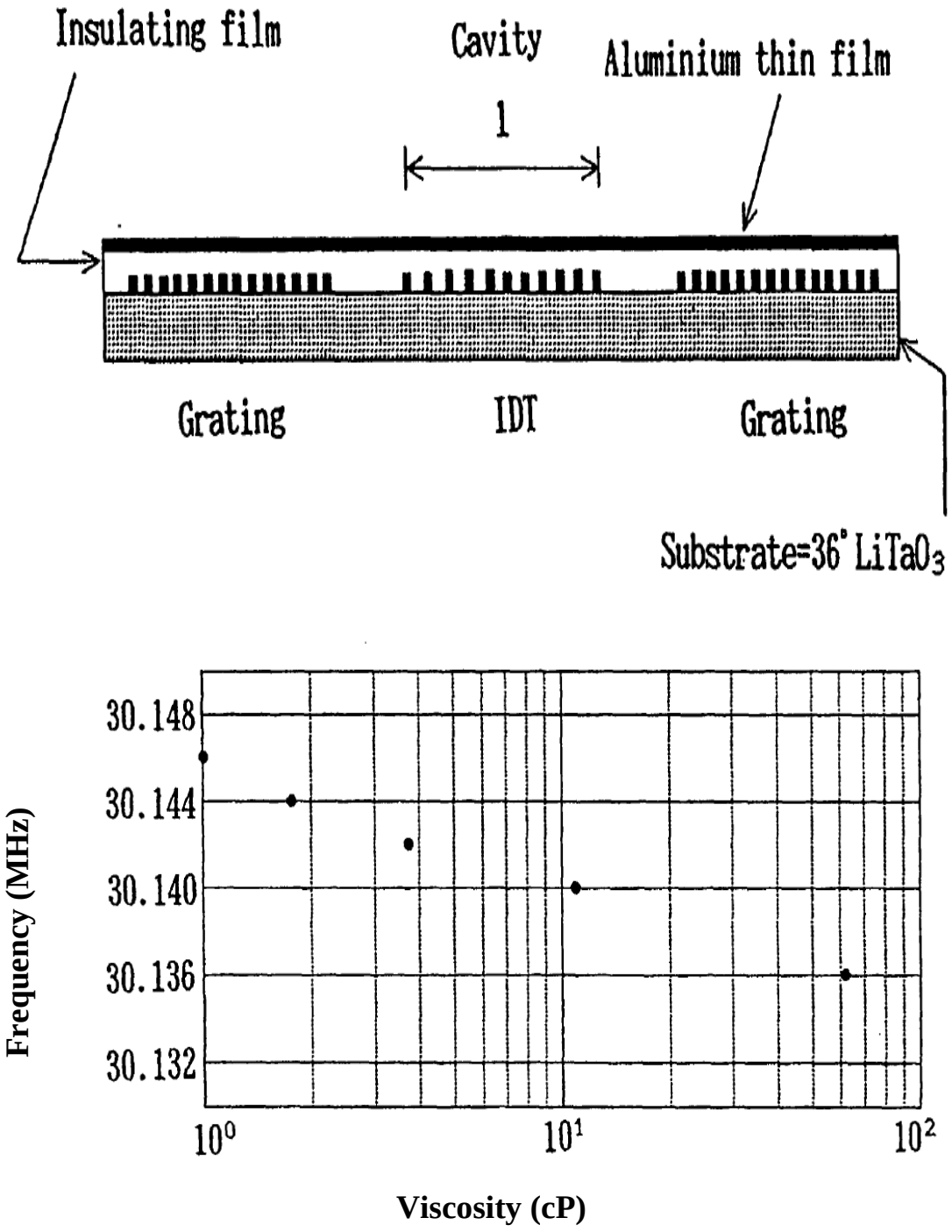

Figure 2.10: Single-port resonator with insulating layer (left) and frequency change against viscosity of water glycerol solutions (right) [72].

2.3 Layer guided acoustic wave devices

In order to improve the sensitivity of SSBW devices, a dielectric guiding layer can be added to the surface of the substrate. This converts the wave into a Love wave [74]. The material used as the guiding layer should have a lower acoustic speed than the device substrate. These were first used as sensors in 1992 [75, 9]

The layer thickness relative to the operating wavelength is related to the sensitivity of the device. The dispersion curve, Figure 2.11, for a Love wave has a sharp transition from one phase speed to another. This is what gives the Love wave device its high mass sensitivity. Aplying a mass to the surface acts like an increase in the layer thickness, so if the device is already positioned on the steep part of the curve a small change in thickness will result in a large change in phase speed. To achieve the best sensitivity, the guiding layer thickness needs to be optimised relative to the wavelength of the wave.

There are many materials that are used as guiding layers. For example SiO_2 [76, 77], silicon-oxy-fluoride [77], Polymethylmethacrylate (PMMA) [9] and the photo resists SU8 [78, 79] and S1813 [80] have all been utilised. The main property needed for a guiding layer is that the acoustic speed of the wave in the layer be lower than the speed of the wave in the substrate.

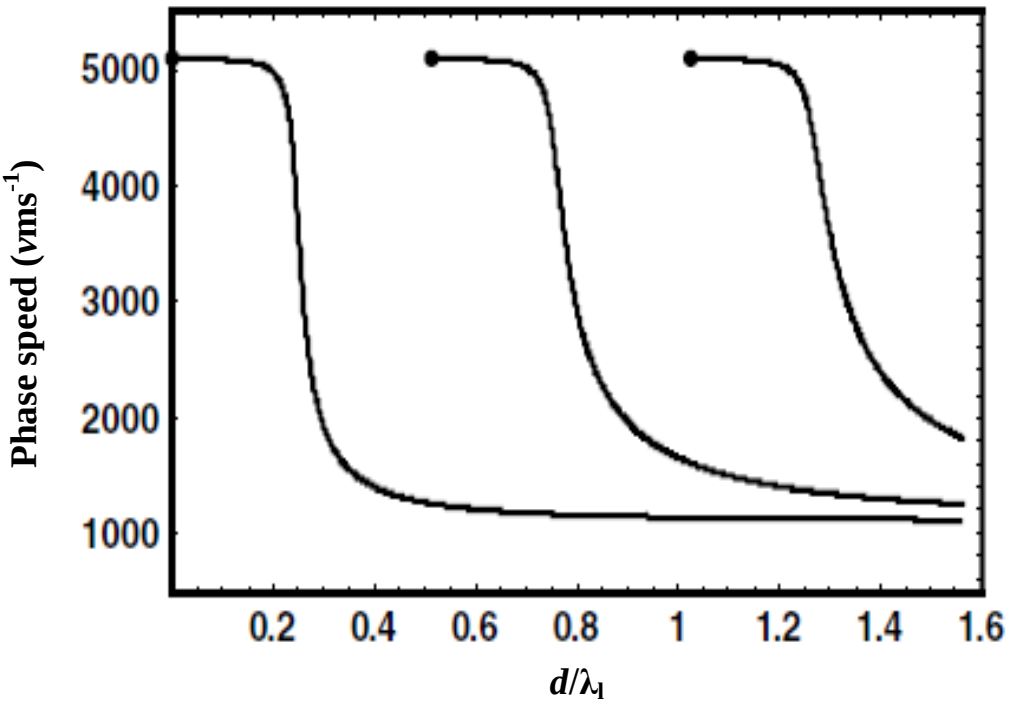

Figure 2.11: dispersion curve for Love wave device, showing wave phase speed against layer thickness divided by the wavelength of the wave.

Layer guiding is not limited to SSBW devices. Work by McHale *et al* [10, 81] and Evans *et al* [82] has shown that a guiding layer can also be aplied to an APM device. Various detailed examinations of the concept and theory of both layer guided APMs and Love waves have been performed by McHale *et al* [83-86]. Li *et al* aplied guiding layers to SH-SAW devices for liquid phase chemical sensing [11].

Love wave devices have been used for a variety of aplications, such as liquid sensing [87, 88], gas sensing [89] and biosensing [90-92]. Layer guided APM devices have also been used for biosensing [93]. It was showed by Newton *et al* that the guiding layer on a device does not have to be continuous between the two sets of IDTs in a delay-line for there to be an increase in sensitivity, provided that both IDTs are covered by the guiding layer [94].

2. 4 Sperm analysis

2.4.1 Sperm anatomy

Spermatozoa, commonly known simply as sperm, are a specialised type of cell. They are produced in the testes, via a process call spermatogenesis, for the purpose of fertilising the female ovum. Sperm cells come in motile and immotile forms, depending on the method of reproduction they are involved in. The nature of mammalian reproduction, for example, requires that the sperm be able to move on their own, ie are motile and can move through the female reproductive tract to reach the ovum [95]. The motility of these cells can be measured. Unlike most cells, sperm contain a haploid number of chromosomes, that is to say half the normal number. This is to allow them to combine with the female ovum, which also has half the usual number of chromosomes, to form a fertilised cell with a full complement of chromosomes.

The sperm cell can be said to be made of three distinct sections, the head, the midpiece and the tail [3]. Figure 2.12 shows a diagram of a mammalian sperm cell.

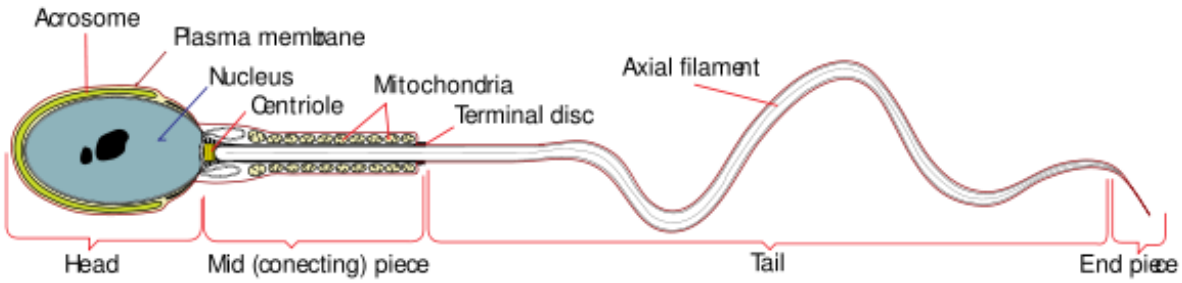

Figure 2.12: Diagram of a mammalian sperm cell (courtesy of Mariana Ruiz Villarreal)

A more detailed description of the cell includes a number of structures:

- **The nucleus -** This is the portion of the cell which contains the DNA, like most other cells. The main difference being that a sperm cell only contains half the number of chromosomes when compared to other cells in the organism, so 23 in a human sperm cell.
- **The Acrosome -** The acrosome contains digestive enzymes capable of eating through the protective layer of the ovum. These enzymes are released by a capacitated sperm upon reaching the ovum. Sperm begin de-capacitated due to chemicals in the seminal fluid, and then chemicals in the female reproductive tract re-capacitate the sperm as the head towards the ovum.

- **The Centriole -** This is a fibrous structure which is important in the mechanics of flagella movement. The centriole is made up of a number of fused microtubules. These are proteins which are important for both cell movement and structure. The axial filament is the centriole extending into the tail of the sperm.
- **The Axial Filament -** This is what causes the whip-like motion of the flagella. The microtubules in the centriole are arranged in such a way that as they slide past each other there forms a discrepancy in the lengths of adjacent tubules. The variations in length cause the flagella to bend and by rapidly altering the length of the tubules the sperm creates a whiping motion.
- **The mitochondria -** Mitochondria convert glucose, a simple sugar, into adenosine triphosphate (ATP) which sperm use to power the movement of the microtubules in the flagella and propel them forward.
- **The Plasma Membrane -** Sperm cells, like all other cells, are coated in a plasma membrane which contains all the component parts and separates them from the external environment. The membrane over the acrosome is important in sperm-ovum recognition.

While most sperm follow the same basic structure, there are variations between species. Figure 2.13 shows microscope images of six different examples of mammalian sperm.

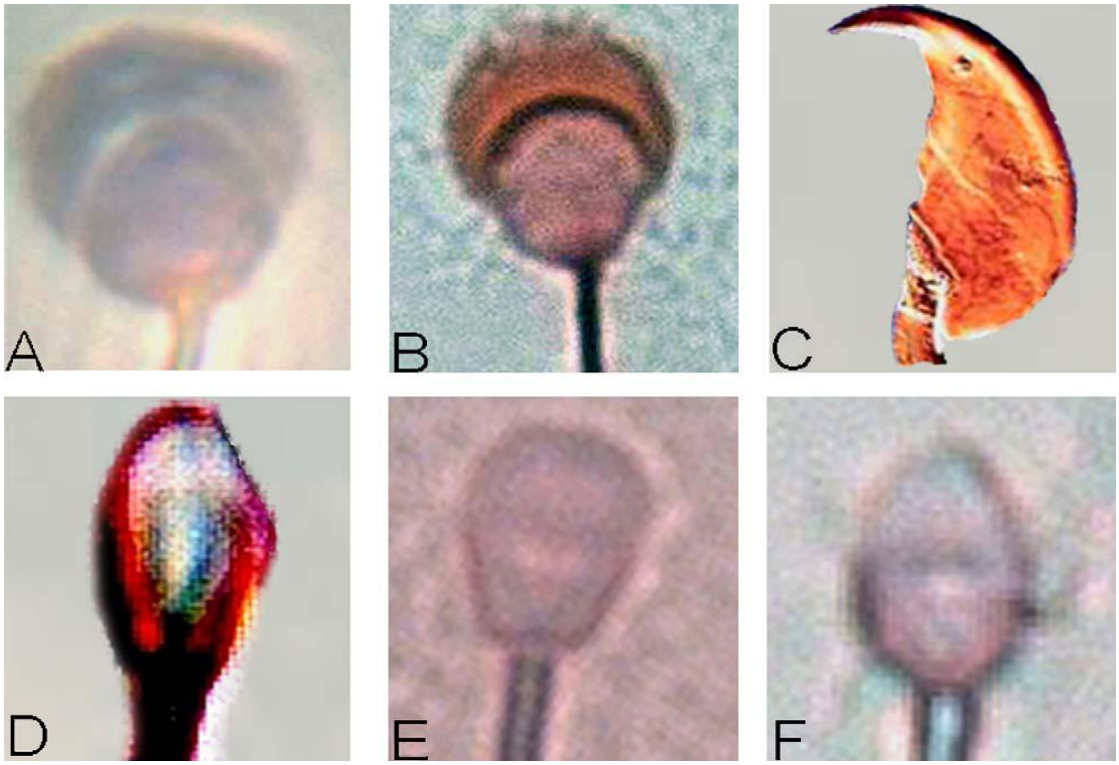

Figure 2.13: Sperm of different mammals (A) guinea pig, (B) rabbit, (C) mouse, (D) stallion, (E) dog, (F) man [3]

2.4.2 Swim method

The swim method of sperm cells has been extensively studied [96, 97] and relies on the tail, or flagellum, of the cell. The microtubules in the centriole cause the tail to flex and move in a whiping motion. By performing this motion repeatedly the cell is able to propel itself forward. This method does require that the sperm be in some kind of liquid for this to be successful. In mammalian conception, the liquid would be cervical mucus in the female reproductive tract. However, sperm are also capable of swimming through other liquids. Cervical mucus substitutes, such as hyaluronic acid, have been used for sperm migration tests [98] as has phosphate buffered saline (PBS) [7].

2.4.3 Sperm assessment

Artificial insemination is a widespread technique in both humans and animals. Central to the success of this process is the viability of the male's sperm. It is, therefore, important to be able to assess the sperm prior to insemination. There are currently a number of different techniques available to do this. All of which are laboratory based techniques which require a skilled operator to perform.

- **Haemocytometers** – These were originally designed for the counting of blood cells but have since been used to count other types of cells and microscopic particles. A haemocytometer is a large microscope slide with a rectangular groove etched into the surface to form a well for the liquid under inspection. The bottom of the well is etched with a grid of known size elements. Using a microscope the cells in the well can be counted and the concentration of the sample extrapolated to the whole of the liquid being assessed. This is a common technique for the assessment of sperm samples [99].
- **CASA** – Computer aided sperm analysis (CASA) refers to a wide range of different techniques, most of which are based on image analysis. While typically used to measure concentration, these techniques can also be used to look at velocity and other motility characteristics [5].
- **Flow cytometry and fluorescent staining** – Flow cytometry involves suspending the sperm in a liquid and sending them in a stream past an electronic detector. The detector works by having the sperm travel through a beam of laser light. Light scattered by the sperm cells is then picked up by a number of light detectors. In addition to the scattered light, fluorescent light can be also be used by

attaching fluorescent particles to the cells. This method can used to analyse thousands of sperm in a sample [6].

Modern agriculture makes extensive use of artificial insemination, whereby the sperm are introduced to the female remotely to the male. Of great importance to this process is the need to ensure that the sperm being used are of a high enough quality to achieve a high chance of conception. The above methods of sperm analysis would be unsuitable for use on a farm to test samples immediately prior to insemination. What is needed is a simpler, compact and automated technique. Su et al demonstrated a compact and light weight optical technique for the analysis of sperm [100].

2.4.4 Sperm Quality Detection Device

In a paper published in 2007, Newton et al demonstrated the use of time of flight (ToF) sensing technique for analysing sperm samples [7]. This technique made use of a QCM as the sensing element in the system. One key point of the paper was establishing that the Sauerbrey equation could be used when analysing the frequency of the QCM. By demonstrating that the bandwidth of the QCM didn't change when sperm were attached to the surface, only the frequency changed, they determined the sperm layer could be treated as a rigid mass.

They made use of a swim channel design which would allow the sperm to self propel towards the sensor where they would bind to the surface. The resultant frequency change showed sperm arrival and thus allowed the ToF of the sperm down the channel to be calculated. They showed that a simple rigid mass model could be used and therefore the Sauerbrey equation could be employed to interpret the data. The result was a method to analyse sperm quality – Sperm Quality Detection Device (SQuaDD).

The sperm used in this project were boar sperm. These are typically 45µm in length and have a dry mass in the range of 6.5 – 9.0 pg [101]. Boar sperm are known to be highly susceptible to cold shock. This is a physiological response of organisms to a sudden drop in temperature, such as freezing. The farrowing rate when using frozen and thawed boar sperm has been shown to be 47 % and 79 % when the sperm are not frozen first [102], suggesting that freezing boar sperm is not ideal.

This chapter has detailed the background and theory relating the project undertaken. In the following chapter the SQuaDD concept is developed upon in a number of ways. The technique is used as an analytical tool and environmental parameters of the procedure are investigated.

3. QCM Based Sperm

Analysis System

3.1 Introduction

This chapter deals with the preliminary experiments looking at the development of a sperm quality sensor based around a quartz crystal microbalance. Work done by Newton *et al* [7] demonstrated the principle that a QCM can be used as a real time sensor to record the time of flight of a sperm sample and to provide an estimated effective mass of individual sperm. The sperm were shown to cause a frequency change which scaled with the number of sperm on the surface of the crystal.

In this chapter a range of operating parameters have been investigated. Initially, experiments were performed to gain an estimate for the effective mass of boar sperm by using a range of different harmonics of a QCM. This involved measuring the frequency change caused by sperm being deposited onto the surface of a QCM and then calculating the total attached mass by reference to the Sauerbrey equation. A complimentary image processing technique was developed to count the number of sperm attached to the surface. A value for the average mass of a boar sperm was then calculated. Next, experiments looked at the viability of the swim cell and QCM as a sperm time of flight (ToF) sensor for sperm quality assessment. Rather than simply measuring the ToF of the sperm, the value calculated for the average sperm mass was used in conjunction with the real time frequency data to show the rate at which the sperm were arriving and the total number reaching the sensor. In so doing it is shown that the ToF system can be used for quantitative analysis of a sperm sample.

To further develop the system as a way of measuring the ToF of the sperm, and so judge their motility, experiments were performed looking at some of the operating parameters of the system. To determine the effect of temperature on the ToF, an egg incubator was used to control the temperature of the experiments. This followed the basic ToF experimental procedure, but with the temperature varying from 23 ^{0}C to 37 ^{0}C. This range covered from a typical room temperature to body temperature.

Experiments were also performed to try and reduce the ToF by chemical means. Progesterone is a substance which is believed to cause hyper activation of mammalian sperm cells [103]. To investigate whether this would have an effect on the ToF, with the hope of reducing the time taken to perform an experiment, experiments were performed in which progesterone was dissolved in a mixture of ethanol and deionised water and then diluted in the PBS swim medium. This mixture of PBS and progesterone was then used in the swim channel instead of just PBS. The ToF was recorded and compared to experiments performed without progesterone present in the swim channel.

3.2 Sperm effective mass

The QCM was used here to measure the mass of a sperm sample. To do this the crystal was placed into a purpose made crystal holder, a photograph of which is shown in figure 3.1 and a diagram in figure 3.2. The holder was designed with a reservoir over the QCM which could hold a column of liquid in contact with the surface of the crystal. The holder also allowed the QCM to be connected into a circuit or other electronic device using a BNC connector. In this case the crystal was connected to an Agilent E5061A network analyser to make measurements. The experiment performed was a three step procedure. First the reservoir was filled with PBS. Next 50 µl of sperm solution was added via syringe to the top reservoir. The sperm were then given an hour to settle onto the surface of the crystal, to assure maximum attachment to the surface. Lastly the reservoir was flushed out with PBS, to remove sperm not bound to the surface, and then refilled with PBS. At each loading the spectrum was recorded for the 7 harmonics being used.

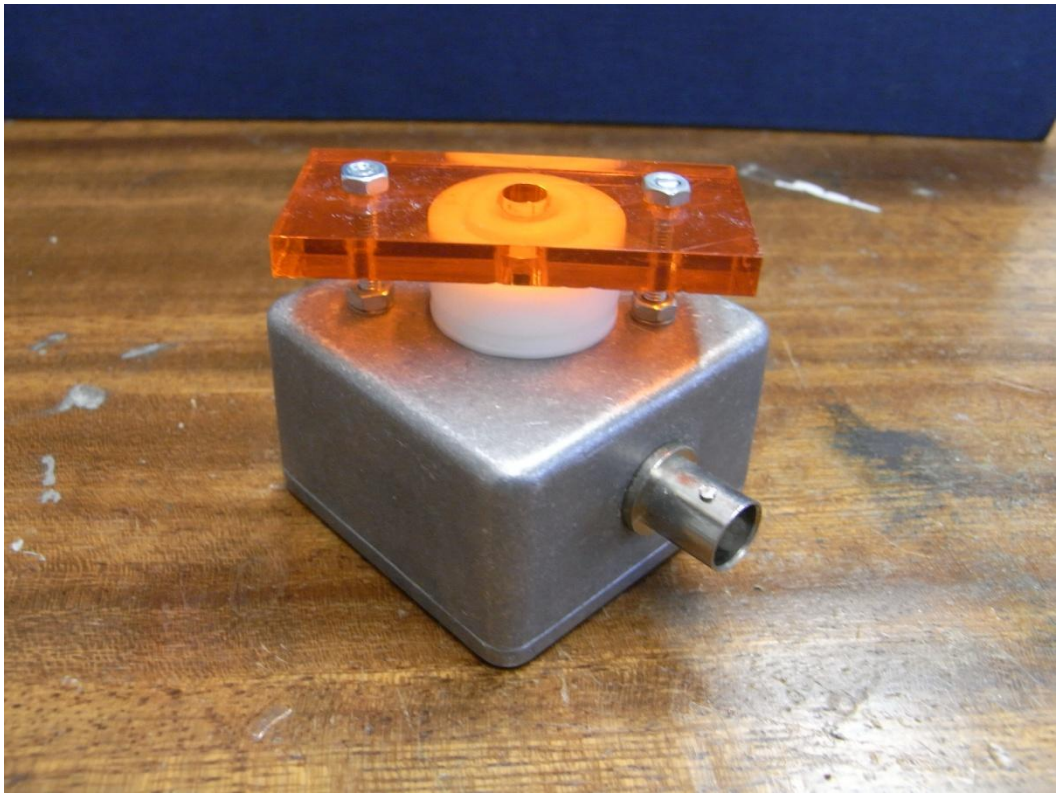

Figure 3.1: Crystal holder used for effective mass measurements.

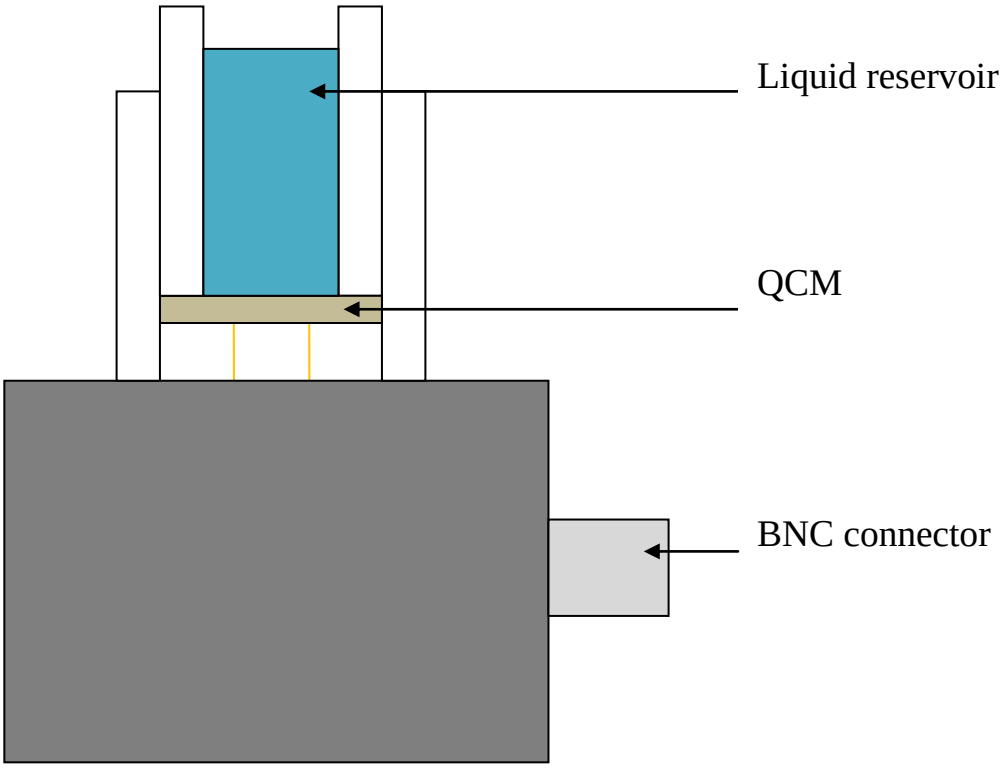

Figure 3.2: Diagram of QCM holder used in effective mass experiments

The boar sperm was suplied by a commercial artificial insemination centre (JSR Genetics, Driffield, UK). The sperm were delivered ready mixed with a diluent (TRI X-CELL from IMV Technologies) and packaged in a plastic bottle. Tri X-cell is a chemical extender designed to increase the sperm life. Tri X-cell is a mixture of Carbohydrates, mineral salts, antioxidants, buffer, antibiotics (gentamycin, amoxycillin and tylosin) and bovine serum albumin. By using this, sperm will remain useable for more than 5 days when stored below 17°C. The sperm solution sample was initially decanted into 3 centrifuge tubes, 25 ml in each. However, the concentration of the sperm is quite low in this form. Two methods were used to achieve a more concentrated sample. Initially the solution was simply left to settle overnight this resulted in the sperm becoming concentrated at the bottom of the tubes. The diluent could then be removed to leave a more concentrated sample. This method proved time consuming as it required several hours for the sperm to settle

The second method was to use a centrifuge to separate the sperm from the diluent. It has been shown that boar sperm can be centrifuged without causing any damage to the sperm [104]. Four 15 ml centrifuge tubes were filled with the sperm solution and then centrifuged at 613 g, 2800 rpm for 10 minutes. This resulted in the sperm becoming concentrated at the bottom of the tubes. The diluent was removed to leave 0.5 ml of the concentrated sperm and 1.5 ml of PBS was added to tubes. This method proved much

more time efficient and led to a more concentrated sample. Figure 3.3 shows an image of a boar sperm taken using a microscope and CCD camera.

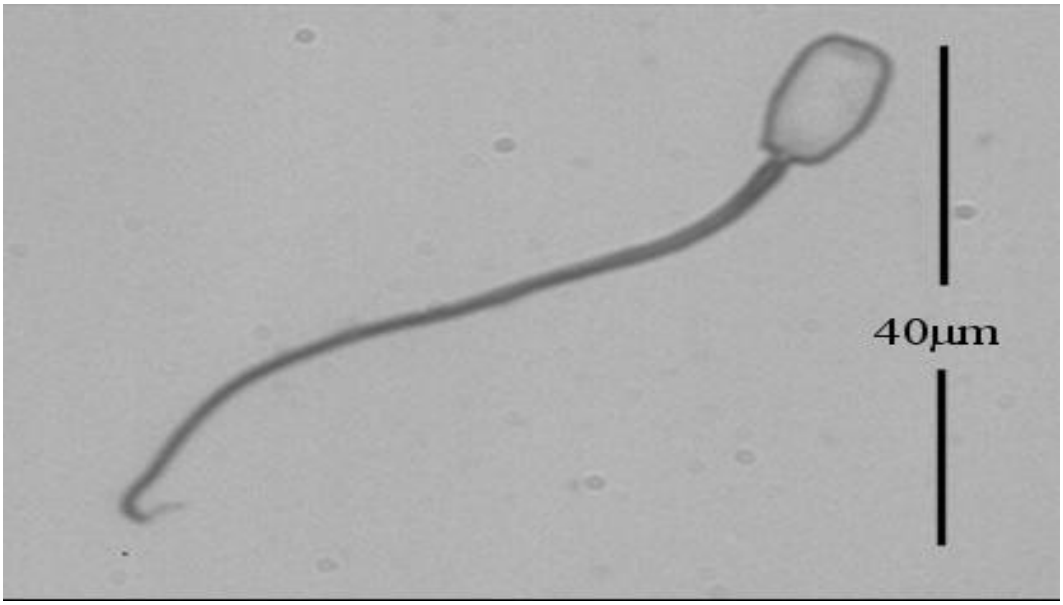

Figure 3.3: Image of boar sperm taken using a microscope and CCD camera.

Figure 3.4 shows part of the network analyser spectrum for a 13.97 mm 5 MHz quartz crystal microbalance. The network analyser causes the QCM to oscillate at a range of frequencies and measures the reflected power from the crystal. The spectrum of a QCM shows resonant peaks at odd integer multiples of the fundamental frequency, these are the harmonics of the crystal. The sensitivity of the crystal is related to the frequency it is oscillating at, so by looking at a range of harmonics the sensor response can be investigated for a range of sensitivities. The frequency and reflected power were recorded for the 1^{st}, 3^{rd}, 5^{th}, 7^{th}, 9^{th}, 11^{th} and 13^{th} crystal harmonics.

Figure 3.4 shows the 7^{th} harmonic resonant peaks for the crystal after each step in the process. The red line on the graph shows the frequency and reflected power for the QCM with PBS in the reservoir of the crystal holder. The purple line shows the spectrum after the boar sperm had been allowed to settle onto the QCM. Finally, the green line represents the crystal after the reservoir had been flushed out and refilled with PBS. As can be seen on the graph, the sperm settling on the surface of the crystal cause a frequency decrease, the difference between the red and purple lines. After the crystal has been rinsed the spectrum doesn't return to its original position, the frequency change is still present. This is shown by the green line. This demonstrates that the sperm have attached to the surface in such a way that they cannot merely be

rinsed off. The frequency change that was recorded was the change between the crystal with PBS and the rinsed crystal with the attached sperm. This was done by taking the frequency which corresponded to the lowest value for the reflected power for each of the two traces. This allowed for a quick method of measuring the frequency change which was objective and consistent.

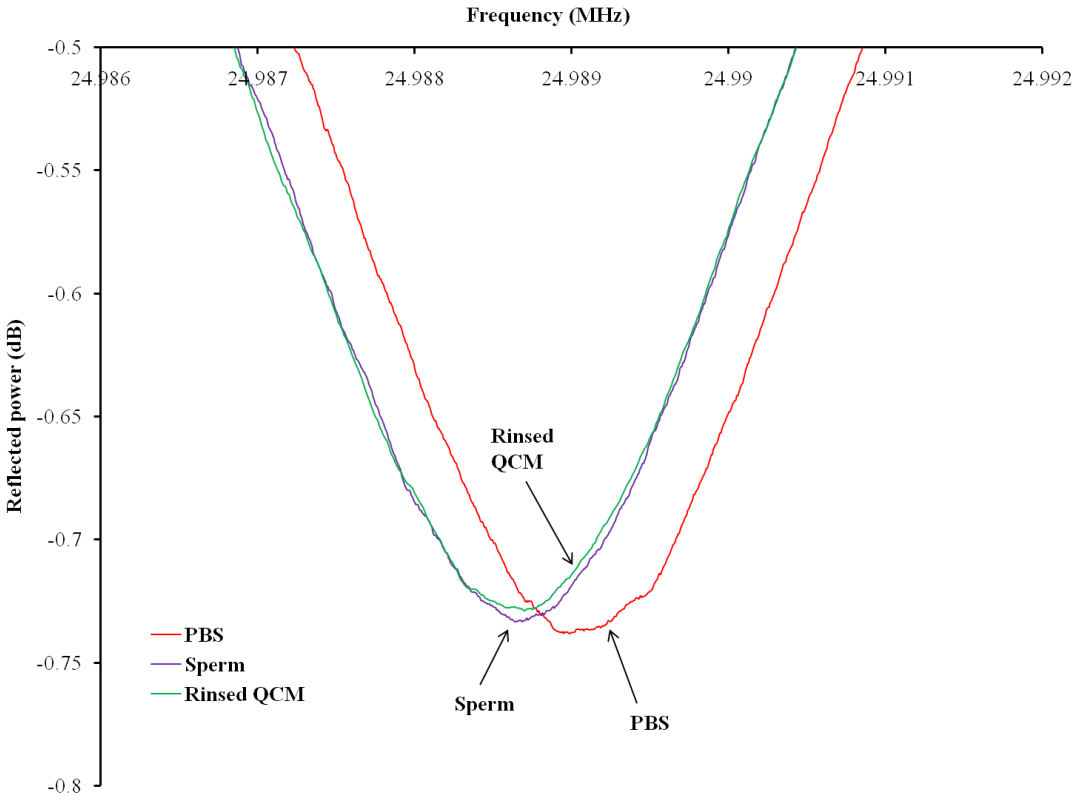

Figure 3.4: Graph showing the network analyser spectrum for a QCM in PBS (red), 50µl of sperm settled onto the surface (purple) and rinsed with PBS (green).

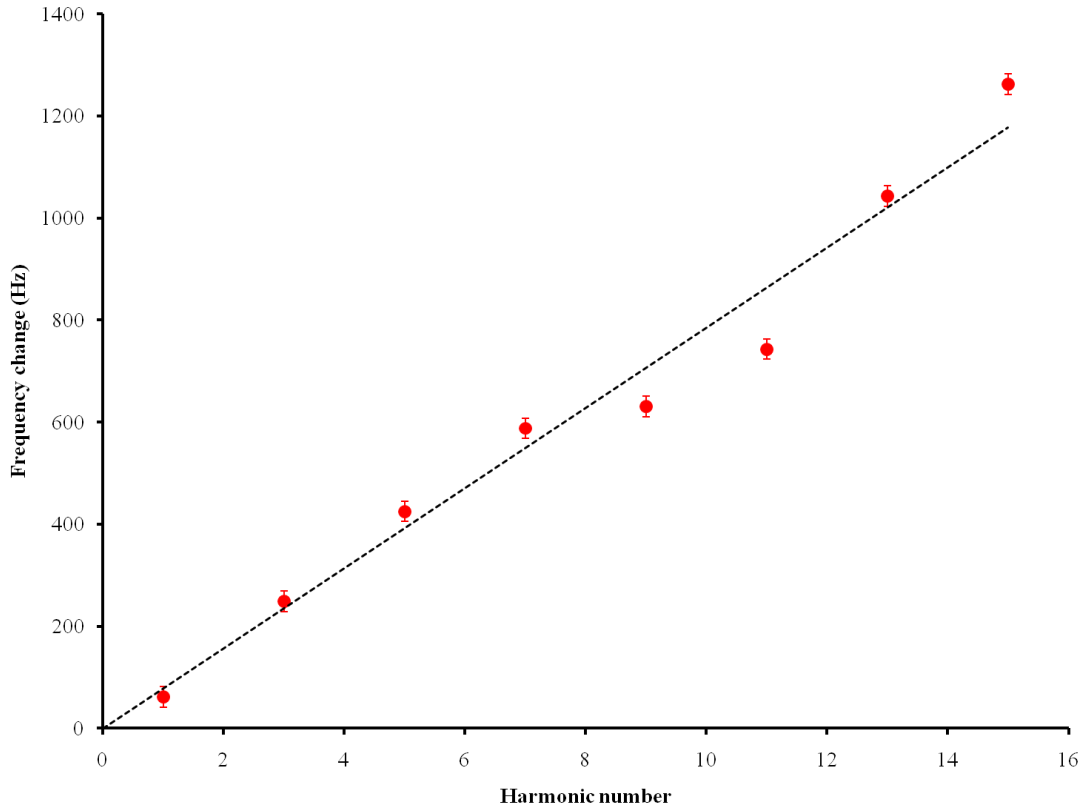

Figure 3.5: Frequency changes caused by attached sperm form a range of crystal harmonics.

Figure 3.5 shows the recorded frequency changes caused by the sperm attaching to the crystal surface. Harmonic number is displayed on the x-axis and the frequency, in MHz, is shown on the y-axis. A clear, linear relationship can be seen between the change in crystal frequency and the harmonic which is being measured. The higher the harmonic, the greater the frequency change recorded. This is consistent with the Sauerbrey equation's assertion that Δf is related to the mass attached to the crystal surface multiplied by the harmonic number. Equation 1 shows the Sauerbrey equation and how it relates the frequency change a QCM experiences to the change in mass attached to the surface.

$$\Delta f = \frac{-2n\Delta m f_0^2}{A\sqrt{\rho_q \mu_q}} \tag{3.1}$$

Equation 1 can be rearranged so that Δm is the subject. This is shown in equation 2.

$$\Delta m = \Delta f \frac{A\sqrt{\rho_q \mu_q}}{-n2 f_0^2} \tag{3.2}$$

Using the frequency changes shown in figure 3.6 and the rearranged Sauerbrey shown in equation 2, the total mass attached to the surface of the crystal can be calculated. The fundamental frequency (f_0=*5.66 MHz)*, density (ρ_q=2.648 gcm^{-3}) and sheer stiffness (μ_q=2.95x10^{11} gcm^2) of quartz and the sensing area (A=0.79 cm^2) all stay the same throughout, while the frequency change in the crystal (Δf) and the harmonic number (n) both change.

Figure 3.6 shows the calculated mass attached to the crystal for each of the harmonics measured. Attached mass is given in µg on the y-axis. The frequency change becomes greater with higher frequencies. However, the n term also increases, as the higher harmonics of the crystal are being used. As a result the value of Δm should remain constant throughout. Any variation in Δm would be due to errors in the measurement of Δf due to noise effecting the signal. In this case it is only the 1st and 11th harmonics that show any significant variation in the value for Δm, while the other harmonics measured show a more consistent value for the mass on the QCM.

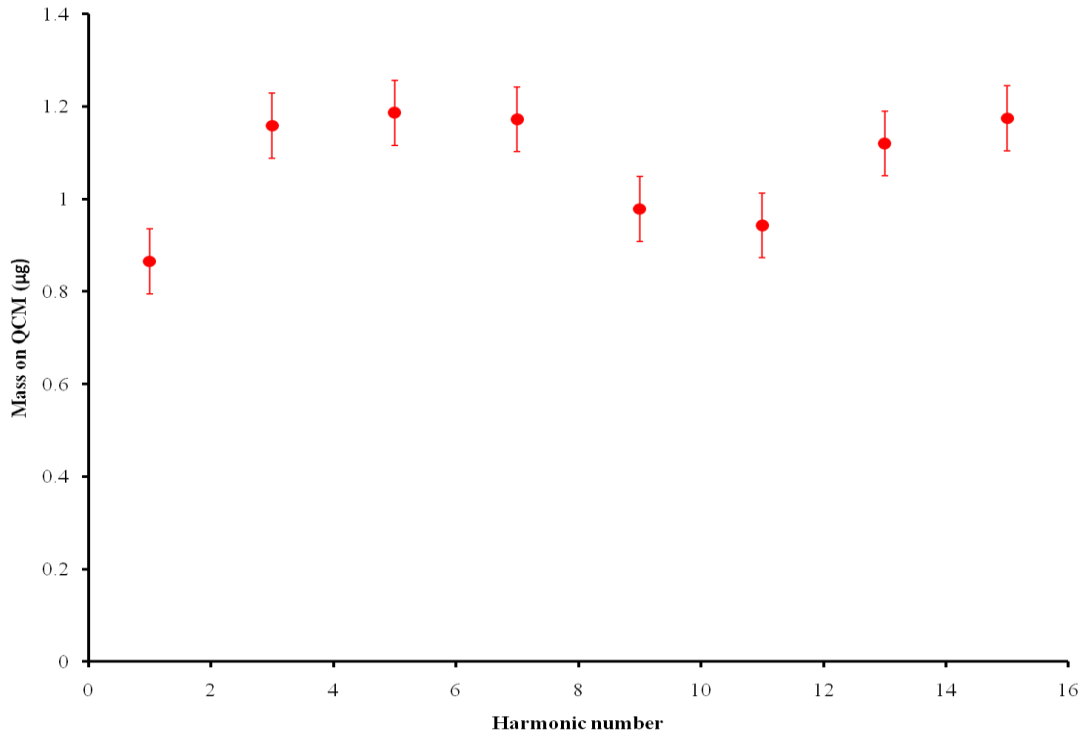

Figure 3.6: Total mass on QCM surface for range of harmonics.

In order to determine the number of sperm attached to the surface of the QCM, images of the crystal were taken using a CCD camera and a microscope. The crystal was viewed at a magnification of 200x, resulting in only a small portion of the crystal being visible. To view the entire crystal multiple images were taken and then merged together using Paint Shop Pro (Corel) to form a mosaic of the whole crystal. ImageJ was then used to analyse the image and to count the number of sperm on the crystal. Figure 3.7 a) shows a portion of the microscope image of the crystal. In addition to the sperm, there are scratches and bits of debris present on the image. The dirt may have been present on the microscope lens, the CCD and on the surface of the crystal itself.

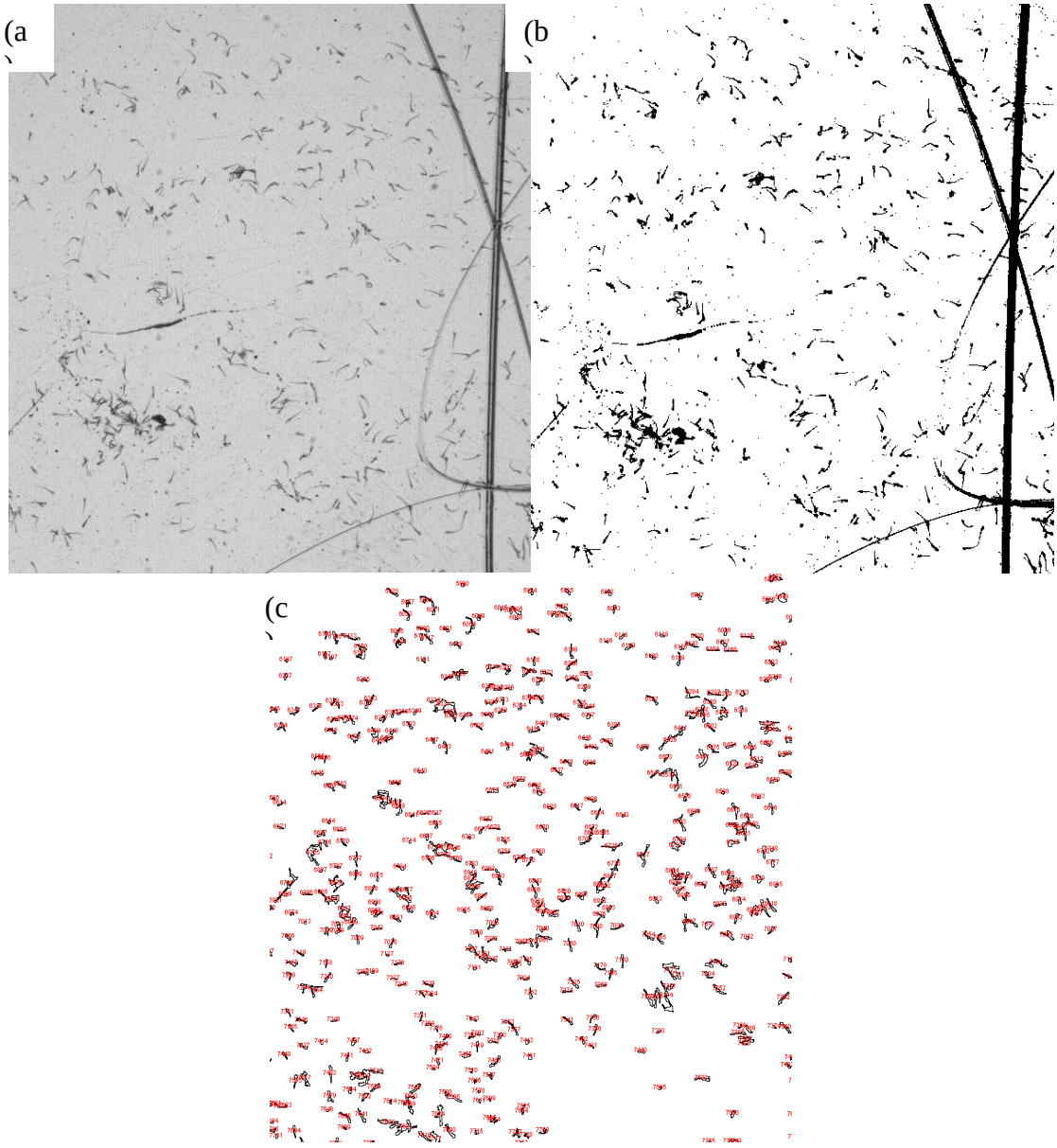

Figure 3.7: a) Image of QCM surface taken under microscope. b) image converted to binary in imageJ. c) particle analyse function used to count sperm on surface.

The full image was imported into ImageJ, where the brightness and contrast were altered and the threshold function used to eliminate many of the artefacts and to convert the image into an 8 bit binary format; this can be seen in figure 3.7 b). Next the "analyse particles" function was used to count the number of sperm, figure 3.7 c). ImageJ allows the particle size to be set so as to eliminate anything on the image which is too big or too small to be a sperm cell. By this method, an estimated 140000 sperm were attached to this particular crystal. This figure for the number of attached sperm directly corresponds to the spectrum taken of the crystal after it has been rinsed, removing any unattached sperm from the reservoir.

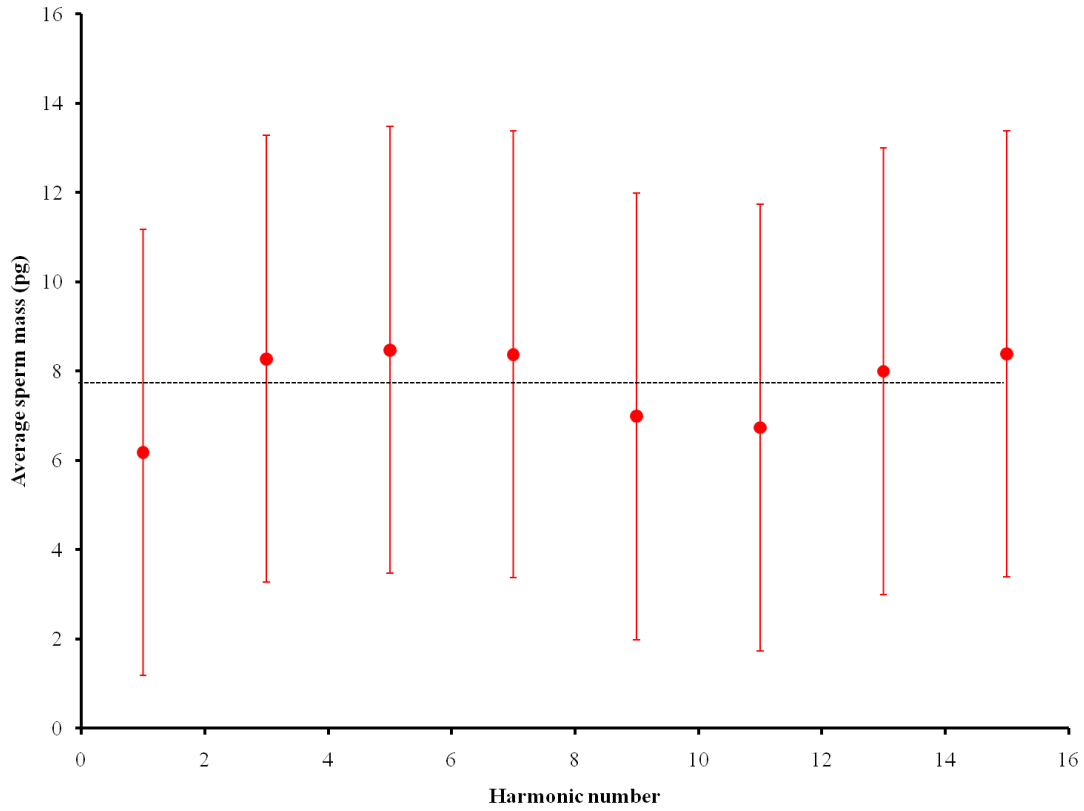

Figure 3.8: Average mass of sperm attached to the surface of QCM.

Given the mass attached to the QCM, calculated in figure 3.7, and the estimate for the number of attached sperm, the average effective mass of the individual sperm was then calculated. This was simply a case of dividing the total mass by the number of sperm. Figure 3.8 shows the average mass per sperm (in ng) plotted against the crystal harmonic. The mass is consistent across the harmonics, taking into account the various errors involved, and gives an average of 8 ± 5 pg. The mass calculated also gives close agreement with the published value of 6.5 – 9.0 pg [101] and the 6.4 ± 1.4pg per sperm effective mass that had previously been calculated by Newton *et al* [7].

3.3 Sperm analysis

3.3.1 Time of Flight

This experiment used a swim cell with 25.4 mm diameter 5 MHz AT-cut QCM (Testbourne 149211-1) acting as the sensing element, figure 3.9 shows both a diagram and image of the experimental set up. This consisted of an inlet port to a channel filled with phosphate buffered saline (PBS). Half way down

the channel is the QCM. After that is a vent to air, which helps to reduce any sensor response due to pressure changes when the sperm sample is introduced into the inlet. The length of the channel was 14.5 cm and the diameter is 0.1 cm and it contained 4 ml of buffer. This was constructed using plastic and PTFE. Rubber o-rings provided a water tight seal. A PLO-10 phase lock oscillator from Maxtek was used to drive the QCM; while an Agilent 53132A universal frequency counter measured the frequency. The frequency counter was connected to a laptop using a GPIB-USB-B cable (National Instruments). To record the data, a program was written in LabVIEW (National Instruments). The program would record the frequency from the frequency counter measured against time and display the data as a graph whilst also saving it to a spread sheet file.

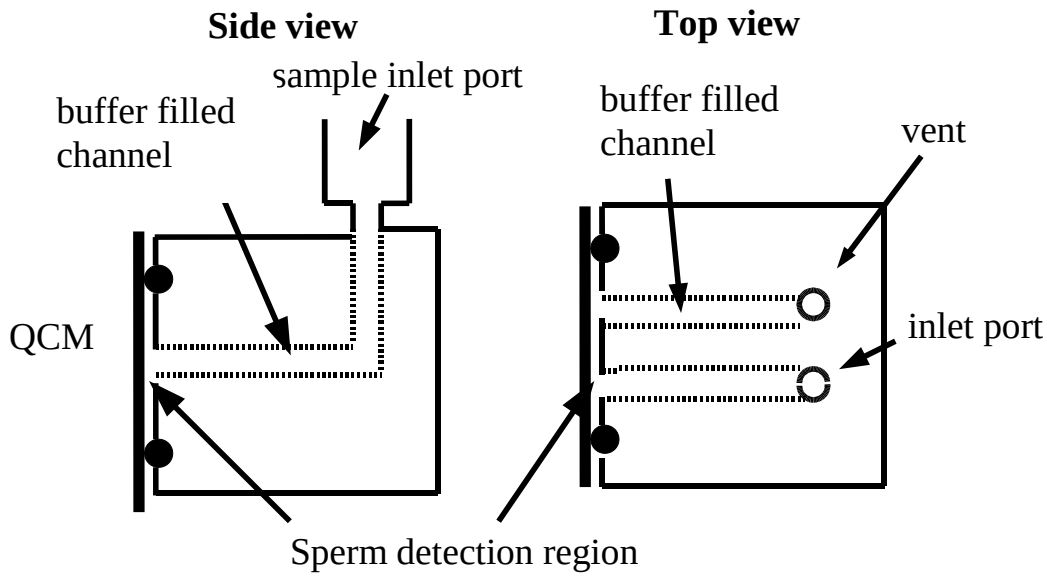

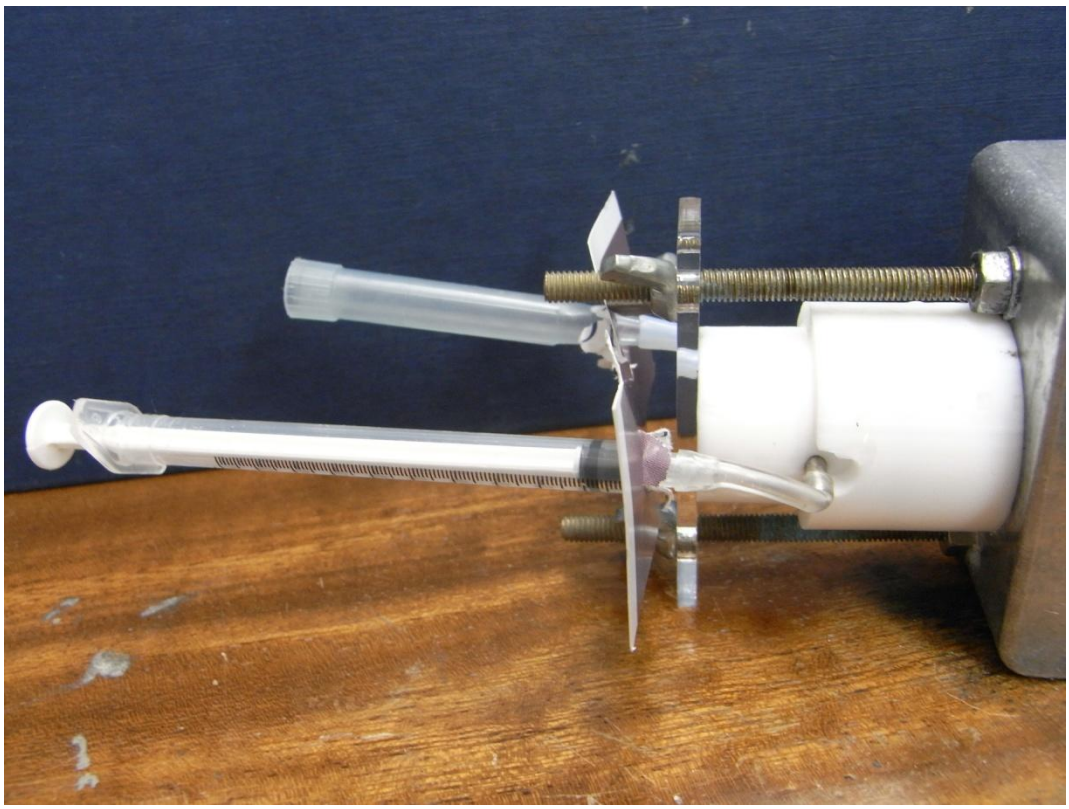

Figure 3.9: Top: diagram of swim cell. Bottom: Image showing the sperm swim cell.

Figure 3.10 shows a typical QCM frequency response, operating at the fundamental frequency, from a ToF experiment. On the graph, time is given in seconds along the x-axis and the crystal frequency is shown in MHz on the y-axis. The introduction of 50 µl of sperm into the channel is zero seconds on the x-axis. After the sperm have been added the frequency remains roughly constant for aproximately 1200 seconds. After this time a frequency change can be seen. The frequency change signifies that the sperm

have made their way down the channel and arrived at the crystal surface. Once at the QCM they begin to attach to the surface and cause the frequency to decrease.

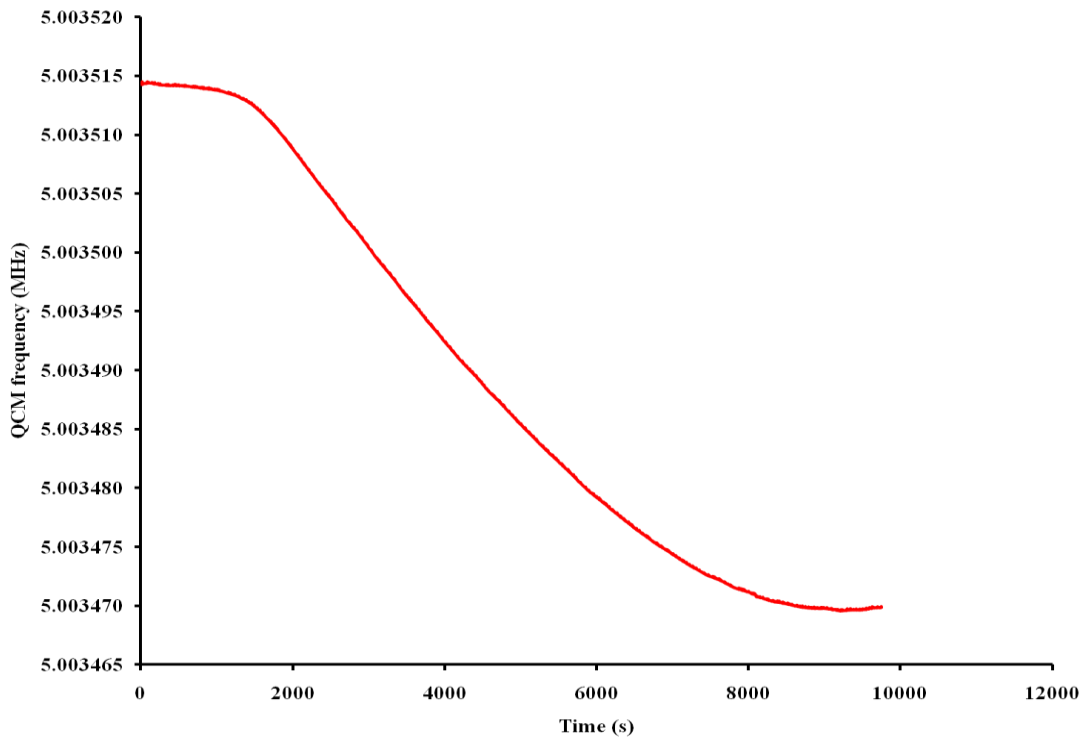

Figure 3.10: QCM frequency against time for ToF experiment, sperm added at zero seconds.

The frequency continues to decrease as more sperm make their way to the QCM and attach to the surface. This frequency decrease continues for a further 90 minutes. After 90 minutes the frequency stops decreasing and the graph begins to level off. This signifies that the arrival of motile sperm at the sensor has ceased.

3.3.2 Rate of sperm arrival

The first thing that was necessary to do in order to analyze the data was calculate the frequency change of the QCM. Using the average sperm effective mass of 8 pg calculated previously; see figure 3.9, and taking the frequency change data, the Sauerbrey equation was used to derive the number of sperm arriving at the QCM. First the frequency change data was converted into a mass change, see equation 2. This mass change value was then divided by the average sperm mass to give the total number of sperm reaching the crystal against time. This is shown in figure 3.11, where the number of sperm and the frequency change follow the same plot. For use in a screening aplication, a simple threshold number of detected sperm would be required. However this does demonstrates that quantitative analysis is also possible with this instrument.

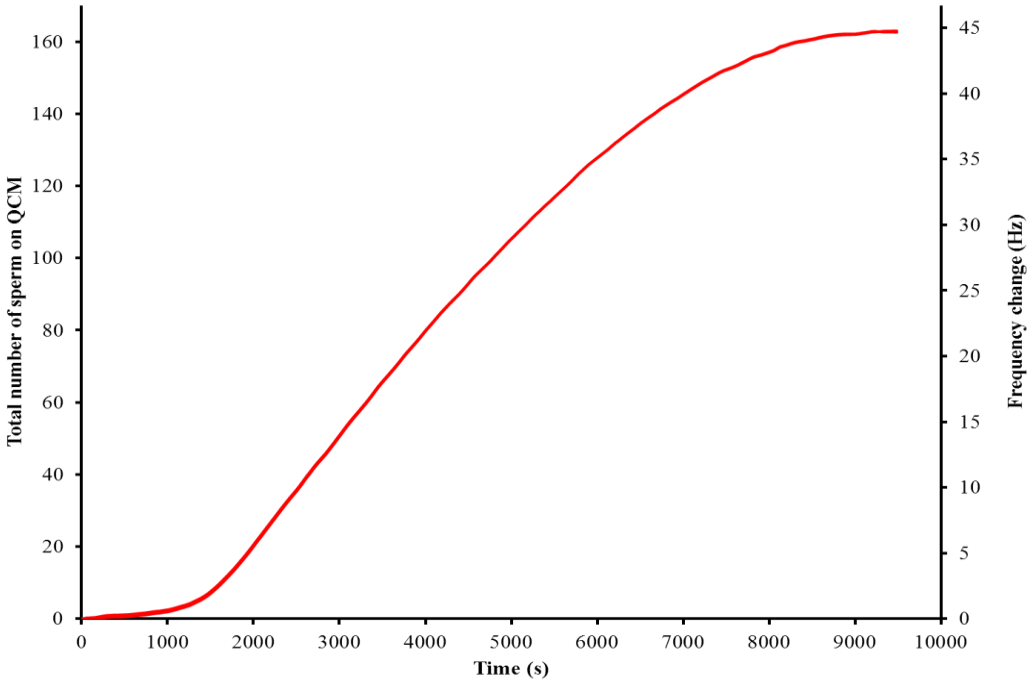

Figure 3.11: Graph showing frequency change and total sperm attached to surface of the QCM.

3.4. Operating parameters of swim channel

Experiments were performed to investigate certain operating parameters of the system. The parameters looked at were the environmental temperature and the chemical makeup of the swim medium.

3.4.1 Effect of temperature

For the experiments performed to investigate the effect of temperature on the sperm time of flight, an Octagon 10 incubator (Brinsea) was used to control the temperature of the experiment. The incubator gave good temperature stability up to 50 ^{0}C. The swim cell was placed into the incubator and the temperature increased to the desired level prior to experiment being performed. Once the swim cell was inside the incubator the channel was filled with buffer and the whole aparatus allowed to reach an equilibrium temperature. The sperm samples were also placed in an incubator at the same temperature as the swim cell. This was done so the sperm solution and the buffer in the swim cell were at the same temperature, and so prevent the QCM from reading any temperature difference when the sample was added.

Figure 3.12 shows the effect of altering the temperature on the ToF of the sperm. The incubator was set at a range of temperatures from 23 ^{0}C to 37 ^{0}C. This range covers from a typical room temperature to body temperature. The results show a decrease in the ToF as temperature increases with almost a 50% fall over the temperature range covered. The scatter observed can be attributed mainly to the experiments being performed at differing lengths of time from the receipt of the samples and the quality of the sperm degrade over time.

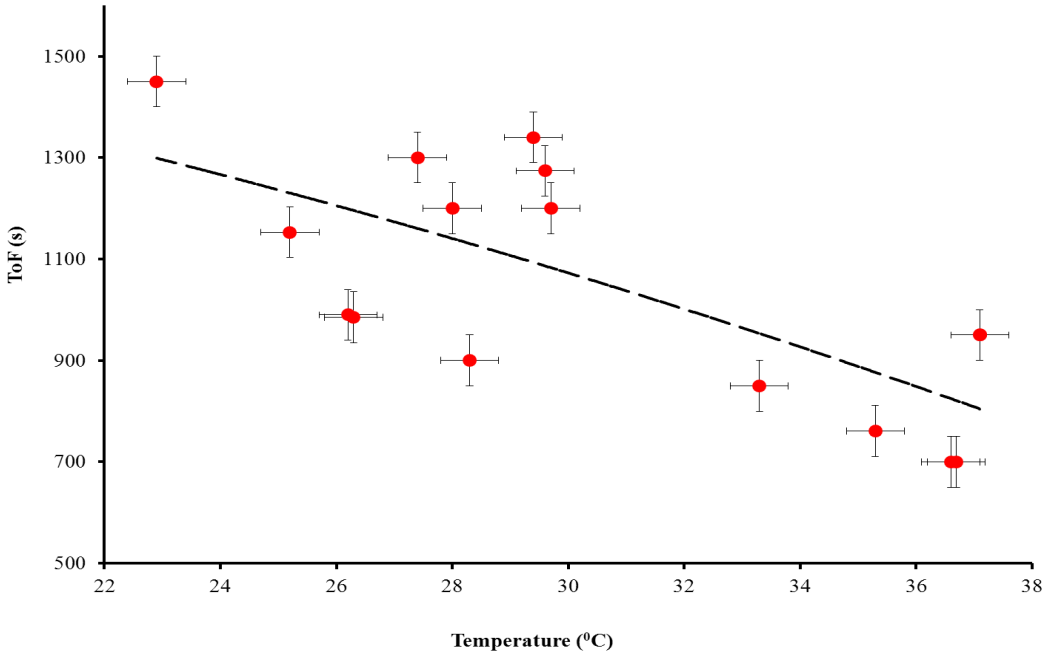

Figure 3.12: Sperm ToF against swim channel temperature.

3.4.2 Effect of progesterone in swim medium

To alter the chemistry of the swim medium, progesterone was added to the PBS. Progesterone is a hormone involved in the female menstrual cycle, embryogenesis and pregnancy. It is also one of a number of substances believed to cause hyper activation of mammalian spermatozoa. The progesterone was first dissolved in ethanol; 15.7 mg in 50 ml of ethanol gave a 1mmol solution. This was further diluted, using PBS, into aliquots ranging from 20 to 90 µMol of progesterone. The temperature of the experiments was kept at a constant 34 ^{0}C for all the experiment with progesterone. Again, the temperature was controlled with an incubator.

Figure 3.13 shows the ToF of various sperm samples and the effect of having progesterone present in the swim channel has on it. The red circles show the time of flight for the range of progesterone concentrations, from 20 to 90 µmol. Then, for comparison, the same experiment was performed with a progesterone concentration of 0 µmol, also with an environmental temperature of 34 ^{0}C. The non-progesterone results are shown by the green triangles.

There is a clear and dramatic difference in the sperm time of flight between the experiments performed with and without progesterone. The presence of progesterone in the swim medium gives a ToF

decrease of almost 50%. A clear connection between the specific progesterone concentration and the sperm ToF was not observed overe the concentration range investigated.

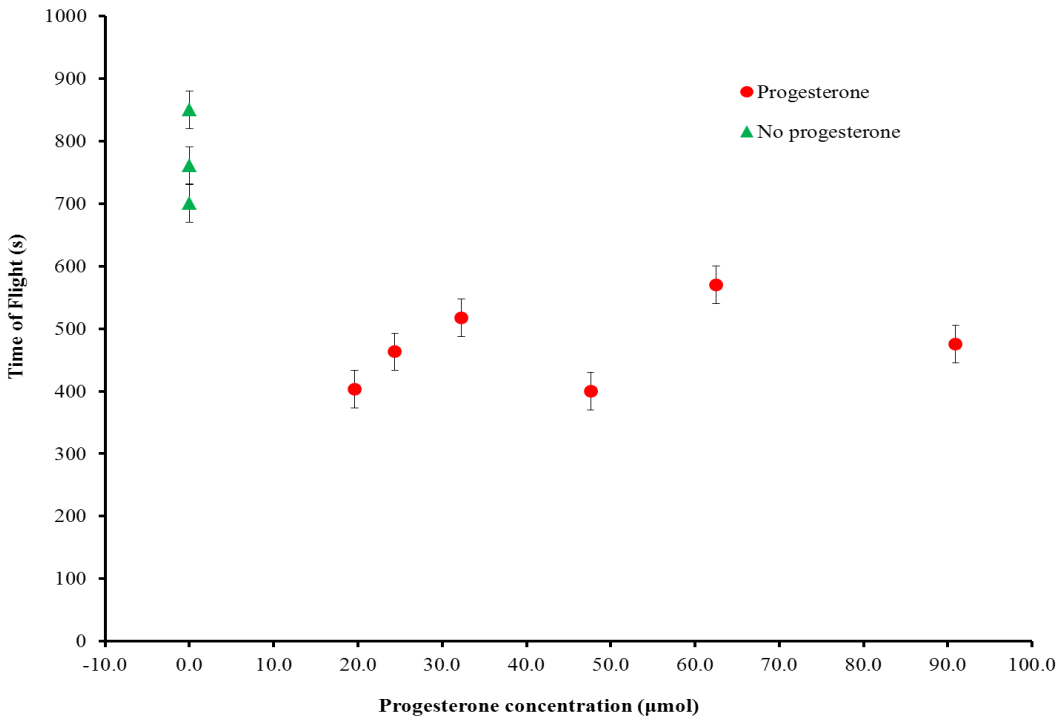

Figure 3.13: Graph showing comparison of ToF for experiments conducted with and without progesterone present in swim channel.

3.5 Discussion

This chapter has shown a ToF technique using a QCM to analyse samples of boar sperm, developing on work done by Newton *et al* [7]. They measured the ToF of sperm samples and determined an effective average sperm mass. Their average sperm mass was determined by manually counting the sperm attached to the surface of the QCM and gave a value of 4.2±3.7 pg.

This work used image processing to speed up the process and hopefully provide a more accurate result. Newton *et al* used a microscope to manually count the sperm attached to the surface of the QCM, a technique that is both time consuming and susceptible to human error. In this work a CCD camera and a microscope were used to capture images of the QCM surface, an image processing program (ImageJ) was then used to count the sperm. This method proved faster than manually counting and resulted in a value of 8±5 pg, which is closer to the literature value of 6.5 – 9.0 pg [101].

The novel aspect of this chapter was to combine the sperm effective mass with the frequency data from the QCM. The frequency data from the QCM was converted into a mass value using the Sauerbrey equation. From the total mass on the surface, the number of sperm on the QCM could be calculated. This would show the rate at which the sperm reach the QCM, as is shown in figure 3.11. This means that the system can be used to make a more detailed investigation of a sperm sample than simply measuring the ToF of the sperm. However, the system could go further still. By plotting the gradient of the sperm arrival graph, figure 3.11, against time it would be possible to show the distribution of sperm arrival, a normal distribution of the sperm in this case. This type of analysis would give a more detailed view of the motility of the sperm in the sample. Changes in the sperm distribution could then be investigated, such as the effect of sperm aging or the effects of progesterone or temperature.

One problem with the system as presented in this chapter was the length of time necessary to perform an analysis. With a ToF of nearly 10 minutes even for the progesterone experiments, and the time for the sperm to stop arriving on top of that, the time for one experiment was unacceptably long. The 6 cm path length could be reduced to lower the ToF, which is investigated in chapter 5, and so reduce the overall time to perform an analysis.

This chapter also examined the effect of progesterone on the ToF of sperm. A recent study by Lishko *et al* [103] examined how progesterone interacts with the sperm. It was shown that progesterone induces calcium influx into the sperm cell triggering, amongst other processes, the hyperativation of the sperm. The work done in this chapter used micromolar concentrations of progesterone, which seems to be above the saturation level for the sperm used. Figure 3.13 shows a significant decrease in the ToF, but no clear relationship between concentration and ToF over the range investigated. Lishko *et al* used nanomolar concentrations and others, such as Teves *et al* [105], use picomolar concentrations. It is likely that micromolar concentrations are well above the threshold level where increasing amounts of progesterone would stop having an effect, explaining the lack of a relationship between progesterone concentration and ToF over the concentration range used here. Further work using smaller concentrations, perhaps picomolar levels, of progesterone would likely show a clearer relationship between the ToF and concentration.

There were a number of areas where the system could be improved. One of the main limitations of the QCM is its sensitivity. It is possible to manufacture significantly more sensitive devices using IDTs. The following chapter describes the development of such a device using a single-port acoustic resonator. Using a single port would maintain the relative electronic simplicity of the QCM, while gaining the improved mass sensitivity of a SAW device.

3.6 Conclusion

It has been shown that the QCM can be used as an effective mass sensor for the sperm. By taking frequency data recorded on a network analyser and aplying the Sauerbrey equation, it was possible to calculate the effective mass of a sperm sample attached to the surface of a QCM. Then, with image processing performed in ImageJ, an estimate for the number of sperm attached to the crystal could be made and so determine a value for the average effective mass per sperm. This would prove important for the sample assessment using the ToF technique. The ToF experiments were successful in giving a value for the time taken for the sperm to make their way down the channel and, using the calculated average effective mass per sperm, a rate at which they arrived. This demonstrated that the time of flight technique with a quartz crystal micro balance provided a viable method for assessing the quality of a sperm sample. Motility was judged by measuring the time of flight and overall quality of the sample could be inferred from the number of sperm reaching the sensor. As such the ToF technique could be used as both a screening technique and for use as an analytical tool.

Experiments varying the temperature showed a general decrease in ToF as the experimental temperature was increased. This suggests that performing the experiments at a temperature higher than that of room temperature would create a more time efficient procedure. Similarly, the presence of progesterone also reduced the ToF of the sperm. However, there was no clear link between the specific concentration and ToF over the range of progesterone concentrations investigated. An experimental procedure that both increased the temperature to a more optimum level and altered the buffer composition, to further increase the speed at which the sperm reach the crystal, would yield results much faster.

There were a number of areas where the system could be improved. One of the main limitations of the QCM is its sensitivity. It is possible to manufacture significantly more sensitive devices using IDTs. The following chapter describes the development of such a device using a single-port acoustic resonator. Using a single port would maintain the relative electronic simplicity of the QCM, while gaining the improved mass sensitivity of a SAW device.

Additional work was needed to improve the swim cell itself. Ideally the channel length would need to be shorter and the cell would need to be easy to manufacture and more compact. Additionally, the electronics used in this chapter, the Agilent frequency counter and the Maxtec oscillator, needed to be replaced by smaller, cheaper and easily fabricated alternatives. This work is detailed in chapter 5.

4. Single-port SAW

Resonators

4.1 Introduction

This chapter deals with the development of a single-port acoustic resonator as a possible alternative to the QCM as the sensing element in the sperm quality analysis system. The limitation of the QCM as a sensing device is mass sensitivity of the device. Due to the practical limit on the thickness of a QCM, it is hard to make a crystal thin enough to resonate at high frequencies without it becoming unusably fragile. Since the frequency is related to the sensitivity, QCMs are limited in how sensitive they can be made. Acoustic wave devices making use of IDTs can achieve much higher frequencies, and so much higher sensitivities, due to the method by which the wave is generated. It is possible to further increase the sensitivity by aplying a guiding layer to the sensor.

Originally, Love wave devices were developed to create a sensor with a much higher sensitivity [9]. Love waves use an IDT based acoustic device and aply a guiding layer to the surface. Work done by Evans *et al* took the concept of layer guiding and aplied it to APM devices [80].

Here guiding layers are used on single port acoustic resonators. Previous work has been reported on single port resonator by Nomura *et al* [72]. Their device consisted of a single IDT and reflectors on either side fabricated on 36 degree rotated Y cut X propagating lithium tantalate (36 YX $LiTaO_3$). They demonstrated that such a device could be used in a liquid and provided a repeatable relation between frequency shift and the viscosity of different glycerol solutions. Their device also contained a thin (5μm) layer of photoresist as an insulator however they did not report the effect of changing this thickness. The purpose of this work was to take the advantages of a single-port sensor; the relative electronic simplicity of a two terminal device compared to a four terminal device such as a delay line sensor, and increase the sensitivity by aplying a guiding layer to the surface.

In this chapter a single type of single-port acoustic wave sensors was used. This device used single-single IDTs with a finger width of 12.5 μm, giving a wavelength of 50 μm. Two metalized reflection gratings, with a finger width of 12.5 μm, formed a resonant cavity with the IDTs at the centre. The reflectors were place 2000 μm from the IDTs, this is equal to 160 wavelengths. While there are many variables which could be investigated, such as the style of the IDTs, the position of the reflectors etc., this chapter limits the investigation to varying the thickness of the guiding layer. The devices were fabricated using standard lithographic techniques, making use of a photomask designed on Autocad and manufactured by JD Phototools.

The initial experiments performed were to investigate the effect of adding a guiding layer to the device on the resonant frequency of the sensors. To do this the IDT bearing surface of the sensors were coated in consecutive, 1.5 µm layers of S1813. Frequency changes caused by the guiding layer were measured and the S1813 layer built up until the sensors no longer gave a usable signal. After this, the sensing properties of the devices were categorized. In order to determine the mass sensitivity of the sensors, a sputter coater was used to build up a layer of gold on the surface of the device by sputtering on consecutive layers. This was performed in two main ways. Firstly, gold layers were sputtered onto devices with a range of guiding layer thicknesses, but keeping the target area position constant for all devices. In this way the relationship between mass sensitivity and guiding layer thickness could be investigated and the optimal layer thickness determined. The layer thickness to sensitivity relationship was then compared to the frequency change caused by the guiding layer to determine the connection between the two. Secondly, gold was sputtered onto different positions on the sensor surface in order to determine the most sensitive area of the device.

In addition to the sensor's response to the aplication of mass, experiments were performed to investigate the sensor response caused by changing the viscosity and density of a liquid in contact with the surface of the sensor. Sensors were coated in guiding layers with a range of thicknesses and then exposed to a water/glycerol solution over a range of glycerol concentrations. The frequency changes measured were then compared to the square root of the viscosity/density product of the liquids used and the results compared to behavior predicted by the Kanazawa and Gordon equation. The relationship between the sensitivity and the guiding layer thickness was also investigated.

4.2 Device production

Photolithography was used for the production of the single-port sensors. A piezoelectric wafer is coated in a photosensitive polymer, in this case the photo-resist S1813, which is patterned by selective exposure to UV light. As S1813 is a positive photo-resist the sections that are to be removed must be exposed to UV light, this is done using a photomask. The exposed sections are then removed using a developer solution, revealing the pattern underneath. The device electrodes are formed on the surface by sputter coating a layer of titanium and then gold. The excess metal, on the areas still coated in S1813, is lifted off using acetone. This leaves the devices permanently fabricated on the surface. Due to the delicate

nature of the manufacture process, the work was carried out in a clean room environment. Figure 4.1 shows a diagram detailing the photolithography process.

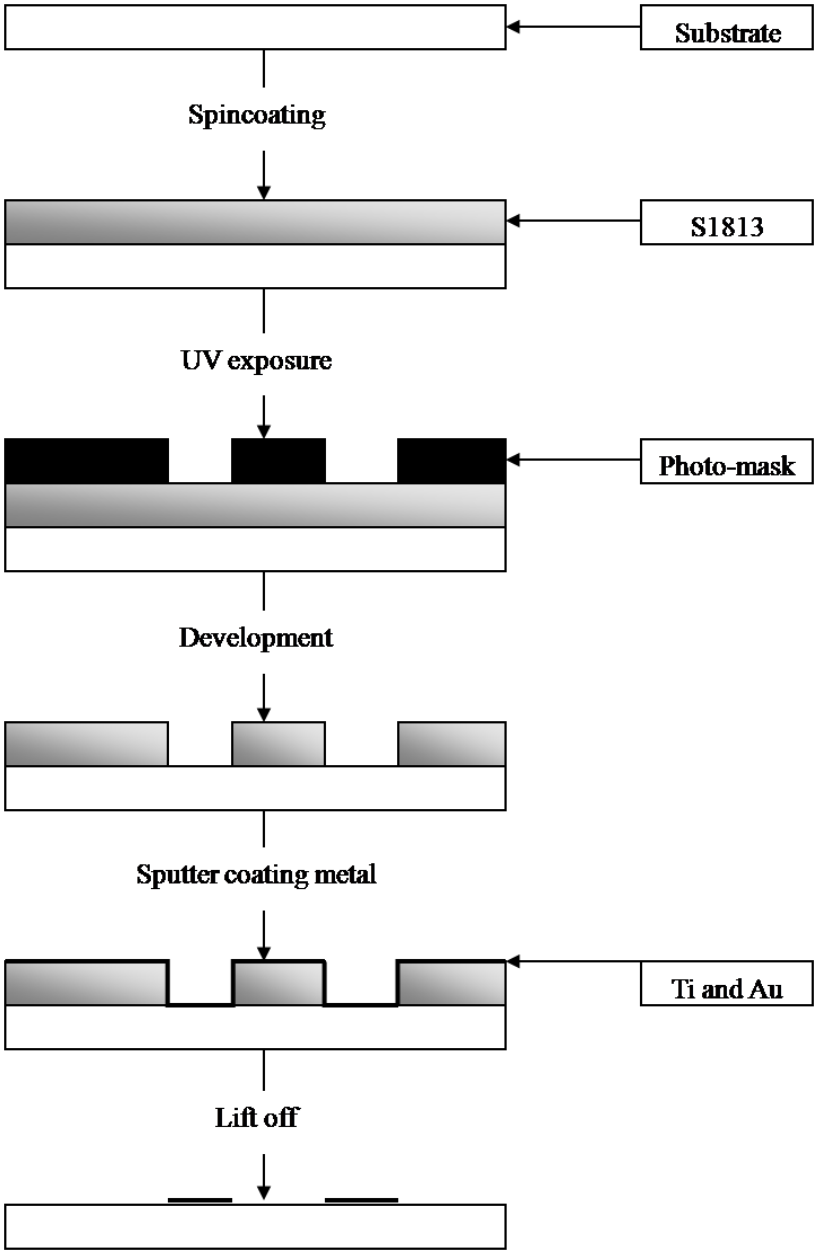

Figure 4.1: Diagram showing the photolithographic process for patterning sensor onto the piezoelectric substrate.

4.2.1 Mask production

For this project a photolithographic mask was designed and produced for the single-port sensor experiments. A photomask is a glass plate with opaque sections, in this case chrome on the surface, which

allows light to be shone through in a defined pattern. The mask was designed using AutoCAD and manufactured by JD Photo Tools.

The mask had both single-single and double-double devices on it. The double-doubles also had 12.5 μm fingers but with a period of 100 μm, giving them double the wavelength of the single-singles. The frequency of the devices was then dependent on the speed of the wave in the substrate. The reflectors were metalized gratings, using titanium and gold, with both the finger width and spacing set to 12.5 μm. The gap between the IDTs and the reflectors was 2000 μm for both types of devices. This chapter only deals with the single-single devices, as the primary variable being investigated was the thickness of the guiding layer, and not the design of the device itself. Figure 4.2 shows the photo-mask design.

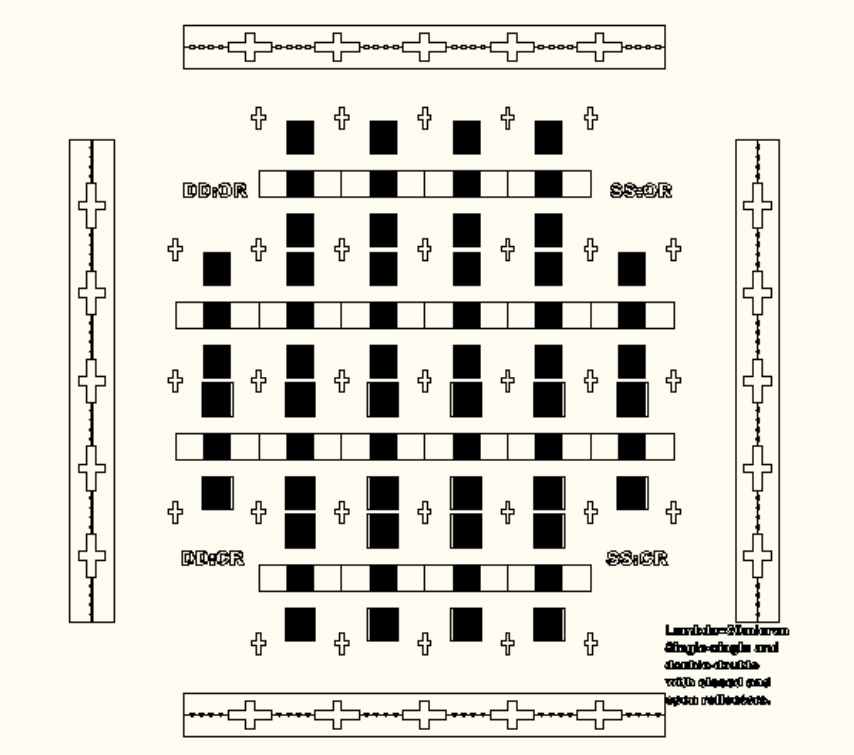

Figure 4.2: Diagram of Autocad schematic of single port photomask used.

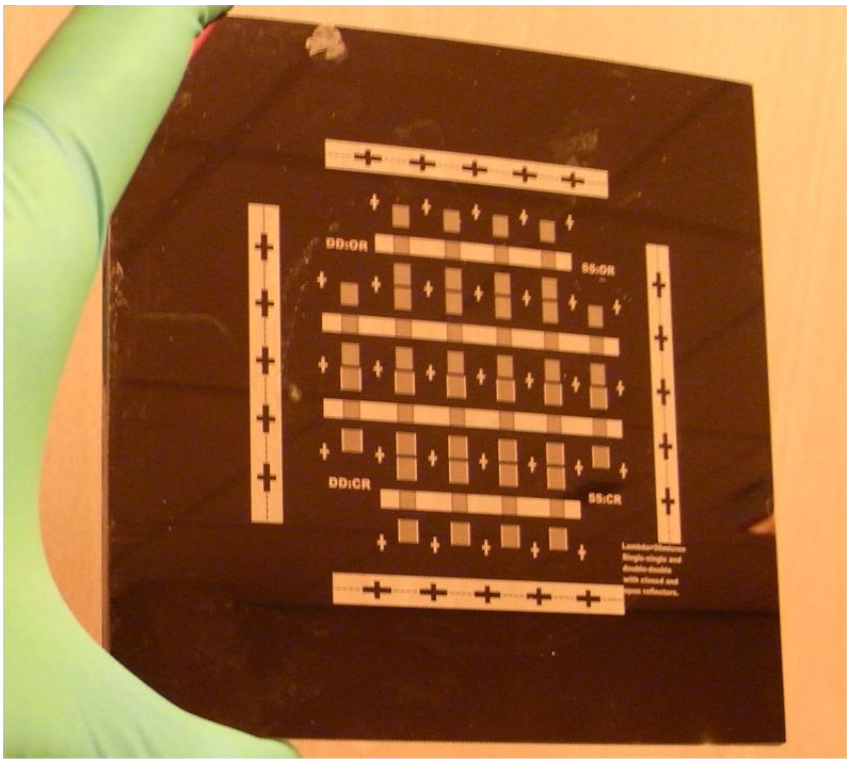

Figure 4.3: Photograph of chrome and glass photomask used.

4.2.2 Wafer preparation

The first step in the production process is to prepare the wafer. Three different substrates were used for this project, $LiNbO_3$, $LiTaO_3$ and SiO_2 (Quartz). Each wafer was 75 mm in diameter and 0.53 mm thick. Wafers were suplied by the The Roditi International Corporation Ltd. The wafers were chemically cleaned in a three step process using acetone, ethyl lactate and isopropyl alcohol (IPA), before being blow dried with nitrogen. This removes organic, ionic and metallic impurities and particulate matter, such as dust. Unlike $LiNbO_3$ or $LiTaO_3$, the surface of the quartz wafers is prone to oxidizing. This oxidization results in hydrogen bonds forming between the surface of the wafer and water molecules in the air. When the S1813 is spun on it will tend to adhere to the water, rather than the surface, resulting in poor adhesion and problems during the development part of the process. To overcome this, the quartz wafers were initially soaked overnight in an adhesion primer solution made by dissolving hexamethyldisilazane (HMDS) in toluene. The HDMS has the effect of chemically removing surface OH groups [106], leaving the S1813 free to adhere to the surface of the wafer. Treating the quartz in this way gives a much higher yield of successful devices.

4.2.3 S1813 spin coating

After the wafers have been cleaned the S1813 is aplied by a high speed spin coating method. For this stage a Laurell Technologies WS-650S spin coater was used in a fume cupboard. Wafers were first placed on a vacuum chuck and 5 ml of S1813 deposited onto the centre of the wafer. The spinning was a two step process; first the wafer was brought up to 500 rpm for 5 seconds, this spread the S1813 evenly across the surface and expelled much of the excess from the surface; the second step had the wafer spun at 3000 rpm for 30 seconds. After the second step is complete the wafer had a uniform layer of S1813 1.5 μm thick.

4.2.4 Baking

After the wafer had been spin-coated with S1813, it was necessary to bake the wafers on a hot plate. The hot plate was preheated to 100 ^{0}C and the wafer was allowed to bake for 75 seconds. Wafers were baked S1813 side down. This meant the S1813 was being directly heated, rather than through the wafer, and dust could not deposit on the surface. It is during the baking that any remaining solvents are removed from the photo-resist. This step is important, as any remaining solvent will adversely affect the photosensitivity of the S1813 and cause it to be unsuitable for reproducing the mask pattern accurately. Under-baking will, therefore, prevent the S1813 from becoming fully photosensitive. Additionally, care must be taken not to over bake the wafer, if this hapens the solubility in the developer will be reduced or the sensitizer will be destroyed.

4.2.5 UV exposure

With the wafer coated and baked, the next step is patterning via high intensity exposure to ultra violet light. A Suss MicroTec MJB4 mask aligner was used for this stage in the fabrication process.

There are a number of considerations in the alignment and exposure process. It is important that the wafers are properly oriented beneath the photo-mask, as the type and quality of the wave produced in the substrate can be dependent on the direction of propagation within the crystal. This is particularly noticeable in the quartz wafers, where changing the propagation direction by 90^0 can be the difference between an SSBW and a Rayleigh wave.

Also, it is critical that both the mask and wafer are clean and free of debris. The wafer is placed on a vacuum chuck and lifted into contact with the photo-mask, this is called contact printing. If there is any dust or other particles between the mask and the wafer, one or both may be damaged as the two are pressed together. If the mask becomes damaged then defects may arise in the pattern and compromise the quality of the devices produced. The S1813 pattern may also be damaged or the wafer itself scratched or even cracked, both occurrences will adversely affect the wave propagation.

With the wafer in such close contact, high resolution patterns can be achieved (2 μm features are possible). UV light is shone through the photo-mask selectively exposing different areas of the wafer, creating a pattern in the photo-resist that will be revealed through developing. Exposure times vary between substrate; $LiTaO_3$ has an exposure time of 1.6 seconds for example, while quartz was exposed for 2.4 seconds. The differences in exposure time between substrates is due to the difference in reflectivity to UV light. The power output of the UV lamp was measured at 50 $mWcm^{-2}$.

4.2.6 Developing

S1813 is soluble in a developer solution S1800 Microposit Developer from Shipley MicroElectr, with the solubility increasing with exposure to UV light. The wafer is submerged in a 1:1 solution of developer and deionized water, development time is then judged by eye. Even unexposed S1813 is soluble in the developer, so care must be taken that wafers are not left in the developer solution too long. Overlong development can lead to features being removed, destroying the device, while under developing will leave S1813 on the surface and stop the metal electrodes attaching. Once fully developed the wafers are rinsed in deionized water, to remove residual S1813 and developer, and dried with nitrogen.

4.2.7 Metallization and lift-off

The final two steps in creating the devices on the surface of the wafer are metallization and lift-off. An Emitech K-575X sputter coater was used for the metallization process. The sputter coater, a diagram of the interior is shown in figure 6, consists of a glass chamber connected to a turbo molecular pump and a rotary pump. There are two targets that can either be used for noble or oxidizing metals. Titanium was used as an adhesive layer that the gold, the conductive layer, would stick to. First the chamber is pumped down to low pressure. As titanium is an oxidizing metal, before coating the sputter coater performs a plasma

cleaning cycle of the titanium target. After the cleaning a titanium layer was sputtered onto the surface of the substrate for 1 minute, followed by 3 minutes of gold. This gave a 10 nm layer of titanium and a 75 nm layer of gold. There is no need to break the vacuum between the deposition of each layer. By this point the top surface of the wafer is fully coated in titanium and gold with the S1813 pattern underneath.

The lift off process involved dissolving the remaining S1813 in a bath of acetone, which also removed the gold on top of the S1813, leaving the devices fully formed on the surface where the metal had been sputtered directly onto the surface of the wafer. The lift of process was helped by a combination of sonication in an ultrasound tank and manual removal using cotton buds.

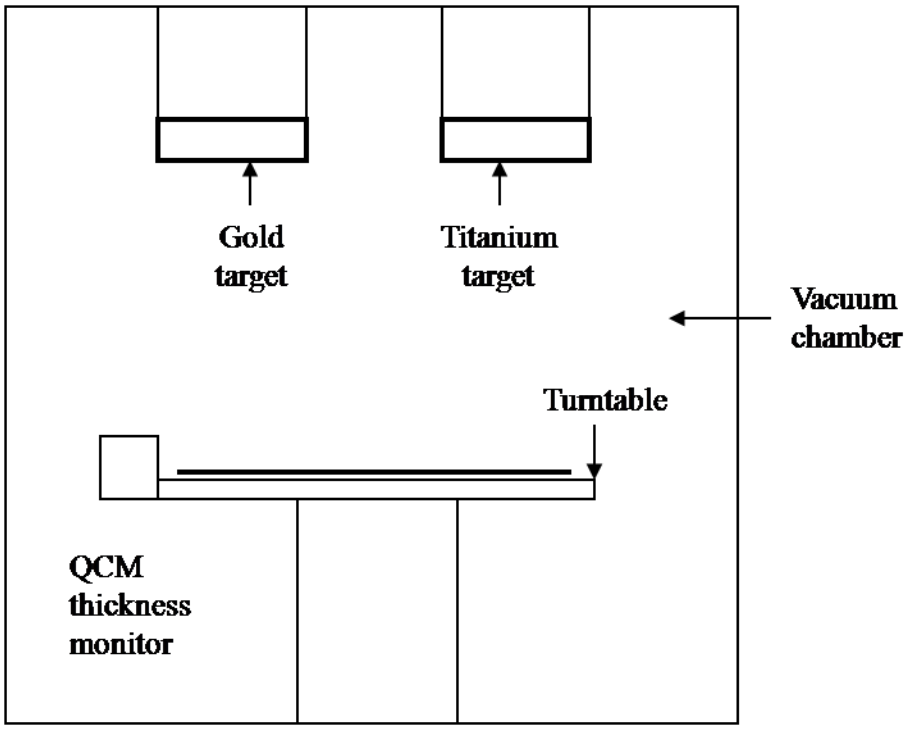

Figure 4.4: Diagram showing the interior of Emitech K575-X sputter coater.

4.2.8 Dicing

With the sensor patterning complete, the wafer needs to be diced up into individual devices. This was done by two methods. The first method was manually dicing the wafers using a glass cutting scribe. The back surface of the wafer was scored with the scribe and the wafer then broken along the score. The advantage of this method is that is both quick and simple. However, the number of usable devices can vary and is entirely dependent on the user's skill.

The second method utilized an automated circular saw, a Tempress model 602. A cutting program was written using the program My T'Mill. The saw was restricted to a single plane, so two programs were necessary in order to cut the devices out. The wafer was rotated through 90^0 in-between the two programs. The wafer was placed onto a vacuum chuck and aligned with the saw blade and a water/lubricant solution flowed over the blade as it cut. The saw scored the wafer, which could then be easily broken apart. This was the preferred method, as the number of usable devices produced is much higher, though the cutting time was much longer.

After both methods, the sensors were cleaned in acetone and a network analyser used to check the spectrum of each device and determine whether they were usable. Figure 4.5 shows an example of a completed single-port sensor, while figure 4.6 shows a typical device spectrum.

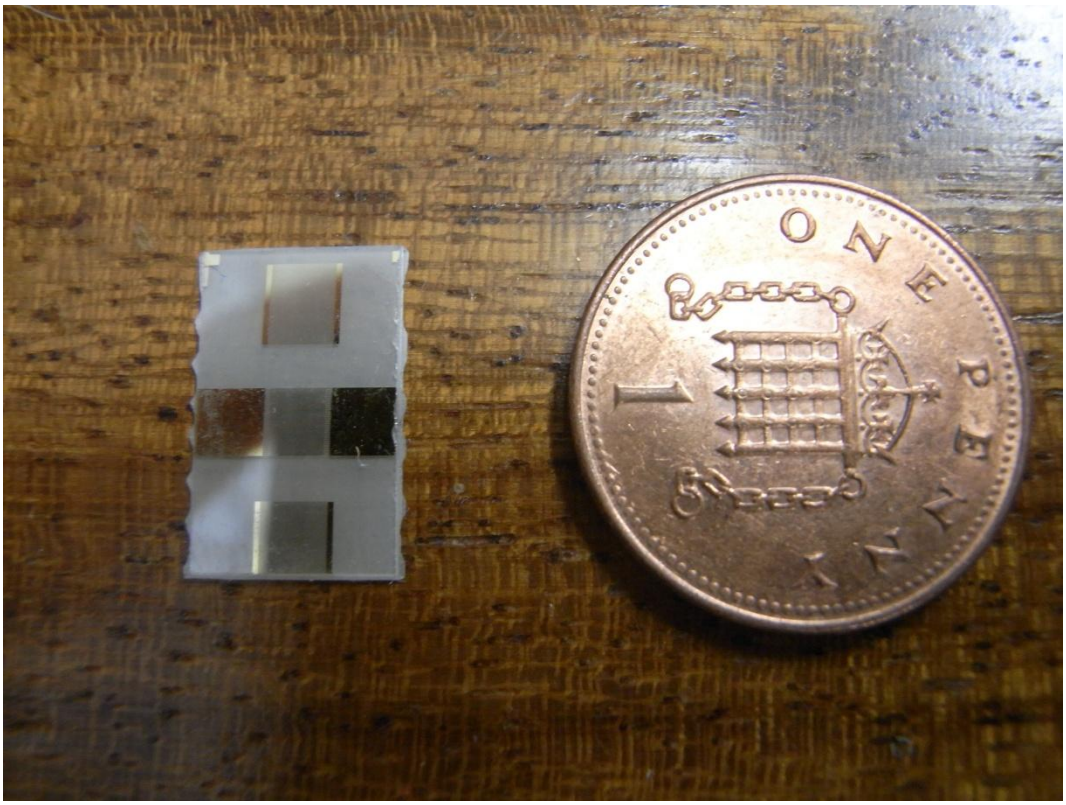

Figure 4.5: Image showing size comparison of single port device.

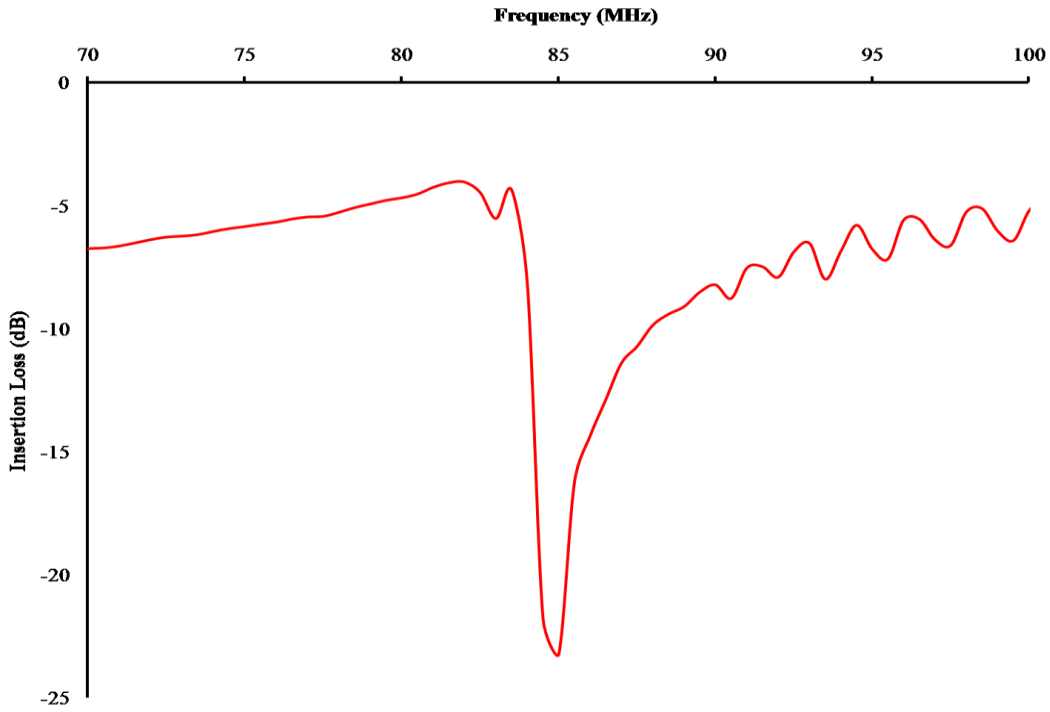

Figure 4.6: Network analyzer spectrum, in air, for completed single port device fabricated on $LiTaO_3$.

4.3 Adding a guiding layer to the single port resonators

4.3.1 Guiding layer build up

As detailed in chapter 2, the addition of a guiding layer to an acoustic wave device has a well defined effect on the frequency of the device. Love wave and other layer guided devices have been shown to exhibit a decrease in frequency which can be plotted as a number of curves. To investigate whether this was true of these single-port resonators, guiding layers were added to the surface and the frequency tracked.

Once a number of devices had been manufactured on $LiTaO_3$ they were coated in a polymer guiding layer composed of the photo-resist S1813. S1813 was chosen as the guiding layer because the wave speed is much less than the wave speed in any of the substrates used (the shear speed of S1813 is 1100 ms^{-1}, while the three substrates used have shear speeds in excess of 3000 ms^{-1}) and the ability to spin coat the S1813 produces a flat and homogenous layer. The S1813 was aplied undiluted via the same spin coating process used during the device fabrication. A succession of 1.5 µm layers were aplied to the electrode bearing face of the sensors. Each layer was baked on for 20 minutes at 120 ^{0}C resulting in polymer cross

linking. The resonant frequency of each device was recorded between each layer being aplied and any frequency changes calculated.

The initial frequency of the devices fabricated on $LiTaO_3$ was 85MHz. As the guiding layer was aplied the sensor frequency began to decrease. Figure 4.7 shows the spectrum of a $LiTaO_3$ sensor as the first four layers of the S1813 were aplied. The 85 MHz peak can be seen to decrease in frequency and become damped down. This continues until the peak is indistinguishable from the noise. The frequency change varies as the guiding layer is added. The first layer of S1813 caused no significant change. The following two layers caused a more dramatic decrease. The second and third layers caused frequency decreases of 10.5±0.5 MHz and 14±1 MHz respectively. When the guiding layer is 6.5 µm thick a second peak forms at 86±0.5 MHz. This follows the same trend as the previous peak and decreases in frequency until it is no longer visible. This trend of new peaks forming continues as the guiding layer gets thicker. Figure 4.8 shows the frequency data of a device fabricated onto a $LiTaO_3$ substrate. The original peak gives a smooth curve on the graph as the frequency decreases. As the guiding layer builds up, the device response begins to degrade and so later peaks do not show such smooth frequency changes. The frequency decrease itself is quite dramatic. The initial peak disapears when the guiding layer is 9 µm thick. By this point the frequency has decreased from 85±0.5 Mhz to 45±0.5 MHz.

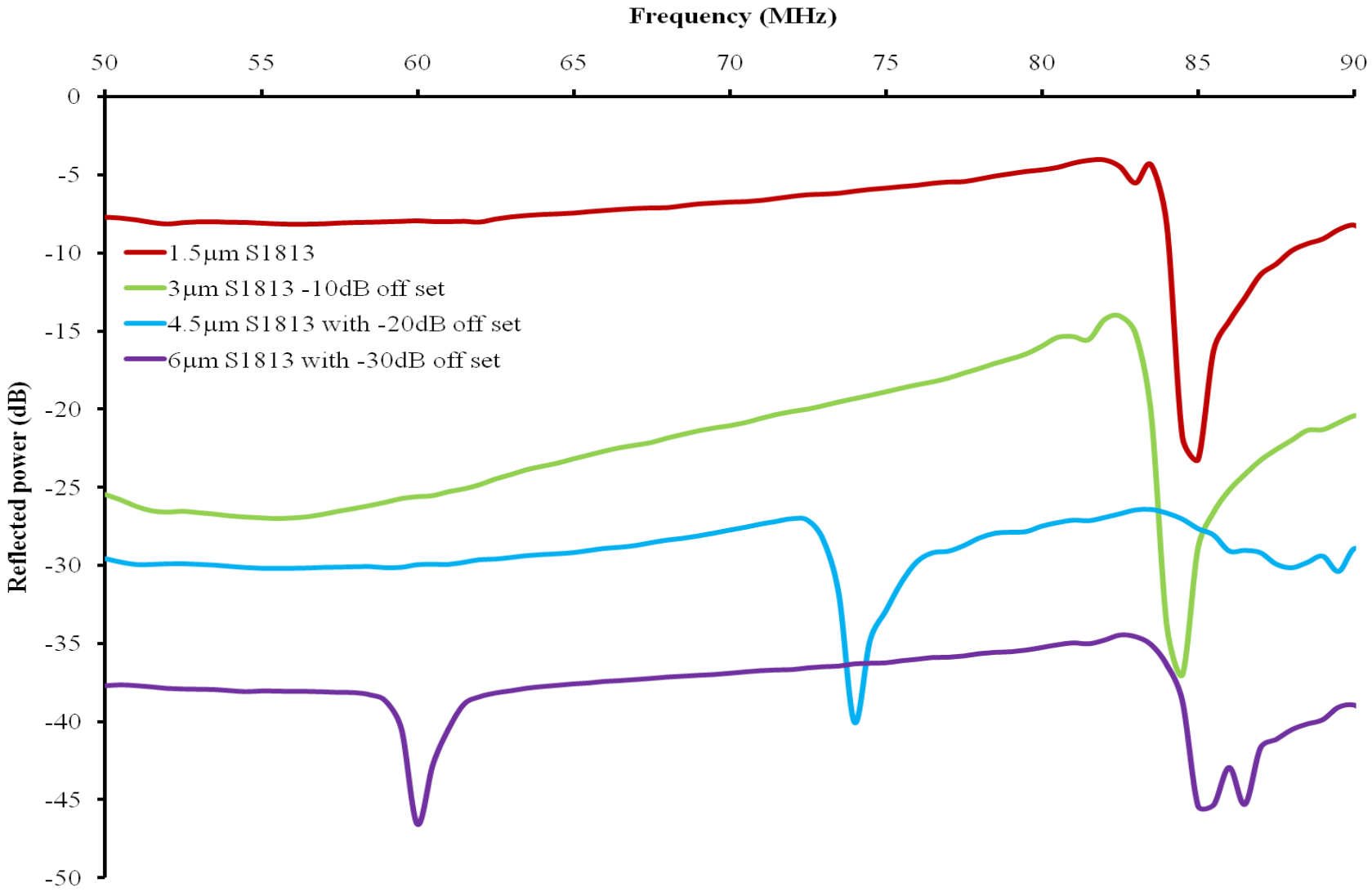

Figure 4.7: Frequency of resonant peak for a $LiTaO_3$ device as first 4.5µm of S1813 guiding layer is built up.

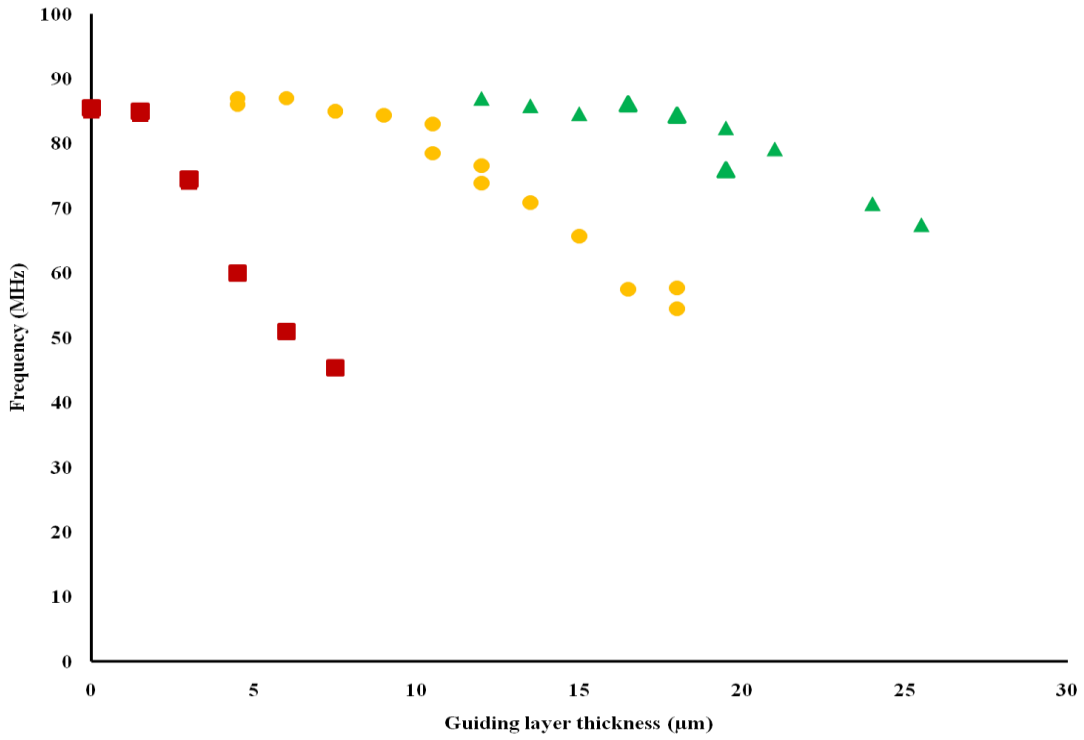

Figure 4.8: Graph showing the resonant frequency of a number of $LiTaO_3$ devices. Primary (red squares), secondary (yellow circles) and tertiary (green triangles) peaks were generated and their frequency tracked.

In addition to $LiTaO_3$, sensors were also fabricated on quartz substrates. Figure 4.9 shows the spectra for a quartz sensor. Like the $LiTaO_3$ sensor, the resonant peak can be seen decreasing in frequency and the 6 µm trace shows a second peak forming. Figure 4.10 shows how the frequency for a quartz device changes as an S1813 guiding layer is aplied. Again, the S1813 is spin coated onto the sensor to form successive 1.5 µm layers. The quartz devices exhibited similar behavior to the $LiTaO_3$ devices. Secondary peaks formed as the main one was damped into nothingness, the frequency decrease was massive (over 50 MHz for the initial peak with a 7.5 µm guiding layer) and the device response degraded as the guiding layer got increasingly thick.

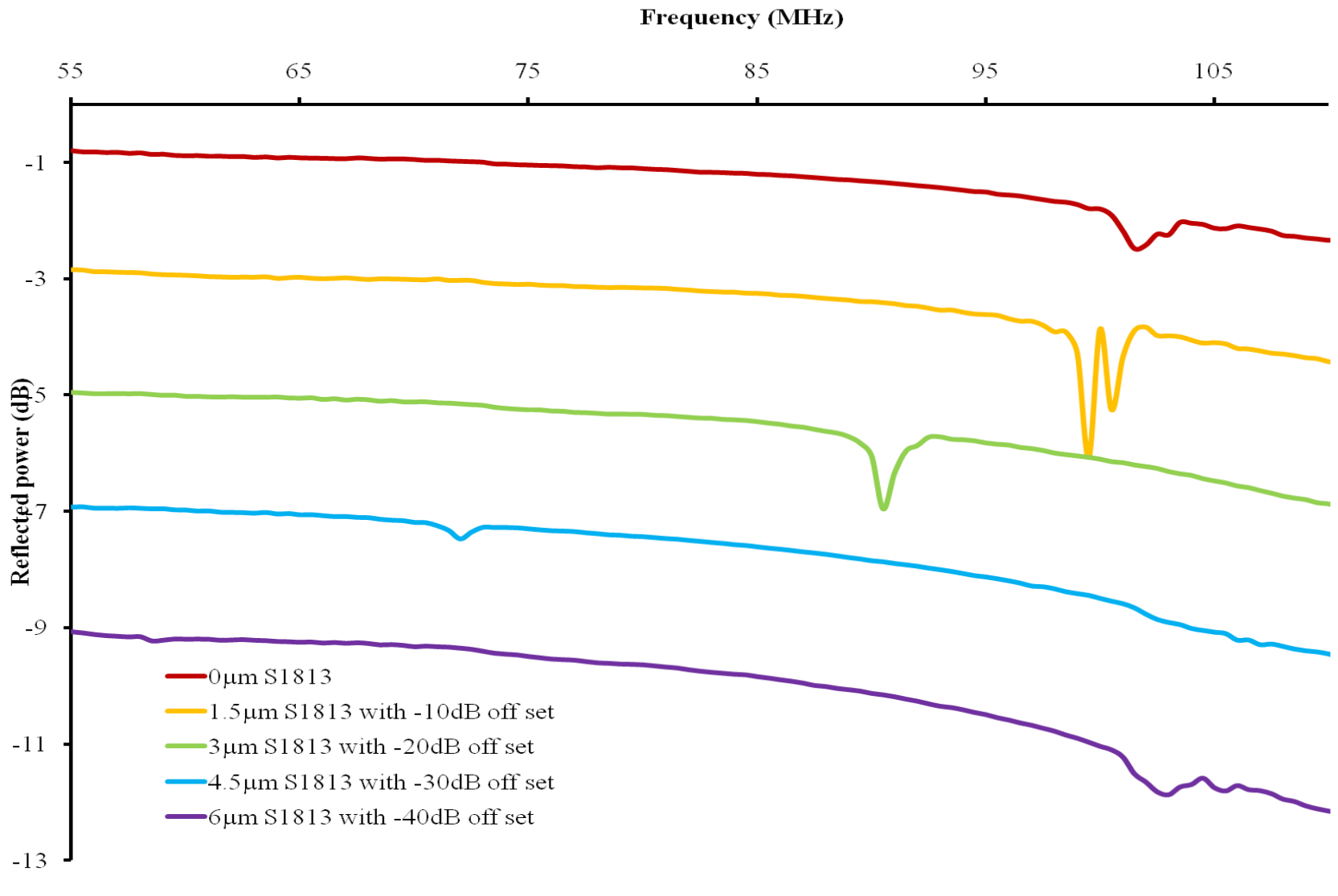

Figure 4.9: Frequency of resonant peak for a quartz device as first 4.5µm of S1813 guiding layer is built up.

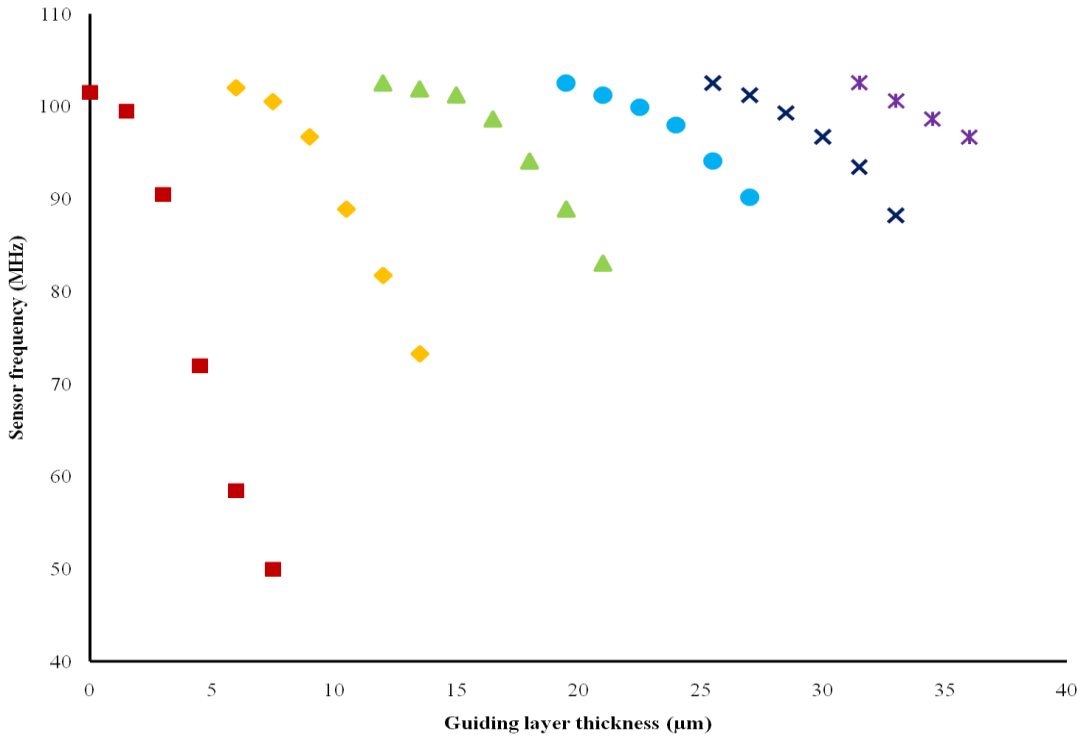

Figure 4.10: Graph showing the resonant frequency of a quartz device as the guiding layer builds up. The frequency of additional peaks was also tracked.

Compared to the $LiTaO_3$ sensors, the quartz devices maintained their usability up to a far higher guiding layer thickness. The $LiTaO_3$ sensors became unusable at a guiding layer thickness of 24 µm. The quartz sensors, by comparison, maintained their quality up to a maximum layer thickness of 37.5 µm. Also, the quartz sensors experience more peaks over the same guiding layer thickness range. Over the first 20 µm of S1813 the $LiTaO_3$ sensor has two resonant peaks. The quartz sensors show three peaks over the first 20 µm of guiding layer. The higher layer thickness before the sensors became unusable, combined with the higher rate of peaks, allows for more resonant peaks to be observed with the quartz sensors. This allows the sensor behavior to be looked at in more detail. The data shows that as the guiding layer increases in thickness, the rate at which the frequency changes decreases. The first peak decreases by over 40 MHz with a guiding layer increase of 6 µm, the second peak decreases by less than 30 MHz for the same increase in guiding layer thickness.

4,4 Mass sensing

The single-port sensors were used for mass sensing experiments. For this an Emitech K-575X sputter coater was used to deposit gold onto the surface. To measure the affect of the guiding layer thickness on sensitivity a 1.5 mm x 5 mm target area was covered in successive layers of gold. A simple mask made out of 3 mm Perspex sheet, using an M-500 laser cutter (Universal Laser Systems), was used to confine the gold to the target area. This target area was centered over the IDTs. With the mask in place, 25 nm layers of gold were sputtered onto devices with guiding layer thicknesses up to 23 µm. The resonant frequency was tracked and the sensitivity calculated, showing the variation in sensitivity with increasing guiding layer thickness

To determine the mass sensitivity on different parts of the sensor, layers of gold were deposited at different distances from the centre of the device. First a range of simple masks were produced out of 3 mm Perspex sheet, using the same laser cutter, to confine the sputtered gold to a well defined 1.5 x 5 mm area. Masks were made with the target area at -6, -4.5, -1.5, 0, 1.5, 3, 4.5 and 6 mm from the centre of the sensor. The masks ensure the same part of the sensor was used each time, to sense the aplied mass. The sputter coater was used to add successive layers of gold to the sensor. Gold was sputtered for 1 minute, giving a thickness of 25 nm, and the device spectrum was taken. This was repeated up to a thickness of 500 nm and changes in the resonant frequency of the sensor tracked. By doing this for several areas of the sensor, a sensitivity profile across the device was determined.

4.4.1 Mass sensitivity and guiding layer thickness

The mass sensing experiments were performed for guiding layer thicknesses from 1.5 µm up to 23 µm. In each case gold was sputter coated onto a target area measuring 1.5 mm x 5 mm positioned directly over the IDTs in the centre of the device. An Emitech K-575X was used to aply the gold to the sensors. Sputtering of each layer lasted 60 seconds, giving a layer 25 nm thick. The spectrum of the device was taken after each layer of gold and the frequency recorded. Any frequency changes were then measured and from there the mass sensitivity calculated for each device. Figure 4.11 shows the frequency change of a

sensor fabricated on $LiTaO_3$. Aplied gold is shown in ng along the x-axis and frequency change is given in Hz on the y-axis. Clearly, the devices do not all behave the same as the gold is aplied, with the 4.5 µm device experiencing the greatest frequency decrease. The 4.5 µm device shows a sharp change in gradient at 50 ng of gold, two lines of best fit have been drawn on the graph to illustrate this.

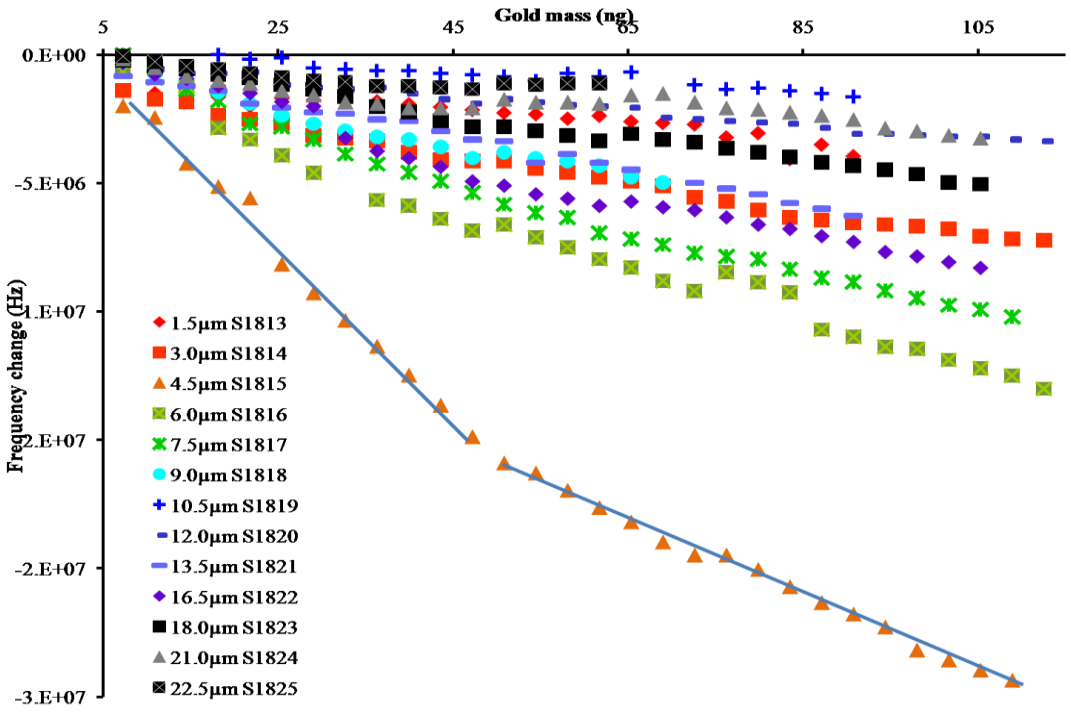

Figure 4.11: Frequency change, for devices fabricated on $LiTaO_3$, plotted against aplied gold mass. Experiment performed for a range of guiding layer thicknesses from 1.5µm to 22.5µm.

From the measured frequency decreases figure 4.12 was produced, showing the mass sensitivity of the sensors against guiding layer thickness. Guiding layer thickness is shown along the x-axis, measured in µm, and the mass sensitivity is shown on the y-axis, measured in Hz μg^{-1} cm^{-2}. The sensitivity seems to follow a repeating pattern, increasing with layer thickness to a point of high sensitivity and then droping down again to almost nothing. The highest mass sensitivity was with a guiding layer thickness of 4.5µm. The sensitivity was worked out for both of the sections shown on figure 4.11. This gave a mass sensitivity of 2302±53 Hz$\mu g^{-1}cm^{-2}$ for the steepest part of the graph and 1110±21 Hz$\mu g^{-1}cm^{-2}$ for the less steep section.

The sensitivity of the steeper section is considerably higher than the value calculated for the other devices used, over double the sensitivity of the second most sensitive with a guiding layer 6 µm thick. The sensitivity for the less steep part shows better agreement with the sensitivity value for the other guiding layer thicknesses. The mass sensitivity apears to be becoming lower overall as the guiding layer increases. It seems unlikely that further increases in the layer thickness will give a more sensitive device than has already been achieved with a 4.5 µm thick guiding layer. This suggests that 4.5 µm is the optimum guiding layer thickness of for these types of device, meaning these single-single devices on a $LiTaO_3$ substrate. Any future mass sensing experiments should be performed using sensors with this thickness of guiding layer.

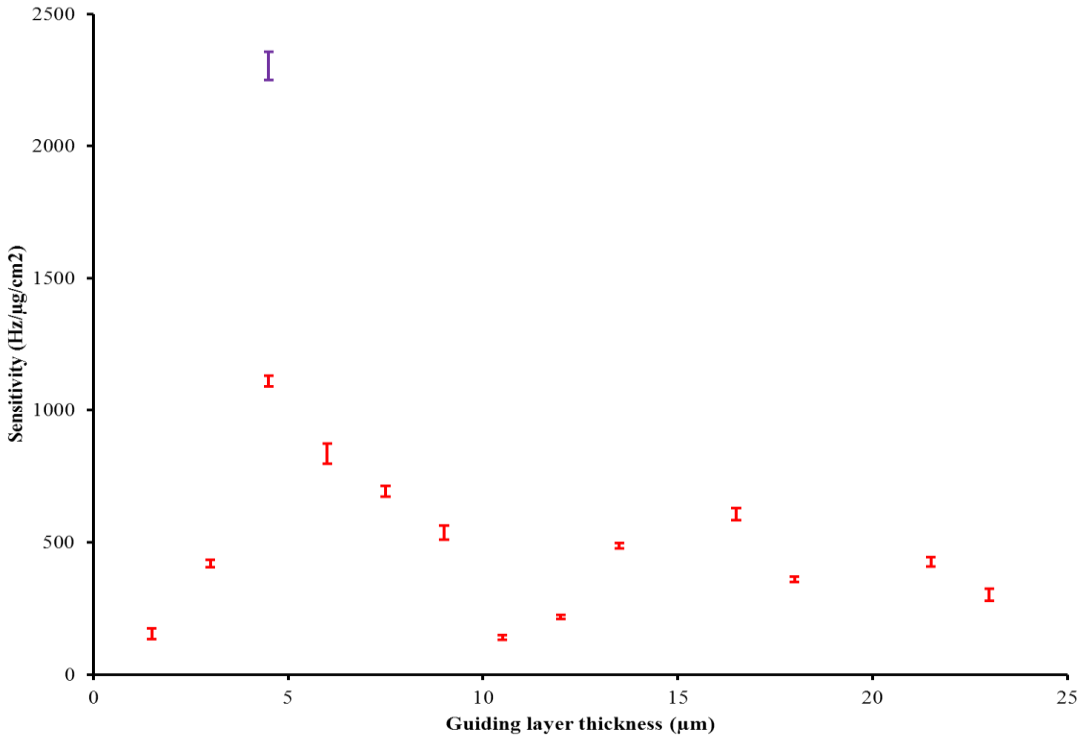

Figure 4.12: Mass sensitivity of $LiTaO_3$ sensors compared to guiding layer thickness. Greatest sensitivity can be seen at 4.5µm where sensitivity is shown for both sections of the plot shown in figure 4.11.

4.4.2 Change in sensitivity over the surface of the device

The previous mass sensing experiments had used the centre of the device as the target area for the gold. Further experiments were performed to determine whether the centre was in fact the apropriate, meaning the most sensitive, area of the sensor to use. To investigate this, several devices were made with the intention of sputter coating gold layers onto the surface and measuring the frequency response from different areas of the sensor. To determine the sensitivity of different parts of the devices, a number of acrylic masks were produced to confine the sputtered gold to a particular target area. The target area was an area 1.5 mm x 5.0 mm for all the devices. Gold was sputtered onto target areas positioned at -6, -4.5, -1.5, 0, 1.5, 3, 4.5 and 6mm from the centre of the device, perpendicular to the IDTs. This is illustrated in figure 15. The sensors were all given a 4.5 µm guiding layer, as this had already been shown to provide the best mass sensitivity, using the centre of the device, from the range of thicknesses tested.

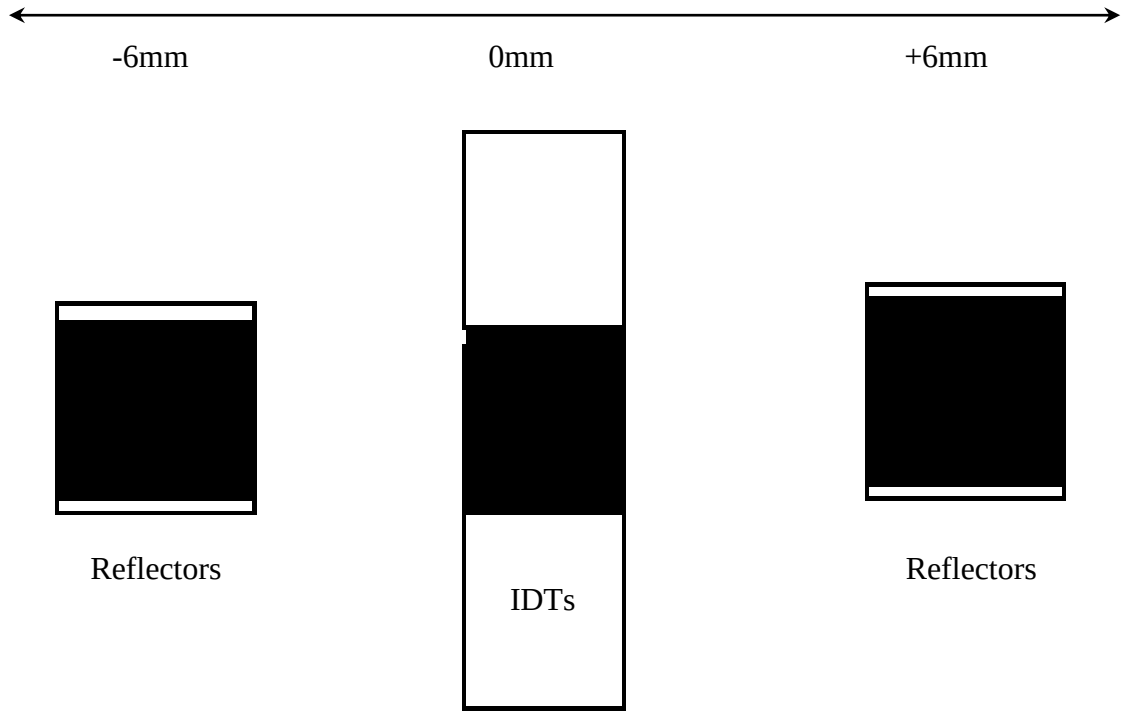

Figure 4.13: Diagram of single port device illustrating target area distance.

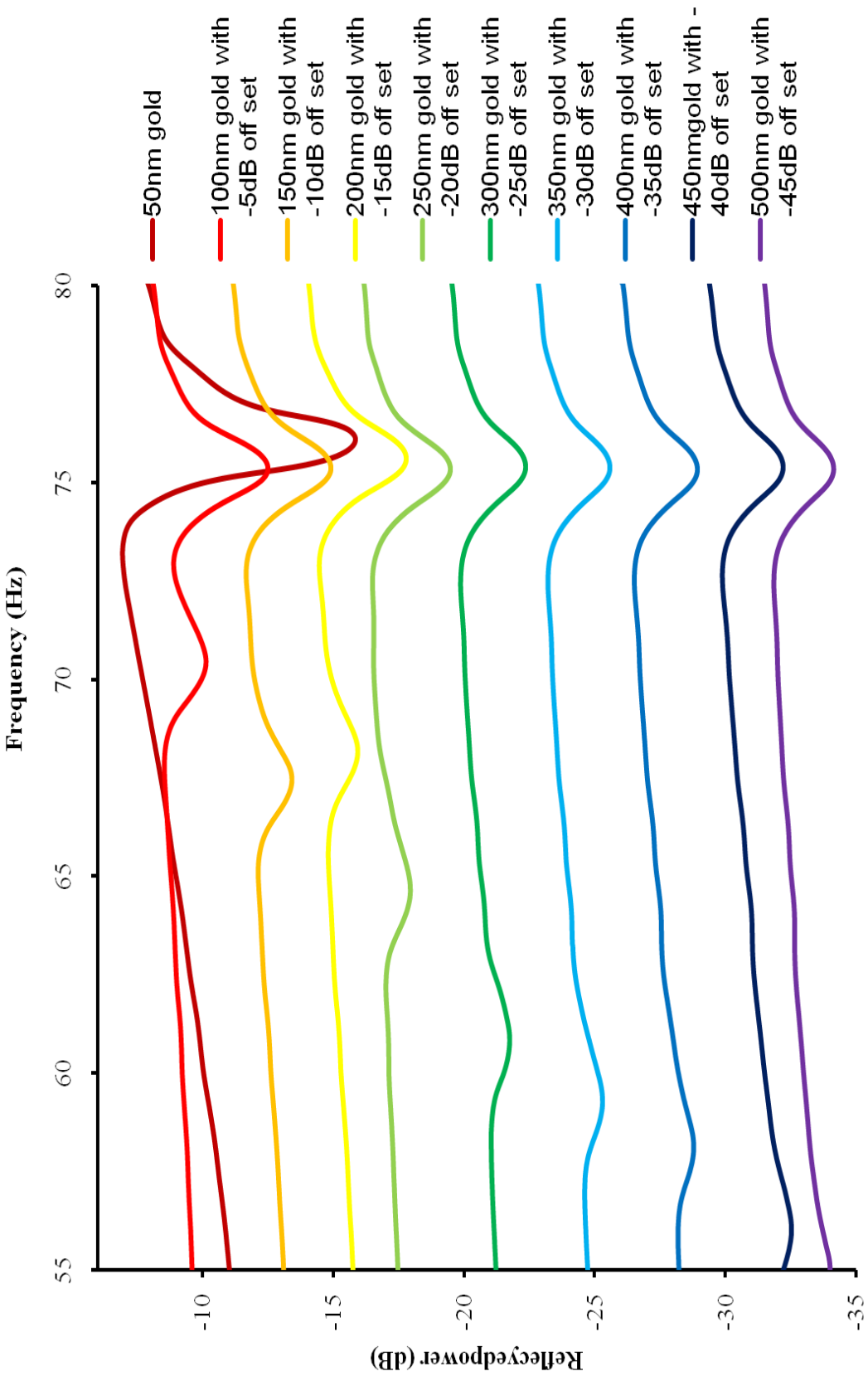

Figure 4.14: Resonant peak of $LiTaO_3$ as consecutive layers of gold are sputtered onto the surface. Target area at -6mm from central IDTs.

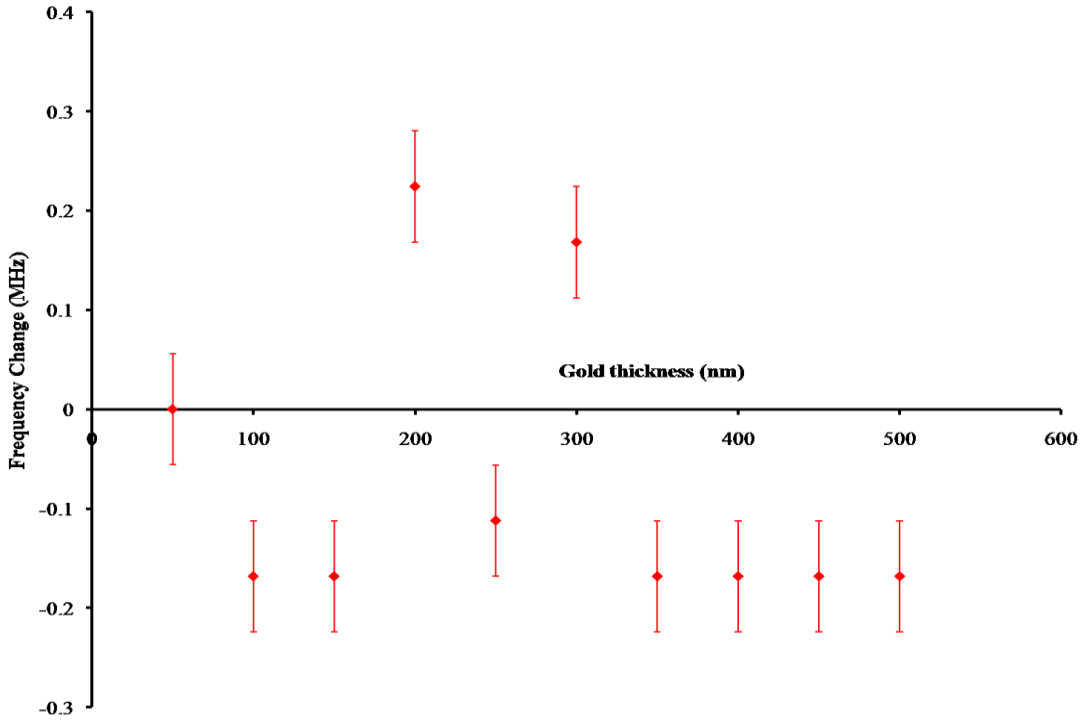

Figure 4.15: Frequency change for $LiTaO_3$ sensor as consecutive layers of gold are sputtered onto the surface. Target area at -6mm from central IDTs.

Figure 4.14 shows the spectra for a target area positioned -6mm from the central IDTs. This places the target area over one of the sensor's reflector banks. The resonant peak is at aproximately 77.16±0.06 MHz, due to the presence of the guiding layer, and gold is sputter coated onto the sensors in a series of 50 nm layers. The device shows no significant frequency change as the gold is aplied, suggesting that the mass sensitivity of this part of the device is low. By measuring the frequency for the lowest value of reflected power for each peak the frequency change was calculated, this is shown in figure 17. There are frequency changes present, but there is no consistent decrease. For thicknesses 100, 150, 350, 400, 450, 500 nm the frequency lower than the original frequency by the same amount. Thicknesses 200 nm and 300 nm show frequency *increases*.

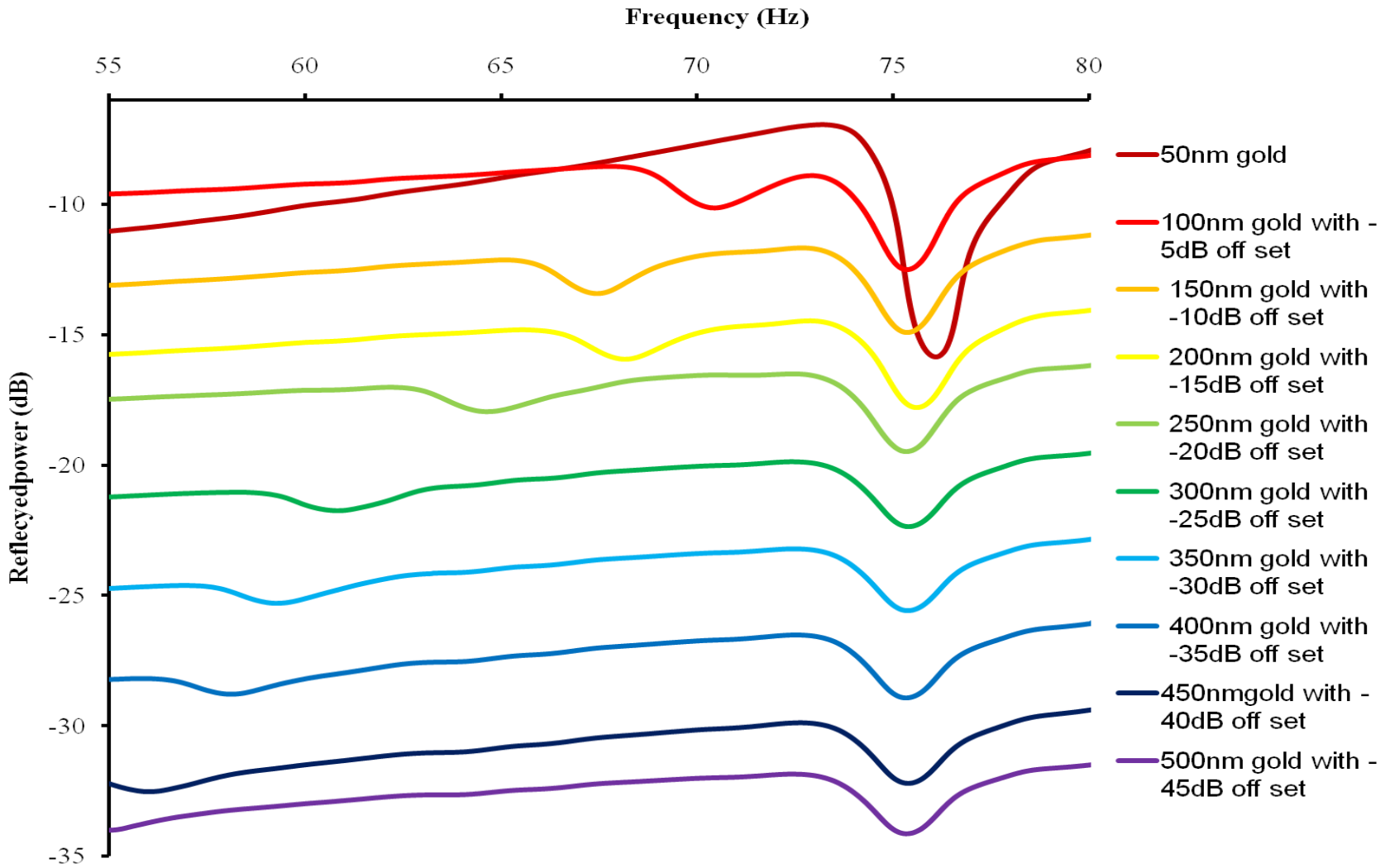

Figure 4.16: Resonant peak of $LiTaO_3$ as consecutive layers of gold are sputtered onto the surface. Target area at -4.5mm from central IDTs.

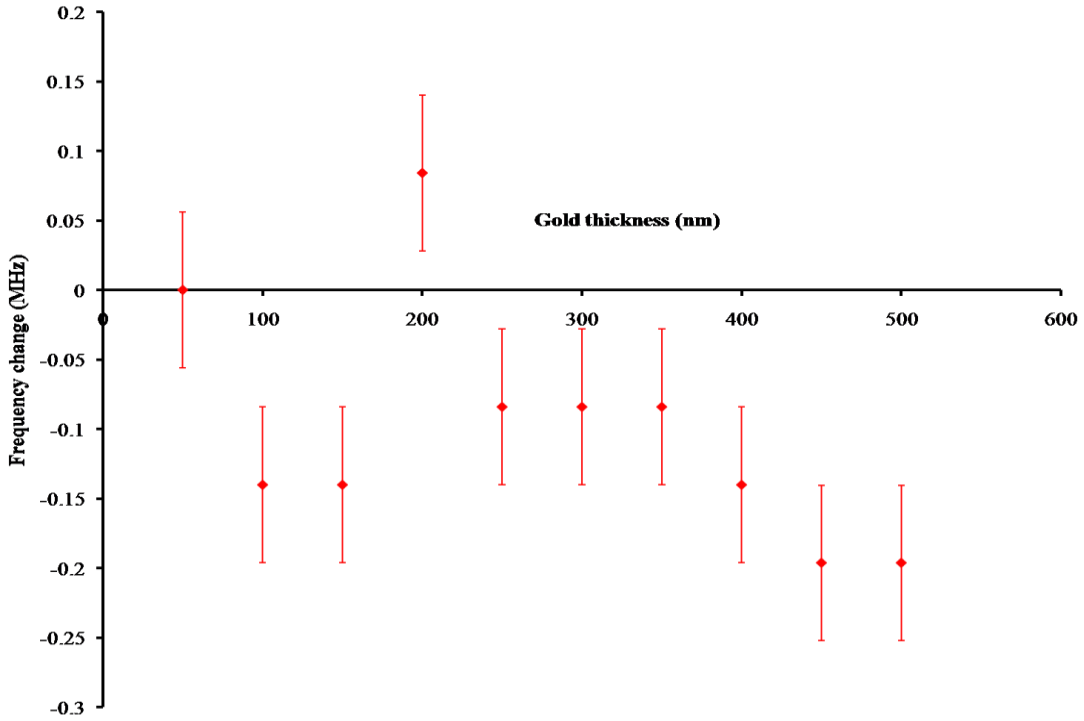

Figure 4.17: Frequency change for $LiTaO_3$ sensor as consecutive layers of gold are sputtered onto the surface. Target area at -4.5mm from central IDTs

Figure 4.16 shows the spectra for the target area -4.5 mm from the centre of the device. Similar to the 6mm spectra, there is no significant frequency change. Figure 4.17 shows the frequency change plotted against the gold thickness for this device. The sensor experiences slightly more of a consistent frequency change than the previous 6 mm device but it is still not significant.

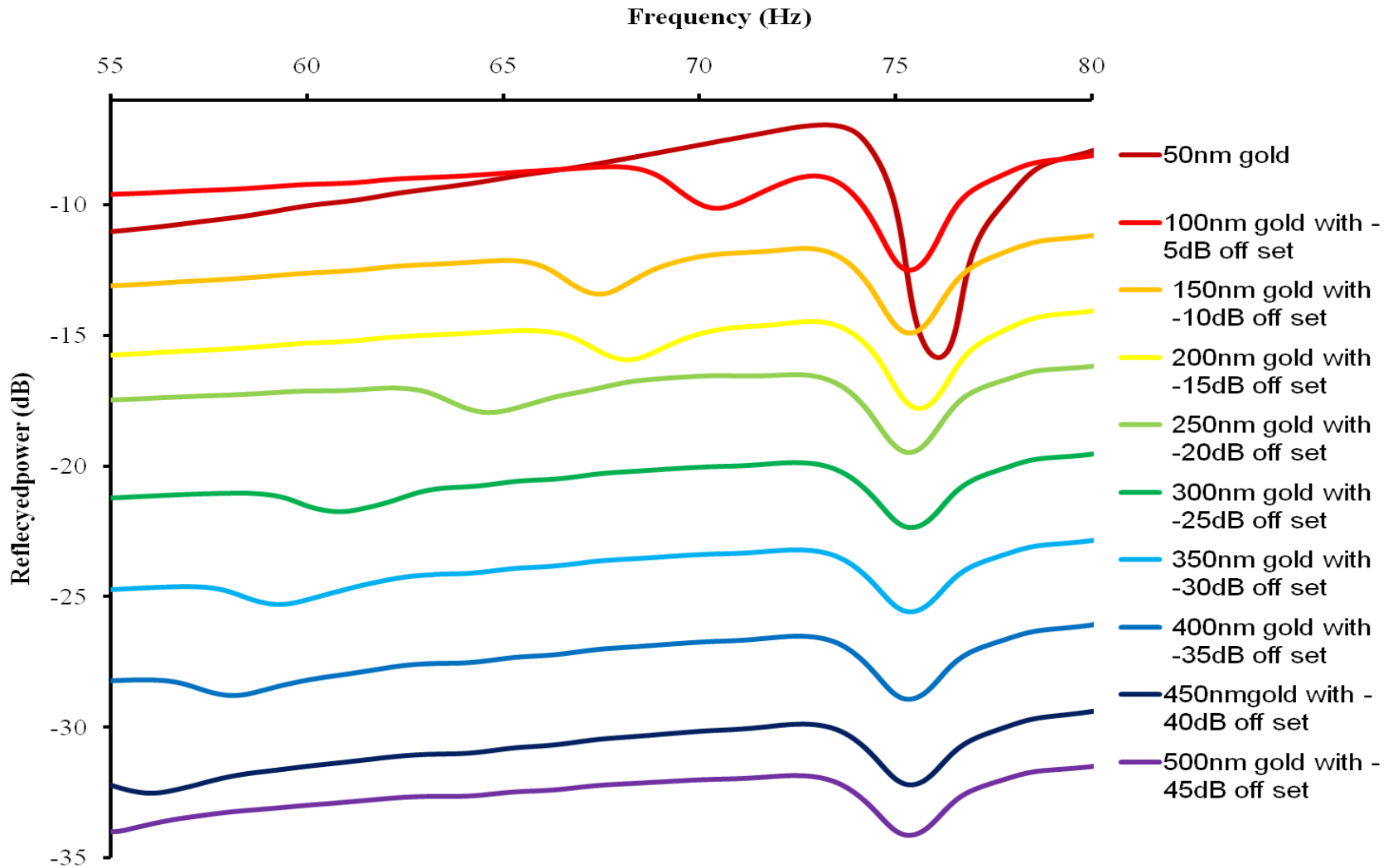

Figure 4.18: Resonant peak of $LiTaO_3$ as consecutive layers of gold are sputtered onto the surface. Target area at -1.5mm from central IDTs.

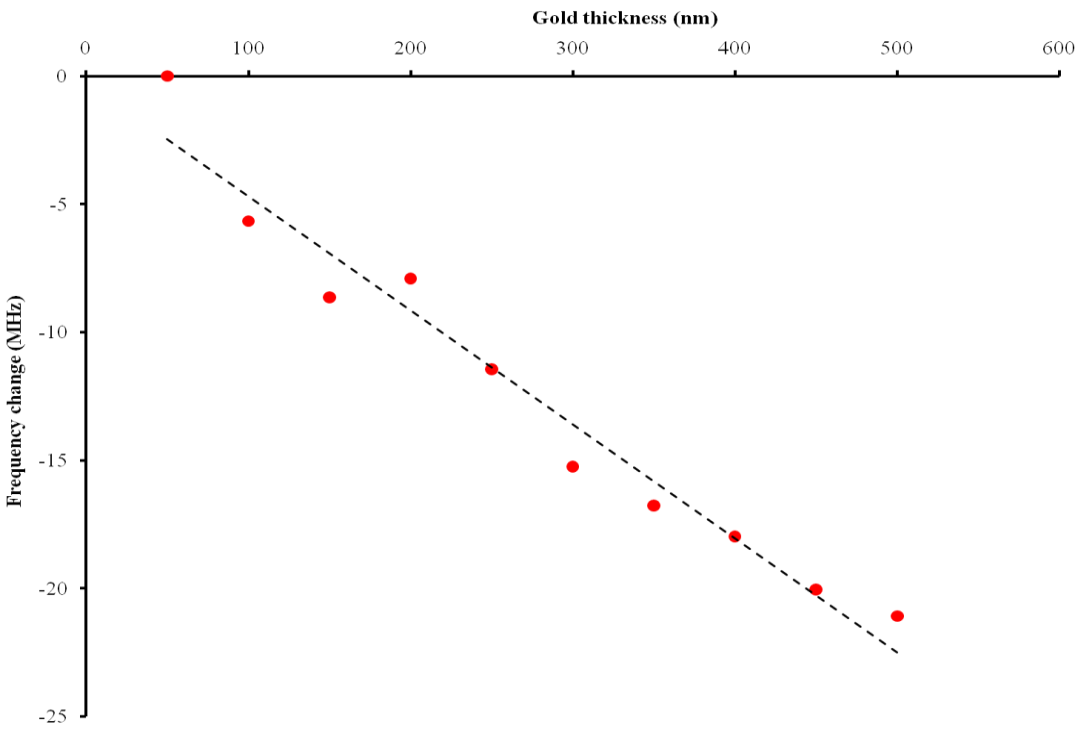

Figure 4.19: Frequency change for $LiTaO_3$ sensor as consecutive layers of gold are sputtered onto the surface. Target area at -1.5mm from central IDTs

Figure 4.18 shows data for a target area positioned -1.5 mm from the centre of the device. The frequency change here is quite significant. There is a peak than can be seen on each trace at ever decreasing frequencies as the gold thickness increases. The frequency of these peaks is tracked and the frequency change displayed in figure 4.19. In this case a clear, linear relationship between the gold thickness and the frequency change can be seen. The frequency drops by a significant amount, over 20 MHz, over a very small thickness range, 500 nm. The rate of frequency decrease is aproximately 44.537 KHz nm^{-1}.

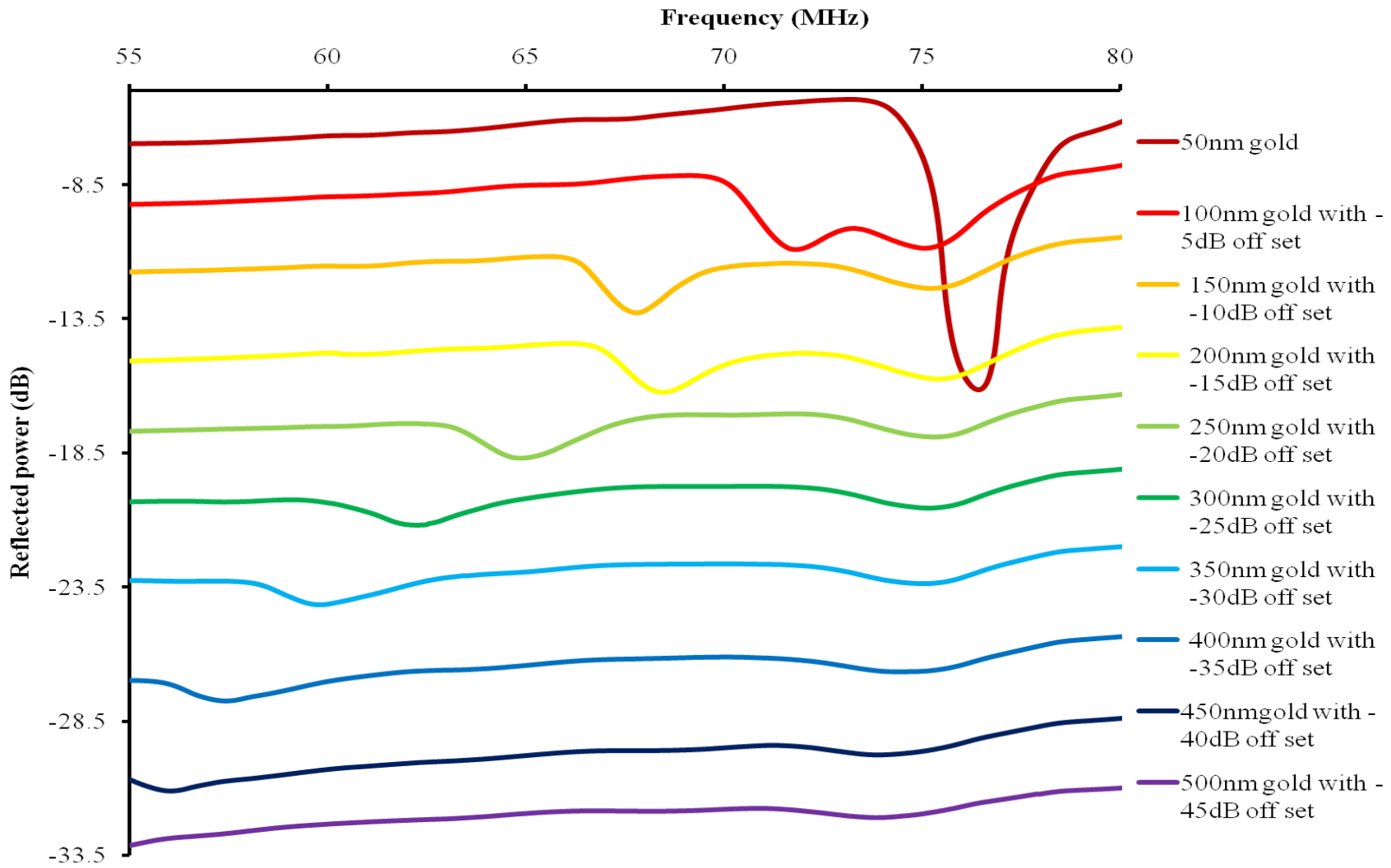

Figure 4.20: Resonant peak of $LiTaO_3$ as consecutive layers of gold are sputtered onto the surface. Target area at 0mm from central IDTs.

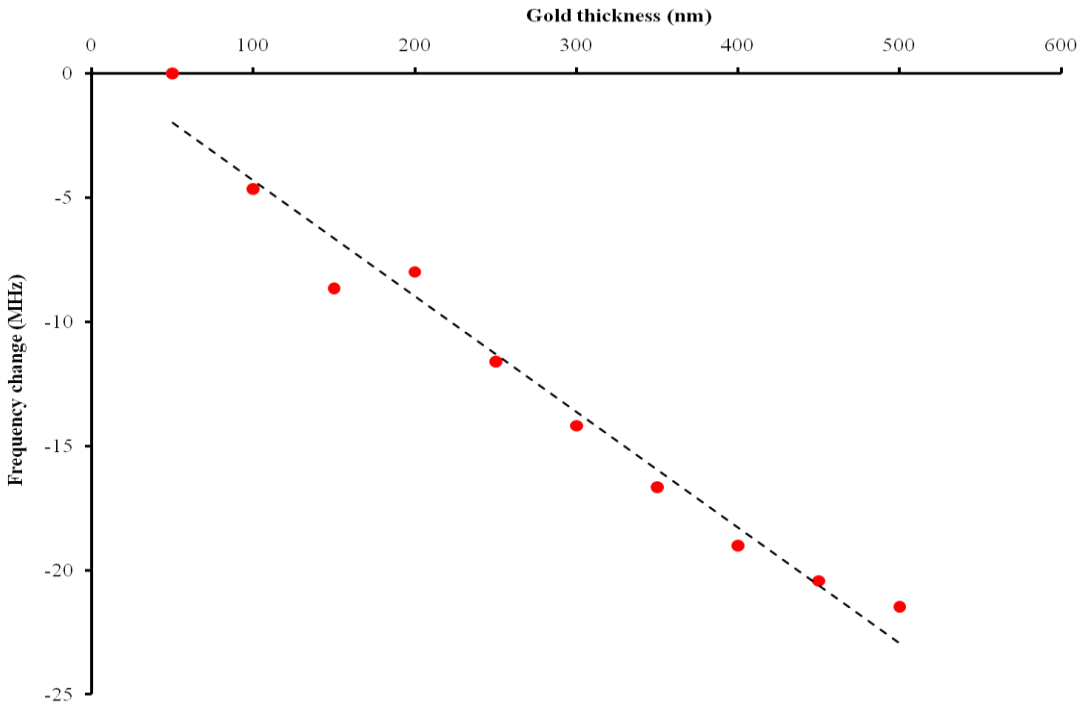

Figure 4.21: Frequency change for $LiTaO_3$ sensor as consecutive layers of gold are sputtered onto the surface. Target area at 0mm from central IDTs

Figure 4.20 is for gold sputtered directly over the central IDTs. Again, there is a well defined peak decreasing in frequency as the gold is sputtered onto the device. Figure 4.21 shows the frequency change for this device. The frequency drop is greater than the 1.5 mm device, aproximately 46.545 KHz nm^{-1}; otherwise it shows the same linear relationship between frequency and gold thickness and the same consistent behavior.

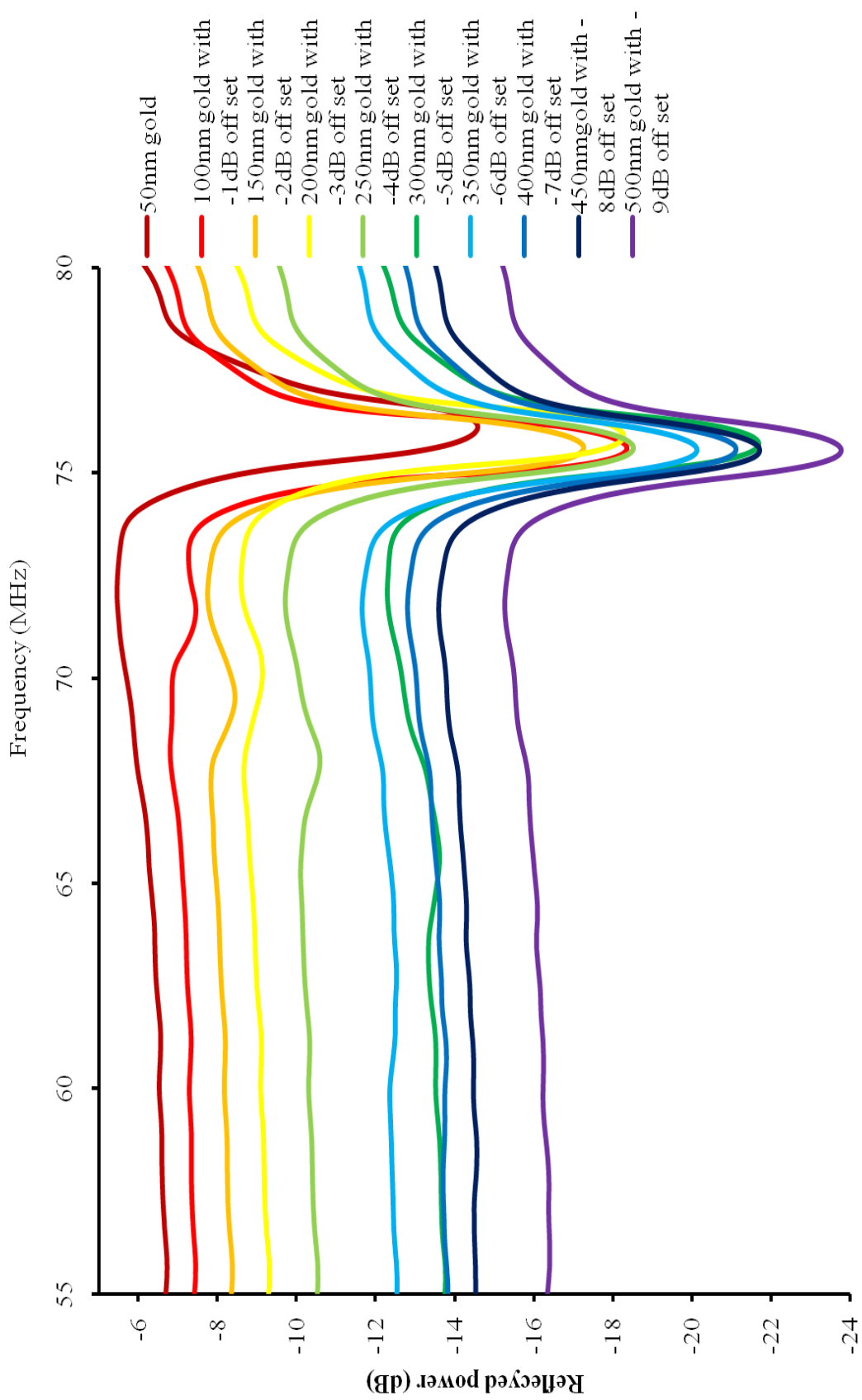

Figure 4.22: Resonant peak of $LiTaO_3$ as consecutive layers of gold are sputtered onto the surface. Target area at +1.5mm from central IDTs.

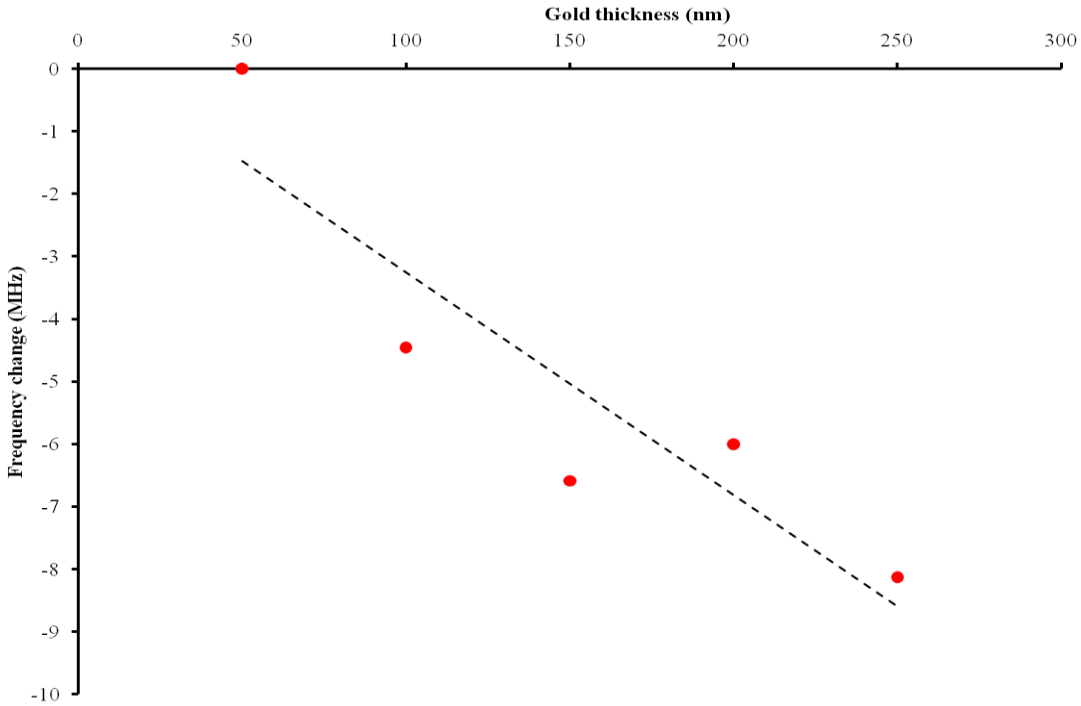

Figure 4.23: Frequency change for $LiTaO_3$ sensor as consecutive layers of gold are sputtered onto the surface. Target area at +1.5mm from central IDTs

Figure 4.22 again shows a device with the gold sputtered on +1.5 mm from the centre. The signal from this device is not ideal, but a small peak can be seen decreasing in frequency as the gold thickness increases, this has been indicated on the graph. These peaks are only aparent up to 250 nm. Still, by measuring the frequency change, figure 4.23 was plotted. Here the rate of frequency decrease is aproximately 35.600 KHz nm^{-1}. This is less than both the 0 mm device and the other 1.5 mm device.

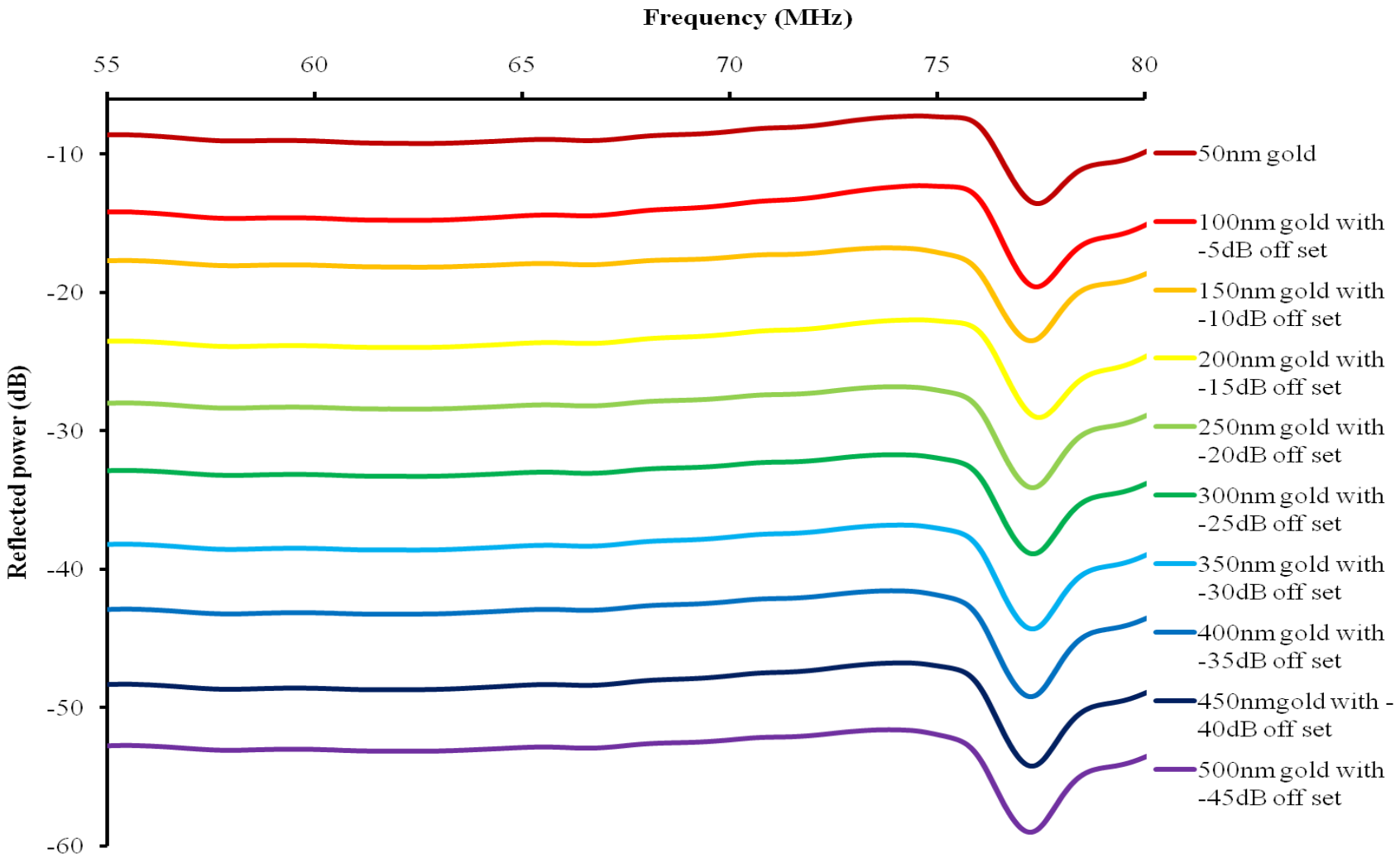

Figure 4.24: Resonant peak of $LiTaO_3$ as consecutive layers of gold are sputtered onto the surface. Target area at 3mm from central IDTs.

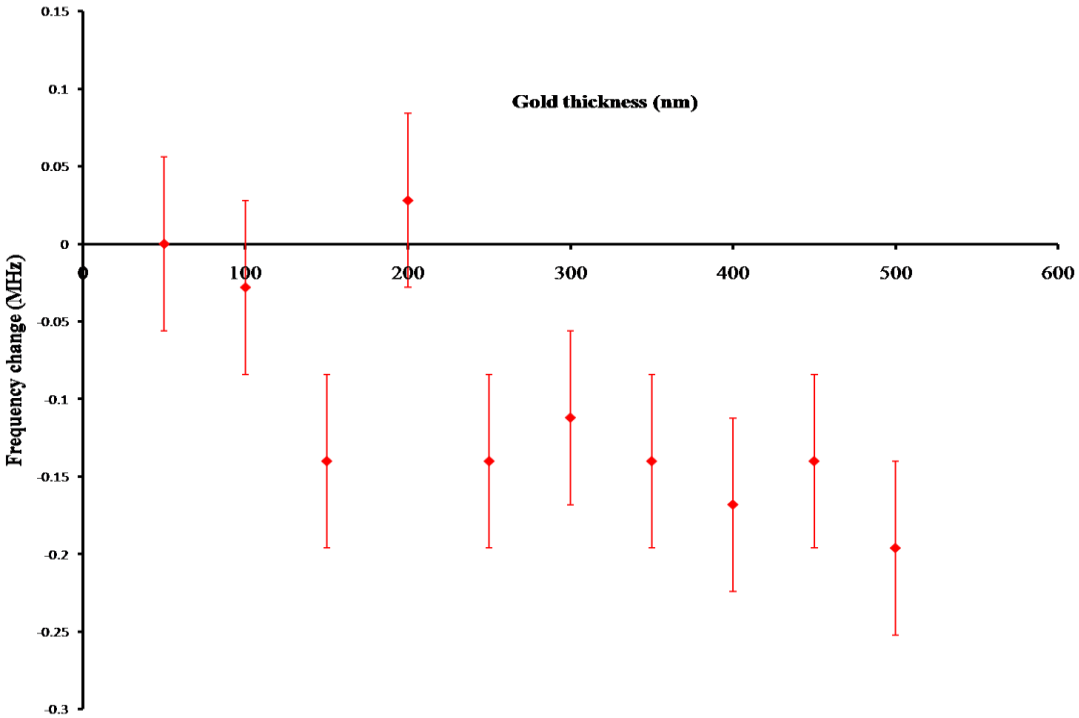

Figure 4.25: Frequency change for $LiTaO_3$ sensor as consecutive layers of gold are sputtered onto the surface. Target area at +3mm from central IDTs

Figure 4.24 shows the spectra from device with the gold sputtered +3 mm from the centre. In this case there is no aparent frequency change of any significance. Figure 4.25 shows the frequency changes. The changes were small and do not show a consistent downward shift.

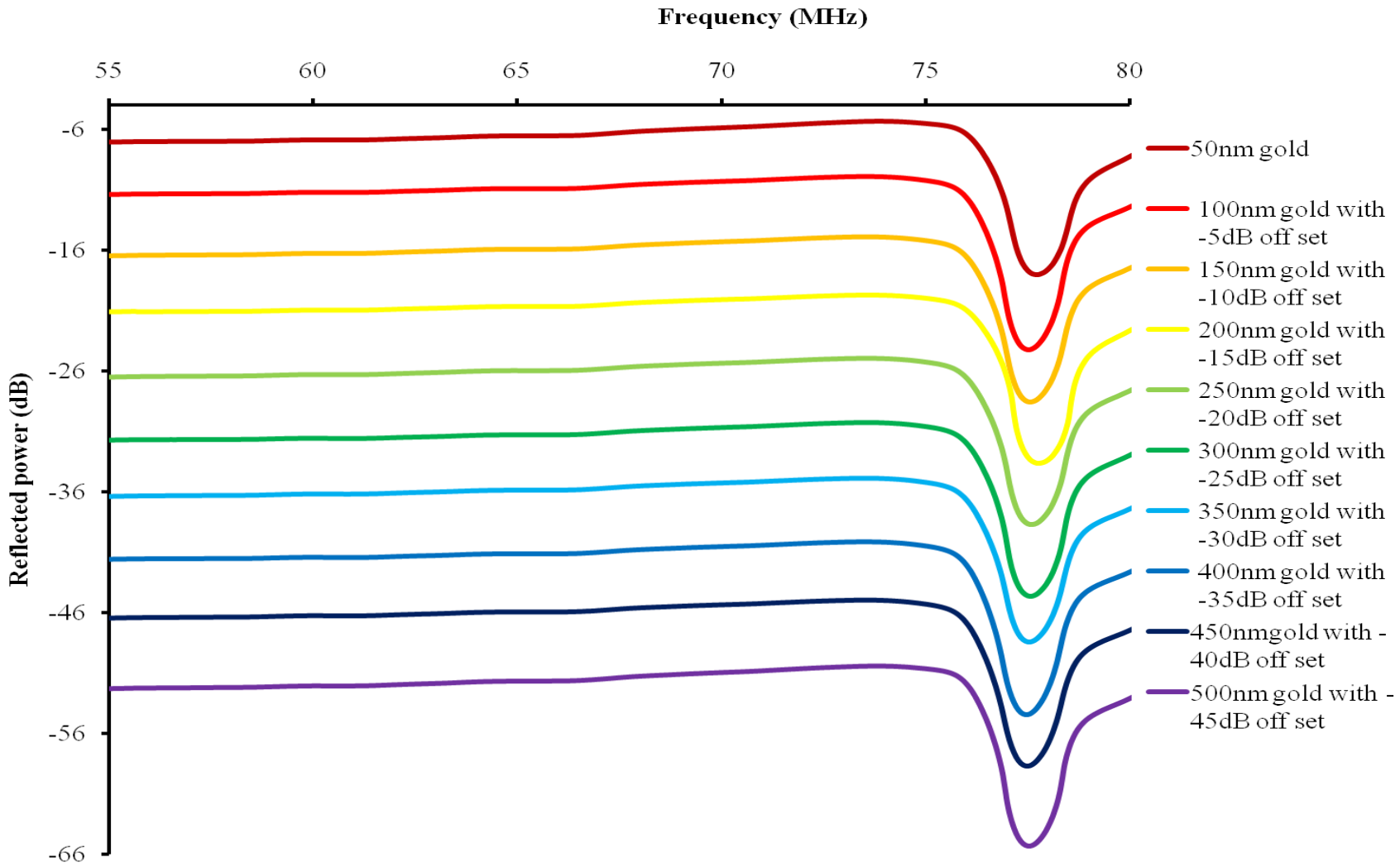

Figure 4.26: Resonant peak of $LiTaO_3$ as consecutive layers of gold are sputtered onto the surface. Target area at +4.5mm from central IDTs.

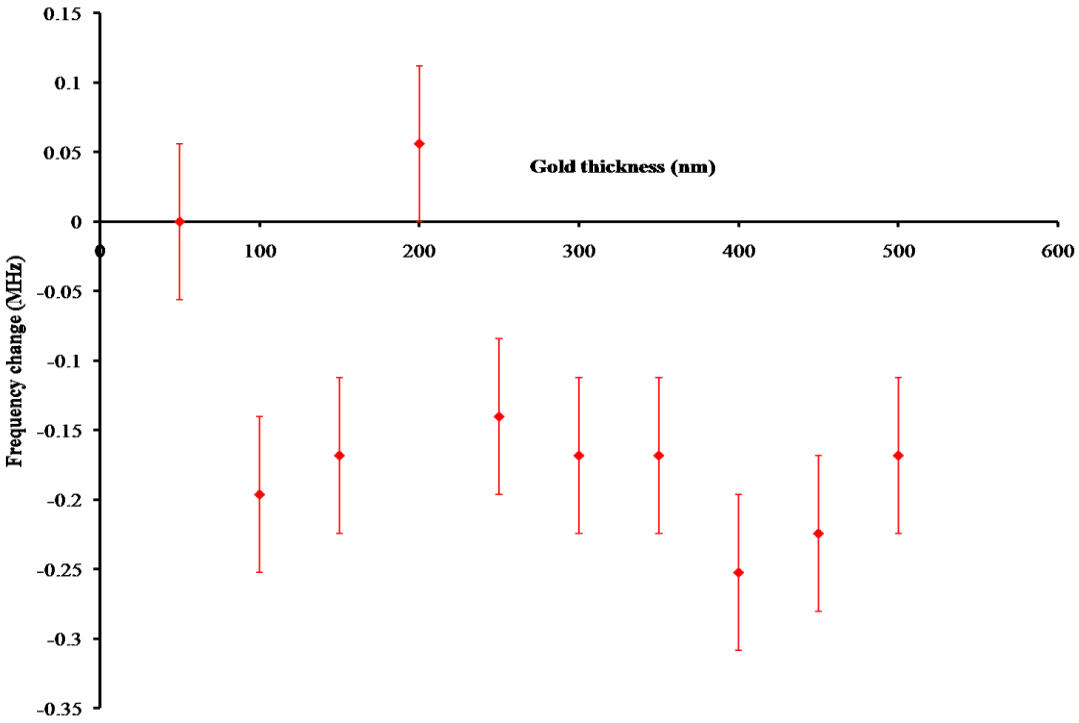

Figure 4.27: Frequency change for $LiTaO_3$ sensor as consecutive layers of gold are sputtered onto the surface. Target area at +4.5mm from central IDTs

Figure 4.26 shows another device with the target area at +4.5 mm, this time on the oposite position from the previous one. No significant frequency change is seen again. Figure 4.27 shows the frequency changes present. Again the changes are small, around 20 KHz, and do not show a consistent decrease.

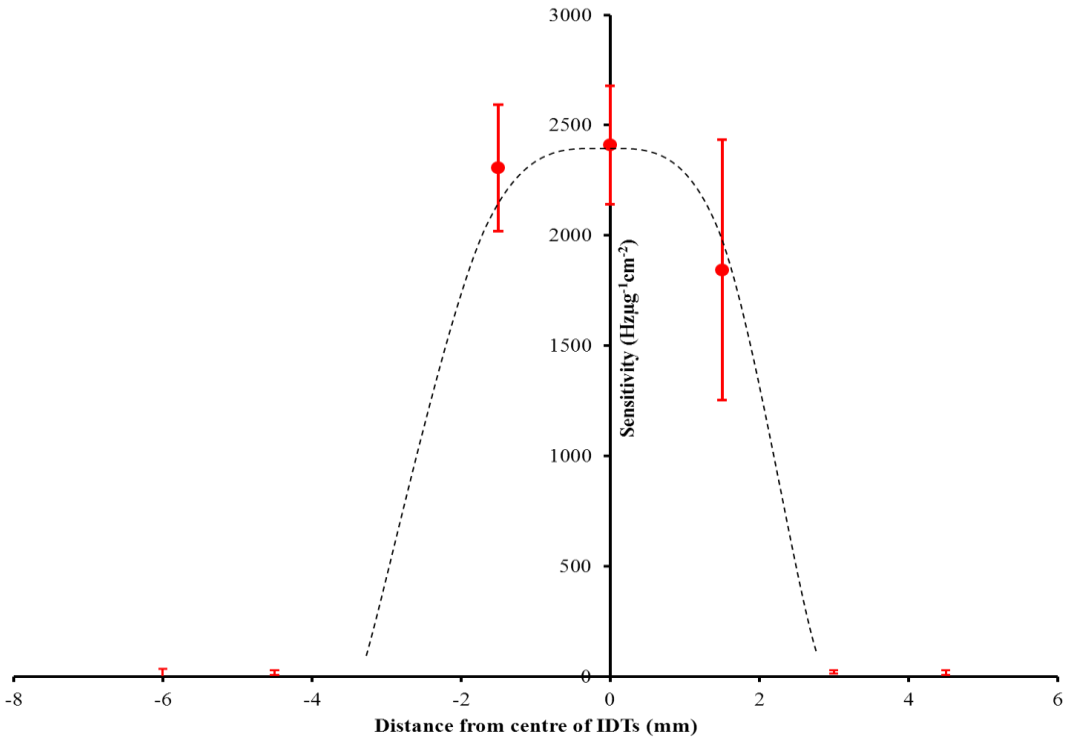

Figure 4.28: Graph showing the sensitivity of the device at different distances from the central IDTs. Device sensitivity apears to be greatest directly over the IDTs.

Given the target area of $7.5x10^{-6}$ m and the gold layer thickness of 50 nm, the mass of gold aplied with each layer is $7.245x10^{-9}$ kg. Figure 4.28 shows the mass sensitivity at the different positions on the sensor. Distance from the centre is given along the x-axis in mm and the sensitivity is shown on the y-axis in Hz μg^{-1} cm^{-2}. The mass sensitivity can clearly be seen to be greatest in the centre of the device, directly over the IDTs. On either side of this central point the sensitivity starts to drop quickly. The discrepancy between the value at -1.5 mm and +1.5 mm is likely due to the rapid change in sensitivity across the device. If a slight error was made in the position of the mask, and so the aplied gold, would result in large variation in sensitivity. At 3mm the sensitivity has droped from 2410±268 Hz μg^{-1} cm^{-2} to almost nothing. It is clear that the centre of the device is the most sensitive part and sensing experiments should make use of this area of the sensor.

4.4.3 Real time mass sensing

Experiments were performed to measure the frequency change caused by mass deposition in real time. A single-port sensor, fabricated on $LiTaO_3$, was connected to an oscillator circuit whilst inside a Semper 2 sputter coater (Nanotech). In addition, there was a 5 MHz QCM connected to a Maxtec oscillator in the same sputter coater. The purpose of the QCM was to have a well characterized

mass sensor present. This allowed the gold thickness to be measured and so the mass attached to the single port sensor. The single port response could then be compared to the attached mass and so determine the sensitivity of the device. The sputter coater was sealed and pumped down to low pressure. Once the chamber was at sufficiently low pressure, gold was sputter coated onto the surface of both the QCM and the single port device. The single port sensor had a mask placed on top of it. This was laser cut from acrylic and served to confine the gold to a 1.5 mm x 5 mm target area in the centre of the device, previously determined to be the most sensitive area of the device.

With both sensors connected to their respective oscillator circuits, the frequency of each was measured using an Agilent frequency counter. Data was then recorded using LabVIEW. The gold was sputtered onto the surface and the frequency recorded simultaneously. Frequency changes caused by the gold could then be calculated. The gold was sputtered in consecutive layers, each lasting 1 minute with a current of 20 mA.

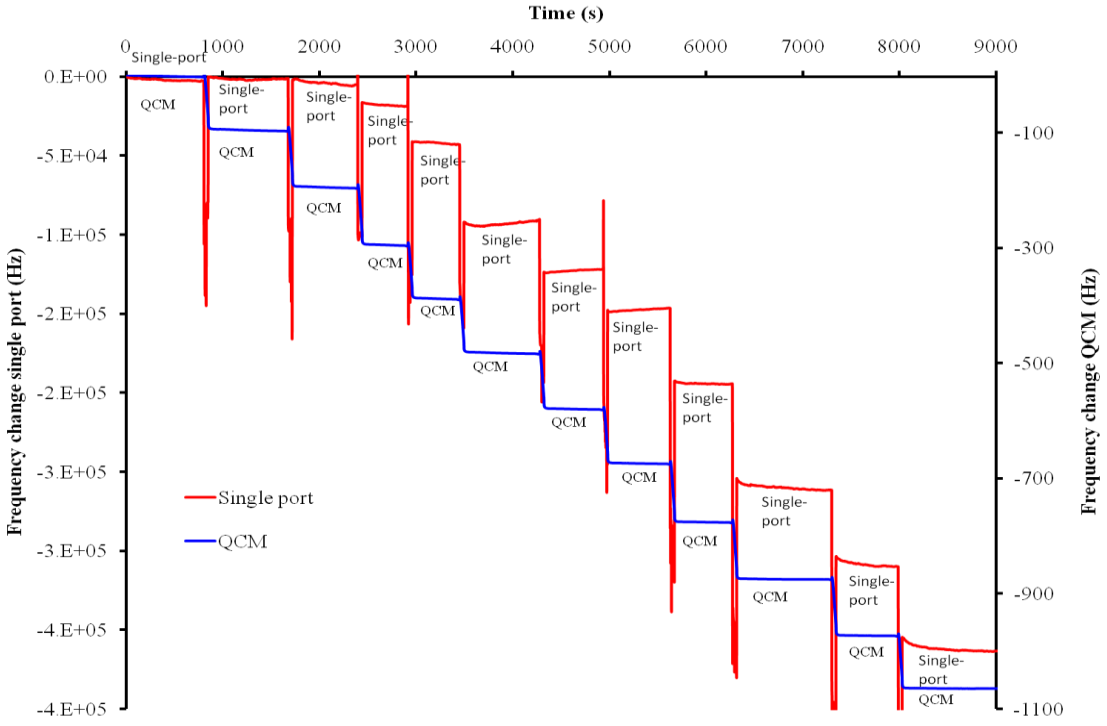

Figure 4.29. Frequency against time for both a $LiTaO_3$ single port sensor (red) and a QCM (blue) whilst gold is being sputtered onto the surface. The single port has a 9µm guiding layer.

Figure 4.29 shows the sensor frequency against time for both a QCM, shown in blue, and a single-port sensor, shown in red. The single port device has a 9µm guiding layer. The spikes in the single port data correspond to the gold being sputtered onto the surface. After the sputtering had stoped the device frequency was allowed to stabilize before gold was sputtered again. This was done multiple

times. The QCM shows a consistent frequency decrease from the gold, droping by aproximately 100Hz each time. The single port, however, does not show such a consistent frequency response. Initial sputtering resulted in a negligible frequency change. As the gold thickness increased so too did the frequency change caused by each aplication of gold. The sputter time and current and the QCM response remain constant, so it seems reasonable to assume the gold being aplied is the same each time. Therefore the varying frequency change from the single port must be due to the device itself.

Figure 4.30 shows the frequency change against gold thickness for sensors on $LiTaO_3$, all with different guiding layer thicknesses. Each device shows a similar response, in that the frequency changes start out small and get larger as the gold thickness increases. The 1.5, 3, 6 µm devices then plateau as the frequency change once again becomes small. The 9 µm device showed the small frequency change to begin with, but did no plateau like the other three devices.

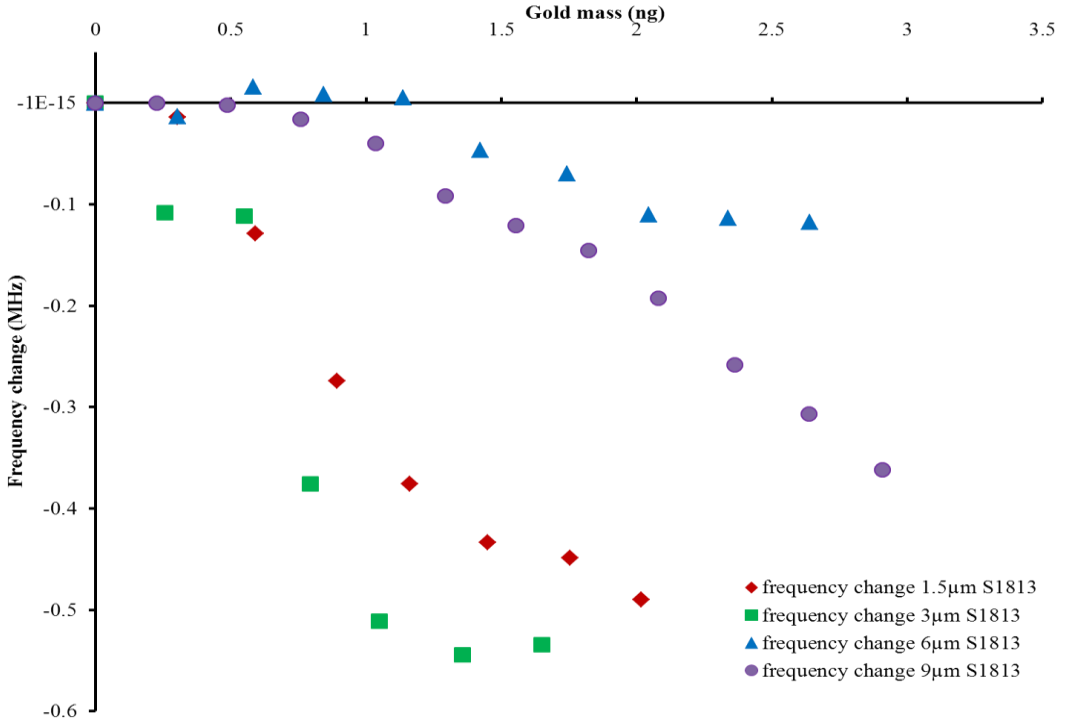

Figure 4.30. Frequency change against aplied gold thickness for several $LiTaO_3$ sensors with different guiding layer thicknesses.

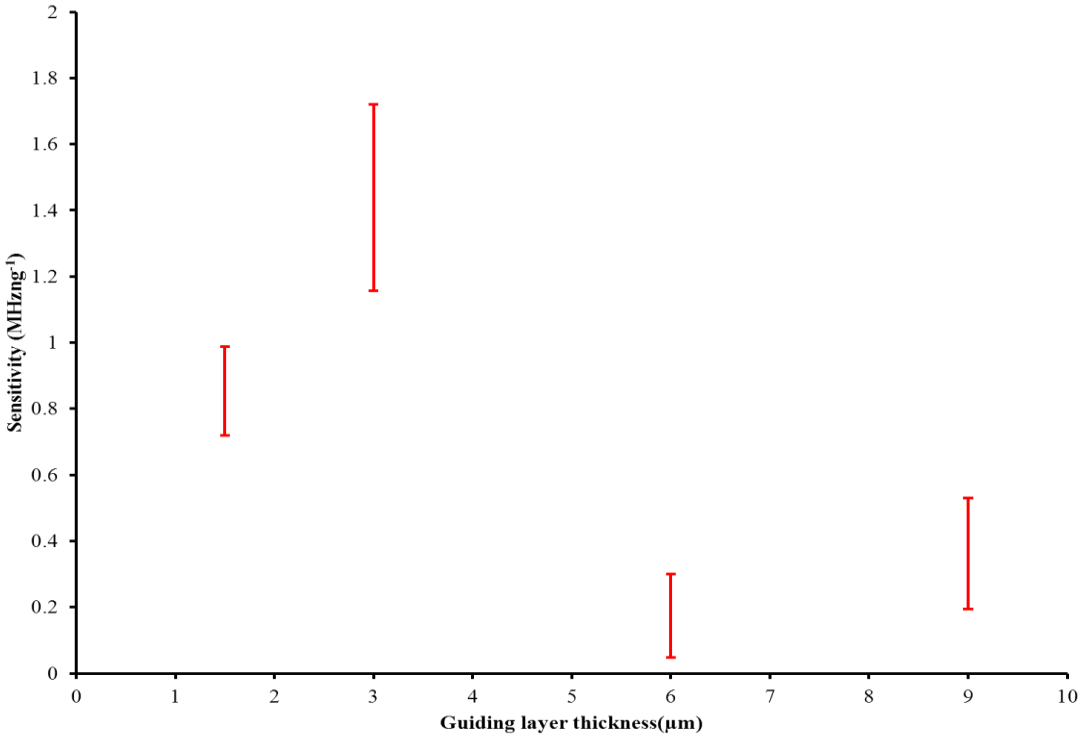

Figure 4.31. Graph showing the sensitivity against guiding layer thickness for $LiTaO_3$ devices inside sputter coater.

Figure 4.31 shows the mass sensitivity of the four devices, given in Hz ng^{-1} cm^{-2}. The sensitivity was calculated from the gradient of the steepest part of each plot. There apears to be some variation in the sensitivity due to guiding layer thickness. From the devices tested the maximum sensitivity was for a guiding layer of 3 µm and the minimum was at 6 µm.

4.5 Liquid viscosity-density measurements

In addition to investigating the mass sensing properties of the single-port sensors, experiments were conducted to investigate the sensor's response to viscosity and density changes of a liquid in contact with the surface of the sensor. The liquid used was a solution of glycerol diluted in de-ionized water. Glycerol was used as it is both water soluble and is a Newtonian liquid. The solution was mixed to concentrations of 5, 10, 20, 30, 40, 50, 60 and 70 % glycerol, measured by weight, using a Kern ALJ 220-4 mass balance, relative to the weight of de-ionised water. sensors were connected up to a network analyser so the spectrum could be recorded. The glycerol solution was pumped, via syringe, into a reservoir above the sensor, the device spectrum taken and the frequency measured. De-ionised water was them pumped through, to rinse off the glycerol, and another spectrum taken with just de-ionised water, to ensure the sensor returned to normal after the glycerol had been removed. The frequency change caused by the liquid, taken relative to the frequency in pure de-ionized water, was then

calculated. This was performed for a range of guiding layer thicknesses, from 1.5 to 13.5 µm of S1813. Frequency changes were then compared to the square root of the viscosity/density product.

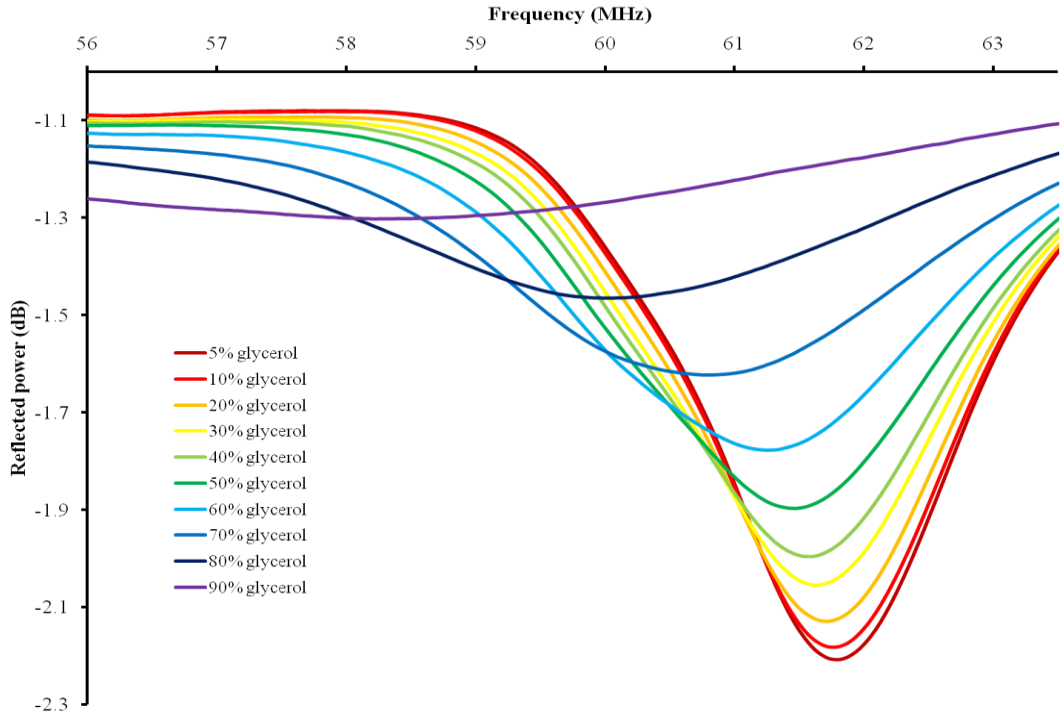

Figure 4.32. Network analyzer spectra of a $LiTaO_3$ sensor, with a 6 µm S1813 guiding layer, for a range of glycerol concentrations in contact with the surface.

Figure 4.32 shows the network analyzer spectrum for a device under several different concentrations of glycerol. Three main effects can be seen hapening to the signal. Firstly, the frequency is decreasing. At 80 % glycerol, the frequency is 3.625±0.003 MHz lower than with de-ionized water. Secondly, the reflected power also increases, from -2.21±0.01 dB to -1.3±0.01 dB in the same glycerol range, suggesting the signal is being damped. Thirdly, the peak is broadening. Figure 4.33 shows the frequency change of the sensor relative to water, shown in Hz on the y-axis, against the glycerol concentration, shown as a percentage on the x-axis.

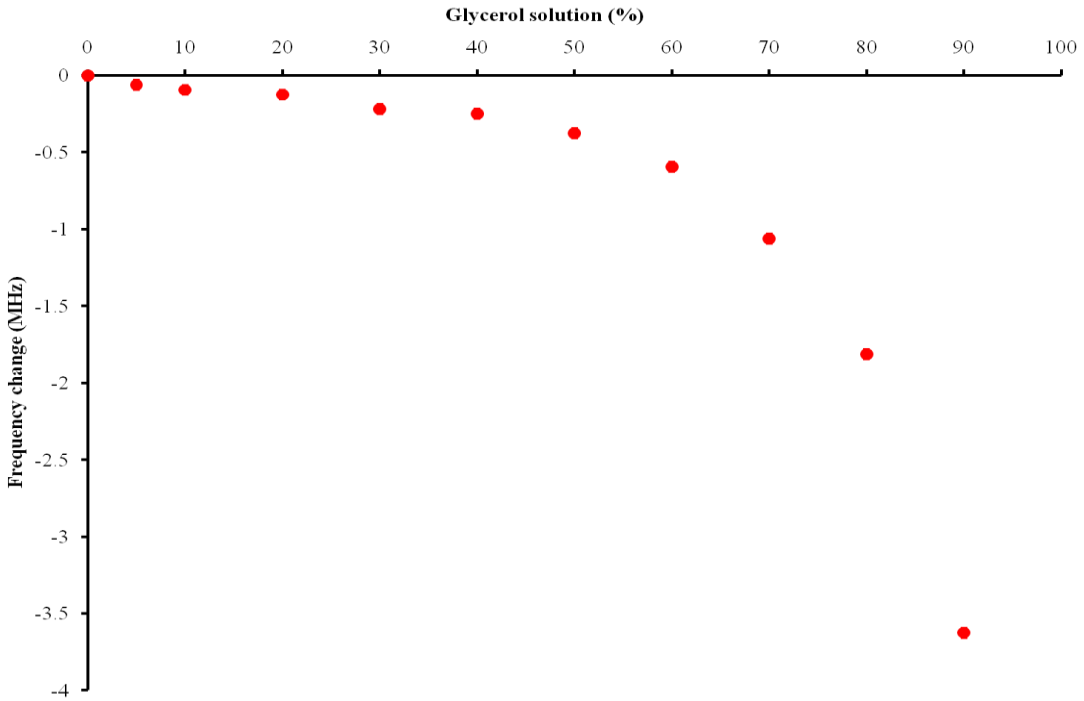

Figure 4.33. Frequency change of a $LiTaO_3$ sensor for a range of glycerol concentrations in contact with the surface.

One of the main limitations of the Sauerbrey equation is that it only aplies to systems involving rigid mass on the surface of a sensor. When using an acoustic sensor in a liquid it is necessary to utilize equation 4.1, which is the Kanazawa and Gordon equation. The Kanazawa and Gordon equation relates the frequency change the crystal experiences to the viscosity and density of the liquid. Here f_0 is the fundamental frequency, ρ_q is the density of the crystal and μ_q is the sheer modulus of the crystal, all the same as in the Sauerbrey equation. The major difference is that instead of a mass component, there is η_l (the viscosity of the liquid) and ρ_l (the density of the liquid).

$$\Delta f = -n f_0^{\frac{3}{2}} \left(\frac{\eta_l \rho_l}{\pi \mu_q \rho_q} \right)^{\frac{1}{2}} \qquad 4.1$$

Equation 4.1 shows that the frequency change is proportional to $(\eta_l \rho_l)^{1/2}$. In figure 4.34 the frequency change from figure 4.33 is plotted against the square root of the product of η_l and ρ_l. If the sensor is exhibiting Kanazawa and Gordon like behavior, then this graph should show a linear relationship between the two. Figure 4.34 shows this to be true. This tells us that when the single-port sensors are operating in a liquid, it is apropriate to us the Kanazawa and Gordon equation.

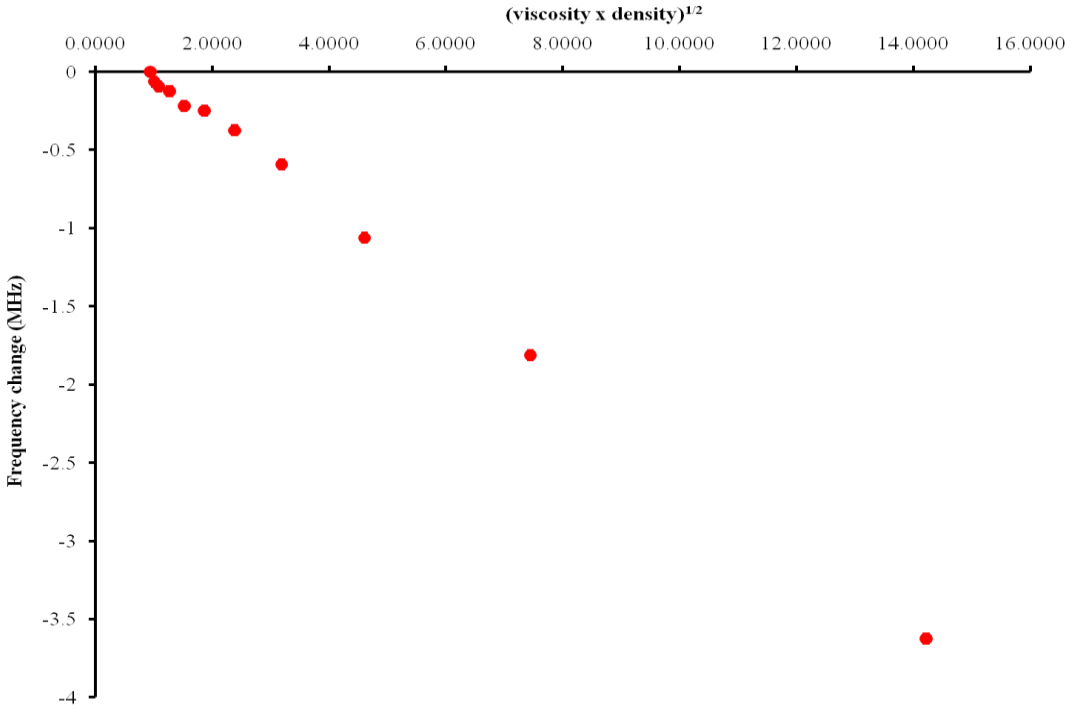

Figure 4.34. Frequency change against square root of viscosity x density for a $LiTaO_3$ sensor. Linear relationship implies Kanazawa and Gordon like behavior.

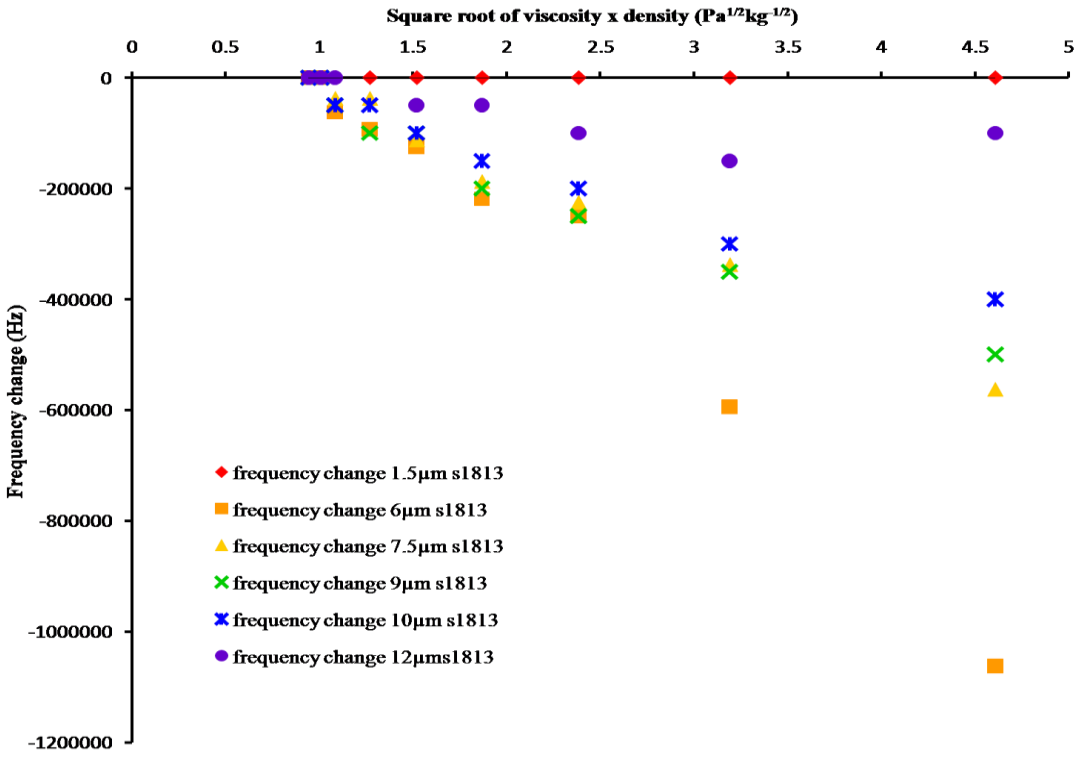

Figure 4.35. Frequency change against square root of viscosity x density for a number of SSOR $LiTaO_3$ devices with different guiding layer thicknesses.

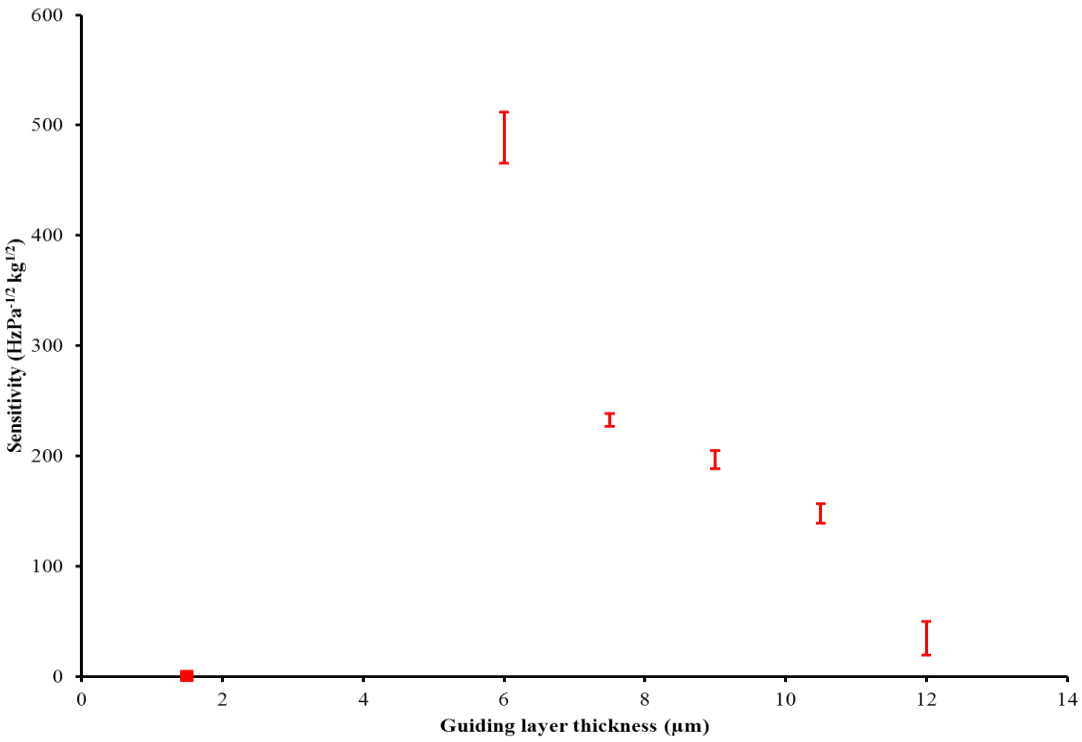

Figure 4.36. Sensitivity against guiding layer thickness for a $LiTaO_3$ sensors.

Figure 4.35 shows the frequency change for several $LiTaO_3$ devices with different guiding layer thicknesses, plotted against the square root of the density-viscosity product. Measurements were taken relative to water. All the devices show a linear relationship between frequency and the square root of the density-viscosity product. The device with the 6 µm frequency change shows the greatest frequency change as the glycerol concentration increases. Figure 4.36 shows the sensitivity of the devices. The maximum sensitivity of the devices tested was with a guiding layer of 6 µm.

When the devices were used for mass sensing (see section 4.1.1) the sensitivity was highest at 4.5 µm. This shows close agreement with the optimum guiding layer thickness for densitiy-viscosity sensing.

4.6 Discussion

Figures 4.8 and 4.10 show the effect on the frequency of the single-port device, for both $LiTaO_3$ and quartz, of increasing the guiding layer thickness. What is clear on both of these graphs is that there is greater attenuation of the signal as the guiding layer thickness increases. This is likely caused by using S1813 as the guiding layer. A polymer such as S1813 is acoustically absorbent, so as the layer thickness increases more of the wave energy is absorbed by the S1813. As a result the strength of the signal decreases, meaning that S1813 may not be the best choice for a guiding layer. An

alternative would be SiO_2, which has been used by Du *et al* [76] and Harding *et al* [77], as SiO_2 absorbs less acoustic energy. Another advantage of SiO_2 is that it is more resistant to harsh chemicals, increasing the range of applications for the sensor.

Figures 4.8 and 4.10 can also be compared to Love wave dispersion curves from the literature. McHale gives a review of the theory behind Love wave devices [83]. His graph of phase speed against the ratio of guiding layer to wavelength, seen in figure 2.11, shows close agreement with the graphs plotting frequency against layer thickness shown in this chapter. This suggests that the layer guided single-ports are behaving in the same way as two-port Love wave devices. McHale also shows the way mass sensitivity changes as the guiding layer thickness increases, showing a repeating pattern similar to that shown in figure 4.12.

It was shown that care needs to be taken when choosing which part of the device to use for sensing, this is shown in section 4.4.2, and specifically figure 4.28. The mass sensitivity changes rapidly across the device, with the peak sensitivity directly over the centre of the IDTs. Any inaccuracy in the target area used could result in a massive change in sensitivity, meaning the device won't be operating at the optimum sensitivity.

Work needs to be done to determine the limit of detection of the single-port sensors. Here the mass sensitivity was limited by the scale and resolution of the network analyser. Due to the method used to measure the frequency changes caused by the gold sputter coater, any frequency changes below 25 kHz would not have been recorded. Even with this limitation the detection limit is comparable to the QCM used in chapter 3. Using a method to that could measure changes of a few Hz would give a vastly superior limit of detection to the QCMs, such as using an oscillator circuit and frequency counter.

Figure 4.29 shows a possible temperature dependence of the single-port devices. There is a sharp spike in the plot when the gold is being sputtered onto the $LiTaO_3$ which is not present in the QCM plot. The way a sputter coated works is by vaporising a gold target so the gold can deposit onto the substrate surface. As a result there is a sharp temperature change as the gold lands on the surface, which causes a frequency change in the $LiTaO_3$ single-port device. Quartz is much less temperature dependant [70] than $LiTaO_3$ and so doesn't show a frequency change. More work would need to be done to investigate the temperature stability of the Single-port sensors when fabricated on $LiTaO_3$ and would provide incentive to use Quartz as an alternative substrate when temperature changes are expected. However, if the single ports are to be used for the purposes of sperm quality assessment, dramatic temperature changes should not be taking place.

Nomura *et al* [72] used a single port acoustic resonator for liquid sensing. In their work a 30 MHz device with a wavelength of 68 μm was fabricated on $LiTaO_3$ using aluminium film IDTs. This

device had a thin 5 μm photoresist layer to insulate the IDTs from the liquid. This device was then used to measure the frequency change caused by a range of water glycerol solutions. From 5 to 85 % glycerol the device undergoes a 9 kHz frequency drop. Figure 4.35 shows frequency changes for the devices used in this chapter when loaded with water glycerol solution. Though the devices in this chapter were 80 MHz, there is a similar relationship between frequency and viscosity.

4.7 Conclusions

Initial experiments showed that the single port sensors responded to the application of a guiding layer. The resonant frequency of the device could be altered depending on the thickness of the layer. The layer thickness was then shown to directly correspond to the mass sensitivity of the devices tested. The optimum thickness was found to be 4.5 μm of S1813. In addition to determining the best guiding layer thickness for improved sensitivity, it was determined that the central IDTs were the most sensitive part of the device.

Experiments were performed to conduct real time mass sensing with single port sensors connected to an oscillator circuit and frequency counter while inside a sputter coater. The QCM present in the chamber showed the gold layers to be consistent throughout. However, the single port sensors did not behave as expected. There was no consistent frequency decrease present. Each sensor exhibited a small change in the initial sputter cycles. The frequency change then became larger to a maximum, before decreasing again. By using the steepest part of the frequency change against sputtered gold graph, a clear relationship between guiding layer thick and sensitivity was shown.

Experiments were performed that showed the sensors could be used in a liquid environment. Comparisons between the frequency and the viscosity/density product of a glycerol solution showed behavior in agreement with the Kanazawa and Gordon equation. It was also shown that the thickness of the guiding layer had an effect on the sensitivity to viscosity and density changes in a liquid. Of the range of thicknesses tested the 6μm.

While the single-ports showed promise as sensors for the sperm analysis system, there were other areas that also needed developing to achieve the stated goal of a compact and simple system. The next chapter details developments in the electronics and swim cell used for the sperm analysis.

5. Sperm Quality

Detection Device

5.1 Introduction

This chapter details the further development of the sperm time of flight system using a QCM as the sensing element. The motivation for developing the ToF technique from the process described in chapter 3 comes from a desire to produce a device that is both more compact, self contained and simple to use.

The market for a sperm analysis device can be split into three main sections: clinical, animal and research. The clinical sector is satisfied with current techniques. Both the animal and research sectors have a need for such a device, in the £100-£150 price band and able to process samples in less than 10 minutes [107].

From the point of view of this project, there were far more factors to take into account when developing a working system than simply the price and the process time. Two main aims of the project were to develop something portable enough to be used in the field and a system simple enough that specialist training was not necessary in order to use it.

To make the system portable, the electronics needed to be rethought. As seen in chapter 3, the aparatus up to this point consisted of large pieces of equipment such as the Agilent frequency counter and the Maxtec oscillator. The Maxtec oscillator was replaced by a circuit designed in house based on a Pierce oscillator circuit. This new circuit makes use of small electrical components that significantly reduced the size compared to the Maxtec. Secondly, the Agilent frequency counter was replaced with a circuit built around a universal frequency to digital converter (UFDC-1). This frequency counter was significantly smaller than the Agilent. Both the oscillator and the frequency counter combined were smaller than just the Maxtec oscillator alone, making the new in house aparatus considerably more compact. The use of such cheap, commercially available components also served to reduce the price, fulfilling one of the criteria set out by the market research. These new pieces of aparatus did, however, introduce their own technical problems, such as an increased signal noise compared to the old setup and reduced accuracy.

The swim channel used in chapter 3 was also replaced with a more compact design that had several improvements over the original. The path length was significantly reduced along with the volume of buffer the cell could hold. The new cells were a modular design made of interchangeable components. This allowed for ease of cleaning and for different cell geometries to be tried.

Using the newly designed swim cells, experiments were performed to compare the performance of the Agilent frequency counter to the UFDC-1 circuit, looking at frequency stability and

frequency change experienced. Sperm samples were added and the frequency change caused compared between the two systems.

Additional control experiments were carried out to ensure that frequency changes were due to live sperm migrating to the sensor and not due to sperm diffusing through the liquid. To do this, aged samples (21 days since delivery) of sperm were compared to “fresh” samples (less than 3 days since delivery). The aged sperm were used in ToF experiments performed alongside fresh sperm experiments and the frequency changes compared. The presence of sperm on the sensors for both kinds of sample was checked visually using a microscope.

5.2 Aim for ideal system

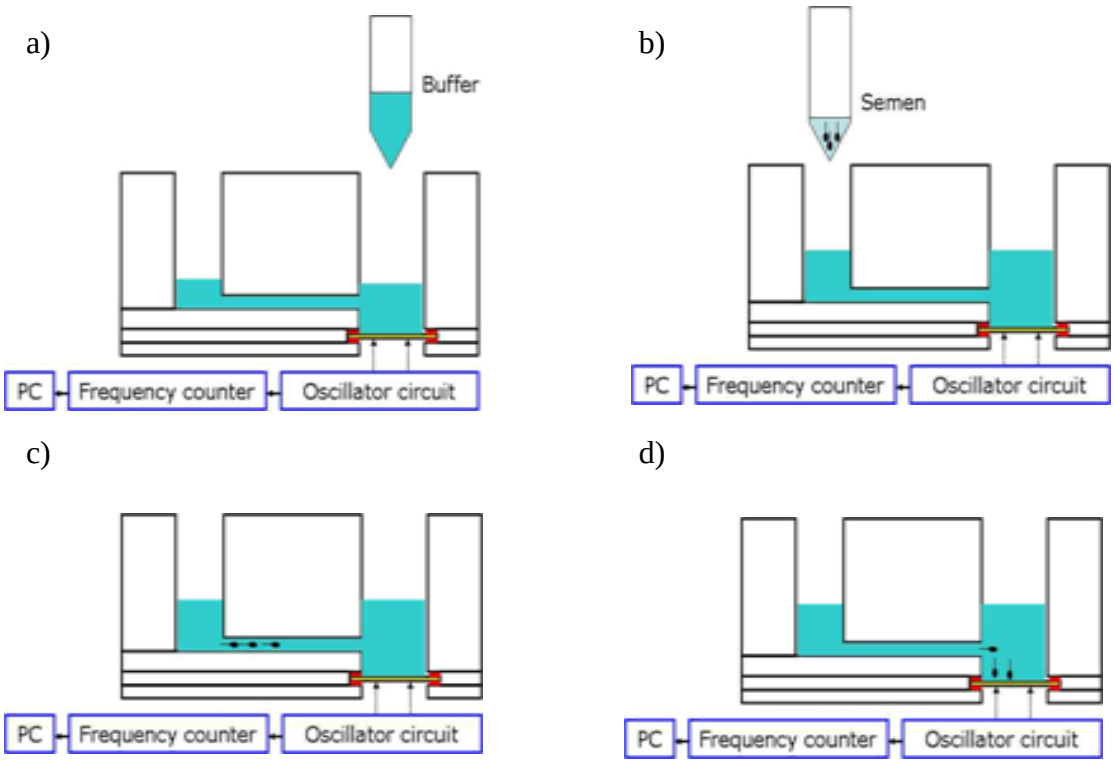

Figure 5.1: Diagram showing intened experimental procedure and setup for sperm ToF system. a) buffer added to swim cell, b) sperm sample added to inlet port, c) sperm self propel down swim channel, d) sperm reach sensor and are detected.

The experimental setup, as outlined in chapter 3, remained essentially unchanged. The system still needs a swim channel. This should be compact, easily cleanable and capable of forming a water tight seal with the QCM. The cell should also contain enough buffer that the added sperm sample is only a small proportion of that amount.

In additon to the cell are the electronics used to drive the crystal, measure the frequency and record the data. To drive the crystal an oscillator is used. In chapter 3 this was the Maxtec phase lock

oscillator, ideally something more compact and cost effective is needed. So far an Agilent frequency counter was used to measure the frequency, again a smaller, low cost alternative would be desirable. Data has so far been recorded using a laptop computer. If possible it would be beneficial to create an intergrated piece of electronics to record and display the data.

The function of the equipment remains the same. To measure the arrival of sperm by monitoring the frequency of a QCM. This still conforms to the process of allowing a sample of sperm to self-propel down a swim channel towards the sensor. Figure 5.1 shows both the experimental setup and procedure.

5.3 Experimental setup

5.3.1 Swim cell

Figure 5.2 shows both a diagram of the swim cell and a photograph of a finished cell. The cell was constructed out of acrylic sheets. These were 3mm in thickness and cut out using an M-500 laser cutter (Universal Laser Systems). The cell was made out of several layers of the acrylic sheets and was bonded together using an acrylic bonder (RS Components).

The cell had an open area above the channel. This served 3 purposes. Firstly it allowed buffer to be added to the cell (1.5 ml of PBS), secondly it provided a vent for pressure to equalise and thirdly the large volume above the channel allowed any chemicals in the semen sample to diffuse into the bulk of the liquid. A second opening, much smaller than the other, provided an entry point at the start of the channel for the sperm to be added.

The swim channel part of the cell was 15mm long and ran from the sperm entry point to the QCM. The cell also had an integrated gasket. This was both to hold the QCM in place and provide a water tight seal around it. The QCM then connected to two spring loaded pin contacts which connect it to the oscillator circuit.

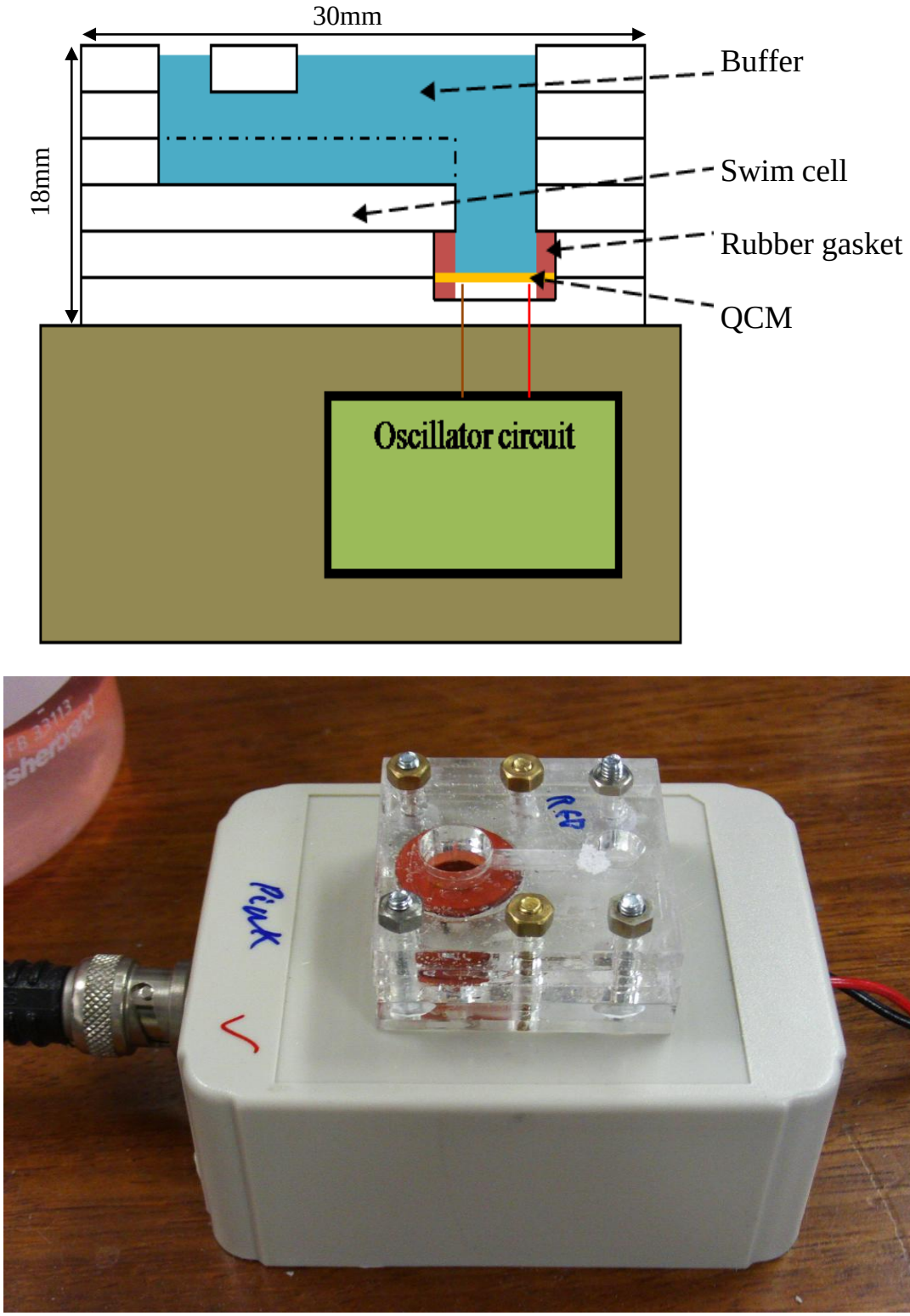

Figure 5.2: Diagram showing swim cell (Top) and photograph of constructed cell on top of box containing the oscillator circuit.

5.3.2 Pierce oscillator circuit

In place of the Maxtec oscillator, a circuit based on the Pierce oscillator circuit was constructed. The main component of this was a MAN-1LN amplifier (Mini-Circuits) [108]. This is a low noise amplifier which has a frequency range of 0.5 MHz to 500 MHz and a gain of 28 dB. The

circuit also contains two 10 pf capacitors, two 100Ω resistors and a 100KΩ resistor. It is then powered by a 12 V suply. Figure 5.3 shows a circuit diagram of the oscillator.

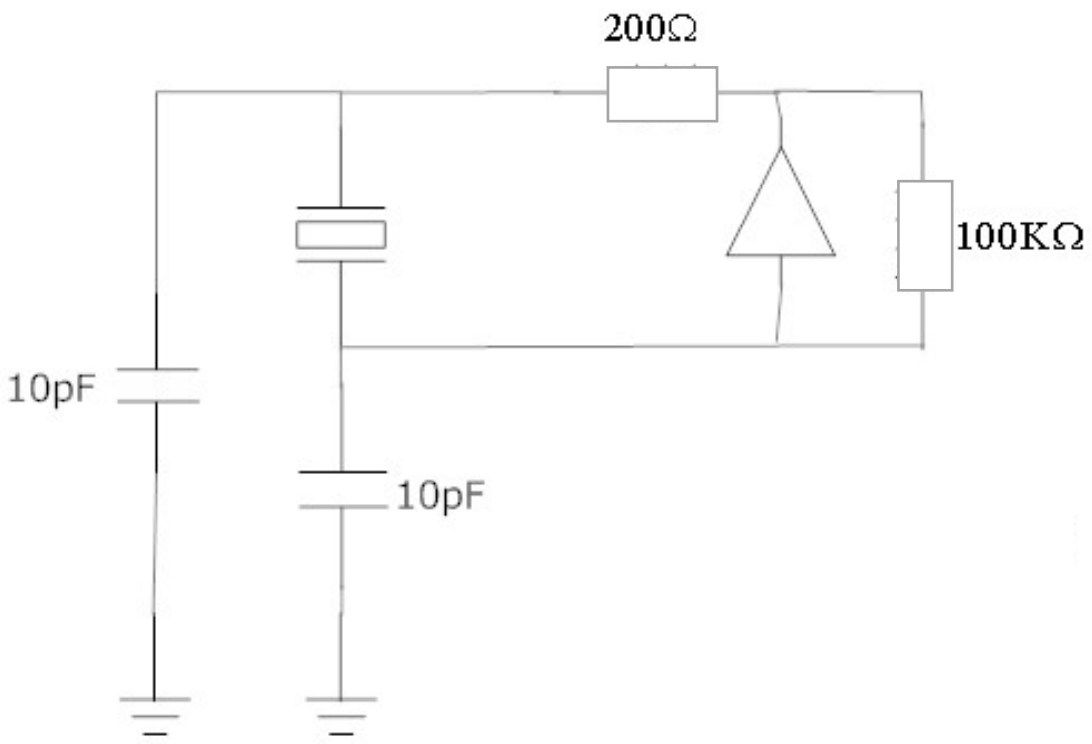

Figure 5.3: Circuit diagram of the in house oscillator circuit.

5.3.3 Mounting the QCM

Several different methods were tried to mount the QCM in the swim cell. One method involved using superglue to attach the crystal to the swim cell. This resulted in two problems. Firstly, there was excessive noise in the signal when this method was used. Secondly, this meant the crystal was permanently attached to the cell, which made cleaning the crystal harder and if either the crystal or cell needed replacing then the other would need to be discarded.

Two different gasket materials that were tried were PTFE and acrylic. Both of these resulted in problems getting an adequate fit. If the gasket was too small the cell would leak and if the gasket was too large then the crystal would break when the two halves of the cell were screwed together. As a result, both of these materials were deemed unsuitable due to the difficulty in securing a water tight seal without damaging the crystal.

A rubber gasket was found to be the best material to use. Using a laser cutter, gaskets were cut from 1 mm thick rubber sheets in shapes and sizes specifically designed to fit the crystal holder. The gaskets were then glued into place using super glue. The advantage of using the rubber gaskets is their

deformability. When the QCM is placed in the holder and the cell screwed together, the gasket will deform to some extent around the crystal. This means the crystal is less likely to crack and will also result in a better seal.

5.3.4 Sperm sourcing

The sperm samples were suplied by JSR Genetics, a commercial artificial insemination centre. Samples came diluted in Tri X-cell (IMV technologies), which is a chemical extender designed to increase the sperm life. Tri X-cell is a mixture of Carbohydrates, mineral salts, antioxidants, buffer, antibiotics (gentamycin, amoxycillin and tylosin) and bovine serum albumin. By using this, sperm will remain useable for more than 5 days when stored below 17^{-}C.

5.3.5 Coated crystals vs. uncoated crystals

In previous work [7, 109], crystal were chemically coated using either Poly-L-Lysine or cysteamine. Both of these substances served as adhesive coatings for the sperm to attach to. However, it was found that sperm would reliably attach to the gold electrodes of an uncoated, polished QCM. This removed the need to coat the crystals and the potential for the coating to fail. The QCMs could then be cleaned by either ethanol or a solution of Papain (Sigma Aldrich) and physical agitation using a cotton bud to remove the attached sperm. In this way the crystal could be reused without the need to re-coat them between experiments.

5.3.6 Multiple measurements using an array of cells

Work was done to construct an array of swim cells all running simultaneously. This was done for two reasons. The first reason was simply to increase the amount of data being recorded. By having multiple cells on the go, frequency data and ToFs for several runs could be recorded much faster. The second reason was so that different parameters could be investigated while keeping the sperm samples the same. Given that the sperm would degrade over time, it would be beneficial to perform experiments with sperm of the same "age". By having multiple cells running, several aliquots could be taken from the same stock sample and experiments performed simultaneously. This could be for data averaging or to perform experiments under different conditions but using the same sperm sample. These different

conditions could include, changing the environment temperature or the chemical composition of the swim medium depending on what was being investigated.

To achieve this it was simply a matter of constructing a number or swim cells, several oscillator circuits and providing power suplies for them all. The Labview program used for the single cell experiments was only designed to receive one set of frequency data. So the program had to be modified slightly so it could handle input from several sources.

5.4 Effect of pressure waves on QCM resonant frequency

One problem encountered was a tendency for the frequency to display periodic oscillations when the cell had PBS in it. These resonances could be in the region of several hundred Hz, as shown in figure 5.4. As previously discussed in chapter 2, these resonances are due to surface normal pressure waves generated by the QCM and are related to the distance between the QCM and the liquid air boundary [39]. This distance changes due to evaporation and the frequency can go through several resonance cycles in a relatively short amount of time.

To reduce this effect two methods were tried. First an acrylic sphere was placed over the QCM. The frequency data for this is shown in figure 5.5. The noise seen in this data is much greater than acceptable. The frequency resonances are either not present or lost within the noise. Unfortunately, the frequency change caused by sperm during a sensing experiment would also be lost within the noise. Secondly, a pressure sensitive adhesive (Blu-tac, Bostik) was tried. A flat sheet of the Blu-tac was inserted into the PBS above the QCM and at an angle of 45^{o}. The effect of this was the elimination of the resonances, but without the excessive noise seen with the acrylic sphere. This is shown in figure 5.6.

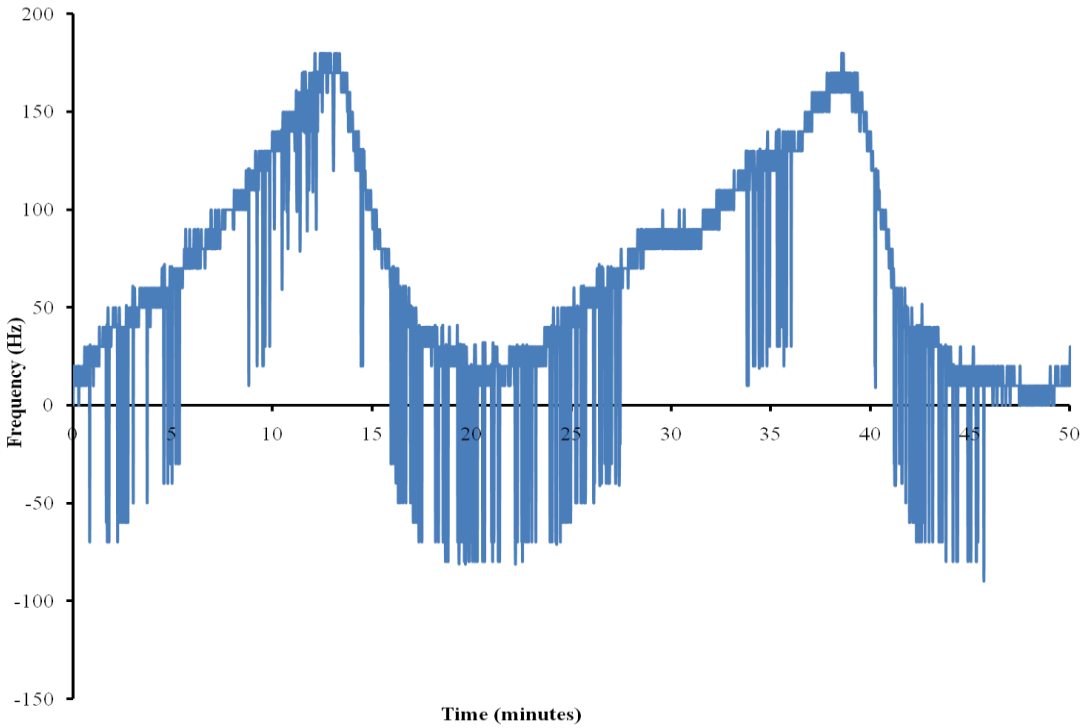

Figure 5.4: Frequency against time for a QCM operating in PBS. Two resonance peaks are clearly visible.

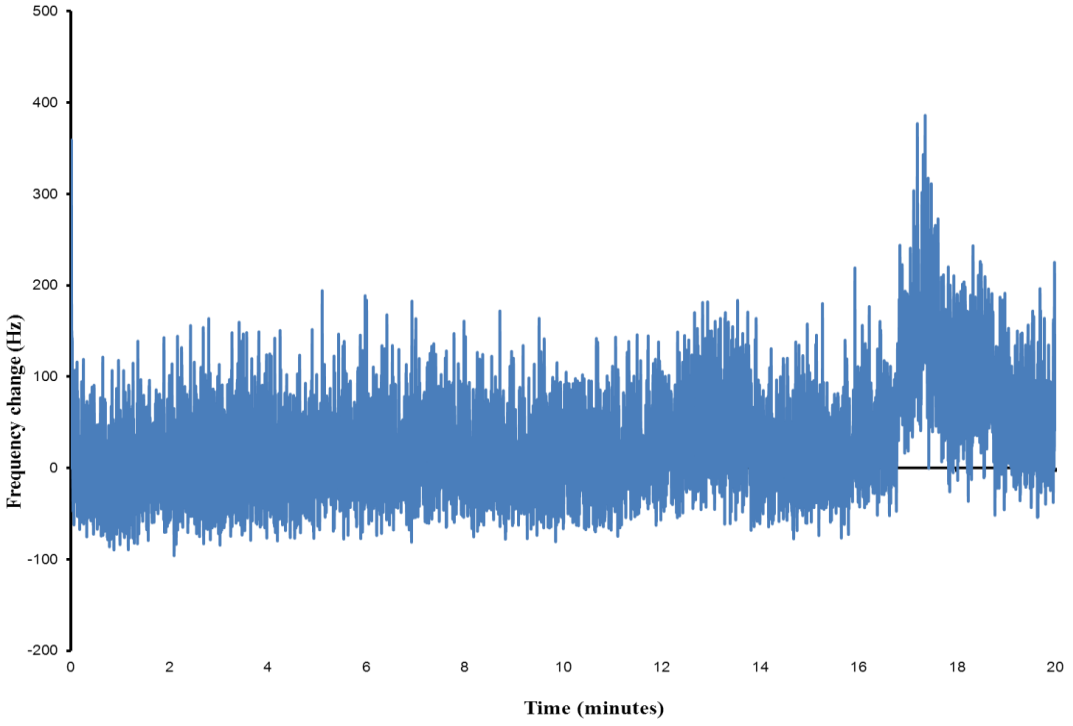

Figure 5.5: Frequency against time for QCM operating in PBS. An acrylic sphere was place over the QCM to eliminate resonances.

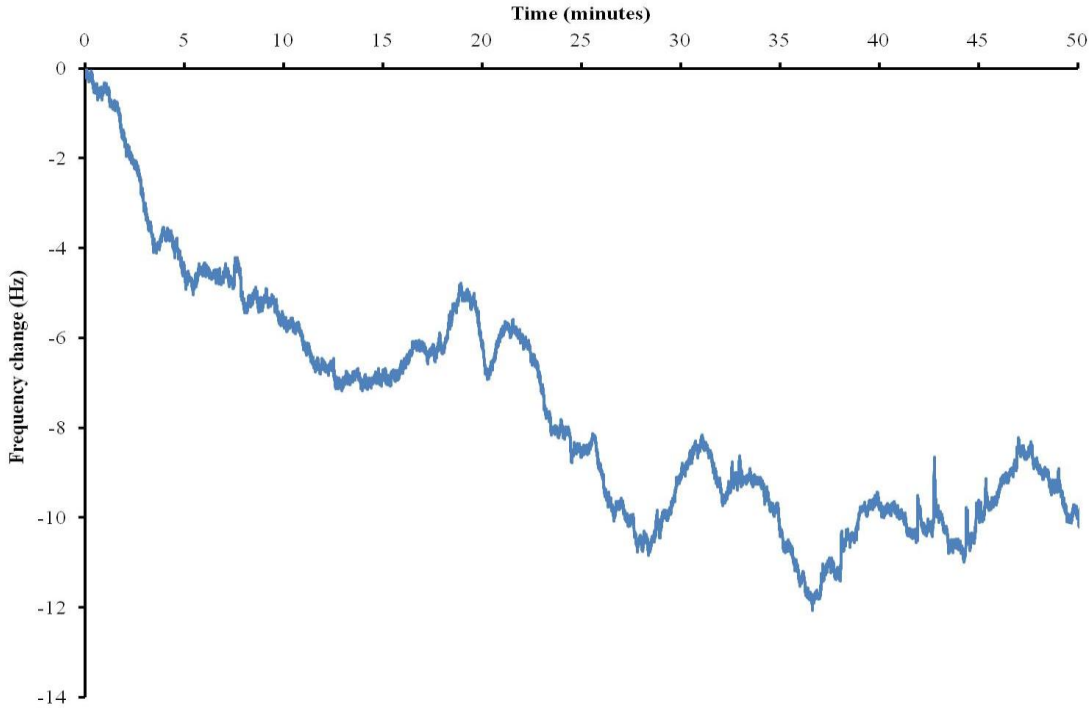

Figure 5.6: Frequency against time for a QCM operating in PBS. In this case a sheet of Blu-tac was place above the QCM, reducing the cyclic resonances.

The evaporation rate of PBS in the swim cell was measured. This was done by first placing a cell, containing a QCM, onto a mass balance. 1.5 ml of PBS was then placed into the cell. The total mass was then monitored over the course of 60 minutes. Using the change in mass, the rate at which the distance between the QCM and the liquid air boundary was changed was calculated. Figure 5.7 shows the depth change of the PBS over time, compared to the frequency of a QCM operating in PBS. The time from peak to trough correspond roughly to depth changes equal to half a wavelength of the pressure wave in the PBS, when the PBS is allowed to evaporate.

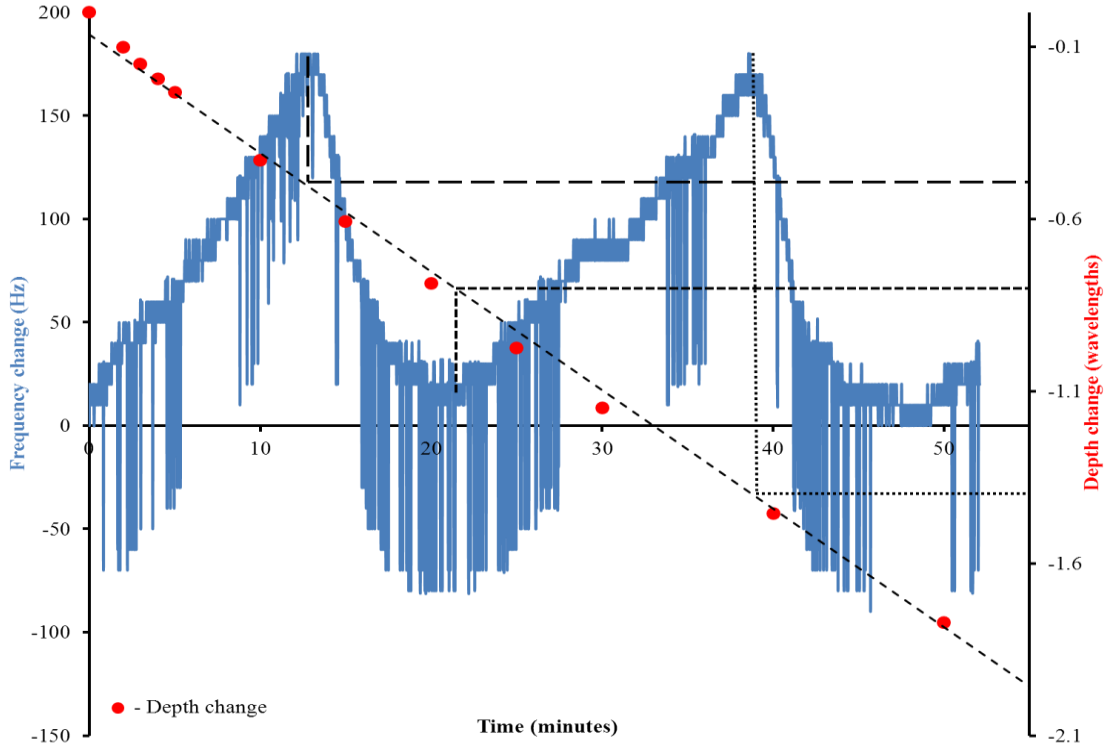

Figure 5.7: Comparison of the cyclic frequency resonances of a QCM in PBS and the change in depth of the PBS over time due to evaporation. Solid black lines indicate the connection between liquid depth change and the frequency resonances.

5.5 Sperm analysis experimental procedure

The experimental procedure was similar to the one detailed in chapter 3. First a 12 mm diameter AT-cut quartz crystal with wrap around electrodes (Laptech XL1052) and fundamental frequency 5 MHz was clamped into the cell between two rubber gaskets, this was done by screwing the base plate to the main part of the cell. The spring loaded contacts in the base connected the crystal directly to the oscillator circuit. This in turn was connected to both the power suply and the frequency counter. 1.5 ml of PBS was added to the cell. With the frequency being recorded using LabView, the crystal was allowed to stabilise. Once this was achieved, an aliquot of sperm was added at the inlet port of the cell and left to self-propel down the swim channel until they reached the sensor at the end and attached to the surface. The time the sperm were added was recorded so that the ToF could be calculated. When the QCM shows a frequency decrease, the sperm have arrived at the sensor.

5.6 Eliminating sperm drift

One concern was whether or not the sperm were in fact self propelling along the channel or reaching the QCM by some other means. Over vigorous use of the pipette when introducing a sperm

sample to the swim cell could give them with enough momentum to drift down the channel. Another possibility is for the sperm to diffuse through the liquid towards the QCM. It is unclear which of the two gives the greatest affect. So steps must be taken to eliminate both.

Initial tests using aged sperm, those which had been received 21 days prior to being used in an experiment, did show a frequency change comparable to that seen using live sperm. This suggests that the aged sperm had reached the QCM by means other than self-propulsion. To overcome this, the swim cell was tilted at a slight angle, 10^{O}, forming a small well at the inlet port. Figure 5.8 shows the frequency data from two samples, one 2 days old and the other 21 days old. In both cases a 10 µl aliquot of sperm was added to the swim channel and the Agilent frequency counter was used to measure the frequency.

The aged sample showed a 40 Hz drop over the course of 20 minutes, compared to a 110 Hz drop from the fresh sample over the same period. So whether the diffusion or momentum gained from the adding process is greatest, tilting the channel seems to help eliminate most of the problem. The aged sperm response is, therefore, sufficiently low to discriminate between the two samples and so allows a screening process to eliminate diffused sperm. In this way a sample could be deemed viable or non-viable. It is worth noting that a screening process simply requires a yes or no answer. So a threshold frequency of, say, 50 Hz would allow viable and non-viable samples to be determined. Figure 5.9 shows images of the QCMs viewed under a microscope. The fresh sperm are present on the QCM in large numbers, while the aged sperm are not.

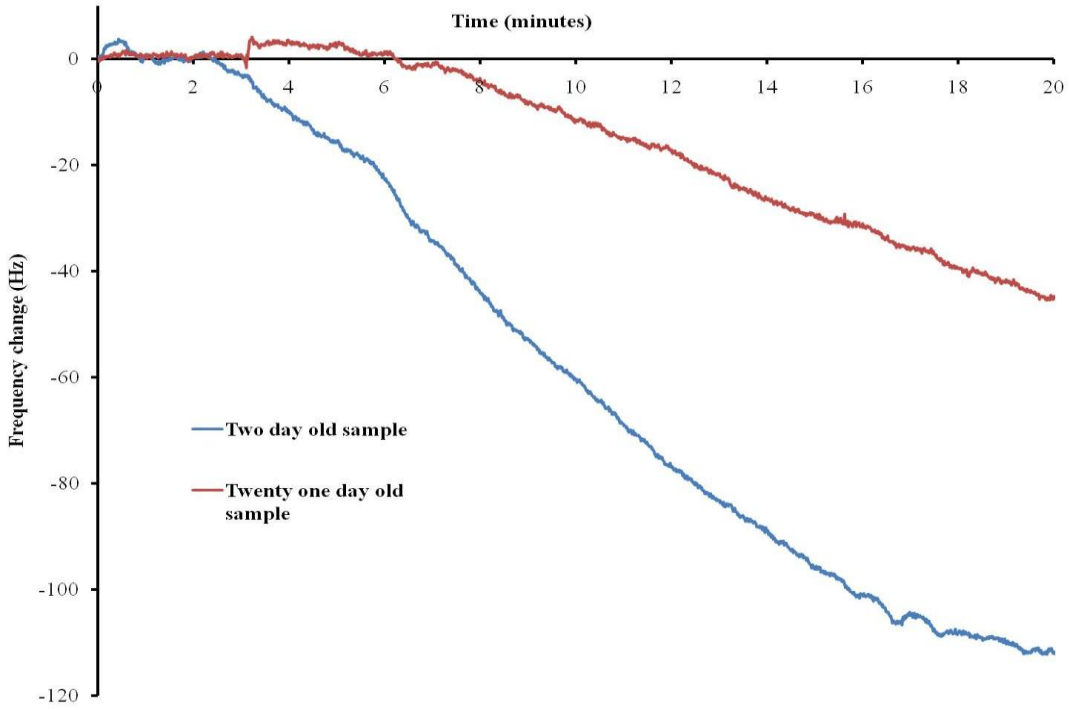

Figure 5.8: Frequency change as a function of time for twenty one day old sample (uper line) and two day old sample (lower line).

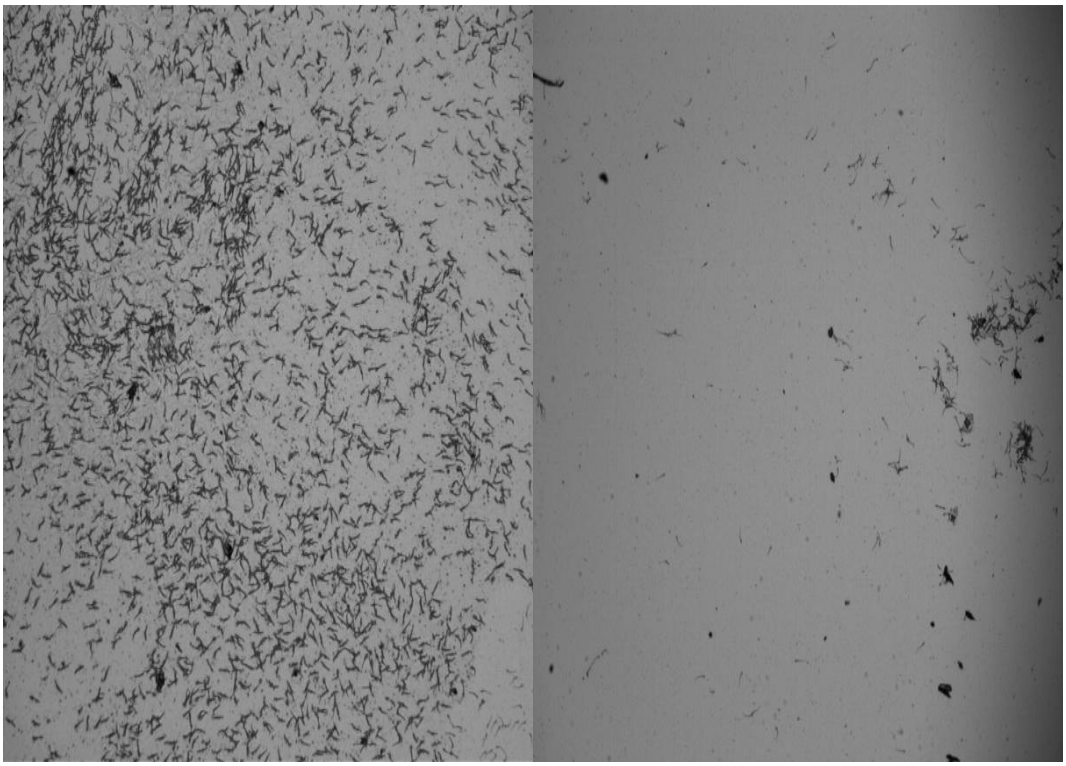

Figure 5.9: Images of QCMs under a microscope for a fresh sample (left) and an aged sample (right).

5.7 UFDC-1 based frequency counter

5.7.1 Electronics

To replace the Agilent frequency counter, a circuit was designed and constructed based around a universal frequency to digital converter (UFDC) [110, 111]. Figure 5.10 shows the constructed circuit. The main advantages of the UFDC were its low cost and small size. The UFDC is single chip, programmable, two channel frequency to digital converter, with 28 pins and an operating frequency range of 0.005 Hz to 7.5 MHz. It is possible to increase this range up to 120 MHz with pre-scaling; this does reduce the accuracy though. It's possible to select the conversion accuracy of the circuit by choosing how the suply voltage and ground connect to the pins on the UFDC. Doing this gives a range of 1 % to 0.001 % on the conversion accuracy. Data is returned as a string of ASCII characters from the serial output pin, via a TTL to USB cable (FTDI TTL-232R-3V3) to the USB port on a computer. The drivers for the FTDI cable allow the USB port to be accessed as a standard COM port. This allowed a program to be written in the Just Basic programming language (www.justbasic.com) to read the data, extract the string for a single value, convert it into a number and store it in a spreadsheet.

Given that the UFDC had a maximum frequency of 7.5 MHz and the QCMs were operating at the third harmonic of 15MHz, it was necessary to add a pre-scalar to divide the input frequency by two. The pre-scalar consisted of a single flip flop, which was connected to the F1 input of the UFDC.

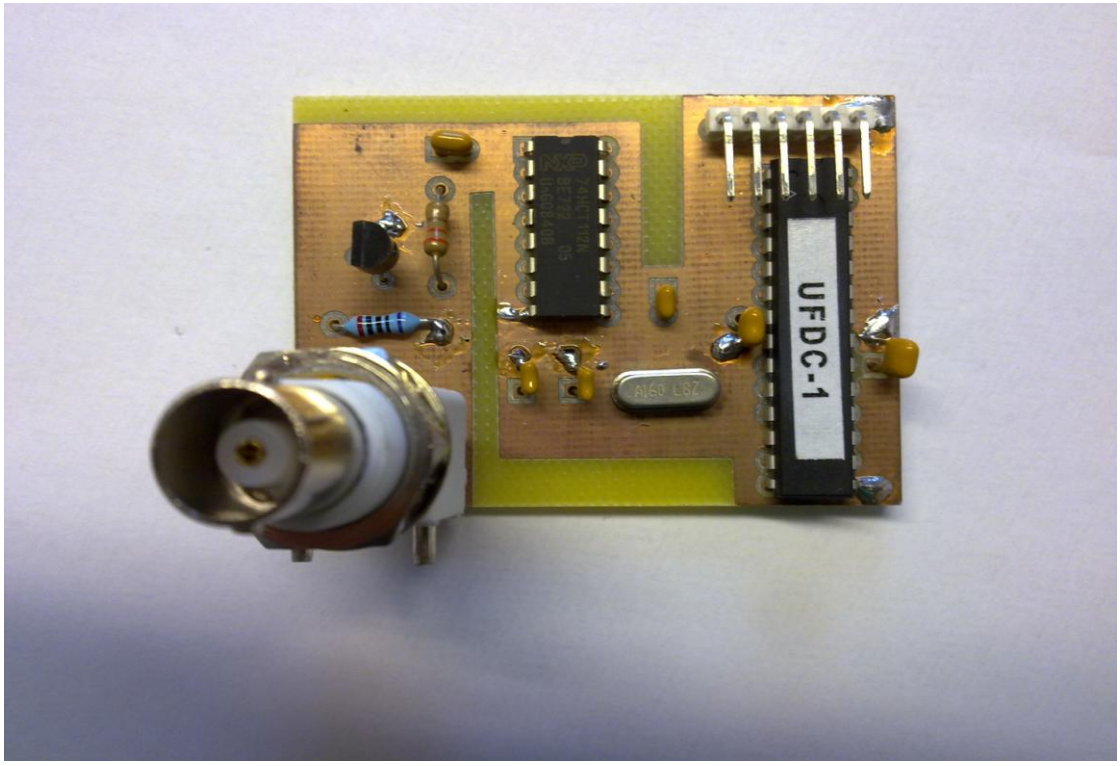

Figure 5.10: Circuit diagram showing complete in-house electronics, including Pierce oscillator circuit and UFDC-1 frequency counter (Top). Image of UFDC-1 base frequency counter.

The UFDC counter and the Pierce oscillator were combined to form the complete electronics; this is shown in figure 5.11. The sinusoidal output of the oscillator circuit was first fed into an FET, which was operating in switch mode from 0 V to 5 V, before being fed into the UFDC. To increase the stability of the signal, the oscillator was powered by a separate DC suply and the UFDC was powered from the USB port on the computer.

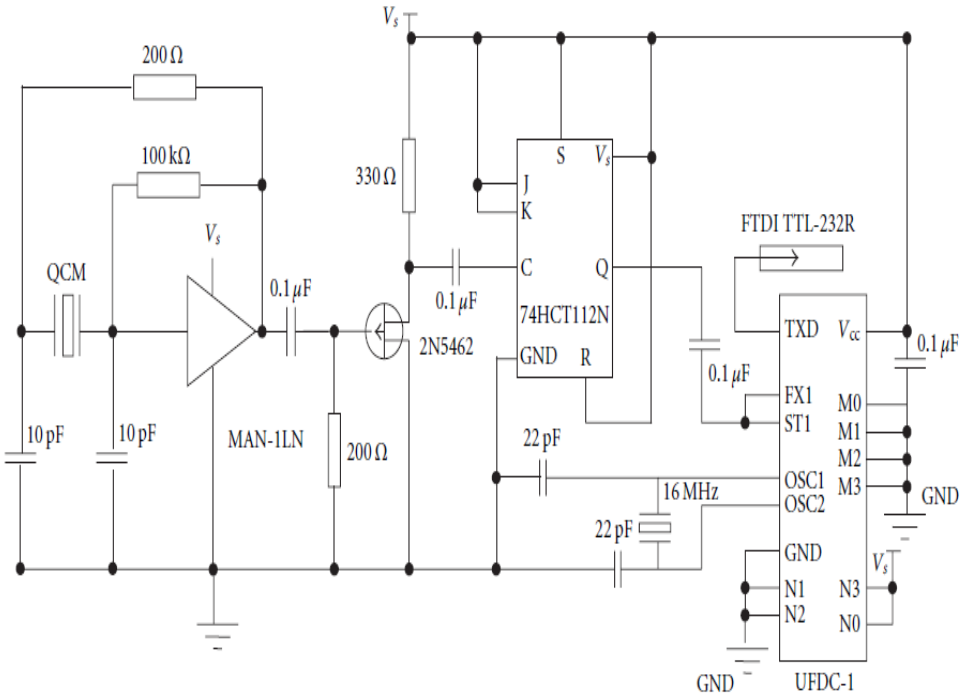

Figure 5.11: Circuit diagram showing both the Pierce oscillator circuit and the UFDC-1 frequency counter.

5.7.2 UFDC and Agilent comparison

Figure 5.12 shows the frequency data for an experiment using the UFDC based frequency counter and a swim cell connected to the Agilent frequency counter for comparison. Following the standard experimental procedure, a 20 µl sample of sperm was added to the two channels. One of the channels was connected to the UFDC-1 frequency counter and the other is attached to an Agilent frequency counter. The experiment was left to run for 40 minutes and the frequency response from both counters compared. The arrival time was similar for both counters, within about 5 minutes of each other. Both also show similar frequency changes, aproximately 60 Hz over the 40 minute experiment. The data for the UFDC counter had a moving average of 20 seconds aplied to it.

The close agreement between the two counters suggests that the UFDC counter is a viable alternative to the Agilent frequency counter.

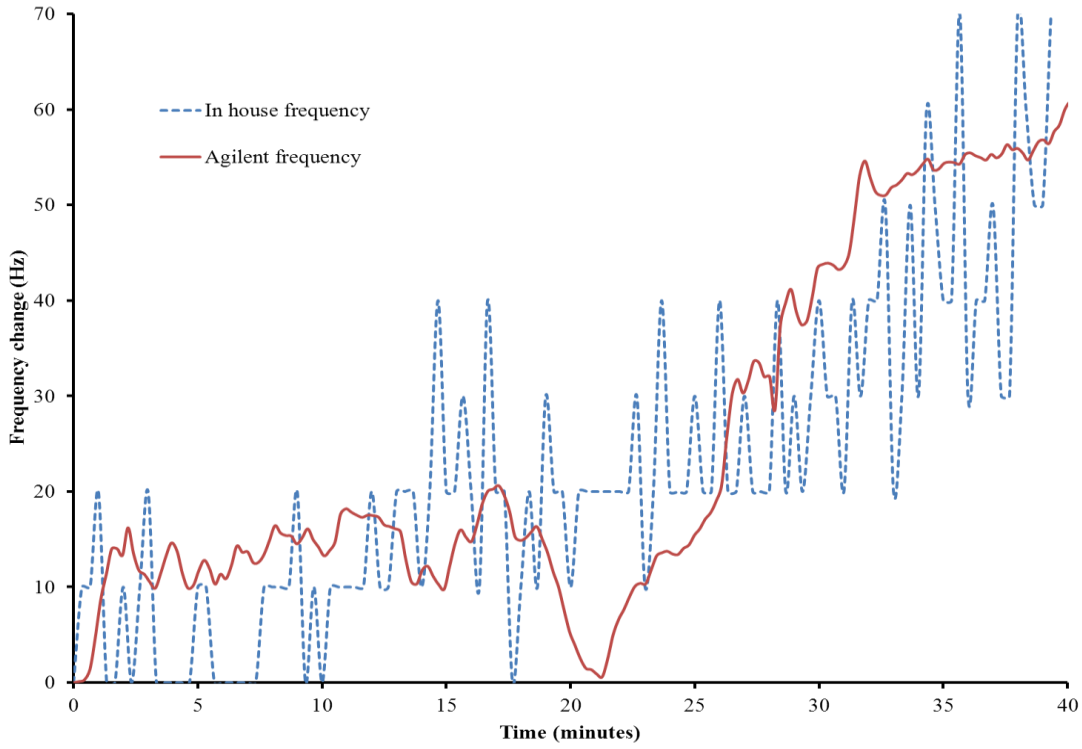

Figure 5.12: Comparrison of the Agilent and UFDC frequency counters.

5.8 Viscosity matching

5.8.1 Glycerol

Due to concerns over whether the Tri X-cell extender would cause a frequency change due to a change in viscosity, other swim media were investigated. The Tri X-cell itself was used. This first involved filtering the stock solution, to remove the sperm, by passing it through a 0.2 µm filter. A swim cell was then filled with 2ml of the liquid and the frequency of the QCM recorded. The Tri X-cell was deemed a failure due to an unacceptable amount of noise present when this was used as the swim medium.

More successful was the use of a water glycerol solution. First the viscosity of the Tri X-cell was measured using a DV-11+ Pro viscometer (Brookfield). A 2 ml sample of the fluid was placed into the viscometer which was connected to a personal computer for the recording of data and to run programs to control the viscometer. The viscosity was measured as 1.4 cp.

Next glycerol was mixed with PBS to produce a medium that exceeded the viscosity of the extender. Given known viscosity values of glycerol solutions, a 20 % solution was chosen as this should have a greater viscosity than the 1.4 cP of the sperm extender. To confirm this, the viscosity of the glycerol solution was also measured using the viscometer. This solution was measured to have a

viscosity of 1.97 cP, which is considerably higher than the extender viscosity. By using this swim medium there should be no frequency response caused by the viscosity of the extender.

5.8.2 Testing glycerol swim medium

Figure 5.13 shows confirmation that a 20 % glycerol solution prevents a frequency change from the sperm extender. The graph shows frequency data from four swim channels, two filled with a 10 % glycerol solution and two with a 20 % glycerol solution. In all four cases 30 µl of the filtered Tri X-cell was added by pipette into the swim cell inlet port. The QCMs for the 10 % channels showed a definite frequency change. Given that the sperm had been filtered out, the frequency change can only be attributed to the tri X-cell. The channels containing the 20 % glycerol solution show signal noise, but no substantial frequency change. This suggests that the increased viscosity and density of the medium has prevented the extender from causing a frequency change.

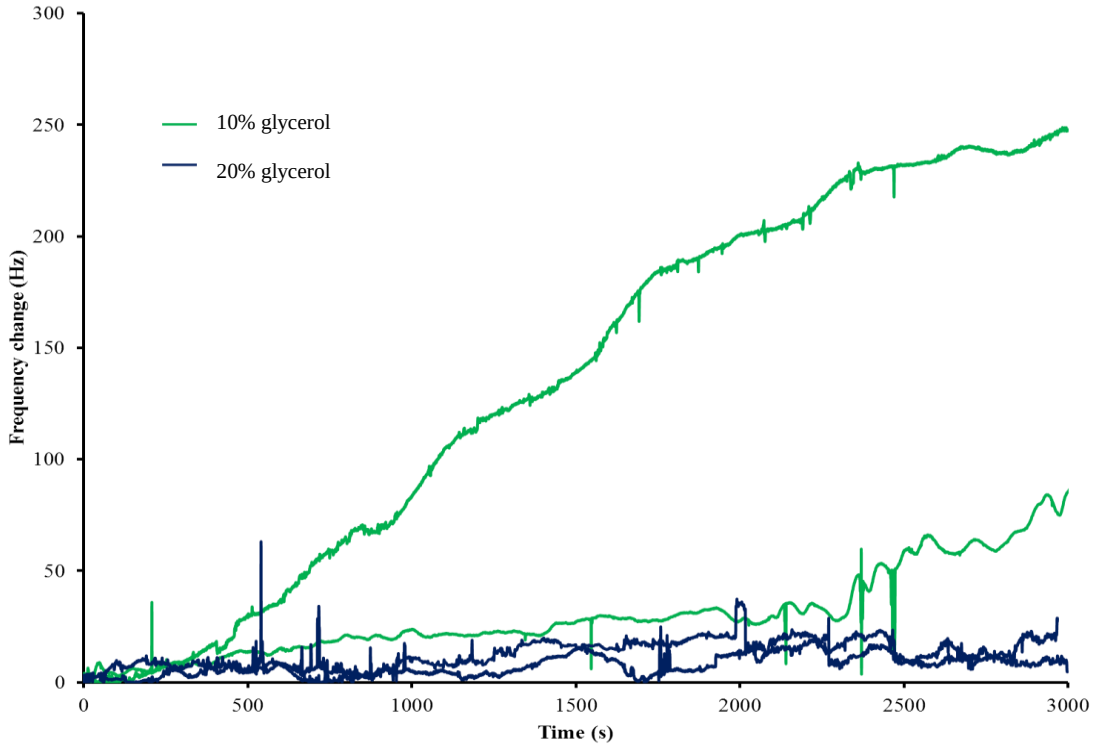

Figure 5.13: Shown are frequency changes caused by sperm samples with a 20% glycerol swim medium (blue) and a 10% swim medium (green)

5.9 Discussion

While the main focus of this work has been to create a device for use with animals, there is still the research sector to consider. In addition to the agricultural industry, it was found that the research sector also saw a need for a simple semen analysis technique [107]. The agricultural industry needed a system which simply gave a yes or no answer about whether the sperm sample was viable. The SQuaDD system offers more functionality than this and so presents an ideal system for studying changes in sperm behaviour, allowing the system to be used to study anything from age of the sperm to the effects of chemicals of their motility.

Preliminary work made use of rough QCMs, which were not considered stable enough. Instead polished crystals were tried and found to be more stable than the rough alternative. This places a price barrier on the SQuaDD system. The rough crystals were approximately £3, while the polished crystals were approximately £25. The higher price would be less of an issue for laboratory based research using the squad system. Re-using the crystals would be more feasible in a lab than when the device is used in the field.

Cleaning off the crystals proved simple enough, though care needed to be taken when choosing what chemical to use. Ideally the QCM needed to be cleaned while still in the holder. Ethanol was used initially. The channel was filled with ethanol and then the channel was cleaned with a cotton bud. However the ethanol was found to cause the Perspex to crack. Papain was used as alternative and was found to be more suitable. The papain was effective at cleaning the sperm off the surface of the crystal, but didn't cause the Perspex to crack.

The Pierce oscillator circuit used in this chapter provided a very stable signal when driving the oscillator circuit, with a noise level of approximately 1 Hz. This was comparable to the noise level of the Maxtec oscillator used in chapter 3. The oscillator was made out of readily available components and proved relatively easy to assemble. This meant that as many circuits as needed couple be manufacture in a short period of time.

The pressure waves were an unintended consequence of the redesign of the swim cell. The cell used in chapter 3 did not have a liquid air boundary parallel to the surface of the crystal. So there is no pressure wave interfering with the frequency of the QCM. The redesigned cell had the QCM directly below the air liquid boundary, resulting in the pressure waves. To overcome these pressure waves, the cell in this chapter had a baffle placed in between the QCM and the surface of the liquid. While the pressure waves were eliminated using this technique, the cell design itself likely needs some consideration.

The UFDC-1 introduces more noise into the system and reduces the accuracy due to the 5 Hz resolution of the chip. The frequency change caused by the sperm is high enough to still be recordable over the noise. Increasing the sample volume for the sperm added to the swim channel would result in a larger frequency change and so overcome the problems of the UFDC-1.

One concern was whether or not the sperm were actually self propelling down the channel or simply drifting down. Figure 5.8 showed that an aged sample and a fresh sample, 21 days and 2 days respectively, showed very different behaviour. So while there was some drift of the sperm down the channel, a live and dead sample can be distinguished.

The SQuaDD system has certain advantages over existing techniques of sperm analysis. Haemocytometers allow the number of sperm to be measured [99]. This is done manually and doesn't allow for the measurement of motility. The various techniques that make up CASA are automated and allow for the measurement of motility [5], but use expensive lab based equipment. Flow cytometry provides an accurate method of counting sperm [6], but doesn't allow for measuring motility and uses complex equipment. SQuaDD allows for the number and motility of the sperm to be measured, while doing so in an automated and simple manner with a relatively small amount of equipment needed. Su *et al* [100] produced a relatively simple technique. However, theirs still required external equipment to analyse the images and didn't have the versatility of the SQuaDD system.

5.10 Conclusion

This chapter focused on several developments in the sperm analysis system from chapter 3. The swim cell was redesigned and a more compact, modular cell created. This new cell offered a number of advantages over the old design. A smaller size meant less buffer was needed and the path length being smaller reduced the time taken to analyse a sample. Also, by making the cell modular different designs could be tried easily. The use of Autocad to create simple designs and a laser cutter to cut acrylic sheets meant that large numbers of cells could be manufactured quickly and easily.

While previous work used chemical coatings to bind the sperm to the surface of the QCM, here a blank polished QCM is used. The sperm bind satisfactorily with the gold electrodes, eliminating the need for a chemical coating. This simplifies the analysis process and removes concerns over whether the crystals are properly coated and also allows them to be reused without time consuming recoating procedures.

The design of the swim cell was shown to give rise to compression waves in the buffer. These caused excess noise. However, it was possible to eliminate the frequency resonances by placing

something between the QCM and the surface of the buffer. An acrylic ball caused the noise recorded to increase to unacceptable levels. A piece of Blu-tac proved more successful, perhaps due to the Blu-tac absorbing the pressure waves rather than reflecting them.

It was shown that both the Agilent frequency counter and the Maxtec phase lock oscillator could be replaced by smaller, cheaper electronics made from commercially available components. The Pierce oscillator circuit successfully drove the QCM and gave a consistent and stable frequency response. The UFDC provided a viable alternative to the Agilent. Despite a lower resolution, the UFDC was able to measure a large enough frequency change to analyse the sperm samples. If the analysis takes the form of measuring a threshold frequency, to provide a simple “yes” or “no” to whether the sample is viable, then the UFDC is more than capable.

6. Conclusions

and

Further Work

6.1 Conclusions

This thesis has presented work developing a simple to use, compact, low cost and versatile sperm analysis system. Chapter 3 expanded on work performed by Newton *et al* [7]. A number of developments were made on their work. Sperm deposition experiments to determine the effective mass of boar semen benefitted from the use of image processing to determine the number of sperm attached to a QCM, rather than counting by eye. Additionally, the effective mass was used along with the frequency change caused by the sperm to determine the rate of arrival. This showed that the system could be used for more in-depth analysis of a sample than the simple measurement of time of flight. The system was also used to measure the effect of environmental temperature and the presence of progesterone, on the sperm ToF. This showed that the system could be used to investigate changes in sperm behaviour due to external factors.

Chapter 4 showed the development of a single-port saw sensor and its characterisation as both a mass and liquid sensor. S1813 guiding layers were added to the surface of the devices and the thickness of this layer varied. The frequency of the devices was tracked as the layer thickness changed, showing a clear relationship between the two consistent with previous work aplying guiding layers to SAW devices. The relationship between layer thickness and sensitivity to both mass and viscosity/density of a liquid was then investigated. This showed a definite optimum layer thickness, 6 µm for mass sensing and 4.5 µm for liquid sensing, and also the ability to control sensitivity by selecting the thickness of the guiding g layer. The single-port have the potential to replace the QCM as the sensing element in the sperm analysis system.

Chapter 5 concentrated on developing the sperm analysis system further. The QCM was kept as the sensing element, but was now driven at the third harmonic or 15 MHz, and work developed the electronics and swim cell used. Two of the electrical components were replaced with in-house built alternatives. The Pierce based oscillator circuit was shown to be an effective method of driving the QCM and a frequency counter using a UFDC-1 was successful in measuring the frequency when analysis experiments were performed. A new swim cell was designed and built which integrated better with the electronics, had a smaller buffer volume, shorter path length and benefitted from a modular design. There was some noise caused by compressional waves forming resonances between the crystal and the surface of the buffer. This problem was eliminated by placing a baffle between the two, thus blocking the waves and preventing the resonances.

The entire body of work constitutes a significant advance in the acoustic wave based method of semen analysis. The SQuaDD system was shown to be versatile, simple to use and steps have been

taken to make it compact and self contained. In addition significant work was done to investigate the use of guiding layers on single-port SAW resonators.

6.2 Further Work

6.2.1 A self-contained system

One of the aims of this project was to produce a small, portable system. To this end the Maxtec phaselock oscillator and the Agilent frequency counter were replaced with the Pierce based oscillator and the UFDC based frequency counter respectively. This, however, left the computer used for recoding the data and the power suplies used to run the entire system. Ideally, SQuaDD should be a self contained system, so further development of the system should find a way of integrating the computer and power suply into the rest of the electronics.

The SQuaDD system requires some way of recording the frequency of the sensor and measuring any frequency changes, the computing power to do this is not very high. The Just Basic program used in chapter 5 performed this and was designed to give an “ok” if the frequency droped by a certain amount. A small computer capable of running the program is all that would be necessary. One possibility would be field programmable gate array (FPGA) chip. This would also replace the UFDC-1 and require significant specialist development. A simpler option would be a micro controller connected to the UFDC-1. The Just BASIC program could still be used, perhaps even simplified, and there would still be a data port to connect to a computer so more detailed analysis of the data could be performed if necessary. To display the results of the analysis, a LCD screen could incorporated into the system.

Currently, the oscillator circuit is powered from a 12V power suply and the UFDC is powered from the USB port on the computer, which is powered by its battery or connected to the mains. If the computer is replaced with something smaller, and so requiring less power to run, then it should become feasible to power the entire system from a portable battery pack. If this could be achieved then the goal of miniaturising the components would have been achieved.

6.2.2 SAW device sensing element

The single-port resonator developed in chapter 4 showed promise as a sensing device. Due to the higher frequency and use of guiding layer, the sensors exhibit higher sensitivity, which would provide numerous advantages.

Greater sensitivity would mean that smaller changes in mass would be measurable. One advantage of which would be decreasing the sperm sample size when performing an analysis. If SQuaDD is to be used for more detailed analysis than simply measuring a threshold frequency change, such as the sperm counting shown in chapter 3, then another advantage of the single-port sensor would be that a more sensitive device would make counting the number of sperm more accurate.

In order for the single-port to be integrated into the system, some changes to the electronics would be needed. Given that the single-ports oscillate at a much higher frequency than the QCMs and that the UFDC-1 has a maximum operating frequency of 7.5 MHz, additional flip flops would need to be added to the pre-scaler.

Additional work could investigate the design of the device itself, partly by changing the substrate used. If a quartz substrate was used, the device would show higher temperature stability but lower piezoelectric coupling. As a result the method of reflection would have to change to a geometric discontinuity or mass loading. However, the improved stability would allow for higher frequency devices and so increase the sensitivity. An investigation into the optimum sized area for the sperm to bind to determine exactly how big the active area of the sensor would need to be. Given that the IDTs proved to be the most sensitive area of the device, this would determine how big the IDTs would need to be.

6.2.3 Aplications of SQuaDD

While SQuaDD has largely been conceived as a device for testing sperm quality prior to insemination, the system could have other aplications. By testing the motility of sperm, SQuaDD could be used to measure the effects such as environmental factors or chemicals on sperm motility. This was touched upon in chapter 3 by investigating both temperature and the use of progesterone as a potential hyperactivant. However, the potential for this type of analysis is much larger.

Erogul *et al* investigated the effects of mobile phone radiation on the motility of human sperm [112]. They used a counting chamber and two experienced observers. The SQuaDD system could potentially be used in such a case to test motility.

SQuaDD could be used to test chemicals believed to cause hyperactivation, beyond progesterone. For example, one study looked at insulin-like growth factor-I (IGF-1) and its effect on sperm motility [113]. SQuaDD has been shown to be effective at testing for changes in motility caused by progesterone and so could also be used with other chemicals.

As well as measuring increases in motility, SQuaDD could also be used to measure deliberate decreases. This would give the potential for testing spermicides etc. Such an aplication opens SQuaDD to use in the contraceptive industry.

The potential exists to use SQuaDD as a home testing kit. A man could analyse his own sperm motility and monitor changes in sperm concentration. In this way changes in diet, environment, fitness etc. and their effect on sperm quality could be monitored.

Remaining with the AI industry, SQuaDD could provide a way of testing new sperm extenders. SQuaDD could monitor the motility of sperm over a number of days to evaluate the effectiveness of an extender.

7. References

1. M. Thibier and H. G. Wagner, World statistics for artificial insemination in small ruminants and swine, Proceedings 14th international congress on animal reproduction, Stockholm, 2-6th July 2000
2. E. S. E. Hafez and B. Hafez, Reproduction in farm animals, Wiley-Blackwell, 2000
3. S. Pesch and M. Bergmann, Structure of mammalian spermatozoa in respect to viability, fertility and cryopreservation, Micron, 2006, 37, p. 597
4. World Health Organization, WHO Laboratory Manual for the Examination of Human Semen and Sperm-Cervical Mucus Interaction, Cambridge University Press, Cambridge, UK, 3rd edition, 1999
5. S. T. Mortimer. CASA - Practical Aspects, Journal Andrology, 2000, 21, p. 515
6. P. Christensen, D. Boelling, K. M. Pedersen, I. R. Korsgaard and J. Jensen. Relationship between sperm viability as determined by flow cytometry and non-return rate of dairy bulls, Journal of Andrology, 2005, 26, p. 98
7. M. I. Newton, C. R. Evans, J. J. Simons and D. C. Hughes. Semen quality detection using time of flight and acoustic wave sensors, Aplied Physics Letters, 2007, 90, p.154103
8. R. M. White and F. W. Voltmer, Direct piezoelectric coupling to surface elastic waves, Aplied Physics Letter, 1965, 7, p. 314
9. E. Gizeli, N. Goddard, C. Lowe and A. Stevenson, A Love plate biosensor utilising a polymer layer, Sensors and Actuators B, 1992, 6, p. 131
10. M. I. Newton, G. McHale and F. Martin, Layer-guided shear acoustic plate mode sensor, Aplied physivs letters, 2003, 82, p. 2181
11. Z. Li, Y. Jones, J. Hossenlop, R. Cernosek and F. Josse, Analysis of liquid-phase chemical detection using guided shear horizontal-surface acoustic wave sensors, Analytical chemistry, 2005, 77, p. 4595
12. P. Curie, La pyroélectricité, C. R. Acad. Sci Paris, 1880, 91, p. 294
13. G. Lipman, Principe de la conservation de l'electricite , Annals de chimie et de physique, 1881, 24, p. 145
14. W. G. Cady, New methods for maintaining constant frequency in high-frequency circuits, Physical Review, 1921, 18, p. 142
15. G. W. Pierce, Piezoelectric Crystal Resonators and Crystal Oscillators Aplied to the Precision Calibration of Wavemeters, Proceedings of the American Academy of Arts and Sciences, 1923, 59, p. 81

16. G. Sauerbrey, The use of oscillators for weighing thin layers and for microweighing, Zeitschrift fur physic, 1959, 155, p. 2333

17. D. S. Ballantine, R. M. White, S. J. Martin, A. J. Ricco, E. T. Zellers, G. C. Frye and H. Wohltjen, Acoustic Wave Sensors Theory, Design and Physico-Chemical Aplications, Academic Press, 1996, p. 142

18. T. Nomura and A. Minemura, Behavior of a piezoelectric quartz crystal in an aqueous solution and the aplication to the determination of minute amount of cyanide, Japanese Chemical Society, 1980, 10, p. 1621.

19. T. Nomura and M. Okuhara, Frequency shifts of piezoelectric quartz immersed in organic liquids, Analytica Chimica Acta, 1982, 142, p. 281

20. K. Kanazawa and J. Gordon, The oscillation of a frequency of a quartz resonator in contact with a liquid, Analytica Chimica Acta, 1985, 175, p. 99

21. K. Kanazawa and G. Gordon, Frequency of a Quartz Microbalance in contact with liquid, Analytical Chemistry, 1985, 57, p. 1771

22. J. W. Grate, S. J. Martin and R. M. White, Acoustic Wave Microsensors Part 2, Analytical Chemistry, 1993, 65, p. 987

23. C.K. O'Sullivan and G.G. Guilbault, Commercial quartz crystal microbalances - theory and aplications, Biosensors and bioelectronics, 1999, 14, p. 663

24. M. Avila, M. Zougagh, A. Escarpa and A. Rıos, Molecularly imprinted polymers for selective piezoelectric sensing of small molecules, Trends in Analytical Chemistry, 2008, 27, p. 54

25. S. Clavaguera, P. Montméat, F. Parret, E. Pasquinet, J. Lère-Porte and L. Hairault, Comparison of fluorescence and QCM technologies: Example of explosives detection with a π-conjugated thin film, Talanta, 2010, 82, p. 1397

26. M. E. Escuderos, S. Sánchez and A. Jiménez, Virgin olive oil sensory evaluation by an artificial olfactory system, based on Quartz Crystal Microbalance (QCM) sensors, Sensors and Actuators B, 2010, 147, p. 159

27. S. Hong, H. Jeongb and S. Hong, QCM DNA biosensor for the diagnosis of a fish pathogenic virus VHSV, Talanta, 2010, 82, p. 899

28. Q. Chen, W.Tang, D. Wang, X. Wu, N. Li and F. Liu, Amplified QCM-D biosensor for protein based on aptamer-functionalized gold nanoparticles, Biosensors and Bioelectronics, 2010, 26, p. 575

29. B. Zhang, J. Yao, H. Yan and W. Fu, Specific binding DNA-based piezoelectric quartz crystal microbalance biosensor array for the study of NF-κB, Sensors and Actuators B, 2010, 149, p. 259

30. S. M. Reddy, J. P. Jones, T. J. Lewis and P. M. Vadgama, Development of an oxidase-based glucose sensor using thickness-shear-mode quartz crystals, Analytica Chimica Acta, 1998, 363, p. 203

31. B. A. Auld, Acoustic fields in solids volume 2, Robert E. Krieger Publishing Company, 1990

32. S. J. Martin, G. C. Frye and A. J. Ricco, Effect of Surface Roughness on the Response of Thickness-Shear Mode Resonators in Liquids, Analytical Chemistry, 1993, 65, p. 2910

33. V. E. Granstaff and S. J. Martin, Characterization of a thickness-shear mode quartz resonator with multiple nonpiezoelectric layers, Journal of Aplied physics, 1994, 75, p. 1319

34. G. McHale, C. Hardacre, R. Ge, N. Doy, R. W. K. Allen, J. M. MacInnes, M. R. Bown, and M.I. Newton, Density-Viscosity Product of Small-Volume Ionic Liquid Samples Using Quartz Crystal Impedance Analysis, Analytical Chemistry, 2008, 80, p. 5806

35. A. Arnau, A Review of Interface Electronic Systems for AT-cut Quartz Crystal Microbalance Aplications in Liquids, Sensors, 2008, 8, p. 370

36. A. Arnau, J. García, Y. Jimenez, V. Ferrari and M. Ferrari, Improved electronic interfaces for AT-cut quartz crystal microbalance sensors under variable damping and parallel capacitance conditions, Review of scientific instruments, 2008, 79, p. 075110-1

37. A. T. Nimal, M. Singh, U. Mittal and R. Yadava,A comparative analysis of one-port Colpitt and two-port Pierce SAW oscillators for DMMP vapor sensing, Sensors and actuators B, 2006, 114, p. 316

38. F. Eichelbaum, R. Borngraber, J. Schroder, R. Lucklum and P. Hauptmann, Interface circuits for quartz crystal microbalance sensors, Review of scientific instruments, 1999, 70,p. 2537

39. B. A. Martin and H. E. Hager, Flow profile above a quartz crystal vibrating in liquid, Journal of Aplied Physics, 1989, 65, p. 2627

40. T. W. Schneider and S. J. Martin, Influence of Compressional Wave Generation on Thickness-Shear Mode Resonator Response in a Fluid, Analytical Chemistry, 1995, 67, p. 3324

41. Z. lin and M. D. Ward, The Role of Longitudinal Waves in Quartz CrystalMicrobalance Aplications in Liquids, Analytical Chemistry, 1995, 67, p. 685

42. R. Lucklum , S. Schranz, C. Behling, F. Eichelbaum and P. Hauptmann, Analysis of compressional-wave influence on thickness-shear-mode resonators in liquids, Sensors and Actuators A, 1997, 60, p. 40

43. S. M. Reddy, J. P. Jones and T. J. Lewis, The coexistence of pressure waves in the operation of quartz-crystal shear-wave sensors, Journal of aplied physics, 1998, 83, p. 2524

44. M. I. S. Veríssimo, J. A. B. P. Oliveira and M. T. S. R. Gomes, Contribution of compressional waves to the identification and quantification of a water contaminant, Sensors and Actuators B, 2010, 151, p. 21

45. Lord Rayleigh, On waves propagating along the plane surface of an elastic solid, Proceeding London Mathamatical Society, 1885, 17, p. 4

46. M. Penza and L. Vasanelli, SAW NOx gas sensor using W03 thin-film sensitive coating, Sensors and Actuators B, 1997, 41, p. 31

47. H. Wohltjen and R. Dessy, Surface acoustic-wave probes for chemical-analysis, 2 - gas chromatography detector, Analytical Chemistry, 1979, 51, p. 1465

48. W. P. Jakubik, M. Urbanczyk, E. Maciak and T. Pustelny, Surface acoustic wave hydrogen gas sensor based on layered structure of palladium/metal-free phthalocyanine, Bulletin of The Polish Academy of Sciences Technical Sciences, 2008, 56, p. 133

49. Y. J. Lee, H. B. Kim, Y. R. Roh, H.M. Cho and S. Baik, Development of a SAW gas sensor for monitoring SO2 gas, Sensors and Actuators A, 1998, 64, p. 173

50. A. T. Nimal, U. Mittal, M. Singh, M. Khaneja, G. K. Kannan, J. C. Kapoor, V. Dubey, P. K. Gutch, G. Lal, K. D. Vyas and D. C. Gupta, Development of handheld SAW vapor sensors for explosives and CW agents, Sensors and Actuators B, 2009, 135, p. 399

51. J. Kondoh and S. Shiokawa, Shear-horizontal surface acoustic wave sensors, Sesnor technology, 1999, 6, p. 59

52. P. Campitelli, W. Wlodarski and M. Hoummady, Identification of natural spring water using shear horizontal SAW based sensors, Sensor and Actuators B, 1998, 49, p. 195

53. M. Berger, A. Welle, E. Gottwald, M. Rapa and K. Längea, Biosensors coated with sulfated polysaccharides for the detection of hepatocyte growth factor/scatter factor in cell culture medium, Biosensors and Bioelectronics, 2010, 26, p. 1706

54. C. Zerroukia, N. Fouratia, R. Lucas, J. Vergnaud, J. Fougniona, R. Zerrouki and C. Pernellec, Biological investigation using a shear horizontal surface acoustic wave sensor: Small “Click generated” DNA hybridization detection, Biosensors and Bioelectronics, 2010, 26, p. 1759

55. D. Deobagkar, V. Limaye, S. Sinha and R.D.S. Yadava, Acoustic wave immunosensing of Escherichia coli in water, Sensors and Actuators B, 2005, 104, p. 85

56. H.Yatsuda, M. Nara, T. Kogai, H. Aizawa and S. Kurosawa, STW gas sensors using plasma-polymerized allylamine, Thin Solid Films, 2007, 515, p. 4105

57. G. Lidner, Sensors and actuators based on surface acoustic waves propagating along solid-liquid interfaces, Journal of Physics D: Aplied Physics, 2008, 41

58. M. Rocha-Gaso, C. March-Iborra, Á. Montoya-Baides and A. Arnau-Vives, Surface generated acoustic wave biosensors for the detection of pathogens: a review, Sensors, 2009, 9, p. 5740

59. J. C. Andle and J. F. Vetelino, Acoustic wave biosensors, Sensors and Actuators A, 1994, 44, p. 167

60. J. D. N. Cheeke and Z. Wang, Acoustic wave gas sensors, Sensors and Actuators B, 1999, 59, p. 146

61. Q. Y. Cai, J. I. Park, D. Heldsinger, M. D. Hsieh and E. T. Zellers, Vapor recognition with an integrated array of polymer-coated flexural plate wave sensors, Sensors and Actuators B, 2000, 62, p. 121

62. R. Dahlnt, M. Grunze, F. Jesse and J. Renkent, Acoustic Plate Mode Sensor for Immunochemical Reactions, Analytical Chemistry, 1994, 66, p. 2888

63. R. Dahint, R. Ros Seige, P. Harder, M. Grunze and F. Josse, Detection of non-specific protein adsorption at artificial surfaces by the use of acoustic plate mode sensors, Sensors and Actuators B, 1996, 35, p. 497

64. J. Ricco and S. J. Martin, Acoustic wave viscosity sensor, Aplied Physics Letters, 1987, 50, p. 1474

65. F. Josse, Acoustic wave liquid-phase-base microsensors, Sensors and Actuators A, 1994, 44, p. 199

66. S. J. Martin, A. J. Ricco, T. M. Niemczyk and G. C. Frye, Characterisation of SH acoustic plate mode liquid sensors, Sensors and actuators, 1989, 20, p. 253

67. F. Josse, R. Dahint, J. Schumacher, M. Grunze, J. Andle and J. Vetelino, On the mass sensitivity of acoustic plate mode sensors, Sensors and Actuators, 1996, 53, p. 243

68. F. Bender, R. Dahint, F. Josse, M . Grunzea and M. v.Schickfubs, Mass sensitivity of acoustic plate mode liquid sensors on ZX-LiNbO3, Journal of the Acoustical Society of America, 1994, 95, p. 1386

69. M. J. Vellekoop, Acoustic wave sensors and their technology, Ultrasonics. 1998, 36, p. 7

70. C. K. Campbell, Surface acoustic wave devices for mobile and wireless communications, Academic press, 1998, p. 285

71. K. Hashimoto, Surface acoustic wave devices in telecommunications modelling and simulation, Springer, 2000, p. 39

72. Tooru Nomura and Tsutomu Yasuda, Surfave Acoustic Wave Liquid Sensors Based on One-Port Resonators, Japanese Journal of Aplied Physics, 1993, 32, p. 2372

73. H. Hsu and J. Shih, Surface acoustic wave olefin/alkyne sensor based Ag(I)/cryptand-22, Sensors and Actuators B, 2006, 114, p. 720

74. B. A. Auld, Acoustic fields in solids volume 2, Robert E. Krieger Publishing Company, 1990

75. G. Kovacs, G.W. Lubking, M. J. Vellekoop and A. Venema, Love waves for (bio)chemical sensing in liquids, Proc. IEEE Ultrasonics Symposium. Tucson, AZ, USA (20–23 Oct., 1992), p. 281

76. J. Du and G L Harding, A study of Love-wave acoustic sensors, Sensors and Actuators A, 1996, 56, p. 211

77. G. Harding, Mass sensitivity of Love-mode acoustic sensors incorporating silicon dioxide and silicon-oxy-flouride guiding layers, Sensors and Actuators A, 2001, 88, p. 20

78. Paul Roach, Shaun Atherton, Nicola Doy, Glen McHale and Michael I. Newton, SU-8 Guiding Layer for Love Wave Devices, Sensors, 2007, 7, p. 2539

79. N. Arana, D. Puente, I. Ayerdi, E. Castano and J. Berganzo, SU8 protective layers in liquid operating SAWs, Sensors and Actuators B, 2006, 118, p. 374

80. M. I. Newton, G. McHale and F. Martin, Experimental study of Love wave devices with thick guiding layers, Sensors and Actuators A, 2004, 109, p. 180

81. G. McHale, M. I. Newton and F. Martin, Layer guided shear horizontally polarized acoustic plate modes, Journal of Aplied Physics, 2002, 91, p. 5735

82. C. R. Evans, S.M. Stanley, C. J. Percival, G. McHale and M. I. Newton, Lithium tantalate layer guided plate mode sensors, Sensors and Actuators A. 2006, 132, p. 241

83. G. McHale, Generalized concept of shear horizontal acoustic plate mode and Love wave sensors, Measurement Science and Technology, 2003, 14, p. 1847

84. G. McHale, M. I. Newton, F. Martin E. Gizeli and K. A. Melzak, Resonant conditions for Love wave guiding layer thickness, Aplied Physics Letters, 2001, 79, p. 3542

85. G. McHale, M. I. Newton and F. Martin, Theoretical mass, liquid, and polymer sensitivity of acoustic wave sensors with viscoelastic guiding layers, Journal of Aplied Physics, 2003, 93, p. 675

86. G. McHale, M. I. Newton and F. Martin, Theoretical mass sensitivity of love wave and layer guided plate mode sensors, Journal of Aplied Physics, 2002, 91, p. 9701

87. A. Turton, D. Bhattacharyya and D. Wood, Liquid density analysis of sucrose and alcoholic beverages using polyimide guided Love-mode acoustic wave sensors, Measurement science and technology, 2006, 17, p. 257

88. J. Du, G. L. Harding, A. F. Coilings and P. R. Dencher, An experimental study of Love-wave acoustic sensors operating in liquids, Sensors and actuators A, 1997, 60, p. 54

89. B. Jakoby, G. M. Ismail, M. P. Byfield and M. J. Vellekoop, A novel molecularly imprinted thin film aplied to a love wave gas sensor, Sensors and actuators, 1999, 76, p. 93

90. G. Kovacs, M. J. Vellekoop, R. Haueis, G.W. Lubking and A. Venema, A Love wave sensor for (bio)chemical sensing in liquids, Sensors and actuators A, 1994, 43, p. 38

91. G. L. Harding , J. Du, P. R. Dencher , D. Barnett and E. Howe, Love wave acoustic immunosensor operating in liquid, Sensors and actuators A, 1997, 61, p. 279

92. M. Saitakis, A. Tsortosa and E. Gizeli, Probing the interaction of a membrane receptor with a surface-attached ligand using whole cells on acoustic biosensors, Biosensors and Bioelectronics, 2010, 25, p. 1688

93. S. M. Stanley, I. A. Dodi, C. R. Evans, S. J. Paston, R. C. Rees, C. J. Percival, G. McHalea and M. I. Newton, Layer guided-acoustic plate mode biosensors for monitoring MHC-peptide interactions, The analyst, 2006, 131, p, 892

94. M. Newton, P. Roach and G. Mchale, ST quartz acoustic wave sensors with sectional guiding layers, Sensors, 2008, 8, p. 4384

95. S. Mortimer, A critical review of the physiological importance and analysis of sperm movement in mammals, Human Reproduction Update, 1997, 3, p. 403

96. J. Bereiter-Hahn, Mechanics of crawling cells, Medical Engineering & Physics, 2005, 27, p. 743

97. V. J. Kay and L. Robertson, Hyperactivated motility of human spermatozoa: a review of physiological function and aplication in assisted reproduction, Human Reproduction Update, 1998, 4, p. 776

98. J. Neuwinger, T. J. Cooper, U. A. Nuth and E. Nieschlag. Hyaluronic acid is a medium for human sperm migration tests. Human Reproduction, 1991, 6, p. 396

99. World Health Organization. WHO Laboratory Manual for the Examination of Human Semen and Sperm-Cervical Mucus Interaction. 3rd ed. Cambridge, United Kingdom: Cambridge University Press; 1999.

100. T. W. Su,.A. Erlinger, D. Tseng and A. Ozcan, Compact and light-weight automated semen analysis platform using lensfree on-chip microscopy, Analytical Chemistry, 2010, 82, p. 8307

101. G. F. Bahr and E. Zeitler, Study of Bull Spermatozoa, Journal of Cell Biology, 1964, 21, p. 175

102. L. A. Johnson, K. F. Weitze, P. Fiser and W. M. C. Maxwell, Storage of boar semen, Animal Reproduction Science, 2000, 62, p 143

103. P. V. Lishko, I. L. Botchkina and Y. Kirichok, Progesterone activates the principal Ca^{2+} channel of human sperm, Nature, 2011, 471, p. 387

104. G. Carvajal, C. Cuello, M. Ruiz, J. M. VaZquez, E. Arseniomartinez and J. Roca, Effects of centrifugation before freezing on boar spermcryosurvival, Journal of Andrology, 2004, 25, p. 389

105. M. E. Teves, F. Barbano, H. A. Guidobaldi, R. Sanchez, W. Miska and L. Giojalas, Progesterone at the picomolar range is a chemoattractant for mammalian spermatozoa, Fertility and Sterility, 2006, 86, p. 745

106. R. Dammel, Diazonaphthoquinone-based Resists, SPIE - The international Society for Optical Engineering, 1993, p. 99

107. R. Rinaldi, Commercial feasibility assessment SQuaDD, Evolution Life Science Ltd, 2006

108. http://www.minicircuits.com/pdfs/MAN-1LN.pdf

109. S. Atherton, C. R. Evans, P. Roach, D. C. Hughes, G. McHale and M.I. Newton. Investigation of operating parameters for a semen quality analysis system. Proceeding of the 2nd International Conference on Biomedical Electronics and Devices, 2009, p. 13

110. S. Y. Yurish, Digital sensors design based on universal frequency sensors interfacing IC, Sensors and Actuators A, 2006, 132, p. 265

111. S. Y. Yurish and N. V. Kirianaki, Universal frequency-to-digital converter for quasi-digital and smart sensors: specifications and aplications, Sensor Review, 2005, 25, p. 92

112. O. Erogul, E. Oztas, I. Yildirim, T. Kir, E. Aydur, G. Komesli, H. C. Irkilata, M. K. Irmak and A. F. Peker, Effects of Electromagnetic Radiation from a Cellular Phone on Human Sperm Motility: An In Vitro Study, Archive of Medical Research, 2006, 37, p. 840

113. S. Selvarajua, I. J. Reddya, S. Nandia, S. B. N. Raob and J. P. Ravindra, Influence of IGF-I on buffalo (Bubalus bubalis) spermatozoa motility, membrane integrity, lipid peroxidation and fructose uptake in vitro, Animal Reproduction Science, 2009, 113, p. 60

8. Publications

P. Roach, S. Atherton, N. Doy, G. McHale and M. I. Newton, SU-8 Guiding Layer For Love Wave Devices, Sensors, 2007, 11, pp. 2539

Sensors **2007**, *7*, 2539-2547

sensors

ISSN 1424-8220

www.mdpi.org/sensors

Full Paper

SU-8 Guiding Layer for Love Wave Devices

Paul Roach*, Shaun Atherton, Nicola Doy, Glen McHale and Michael I. Newton

School of Science and Technology, Nottingham Trent University, Clifton Campus, Nottingham. NG11 8NS. United Kingdom

* Author to whom correspondence should be addressed; Email: Paul.Roach@ntu.ac.uk;
Tel: +44(0)115-848-8062; Fax: +44(0)115-848-6616

Received: 1 October 2007 / Accepted: 31 October 2007 / Published: 1 November 2007

Abstract: SU-8 is a technologically important photoresist used extensively for the fabrication of microfluidics and MEMS, allowing high aspect ratio structures to be produced. In this work we report the use of SU-8 as a Love wave sensor guiding layer which allows the possibility of integrating a guiding layer with flow cell during fabrication. Devices were fabricated on ST-cut quartz substrates with a single-single finger design such that a surface skimming bulk wave (SSBW) at 97.4 MHz was excited. SU-8 polymer layers were successively built up by spin coating and spectra recorded at each stage; showing a frequency decrease with increasing guiding layer thickness. The insertion loss and frequency dependence as a function of guiding layer thickness was investigated over the first Love wave mode. Mass loading sensitivity of the resultant Love wave devices was investigated by deposition of multiple gold layers. Liquid sensing using these devices was also demonstrated; water-glycerol mixtures were used to demonstrate sensing of density-viscosity and the physical adsorption and removal of protein was also assessed using albumin and fibrinogen as model proteins.

Keywords: Love wave, SU-8, SU-8 guiding layer, SH-SAW

---

1. Introduction

Surface acoustic wave (SAW) devices are widely used in sensing applications with a number of variants being used in many research fields [1, 2]. One of the simplest types of SAW device uses a Rayleigh wave, which propagates with an elliptical particle displacement through the substrate parallel

to the direction of the wave. The energy of the wave is not confined to the surface, although the amplitude of the wave decays into the depth of the substrate. These types of sensors cannot be used in liquids due to the direction of mechanical displacement allowing dampening of the wave to occur. Shear horizontally polarized SAWs (SH-SAW), propagating with a particle displacement perpendicular to the wave motion, can be used in liquids but similarly are not confined to the surface of the substrate. Love waves may be propagated when an overlayer is added on the surface of a SH-SAW or surface skimming bulk wave (SSBW) device. Such a wave will be supported if the guiding layer material has a shear speed less than that of the substrate [3]. An enhancement in device sensitivity can therefore be achieved, with Love waves offering one of the highest mass sensitivities. Love wave sensors have been used for a variety of applications including the detection of biological analytes [4, 5] liquid properties [6, 7] and evaporation kinetics [8].

Due to their ability to be used in an aqueous environment and their sensitivity, Love wave sensors are often used as biosensors. Different guiding layer materials have been reported such as polymethylmethacrylate (PMMA) [9, 10] positive photoresists [11] SiO_2 [12] and multi-layer polymer/SiO_2 structures [13]. Although silica guiding layers display low acoustic losses in the MHz range their fabrication by deposition techniques is lengthy, and thick layers (~6 μm) are required to support a Love wave if quartz substrates are used due to the materials' similar acoustic velocities [14]. Thin polymer layers (~2 μm) will support a Love wave and can be spun on relatively easily. PMMA based devices exhibit lower sensitivities compared to silica, possibly due to the high internal losses occurring in the guiding layer.

One of the disadvantages of using Love wave devices is that the interdigital transducers (IDTs) are on the same side as the sensing surface. The operation of such devices in liquids can result in electrical short circuits. Harsh liquids may even damage the IDTs. For these reasons the guiding layer is often extended across the whole face of the device to avoid the use of complicated o-rings and sealed units. The use of different materials to protect the IDTs has been reported – specifically SU-8, an epoxy based negative photo resist [15]. SU-8 was used only as a protective layer to cover the IDTs whilst silicon dioxide was deposited as a guiding layer material between the IDTs. These devices were made in a multistage process, wherein silicon dioxide was grown by chemical vapour deposition, patterned between the IDTs by photolithography, with SU-8 being applied in a later process. SU-8 is spun on to a desired thickness and soft baked to remove solvent. Reactive sites within the SU-8 polymer are created during UV irradiation, which, upon heating cross-link to form a strong, hard, chemically inert surface resilient to acids, bases and solvents. [16] By using SU-8 as a guiding layer covering the IDTs any complicated and time consuming deposition of silicon dioxide wave guide layers would be reduced to a simple spin-on process. Devices would be sensitive, durable and chemically resistant.

Here we present use of SU-8 as a Love wave guiding layer material. SU-8 is assessed in terms of the thickness required to support a Love wave, with the first mode being examined. Frequency and insertion loss of the devices were monitored with increasing guiding layer thickness. The sensitivities of devices with different thickness SU-8 guiding layers were assessed by gold deposition, and liquid sensing was demonstrated using water-glycerol mixtures and protein adsorption studies.

2. Experimental Section

Love wave devices were fabricated on ST-cut quartz with propagation orthogonal to the crystal direction. The IDTs consisted of sputtered gold (80 nm, Emitech) over titanium (10 nm, Emitech) as an adhesive layer, deposited using an Emitech K757X sputter coater. A single-single finger design was used. Finger widths and spacings were 12.8 μm, with each IDT being 4.5 mm in length, with an aperture of 4 mm and IDT centre-centre distance of 12 mm. SU-8 is a negative photoresist requiring a multistage process to form a semi-rigid layer. Parameters were defined such that the polymer was spin coated onto a device to achieve a desired thickness, soft-baked to remove solvent before UV exposure and hard-baking to allow cross linking to take place. Once hard-baked SU-8 has the advantage over other polymers often used as a guiding layer material being mechanically reliable and almost completely chemically inert. The thickness of each layer was determined by stylus and optical profilometry, being measured at 0.56 μm. The SU-8 guiding layers were successively built up using SU-8-10 (Microposit) diluted in 1-methoxy-2-propanol acetate (Aldrich, 98+%). These were spun to achieve a single layer thickness of 0.56 μm (verified using a Veeco Dektak 6M stylus profiler and an optical Veeco Dektak 3 surface analysis system.) Each layer added was prebaked at 55 ^{o}C 10 min, cooled to room temperature and exposed to UV using a Mega LV202E UV exposure unit, before being postbaked at 55 ^{o}C 10 mins and 95 ^{o}C 5 mins. Multiple 30 nm gold layers were used as a model for rigid mass, being sputtered on the centre of the Love wave propagation path up to 450 nm using an Emitech K575X fitted with a film thickness monitor. A mask was used to define a small area of 8 mm^2 onto which the gold was sputtered. Device spectra were recorded using an Agilent E5061A network analyser. Glycerol/water mixtures were pumped over the sensor using a Watson Marlow peristaltic pump. Glycerol (Sigma 98%) was diluted with distilled deionised water. Protein flow experiments were conducted with solutions being continually flown over the sensor surface at 1 ml min^{-1} by syringe pumps (Razel R100-EC). Protein solutions were prepared immediately prior to use at a concentration of 1 mg ml^{-1} in phosphate buffered saline (PBS, Sigma, tablets) using bovine serum albumin (Sigma, fraction V, lyophilized powder) and bovine fibrinogen (Sigma, type I-S, lyophilized powder) Temperature stability of 24 ± 0.1 ^{o}C was achieved using an Octagon 10 incubator. The Love wave device was used as the feedback element in an oscillator circuit consisting of cascaded amplifiers (Minicircuits ZFL-500LN), a 50 MHz high pass filter and 150 MHz low pass filter (Minicircuits BHP-50 and BPL-150), a power splitter (M/A com T1000) and a frequency counter (Agilent 53132A) interfaced to a microcomputer.

3. Results and Discussion

Signal characteristics of devices were recorded during the build up of successive layers of SU-8 photoresist. As the guiding layer thickness increases it is expected that the acoustic wave will gradually move from propagating entirely in the quartz as a surface skimming bulk wave (SSBW) to being confined at the surface of the substrate or travelling within the guiding layer as a Love wave. As this happens the velocity of the wave will decrease and so it is expected that a decrease in resonant frequency will also occur. The additional mass loading caused by the guiding layer will also contribute to a drop in frequency. Trends in frequency and amplitude of the signal over the first mode are shown in Figure 1. The signal attenuation initially decreased with increasing guiding layer thickness, reaching

a minimum of -15 dB at ~1 μm (z = 0.02). An increase in the amplitude of the signal demonstrates that more of the acoustic energy is located near the surface of the device which is consistent with previous reports using quartz substrates [11]. Additional layers of SU-8 gave rise to a gradual decrease in insertion loss due to the dampening of the overlayer, although it is well known that higher order modes can be observed with increasing thickness [3, 11].

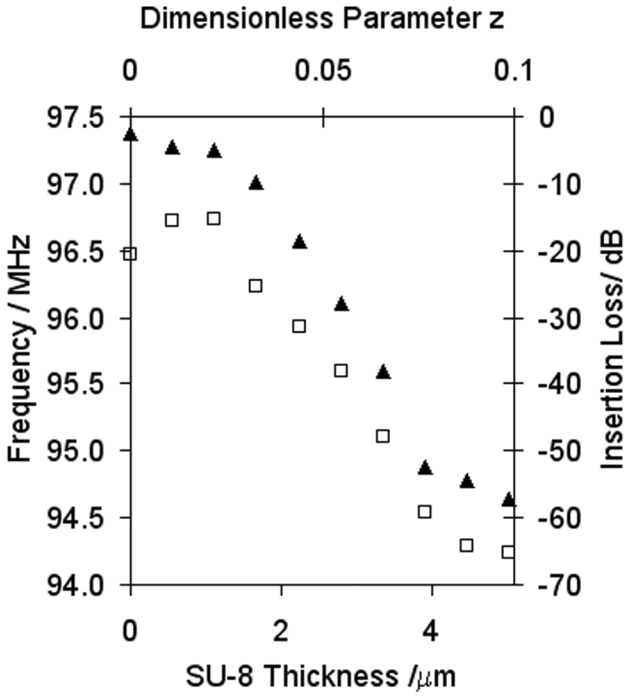

Figure 1. Signal characteristics covering the first mode of an SU-8 guiding layer Love wave device. Frequency (closed triangles) and insertion loss (open squares) shown as a function of guiding layer thickness and dimensionless parameter $z = d/\lambda_{IDT}$.

The mass sensitivity of devices with a range of guiding layer thicknesses chosen to cover the first mode has been investigated. For acoustic wave sensors without a guiding layer it usual to assume that the frequency change resulting from the addition of rigid mass is directly related to a change in phase velocity and hence a Sauerbrey type relation exists. For guided waves there may be significant dispersion and the frequency dependence of rigid mass loading onto a Love wave device may not be directly proportional [3, 17]. However if upon the addition of mass the change in guiding layer thickness is infinitesimal such that the operating point is not moved significantly down the dispersion curve, as in our experiments, then a Sauerbrey type proportionality may be observed [18]. If this is assumed then the mass loading effects of metalized layers on top of a guiding layer provide a simple route to defining the sensitivity of Love wave devices. All devices showed a linear relationship between frequency change as a function of increasing mass of gold, as shown in Figure 2.

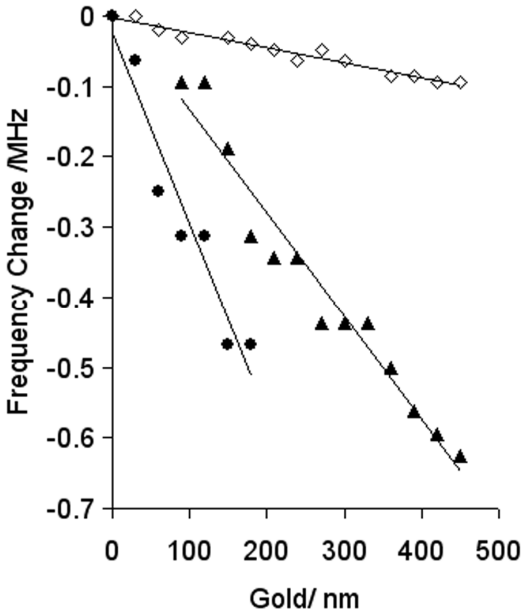

Figure 2. Relationship between mass loading and frequency of a SSBW device (open diamonds), and Love wave devices having guiding layers 1.12 μm thick (closed triangles) and 2.24 μm (closed circles).

A greater change in frequency was observed when depositing gold layers on all SU-8 devices compared to an uncoated device. The linear regions of the signal change was used to calculate the sensitivity of the devices in terms of a frequency change observed for mass loading of gold per unit area, Figure 3. From Figure 1 it would be expected that the most sensitive region would be where small changes in guiding layer thickness cause the largest changes in frequency, i.e. the middle of the mode. Indeed a sharp maximum in sensitivity was measured at ~350 Hz/ng/mm^2 at a guiding layer thickness of ~2 μm (z = 0.04), Figure 3. This corresponds well with the experimental dispersion curve data (Figure 1), relating to a point where the maximum frequency changes are observed with increasing guiding layer thickness.

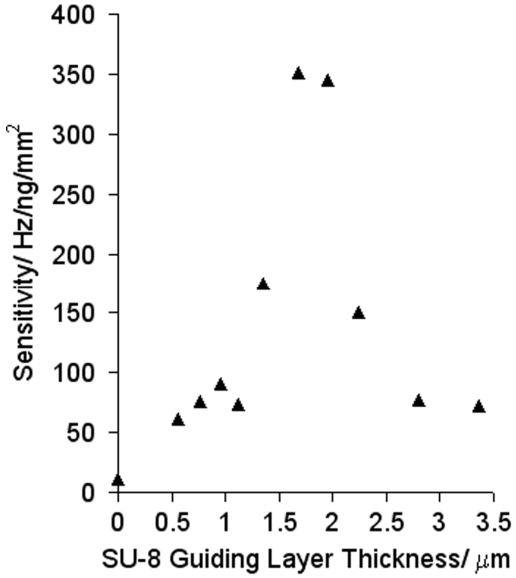

Figure 3. Frequency sensitivity of Love wave devices.

To demonstrate the use of SU-8 Love wave devices in liquid sensing, flow experiments were conducted to compare an SSBW device to a Love wave device with a 2 μm thick SU-8 guiding layer. Devices were clamped such that glycerol-water mixtures could be in contact with their sensing surface. Liquid was injected into the flow cell using a peristaltic pump with the flow direction perpendicular to the acoustic wave propagation; after the liquid was introduced the pump was halted until the next concentration was introduced. A stable signal was achieved oscillating in water, changing the liquid for 30% and 50% glycerol solutions before washing again with water, Figure 4.

The propagating acoustic waves' amplitude is attenuated by the liquid overlayer such that it decays with a penetration depth $\delta = \sqrt{\eta_l / (\pi f_0 \rho_l)}$, where ρ_l and η_l are the liquid density and viscosity respectively. For non-guided acoustic waves the Kanazawa and Gordon relationship [19] between frequency change and square root of the density-viscosity product is assumed to hold. For Love wave devices this may not be assumed due to the considerations discussed previously for mass loading. However, again, if the operating point of the sensor is not moved significantly down the dispersion curve then proportionality between the square root of the density-viscosity product and the change in frequency may be observed.

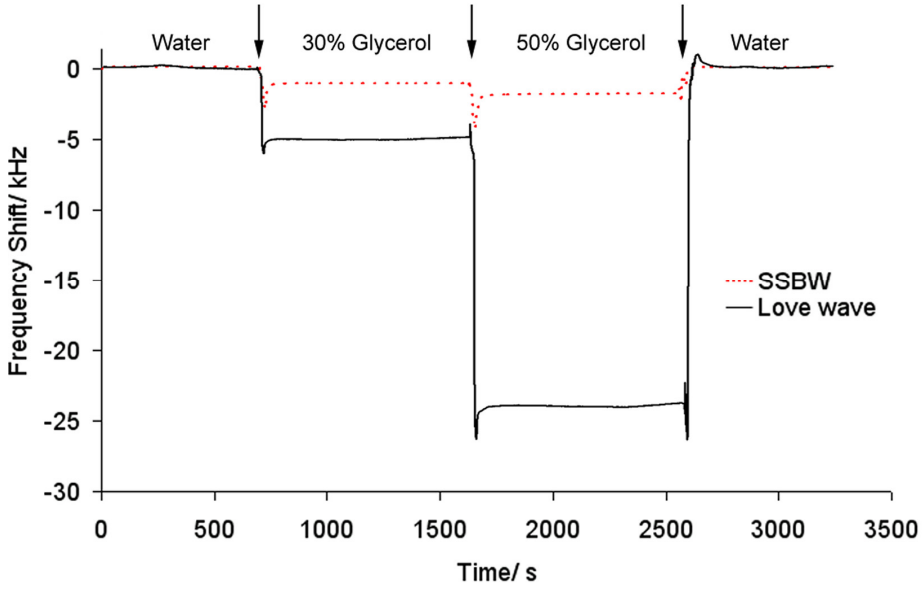

Figure 4. Liquid sensing of an SSBW device (dotted red line) and a Love wave device with an SU-8 guiding layer (solid black line), using water-glycerol mixtures. Arrows indicate points when liquid in contact with the sensor was exchanged.

As the device is oscillated in more viscous liquids the operating frequency will decrease, shown by the stepwise drops in frequency in Figure 4 as the glycerol fraction was increased. Both the devices tested returned to their original oscillating frequency when water is replaced over the sensors, indicating that no residual glycerol remained or any changes occurred to the sensor surfaces. The Love wave device shows a much higher sensitivity compared to the SSBW device, giving frequency shift more than 4 fold and 12 fold greater than the SSBW device for 30% and 50% glycerol solutions respectively (relative to water).

Initial spikes in frequency were observed due to the peristaltic pumping motion of the liquid when flushed over the crystal (causing pressure waves). Thermal drifting is often a problem during liquid sensing, wherein even small changes in temperature alter the viscosity of the media and effect the sensor itself. However, the SU-8 Love wave device showed good stability when in contact with water-glycerol mixtures, with only slight frequency drift of ~11 Hz min^{-1}. The greater stability of SU-8 compared to PMMA when in contact with water has previously been reported [20]. As SU-8 is highly chemically inert [16], it is anticipated that such devices will be stable under most chemical conditions. This may be particularly useful when measuring properties of corrosive or easily contaminated liquids such as ionic liquids.

To demonstrate the use of SU-8 Love wave devices for the detection of biomolecules, the adsorption of two serum proteins was examined. Bovine serum albumin (BSA) is a small globular protein and fibrinogen is a much larger rod-like protein, both found in high abundance in serum and are often used as model proteins in adsorption studies.[21] PBS was flown over a Love wave device having a 2 μm thick SU-8 guiding layer before the inlet of protein solution. Frequency shifts observed suggest that both albumin and fibrinogen adsorb onto the SU-8 surface upon injection over the sensor (Figure 5, point a). Following adsorption any loosely adhered or unbound protein was removed during a PBS rinse (figure 5, point b) which is shown by a slight upward shift in frequency. Albumin adsorption gave rise to a much lower change in frequency (~370 Hz) compared to fibrinogen (~1330 Hz) which is expected due to its smaller mass and differences in surface chemistry. Fibrinogen was also found to adsorb at a faster rate. These observed trends in adsorption compare well with those previously reported for these two proteins, bearing in mind the wettability of SU-8 being neither highly hydrophilic nor hydrophobic (water contact angle 80° [22]). A more detailed discussion of protein adsorption profiles and how this relates to protein-surface interactions can be found elsewhere [21].

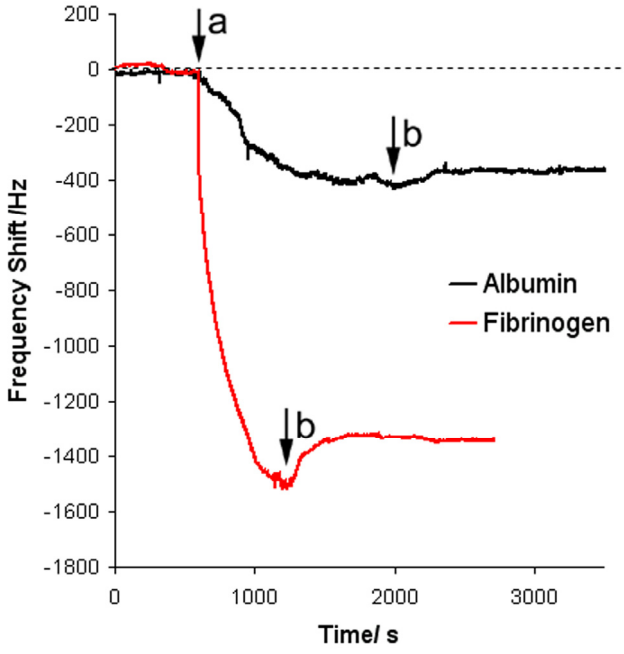

Figure 5. Protein detection using an SU-8 Love wave device. Arrows indicate points when solutions over sensors were exchanged, a) protein solution injected, prior to a) and at b) PBS solutions injected. Adsorption of albumin (black line) and fibrinogen (red line) was detected.

Conclusions

A negative epoxy-based photoresist, SU-8, was investigated as a Love wave guiding layer material. Signal characteristics were investigated in terms of guiding layer thickness. Observed trends in frequency and insertion loss were as expected for quartz Love wave devices. Frequency decreased with increasing guiding layer thickness, whilst insertion loss reached a minimum of ~-15 dB. Such low insertion losses are not common for these devices and may relate to the acoustic properties of SU-8. Sensitivity was assessed by the deposition of gold layers between the IDTs, showing a linear response in terms of frequency for all devices tested. A maximum sensitivity was achieved with a guiding layer thickness of ~2 μm (z = 0.04). Liquid sensing was also tested using water-glycerol mixtures, demonstrating the enhanced sensitivity of the Love wave device over an SSBW. Acoustic wave sensors are often used to assess viscosity-density of liquids although are often limited to those chemicals which will not damage the guiding layer The excellent stability of the devices when in contact with liquid highlights the applicability of SU-8 Love wave devices for sensing chemicals which may corrode/ dissolve/ swell or otherwise distort other polymers used as guiding layers.. The chemical stability of hard-baked SU-8 has been used by others to protect IDTs whilst another material is used as a wave guide. Protein adsorption experiments show the applicability of these sensors to detect biomolecules, showing a comparably larger frequency shift for fibrinogen adsorption than albumin and also a faster rate of adsorption for fibrinogen as expected. Here we have demonstrated the ease of fabrication and effectiveness of SU-8 based Love wave devices.

Acknowledgements

This work was funded by EPSRC grant EP/C536630/1.

References and Notes

1. Thompson, M.; Stone, D. *Surface Launched Acoustic Wave Sensors: Chemical Sensing and Thin Film Applications*, John Wiley and Sons: New York, 1997.
2. Lucklum, R.; Hauptmann, P. Acoustic Microsensors – The Challenge Behind Microgravimetry. *Anal. Bioanal. Chem*. **2006**, *384*(3), 667-682.
3. McHale, G.; Generalized Concept of Shear Horizontal Acoustic Plate Mode and Love Wave Sensors. *Meas. Sci. Technol*. **2003**, *14*, 1847-1853.
4. Melzak, K.A.; Ellar, D.J.; Gizeli, E. Interaction of Cytolytic Toxin CytB with a Supported Lipid Bilayer: Study Using an Acoustic Wave Device. *Langmuir* **2004**, *20*(4), 1386-1392.
5. Schlensog, M.D.; Gronewold, T.M.A.; Tewes, M.; Famulok, M.; Quandt, E. A Love-Wave Biosensor Using Nucleic Acids as Ligands. *Sens. Actuators B* **2004**, *101*(3), 308-315.
6. Melzak, K.A.; Martin, F.; Newton, M.I.; McHale, G.; Gizeli, E. Acoustic Determination of Polymer Molecular Weights and Rotation Times. *J. Polymer Sci. B* **2002**, *40*(14), 1490-1495.
7. Turton, A.; Bhattacharyya, D.; Wood, D. Liquid Density Analysis of Sucrose and Alcoholic Beverages using polyimide Guided Love-mode Acoustic Wave Sensors. *Meas. Sci Technol*. **2006**, *17*, 257-263.

8. Razan, F.; Rebiere, D.; Dejous, C.; Monin, D.; Joanicot, M.; Conedera, V. Determination of Menthol Kinetic Constants with Love-Wave Device. *Sens. Actuators B* **2006**, *118*(1-2), 368-373.
9. Gizeli, E.; Lowe, C.R.; Liley, M.; Vogel, H. Detection of Supported Lipid Layers With the Acoustic Love Waveguide Device: Application to Biosensors. *Sens. Actuators B* **1996**, *34*, 295–300.
10. Harding, L.G.; Du, J. Design and Properties of Quartz-Based Love Wave Acoustic Sensors Incorporating Silicon Dioxide and PMMA Guiding Layers. *Smart Mater. Struct*. **1997**, *6*, 716–720.
11. Newton, M.I.; McHale, G.; Martin, F. Experimental Study of Love Wave Devices With Thick Guiding Layers. *Sens. Actuators A* **2004**, *109*, 180–185.
12. Jakoby, B.; Ismael, G.M.; Byfiled, M.P.; Vellekoop, M.J. A Novel Molecularly Imprinted Thin Film Applied to a Love Wave Gas Sensor. *Sens. Actuators A* **1999**, *76*, 93-97.
13. Du, J.; Harding, L.G. A Multilayer Structure for Love-Mode Acoustic. *Sens. Actuators A* **1998**, *65*, 152-159
14. Du, J.; Harding, G.L.; Ogilvy, J.A.; Dencher, P.R.; Lake, M. A Study of Love-Wave Acoustic Sensors. *Sens. Actuators A* **1996**, *56*, 211-219.
15. Arana, N.; Puente, D.; Ayerdi, I.; Castano, E.; Berganzo, J. SU8 Protective Layers in Liquid Operating SAWs. *Sens. Actuators B* **2006**, *118*, 374-379.
16. LaBianca, N.; Gelorme, J.D. High aspect ratio resist for thick film applications. *Proc. SPIE*, **1995**, 2438, 846-852
17. McHale, G.; Newton, M.I.; Martin, F. Theoretical Mass, Liquid, and Polymer Sensitivity of Acoustic Wave Sensors With Viscoelastic Guiding Layers. *J. Appl. Phys*. **2003**, *93*(1), 675-690.
18. Sauerbrey, G. The Use of Quartz Oscillators for Weighing Thin Layers and for Microweighing. *Z. Phys*. **1959**, *155*, 206-222.
19. Kanazawa, K.K.; Gordon, J.G. The Oscillation Frequency of a Quartz Resonator in Contact With a Liquid. *Anal. Chim. Acta*. **1985**, *175*, 99-105.
20. Hossenlopp, J.; Jiang, L.; Cernosek, R.; Josse, F. Characterisation of Epoxy Resin (SU-8) Film Using Thickness-Shear Mode (TSM) Resonator Under Various Conditions. *J. Polymer Sci. B* **2004**, *42*, 2373-2384.
21. Roach, P.; Farrar, D.; Perry, C.C. Interpretation of Protein Adsorption: Surface-Induced Conformational Changes. *J. Am. Chem. Soc*. **2005**, *127*, 8168-8173.
22. Shirtcliffe, N.J.; Aqil, S.; Evans, C.; McHale, G.; Newton, M.I.; Perry, C.C.; Roach, P. The use of high aspect ratio photoresist (SU-8) for super-hydrophobic pattern prototyping. *J. Micromech. Microeng*. **2004**, *14*, 1384–1389.

C. R. Evans, S. Atherton, D. C. Hughes, G. McHale and M. I. Newton, Assessing sperm motility using acoustic plate mode devices, Proceedings Of The 2007 IEEE International Frequency Control Symposium-Jointly With The 21st European Frequency And Time Forum, 2007, pp. 4

Assessing sperm motility using acoustic plate mode devices

C.R.Evans, S.Atherton, D.C.Hughes, G.McHale and M.I.Newton
School of Biomedical & Natural Sciences
Nottingham Trent University
Clifton Lane, Nottingham NG11 8NS, UK
e-mail glen.mchale@ntu.ac.uk

***Abstract*— In this work we report a simple time of flight technique for assessing the number and motility of pig sperm in a semen sample. Acoustic plate mode (APM) devices have been employed as the sensor element at the end of a channel down which sperm swim. Combining the APM data with conventional microscopy, an estimate of 18.9±4.8pg for the pig sperm effective mass at 52MHz APM devices is derived.**

I. INTRODUCTION

Accurate and precise determination of viable sperm concentration is an important issue for the Artificial Insemination (AI) industry. AI of farm animals is common practice in the agriculture industry with more than 100 million inseminations performed globally each year. Crucial to the success of insemination is not only the number of sperm in a semen sample but also the motility of the sperm. Motility is the term used to describe the motion and activity of sperm in a semen sample. Counting chambers or haemocytometers are used for routine sperm counts. However, multiple measurements are required to achieve an acceptable precision and accuracy which makes the procedure time consuming. The main disadvantages of these methods are the inaccuracy due to the rapid movement of the cells at high magnification and the tedious nature of the work for the human operator. A more objective assessment of sperm motility can be achieved with a laboratory based instrument called a computer-assisted semen analyzer CASA [1] which can give a measure of different aspects of sperm movement. The combination of flow cytometry and fluorescent staining [2] provides a technique to analyze thousands of sperm per sample and achieve a higher precision than is obtained with a CASA systems. The drawback of these technologies is the price of equipment and the need for a skilled operator. In this work we report a simple time of flight technique using acoustic plate mode (APM) devices that has the potential to be an inexpensive field instrument for assessing the number and motility of sperm immediately prior to insemination.

II. EXPERIMENTAL

The APM devices were fabricated on 36° rotated Y-cut X propagating lithium tantalate of thickness between 530-540 μm. The interdigital transducers (IDT) were of a double-double design with 10μm finger widths and spaces, 50 repeat patterns, a 2000μm aperture, a path length of 8mm giving a fundamental frequency of 52MHz. The fingers consisted of 40 nm of titanium followed by 200 nm of gold deposited by sputter coating. Both faces of the APM device were coated in poly-L-lysine by initially cleaning with ethanol, then ozone treated for 30 minutes. The devices were then placed in poly-L-lysine solution overnight; the devices were then washed in the PBS buffer to remove any excess. The face of the device not containing the IDT's was used as the sperm detection region. The APM device was used as the feedback element in

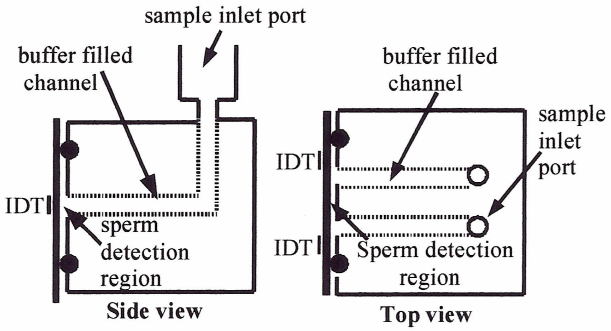

an oscillator circuit consisting of cascaded amplifiers

Figure 1. Schematic diagram of experimental arrangement

(Minicircuits ZFL-500LN), a 50MHz high pass filter and 150MHz low pass filter (Minicircuits BHP-50 and BPL-150), a power splitter (M/A com T1000), a pi phase shifter and a frequency counter (Agilent 53132A) interfaced to a microcomputer. Figure 1 shows a schematic diagram of the test cell, sperm were introduced at the inlet port and move through the channel to a sperm detection region comprising the APM device with sperm adhesive poly-L-lysine coating. The channel length was set to approximately 6.5 cm which would mean that the earliest expected arrival of the first sperm would be after 14 minutes [3,4] and this would be followed by a distribution of arrival times. As the sperm have to be motile

to travel to the APM device, the time of arrival is a measure of their motility. Pig semen samples were supplied by a commercial artificial insemination centre (JSR Genetics, Driffield, UK). Prior to dispatch the semen was mixed with a dilutent (Androhep), cooled to 17°C packaged in plastic bottles, and delivered by overnight postal service. This medium is suitable for up to 5 days storage at ambient temperature.

III. RESULTS AND DISCUSSION

Figure 2 shows a typical change in frequency for a period of 110 minutes; a 0.2ml pig semen sample was introduced at 31 minutes. At 19 minutes from the introduction of the semen a fall in frequency is observed which is completed after a further 23 minutes and shows a frequency decrease of 1780±160Hz. Josse et.al. have reported that the sensitivity for a 52 MHz APM device is around 73.3Hz/ng mm^{-2} [5].

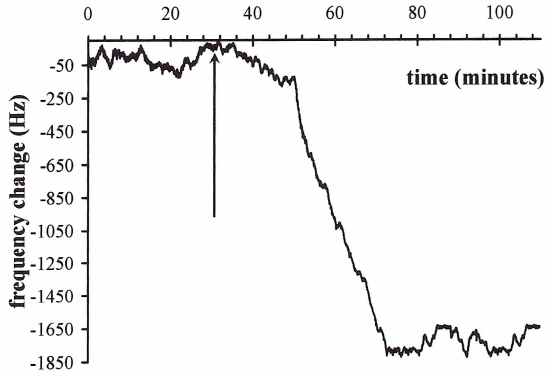

Figure 2. Frequency change of APM device following the semen sample introduced at 31 minutes as shown by the arrow.

Using this sensitivity value and the frequency fall observed, the mass of sperm attached to the sensing area of the APM is 390±35ng. Estimation of the number of attached sperm was made using a poly-L-lysine coated glass slides in place of the APM one hour after introducing the sperm. The slides were checked using conventional microscopy to identify the sperm concentration present. An area of 0.36mm x 0.49 mm on the glass slide at the end of the flow cell gave 237±40 sperm and this equates to 21500±3600 sperm in the path between the IDT's of the APM device.

Figure 3 is a microscope image of a porcine sperm showing that the head is approximately 8µm and overall length of 50 to 60 µm. Given that the penetration depth of acoustic waves in water at 52MHz is only 78nm and will only probe a small part of the attached sperm, we have considered if the attachment of sperm may be approximated by the Sauerbrey equation using an effective mass. In a previous report we have used 5MHz quartz crystal microbalance [6], and fitted the resonance curve with a Butterworth van Dyke model to extract the crystal resistance with and without attached sperm. This showed that little change occurred in the crystal resistance due to the sperm attachment even though a frequency shift was observed. This confirmed that a simplified model based on the Sauerbrey equation and a sperm effective mass could in practice be appropriate. Previous studies have estimated a dry head mass of 13pg [7] and up to 70% of the sperm mass to be made up of water [8]. Using the estimate for the number of sperm and the frequency change of the APM, the effective mass of pig sperm on a 52MHz APM device is 18.9±4.8pg.

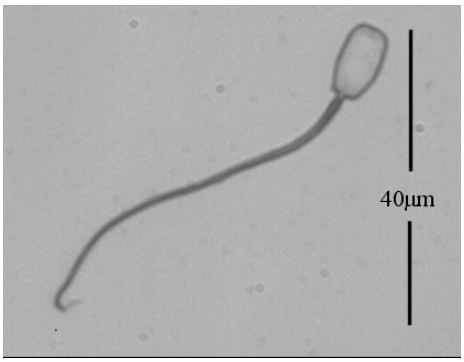

Figure 3. Microscope image of porcine sperm

IV. CONCLUSION

In this article we have demonstrated that acoustic plate mode devices may be employed as the sensor element for a time of flight method to determine sperm motility in a semen sample. One of the main issues that require addressing before the device would be suitable for routine screening is the shelf life associated with the poly-L-lysine coating, preliminary test suggest that cysteamine appears more promising but require further investigation.

REFERENCES

[1] S.T.Mortimer "CASA—Practical Aspects", J. Androl. vol. 21, 2000 pp. 515-524

[2] P.Christensen, J.P.Stenvang and W.L.Godfrey. "A Flow Cytometric Method for Rapid Determination of Sperm Concentration and Viability in Mammalian and Avian Semen" J Androl vol. 25, 2004, pp. 255-264

[3] M.Hirai, A.Boersma, A.Hoeflich, E.Wolf, J.Foll, T.R.Aumuller and J.Braun "Objectively measured sperm motility and sperm head morphometry in boars (Sus scrofa): relation to fertility and seminal plasma growth factors" J Androl vol. 22 2001 pp. 104-110

[4] C.Holt, W.V.Holt, H.D.Moore, H.C.Reed and R.M.Curnock. "Objectively measured boar sperm motility parameters correlate with the outcomes of on-farm inseminations: results of two fertility trials"J Androl vol. 18, 1997 pp. 312-323

[5] F.Josse, R.Dahint, J.Schumacher, M.Grunze, J.C.Andle and J.F.Vetelino. "On the mass sensitivity of acoustic-plate-mode sensors" Sen. Actuator. A: Physical, vol. 53, 1996, pp. 243-248.

[6] M.I.Newton, C.R.Evans, J.J.Simons and D.C.Hughes. "Semen quality detection using time of flight and acoustic wave sensors" Appl. Phys. Lett. Vol. 90 2007 154103 doi: 10.1063/1.2721858

[7] G.P.Bahr and E.Zeitler "Study of bull spermatozoa; quantitative electron microscopy" J. Cell. Biol. vol. 21, 1964, pp. 175-189

[8] L.B.Da Silva, J.E.Trebes, R.Balhorn, S.Mrowaka, E.Anderson, D.T.Attwood, T.W.Barbee. J.Brase, M.Corzett, J.Gray, J.A.Koch, C.Lee, D.Kern, R.A.London, B.J.MacGowan, D.L.Matthews and G.Stone "X-ray laser microscopy of rat sperm nuclei " Science, vol. 258 1992 pp. 269-27

S. Atherton, C. R. Evans, P. roach, D. C. Hughes, G. McHale and M. I. Newton, Investigation of Operating Parameters For A Semen Quality Analysis System, Biodevices 2009: Proceedings Of The International Conference On Biomedical Electronics And Devices, 2009, pp. 13

INVESTIGATION OF OPERATING PARAMETERS FOR A SEMEN QUALITY ANALYSIS SYSTEM

S.Atherton, C.R.Evans, P.Roach, D.C.Hughes, G.McHale and M.I.Newton
School of Science and Technology,
Nottingham Trent University, Clifton Lane, Nottingham
NG11 8NS, UK
*. *Email: shaun.atherton@ntu.ac.uk*

Keywords: Sperm, semen, motility, acoustic wave, QCM, time of flight

Abstract: To increase the success rate of Artificial Insemination (AI) in animals, it is important that the semen sample is of a high quality. The quality is related to both the number and motility of sperm present. Numerous methods of analysing semen samples exist, but these are generally expensive and/or laboratory based. A useful alternative would be an inexpensive simple system that could be used in the field immediately prior to insemination. We present a time of flight (ToF) technique using a quartz crystal microbalance (QCM). In this system the sperm are introduced at one end of a liquid filled swim channel and self propel to a QCM sensor at the other end. A chemical coating is applied to the QCM to bind the sperm and from the frequency change the number of attached sperm and their ToF can be measured. We report the effect of temperature and the introduction of small quantities of progesterone into the swim channel on the sperm ToF. Results show the QCM can be used to detect the arrival of the sperm and that increasing temperature and the presence of progesterone are both shown to decrease the ToF.

1 INTRODUCTION

Within the Artificial Insemination (AI) industry it is important to be able to measure the concentration of viable sperm in a sample. AI is a common procedure in farm animals, more than 100 million inseminations are performed globally every year. It is not only the number of sperm in a semen sample that is crucial to the success of the insemination process, but also the motility of the sperm. Whilst having a large number of motile sperm in a sample is not a guarantee of fertility, it is an excellent indicator of semen quality.

Two optical methods of performing sperm counts are the haemocytometer and counting chambers. The drawback of these methods is that multiple measurements are needed to achieve an acceptable level of precision, resulting in a more time consuming procedure. The reason for the relative inaccuracy of these methods is due to the rapid movement of the sperm under high magnification and the tedious nature of the work for the human operator. It is possible to perform a more objective assessment of sperm motility using a computer assisted semen analyzer (Mortimer, 2000), which is a laboratory based instrument that can measure different aspects of the sperm movement. To further increase precision, a combination of fluorescent staining and flow cytometry can be used to analyze thousands of sperm in a sample (Christensen et al, 2005). The common drawback with all of the above techniques is the price of the equipment itself and the need for a skilled operator.

In some species the sample may be successfully frozen and thawed before use however this is not always the case. The sperm of other species cannot be successfully frozen and so a fresh sample, with a shelf life of only a few days, must be used. Increasingly, AI is being used for equine applications and recent changes in UK legislation (Artificial Insemination of Mares Order 2004) mean that lay (non-Veterinary) and farm workers are now being trained to perform such inseminations. For sport equine applications the cost of semen for a single mare to be covered may exceed £1000. Semen analysis is currently a specialist, subjective and skilled process that is normally carried out under laboratory conditions. Given these trends, a low cost, simple to use and objective technique to assess the quality of the semen, particularly under field conditions just before insemination, would greatly

improve the quality and practice of artificial insemination in animals. It would also provide an easier and more cost effective method for monitoring male animal fertility and breeding male welfare.

Acoustic wave sensors detect very small changes in mass attached to their surface and often contain a sensitizing layer that can recognize and bind the species to be detected onto the mass sensitive surface. The quartz crystal microbalance (QCM) is the most widely used acoustic wave device for sensor applications.

$$\Delta f = -2.26 \times 10^{-6} f^2 \Delta m/A \quad (1)$$

The Sauerbrey equation (Sauerbrey, 1959) relates the change of the crystals resonant frequency to the change in rigid mass on the crystal surface; this is shown for AT cut quartz in equation 1 where Δf (in Hz) is the change in frequency that occurs for an increase in mass Δm (in grams) on the surface of area A (in cm^2) with a crystal resonant frequency of f (in Hz) and the constant comes from the crystal materials properties. A well-designed oscillator circuit can still resonate a crystal even under the high damping caused by immersion in a liquid. The change in mass rigidly attached to the surface still causes a proportional change in frequency although changes in other parameters such as the liquids viscosity and density will also cause changes in frequency. The acoustic wave will only sense mass changes within a short distance into the liquid called the penetration depth. (Kanazawa & Gordon, 1985) Previous studies have shown up to 70% of the sperm mass to be made up of water (Da Silva et al, 1992) so it is not obvious how the attachment of a sperm will change the QCM response. In a preliminary report (Newton et al, 2007) we have fitted the resonance curves of 5MHz QCM to the Butterworth van Dyke model and this has shown that the sperm may be treated a rigid mass and so a model based on the Sauerbrey equation is appropriate when using an *effective mass* of around 5pg. For other operating frequencies or other species sperm this effective mass would be different.

In this report we extend this preliminary work to investigate the effect of environmental parameters on the time of flight (ToF). For any practical measurement technique it is essential the time the measurement takes is sufficiently short to be usable. For a portable field instrument then power consumption may also be an issue therefore the first parameter we investigate is operating temperature and we consider a range from room temperature to body temperature.

Progesterone is a steroid hormone involved in female menstrual cycle, pregnancy and embryogenesis of humans and other species. It is one of a number of substances said to cause hyperactivation of mammalian spermatozoa and its presence may therefore affect the time of flight; the effect of adding progesterone to the swim medium is reported.

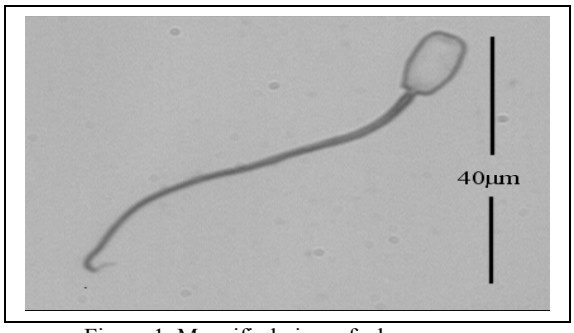

Figure 1. Magnified view of a boar sperm.

2 EXPERIMENTAL

Figure 2 shows a schematic diagram of the experiment. This consists of an inlet port to a channel filled with phosphate buffered saline (PBS) buffer. At the other end of the channel is a quartz crystal followed by a vent to air preventing pressure changes being recorded in the QCM response when a semen sample is added. Sperm are introduced at the inlet port and are self propelled through the channel to the QCM where they are detected. A volume of 20µl of the semen was used and added using a Gilson pipette. The channel length was set to approximately 14.5 cm and contained 4ml of PBS; note that for any practical field instrument the swim channel length could be considerably reduced to give an analysis time under 5 minutes. The sensing element in the experiments was a 5MHz AT-cut quartz crystal (Testbourne 149211-1). A Maxtek PLO-10 phase lock oscillator was used to drive the crystal and the resonant frequency was measured with an Agilent universal frequency counter interfaced to a computer.

To sense the sperm it was necessary to get them to adhere to the surface of the QCM. To achieve sperm adhesion to the crystals they were coated in either Poly-L-Lysine (Sigma-Aldrich) or cysteamine (Sigma-Aldrich). Crystals were initially cleaning with ethanol then ozone treated for 30 minutes. They were then placed in either poly-L-lysine (as supplied), or a cysteamine solution of 1mmol in toluene and left overnight. The devices were then washed in PBS buffer to remove any excess. The

cysteamine coating were found to be the most reliable method of binding the sperm to the surface as poly-L-lysine shows significant variability from batch to batch.

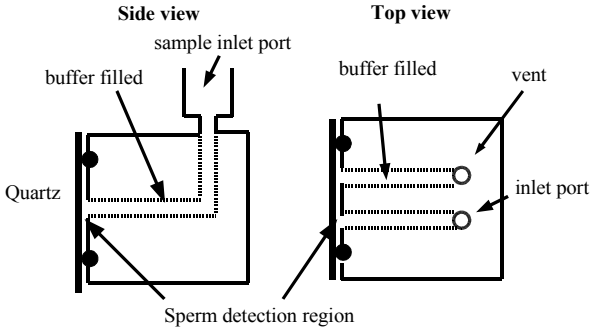

Figure 2. Schematic diagram of swim channel

To provide temperature control to the experiments the swim channel was housed inside an Octagon 10 incubator. This allowed the temperature to be controlled so as to investigate the effect this would have on the sperm ToF. For these the temperature was varied from 23-45ºC. The incubator also allowed the temperature to be kept constant across all the progesterone experiments.

When looking at the effects of progesterone, (Sigma-Aldrich) different concentration were added to the PBS in the swim channel. Firstly 15.7mg of progesterone was dissolved in 50ml of ethanol. This mixture was diluted in PBS at concentration of 20-90µmol.

The porcine semen was supplied by a commercial artificial insemination centre (JSR Genetics, Driffield, UK). The semen was received already mixed with a dilutant (Androhep), cooled to a temperature of 17ºC and packaged in plastic bottles. The androhep allowed the semen to be stored for up to 5 days at ambient temperature. However, this does result in the concentration of semen in the mixture being quite low. To get a more concentrated sample a centrifuge was used to separate the sperm from the androhep. To achieve this, sealable microtubes were filled with 50µl of the androhep and semen mixture and these were centrifuged for 40 seconds. This resulted in the sperm being concentrated at the bottom of the tube. The androhep was removed with the pipette and 50µl of PBS was added to one of the tubes. The PBS and sperm were mixed together, this mixture was removed with the pipette and added to the next tube and the process was repeated for all 15 tubes. What was left was a more concentrated sperm sample mixed with 50µl of PBS.

3 RESULTS AND DISCUSSION

Figure 3 shows the QCM frequency response to sperm binding on the surface. The arrow shows the time at which the semen sample was introduce to the inlet of the swim channel. The arrival of the sperm is signified by a decrease in the frequency of the sensor with the fastest ToF of approximately 20 minutes.

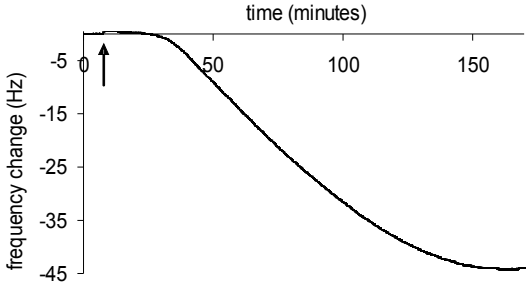

Figure 3. Graph showing the frequency decrease indicating sperm arrival

The frequency continues to drop as more sperm make their way to the QCM and bind to the surface. This continues for another 120 minutes until further arrival of motile sperm finishes.

Using the previously determined sperm effective mass and taking the rate of frequency change from figure 1, the Sauerbrey equation can be used to derive the rate of sperm arrival and this is shown in figure 3. For use in a screening application, a simple threshold number of detected sperm would be required however this demonstrates that quantitative analysis is also possible with this instrument.

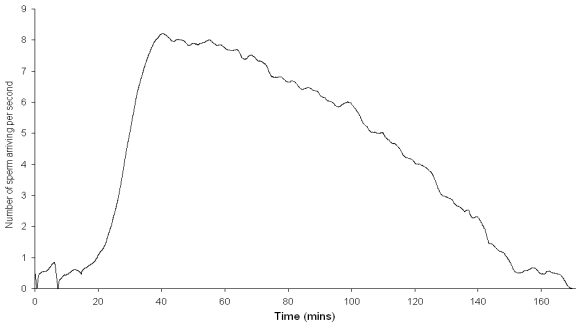

Figure 4. Number of sperm arriving at the QCM over the course of the experiment.

Figure 5 is a plot of the ToF of the sperm against the temperature of the environment. The results show a decrease in the ToF as temperature increases with almost a 50% fall between room temperature

and body temperature. The scatter observed can be attributed mainly to the experiments being performed a differing lengths of time from the receipt of the samples and the quality of the semen degrades over time.

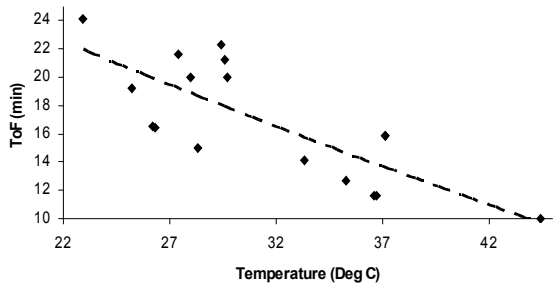

Figure 5. The time of flight for fastest sperm arrival as a function of temperature

To further speed up the measurement, progesterone was used to cause hyperactivation in an attempt to decrease the sperm ToF; the results of this are shown in figure 6. Comparing the non-progesterone experiments with the progesterone ones we see a significant decrease in the ToF of the sperm however for the full range investigated there was little effect from the progesterone concentration.

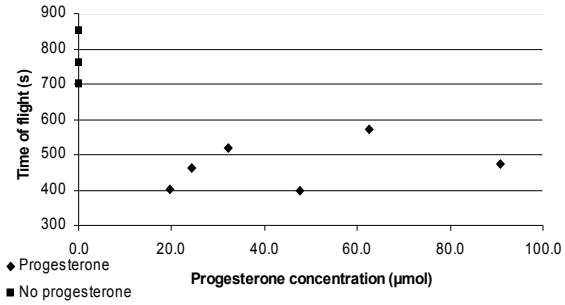

Figure 6. Time of flight as a function of progesterone concentration

4 CONCLUSION

We have demonstrated that a time of flight technique with an acoustic wave sensor provides a viable method for determining the quality of a semen sample both as a screening technique and as an analytical tool. The cysteamine coating on the QCM proved to be the more reliable method of binding the sperm to the surface. Experiments varying the temperature showed a general decrease in ToF as temperature is increased suggesting that body temperature would be the optimum value. The presence of progesterone also reduces the ToF however this was not concentration dependent over the range investigated. Whilst the laboratory based instrument reported here used commercial sensor crystals, the cost of quartz crystals employed more generally in electronic oscillator circuits are inexpensive and are still offer a mass sensitive surface. Using such crystals, pre-treated with cysteamine, would reduce costs sufficiently to offer the possibility of a disposable element. With a modification to the swim channel length to bring down the measurement time, this technique then becomes a powerful tool for routine monitoring of animal reproductive health and investigating factors that affect the semen motility of animal.

5 REFERENCES

Mortimer, S. T., 2000, CASA - Practical Aspects, J.ournal Andrology, 21, p.515-524

Christensen, P., Boelling, D., Pedersen, K. M., Korsgaard, I. R., & Jensen, J., 2005, Journal of Andrology, 26

Sauerbrey, G., 1959, Zeitschrift für Physik, p.155-206

Da Silva, L. B., Trebes, J. E., Balhorn, R., Mrowaka, S., Anderson, E., Attwood, D. T., Barbee, T. W., Brase, J., Corzett, M., Gray, J., Koch, J. A., Lee, C., Kern, D., London, R. A., MacGowan, B. J., Matthews, D. L., & Stone, G., 1992, X-ray laser microscopy of rat sperm nuclei, Science, 258, p.269-271

Kanazawa, K., & Gordon, J. G., 1985, Frequency of a Quartz Crystal Microbalance in contact with a liquid, Journal of Analytical Chemistry, 57, p.1770-1771

Newton, M. I., Evans, C. R., Simons, J. J., & Hughes, D. C., 2007, Semen quality detection using time of flight and acoustic wave sensors, Applied Physics Letters 90(15)

M. I. Newton, S. Atherton, R. H. Morris, S. M. Stanley, C.R. Evans, D. C. Hughes and G. McHale,

Low-Cost QCM Sensor System for Screening Semen Samples, Journal of Sensors, 2010

Hindawi Publishing Corporation
Journal of Sensors
Volume 2010, Article ID 326365, 5 pages
doi:10.1155/2010/326365

Research Article

Low-Cost QCM Sensor System for Screening Semen Samples

Michael I. Newton, Shaun Atherton, Robert H. Morris, Simon M. Stanley, Carl R. Evans, David C. Hughes, and Glen McHale

School of Science and Technology, Nottingham Trent University, Clifton Lane, Nottingham NG11 8NS, UK

Correspondence should be addressed to Michael I. Newton, michael.newton@ntu.ac.uk

Received 8 September 2010; Revised 28 October 2010; Accepted 23 November 2010

Academic Editor: S. C. Mukhopadhyay

Artificial insemination is a well-established part of modern agricultural practice. A viable semen sample is judged by the total number of spermatozoa (sperm) in the sample and the motility of the sperm. In this paper, we report the development of a reusable measurement cell and electronics for screening semen samples based on the Quartz Crystal Microbalance (QCM) and Universal Frequency to Digital Converter (UFDC-1) to produce a low-cost sensor system. After introducing the semen sample at one end of the measurement cell, sperm swim down a channel before causing a frequency change on the QCM. Data is presented that shows the different frequency changes using a commercial frequency counter caused by porcine semen samples, one two days old and one twenty one days old. Similar data is presented for a motile semen sample measurement using the low-cost UFDC-1.

1. Introduction

Artificial insemination of animals is a routine element in modern agricultural practice. For most species, semen can reliably be frozen and stored for long periods of time before being thawed and used. For some species, however, the freezing process is less reliable requiring that the semen be shipped chilled and used within several days. Semen analysis is currently a specialist, subjective, and skilled process that is normally carried out under laboratory conditions. The tests usually look at the number of spermatozoa (sperm) in a given volume of semen and also their ability to swim, that is, their motility. Most samples are analysed using optical techniques such as a haemocytometer or counting chamber [1]. Alternatively, they may rely on expensive computer aided semen analysis [2] or a combination of fluorescent staining and flow cytometry to analyze thousands of sperm in a sample [3]. These laboratory-based techniques are not suitable for use on a farm to test samples immediately prior to insemination. Under such conditions, a robust instrument that gives a simple yes or no answer without requiring complex sample preparation or interpretation of results is required. In a first report in 2007, we suggested that a simple time of flight technique using an acoustic wave sensor could provide a real-time screening technique for monitoring the motility of sperm in a semen sample [4]. The screening process is not designed to give a detailed analysis of a sample but rather determine if there is greater than a threshold number of motile sperm. It is known that the operation of a quartz crystal microbalance (QCM) or thickness shear mode device depends on the density and viscosity of the medium [5] and that sperm represent a complex object which extends beyond the penetration depth of a QCM. To demonstrate that sperm attachment could be treated like a rigid mass, the frequency change of a quartz crystal due to attached sperm was measured, and the number of attached sperm counted under a microscope [4]. It was demonstrated that the attachment of the sperm to the QCM could be modelled using the Sauerbrey equation [6] with an "effective" mass for a single porcine sperm of around 5 pg.

The technique was then further developed to consider some of the operating parameters including the effect of temperature and the presence of progesterone in the swim media [7]. In this paper, we report the development of a suitable swim cell and electronic measurement system based on the universal frequency to digital converter (UFDC-1, IFAC) that offers a low-cost sensor system suitable for screening a semen sample at the point of use on a farm.

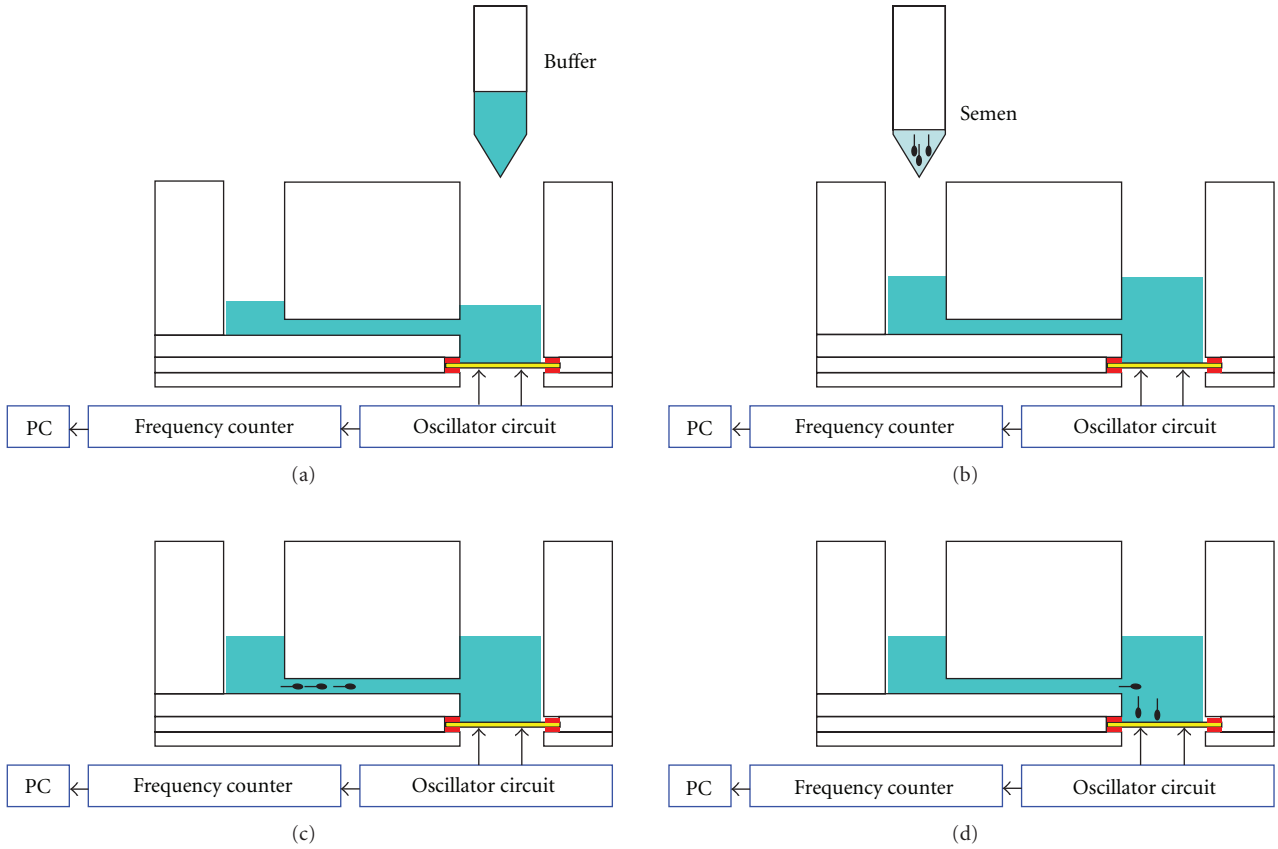

Figure 1: Schematic diagram of the acrylic swim channel with the quartz crystal (yellow) held in place with rubber gasket (red). The measurement sequence starts with buffer introduced into the swim cell (a). The semen sample is introduced at the opposite end of the swim channel to the quartz crystal (b). The sperm swim down the swim channel (c) and attached to the quartz crystal causing a frequency change (d).

2. Materials and Methods

Figure 1 shows a schematic diagram and example sequence of a typical experiment. The "swim" cell was produced using acrylic sheet cut on an M-500 laser cutter (Universal Laser Systems) and bonded using Extrufix (Bostik). A 12 mm diameter AT-cut quartz crystal with wrap around electrodes (Laptech XL1052) and fundamental frequency 10 MHz was clamped into the cell using rubber gaskets. Contact was made to the crystal using spring-loaded contacts directly connected to the oscillator circuit described below. The swim cell provided an opening for introducing the 1.5 mL of phosphate buffered saline (PBS) swim media (Figure 1(a)) and a smaller opening at the end of a 15 mm long swim channel for introduction of the semen sample (Figure 1(b)). After the semen is introduced, the sperm swim down the channel (Figure 1(c)) attaching to the quartz crystal at the end (Figure 1(d)) causing a change in the resonant frequency. For the initial development work, a universal frequency counter (Agilent 53132A) interfaced to a computer was used to measure the frequency every half a second. The instrument is intended as a screening device rather than an analytical device so it is only required to test against a threshold frequency change.

The porcine semen was supplied by a commercial artificial insemination centre (JSR Genetics, Driffield, UK). Commercial suppliers usually provide the semen in buffer and include other chemicals to prolong semen life. This allows the semen to be stored unopened for up to 5 days below 17°C without extensive deterioration in semen motility. To attain a sample of immotile sperm for comparison, we stored an unopened sample for 21 days prior to use. In our previous reports [4, 7], we investigated coatings of cysteamine and Poly-L-Lysine on the quartz crystal that would act as an adhesive layer for the sperm. In this work, we found that a clean gold electrode on a polished quartz crystal was as efficient and more reliable than the chemical modifications previously tested; this could then be cleaned for repeated usage using a Papain solution (Sigma Aldrich P3375-25G) or physical agitation with a cotton bud and adequate rinsing with PBS solution.

The design of a low-cost high-stability quartz oscillator for operation in liquids is challenging and has recently been reviewed by Arnau [8]. In this work, we have produced a simple circuit based on the Pierce oscillator using a MAN-1LN amplifier (Mini-Circuits). The MAN-1LN is a low-noise amplifier operating from 0.5 MHz to 500 MHz with a gain of around 28 dB operating from a nominal 12 V

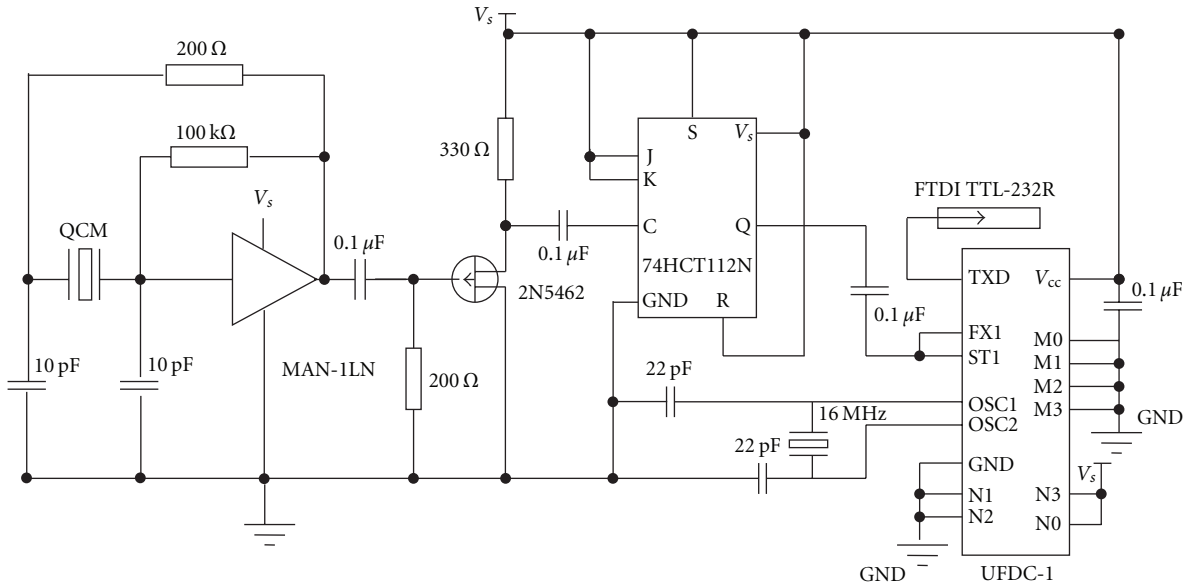

Figure 2: Schematic diagram of the oscillator and frequency counter electronics.

supply. This oscillator offers good long-term stability giving a frequency drift of around 2 Hz in an hour in the air. In PBS, the two-sample Allan variance for the oscillator has been calculated to be 3×10^{-7} which is comparable to the results reported for a 2 MHz oscillator in water by Rodriguez-Pardo et al. [9] although our value is greater than they report for a 9 MHz QCM. A UFDC-1 universal frequency to digital converter [10] was used as a low-cost replacement for the Agilent frequency counter. The UFDC-1 is a 28 pin single-chip programmable two-channel frequency-to-digital converter, operating over the frequency range 0.05 Hz to 7.5 MHz; this range can be extended to 120 MHz with prescaling although this results in an accuracy reduction. The conversion accuracy is programmable from 1% to 0.001% and is determined by selecting which of the four pins on the UFDC-1 labelled N0–N3 are connected to either the supply voltage or ground: the mode of operation is selected in a similar way using pins M0–M3. Data is returned as a string of ASCII characters (note that the number of decimal places shown by this string is not the same as the actual accuracy of the conversion) from the serial output pin (TXD). The serial output is ideal for use with a USB to TTL serial cable (FTDI TTL-232R-3V3). The UFDC-1 operates from a single power supply of between +4.5 V and +5.5 V which is taken from the USB port. The FTDI drivers enable the USB to be accessed as a standard COM port. A program was written in the free programming language Just Basic (http://www.justbasic.com/) to read the data from the COM port, extract the string for a single value, convert to a number, and store it to a spreadsheet file. Given the maximum frequency of the UFDC-1 without prescaling is 7.5 MHz, operation of the QCM in the "swim cell" at 10 MHz was above this frequency, and requires a divide by two pre-scalar. The thickness of the crystal reduces with increasing frequency and whilst the 10 MHz are sufficiently robust, 15 MHz crystals proved to be too fragile for practical operation in this application. In addition to the oscillator, the circuit diagram in Figure 2 shows the frequency counter and buffer circuit. The sinusoidal output of the oscillator has a peak-to-peak amplitude around 7 V which is fed into an FET operated in switch mode between 0 V and +5 V from the USB. The digital signal is then fed into a divide by two circuit consisting of a single flip flop on a 74HCT112N and then into the F1 input of the UFDC-1 operating in mode zero (single-channel frequency measurement); for improved stability, the analogue part of the circuit (oscillator) was operated from a dc battery supply and LM3171 voltage regulator and the digital part of the circuit supplied from the +5 V of the USB. Figure 3(a) shows a photograph of the swim cell with the box below including the oscillator circuit, and Figure 3(b) shows a photograph of the circuit board for the UFDC-1 frequency counter circuit.

3. Results and Discussion

Whilst initial stability tests in the air were good, when the cell contained only PBS, it exhibited periodic oscillations in the frequency of several hundred Hz. In the experiments with water, the change in depth required to move through one pressure wave resonance cycle is only about 70 μm [11], and in an open cell of the type we are using, this can occur by evaporation of the PBS in a relatively short time. As a result of this, we used a simple flat sheet of pressure sensitive adhesive (Blu-tac, Bostik) inserted into the PBS above the QCM at an angle of 45 degrees, and this reduced the frequency drift on the bench top in an open lab to around 10 Hz in 40 minutes.

Semen samples were introduced using a pipette and vigorous use could result in the sample attaining sufficient momentum so as not to reflect the actual motility of the sperm. Initial tests with the aged semen did show a significant

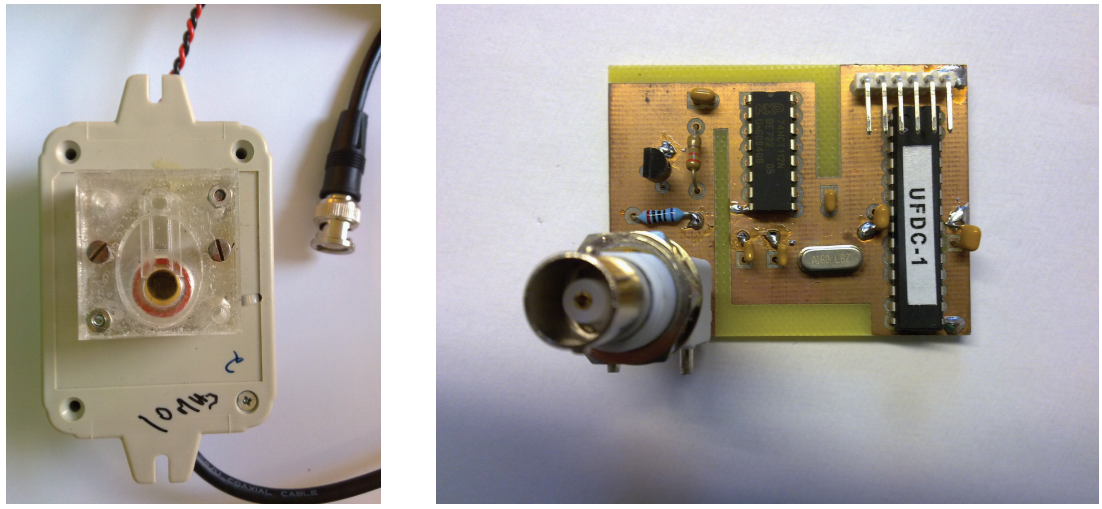

(a) (b)

Figure 3: (a) Image of quartz crystal in acrylic cell with the oscillator circuit in the box under the cell. (b) Image of UFDC-1 circuit.

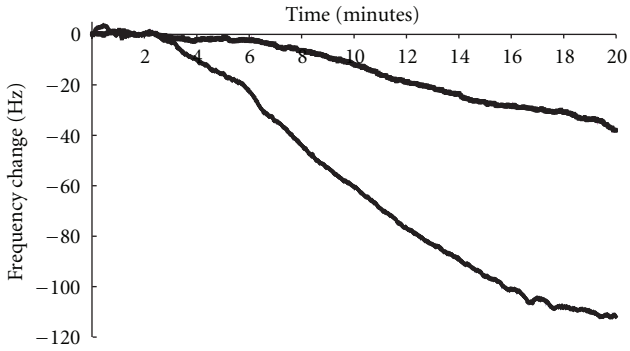

Figure 4: Frequency change as a function of time for twenty one day-old sample (upper line) and two-day-old sample (lower line).

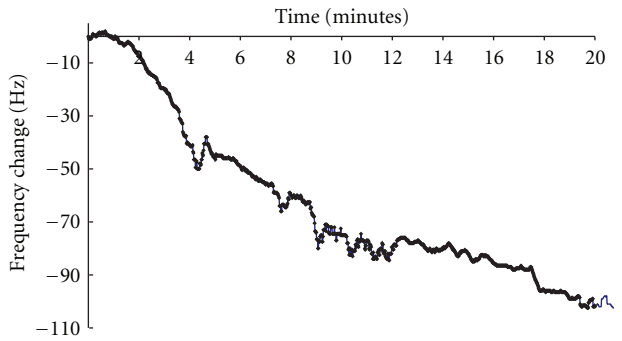

Figure 5: Frequency change as a function of time for the UFDC-1 from introduction 50 μL of four-day-old semen sample.

effect which could be comparable in frequency shift to "live" semen that was several days old. A simple tilting of the whole swim cell by ten degrees reduced the effect of this to a manageable level by effectively providing a small well. Figure 4 shows the data using the Agilent frequency counter for 10 μL of 2-day-old semen sample and a 21-day-old semen sample of the same volume. Although a change of 35 Hz is observed over twenty minutes, this is sufficiently low to discriminate a viable from nonviable semen sample for a simple screening application and probably represents simple diffusion. Remembering that screening just requires a simple "yes" or "no" if the sample is viable or not, after a given measurement time of say 10 minutes, the "yes" answer would be given if the frequency change had exceeded 50 Hz; otherwise, the "no" would be given. Most of the semen in the older sample was still visibly collected in the well whilst for the 2-day-old sample significant observed at the QCM. Sufficient data is collected to allow checks that the system is working correctly as, a frequency change of greater than say 1 kHz would represent a fault having occurred and render the current measurement invalid. In Figure 5, we show the frequency change as a function of time for the UFDC-1 from introduction of 50 μL of four-day-old semen. A moving average has been applied to the UFDC data which has a frequency resolution of 5 Hz; data was collected from the UFDC-1 every second. Whilst a slightly lower overall frequency change is observed than shown by the Agilent frequency counter in Figure 4, this is consistent with the aging of the semen sample.

4. Conclusions

The reusable sensor system we have reported here is designed for simple screening for sufficiently motile sperm in a sample; that is, that a threshold frequency change has been exceeded. As commercial semen samples are significantly diluted with an extender to maintain the quality during transport, this threshold will depend on the particular application. The oscillator circuit presented is simple, inexpensive, and sufficiently stable for such an application. The frequency counter comprised of the UFDC-1 and TTL-USB cable,

forms a complete low-cost and light-weight system such that the components of the circuit shown in Figure 3(b) with the cable is under US$50; this may provide a suitable platform for other QCM-based applications. An improved "swim cell" design will incorporate the angle and the baffle to prevent resonance conditions being encountered. This system should allow for a great improvement in the reliability and ease of use of onsite field measurements of sperm motility.

Acknowledgments

This work has been supported by the UK Engineering and Physical Sciences Research Council (EPSRC) under Grant no. EP/E063489/1 and Higher Education Innovation and Regional Fellowship (HIRF409).

References

[1] World Health Organization, *WHO Laboratory Manual for the Examination of Human Semen and Sperm-Cervical Mucus Interaction*, Cambridge University Press, Cambridge, UK, 3rd edition, 1999.

[2] S. T. Mortimer, "CASA—practical aspects," *Journal of Andrology*, vol. 21, no. 4, pp. 515–524, 2000.

[3] P. Christensen, D. Boelling, K. M. Pedersen, I. R. Korsgaard, and J. Jensen, "Relationship between sperm viability as determined by flow cytometry and nonreturn rate of dairy bulls," *Journal of Andrology*, vol. 26, no. 1, pp. 98–106, 2005.

[4] M. I. Newton, C. R. Evans, J. J. Simons, and D. C. Hughes, "Semen quality detection using time of flight and acoustic wave sensors," *Applied Physics Letters*, vol. 90, no. 15, Article ID 154103, 2007.

[5] K. K. Kanazawa and J. G. Gordon, "The oscillation frequency of a quartz resonator in contact with liquid," *Analytica Chimica Acta*, vol. 175, no. C, pp. 99–105, 1985.

[6] G. Sauerbrey, "The use of quartz oscillators for weighing thin layers and for microweighing," *Zeitschrift Fur Physik*, vol. 155, pp. 206–222, 1959.

[7] S. Atherton, C. R. Evans, P. Roach, D. C. Hughes, G. McHale, and M. I. Newton, "Investigation of operating parameters for a semen quality analysis system," in *Proceedings of the 2nd International Conference on Biomedical Electronics and Devices (BIODEVICES '09)*, pp. 13–16, January 2009.

[8] A. Arnau, "A review of interface electronic systems for AT-cut quartz crystal microbalance applications in liquids," *Sensors*, vol. 8, no. 1, pp. 370–411, 2008.

[9] L. Rodriguez-Pardo, J. Fariña, C. Gabrielli, H. Perrot, and R. Brendel, "Resolution in quartz crystal oscillator circuits for high sensitivity microbalance sensors in damping media," *Sensors and Actuators B*, vol. 103, no. 1-2, pp. 318–324, 2004.

[10] S. Y. Yurish, "Digital sensors design based on universal frequency sensors interfacing IC," *Sensors and Actuators A*, vol. 132, no. 1, pp. 265–270, 2006.

[11] S. M. Reddy, J. P. Jones, and T. J. Lewis, "Use of combined shear and pressure acoustic waves to study interfacial and bulk viscoelastic effects in aqueous polymeric gels and the influence of electrode potentials," *Faraday Discussions*, vol. 107, pp. 177–196, 1997.

N. J. Shirtcliffe, G. McHale, S. Atherton, M. I. Newton, An Introduction to Superhydrophobicity,

Advances in Colloid and Interface Science, 2010, 161, pp. 124

Advances in Colloid and Interface Science 161 (2010) 124–138

Contents lists available at ScienceDirect

Advances in Colloid and Interface Science

journal homepage: www.elsevier.com/locate/cis

An introduction to superhydrophobicity

Neil J. Shirtcliffe *, Glen McHale, Shaun Atherton, Michael I. Newton

School of Science and Technology, Nottingham Trent University, Clifton Lane, Nottingham NG11 8NS, UK

ARTICLE INFO

Available online 10 November 2009

Keywords:
Superhydrophobic
Rough
Lotus effect
Ultrahydrophobic
Textured

ABSTRACT

This paper is derived from a training session prepared for COST P21. It is intended as an introduction to superhydrophobicity to scientists who may not work in this area of physics or to students. Superhydrophobicity is an effect where roughness and hydrophobicity combine to generate unusually hydrophobic surfaces, causing water to bounce and roll off as if it were mercury and is used by plants and animals to repel water, stay clean and sometimes even to breathe underwater. The effect is also known as The Lotus Effect® and Ultrahydrophobicity. In this paper we introduce many of the theories used, some of the methods used to generate surfaces and then describe some of the implications of the effect.

Contents

* Corresponding author.
E-mail address: neil.shirtcliffe@ntu.ac.uk (N.J. Shirtcliffe).

0001-8686/$ – see front matter © 2009 Elsevier B.V. All rights reserved.
doi:10.1016/j.cis.2009.11.001

1. Basics of superhydrophobicity

1.1. Interfacial tensions between solids, liquids and gases

To understand superhydrophobicity we begin by considering the surface of a liquid. At the surface, molecules of a liquid have fewer neighbours than those in the bulk. The resulting difference in interaction energy manifests itself as surface tension, γ_{LV}; a force that acts to reduce the surface area of a free liquid. Traditionally, surface tension can be regarded as a force per unit length and is given in units of N m^{-1} or as energy per unit area J m^{-2} [1]. When a volume of liquid can freely adjust its shape, it does so to minimize its surface free energy and since the shape with the smallest surface area is a sphere, a droplet of a liquid tends towards this shape. However, most water droplets we see in nature do not exist as spherical shapes. Larger droplets and droplets that touch surfaces are distorted by gravity and by the interaction between the water and the solid.

By considering dimensional arguments for the force due to surface tension and that from gravity, we can see that surface tension can become dominant at small sizes. Surface tension forces scale as a function of length, R, whereas gravitational forces scale with the mass of the drop, which depends upon a length cubed, R^3, and the density of the liquid, ρ. The ratio of gravitational to surface tension forces for a droplet scales as $\rho g R^3/\gamma_{LV} R \sim R^2$ (where $g = 9.81$ m s^{-2} is the acceleration due to gravity), and so is large when the length scale is large, but vanishes as the length scale becomes small. This means that the dominant force crosses over from being gravity to surface tension as the characteristic size in a system reduces. If we plot these two lines for water on Earth as in Fig. 1 they cross at a size of 2.73 mm, which is called the capillary length for water, $\kappa^{-1} = (\gamma_{LV}/\rho g)^{1/2}$. For drops much smaller than this, as a simple rule an order of magnitude smaller (i.e. <0.273 mm), surface tension dominates. The cross-over from gravity to surface tension dominated behaviour can be seen in a simple paper-clip experiment. A large metal paper-clip lowered carefully onto the surface of water breaks the "skin" and sinks, whereas a small paper-clip remains resting on the surface of the water[1]; it does not truly float, but appears to do due to the "skin effect" of water caused by surface tension. In the natural world, insects are of a size that surface tension is the dominant force. It is, therefore, hardly surprising that, in a world full of ponds and streams, many insects (and spiders) have natural morphological adaptations that enable them to either break through the surface of water or to rest and move on its surface [2,3]. Some insects walk and skate on water and others can carry a film of air underwater that acts as an artificial gill (known as a "plastron").

1.1.1. Interactions with surfaces

Surface tension, γ_{LV}; relates to the existence of an interface between a liquid and a vapour and is only one example of an interfacial tension. When a droplet of water rests on a solid, two further interfaces, the solid–liquid and solid–vapour, become relevant and also provide interfacial tensions γ_{SL} and γ_{SV}. The balance between these three interfacial forces determines whether a droplet resting on a solid will eventually be pulled out into a film or whether it will remain as a droplet and, if so, the extent of its footprint on the solid surface. On a smooth and flat surface the interaction energy per unit area for a dry surface is γ_{SV}, but for the same surface coated in a thin layer of a liquid there are two interfaces with a combined interaction energy per unit area of $\gamma_{SL} + \gamma_{SV}$. The condition for film formation on a smooth and flat surface is therefore that the energy is lowered [4,5], i.e.

$$S = \gamma_{SL} + \gamma_{LV} - \gamma_{SV} > 0 \quad (1)$$

where S has been defined as the spreading power. When the surface is complex in shape, such as at a join between fibres, droplets will be drawn into non-spherical shapes as they try to minimize their total surface free energy by varying the relative areas of the three interfaces, whilst maintaining their volume [6]. The size of droplet will determine to what extent gravitational energy is also a controlling factor. For example, a small droplet of water resting on a horizontal surface will adopt a shape close to a spherical cap, whereas a larger droplet will be flattened into a puddle by gravity.

When a film is not formed and a droplet remains on a surface in a partial wetting state, there is an equilibrium contact angle, θ_e, at the edge of the droplet. This is the tangent angle of the liquid–vapour interface at the three-phase (solid–liquid–vapour) contact line (Fig. 3). The contact angle is independent of droplet size and is described by the Young equation [1],

$$\cos\theta_e = \frac{(\gamma_{SV} - \gamma_{SL})}{\gamma_{LV}} \quad (2)$$

This concept of a single equilibrium contact angle is an idealized view and does not take into account contact angle hysteresis and how the droplet arrived at its resting state through advancing or receding on the surface. For smooth and flat surfaces and water the lowest possible contact angle is 0° (although this can correspond with many values of S) and the highest possible angle is probably less than 120° and is found on fluoropolymers, such as PTFE (Teflon®).

1.1.2. Superhydrophobicity of leaves

The leaves of the sacred Lotus are unusual in that water rolls off them in balls with contact angles much greater than that on flat PTFE. As droplets roll away they gather and transport dust and leave the surface of the leaves clean; this has become known as the Lotus effect® [7,8]. Highly mobile droplets of water on leaves with a contact angle in excess of 150° appear to be quite common in the plant world, example crop plants including the cabbage family (*brassica*), garden peas (*Pisum sativum*) and Taro (*Colocasia esculenta*) and ornamentals including Hosta (*Hosta*), Lady's Mantle (*Alchemellia*) and Lupin (*Lupinus*) (Fig. 2).

The leaves achieve this effect by creating a surface that is both rough and hydrophobic. The roughness enhances the effect of the surface chemistry to produce the superhydrophobicity. Because the waxes plants use to create superhydrophobicity are quite oleophilic, the contact angle to oils is quite low. In this case the roughened waxes increase the interaction of the oil with the surface and cause the leaves to be self poisoning, i.e. oils spread on them better (wider in extent and faster) than they do on equivalent flat surfaces.

1.2. Hydrophobicity, hydrophilicity and superhydrophobicity

A completely hydrophilic (or wetting) surface is one on which a film forms so that Eq. (1) is valid and for $S = 0$, Eq. (2) shows the threshold for this corresponds to $\theta_e = 0°$. A completely hydrophobic surface would be one for which it was energetically unfavourable for a

[1] For a video of the paper-clip experiment see: http://www.naturesraincoats.com/Introduction.html.

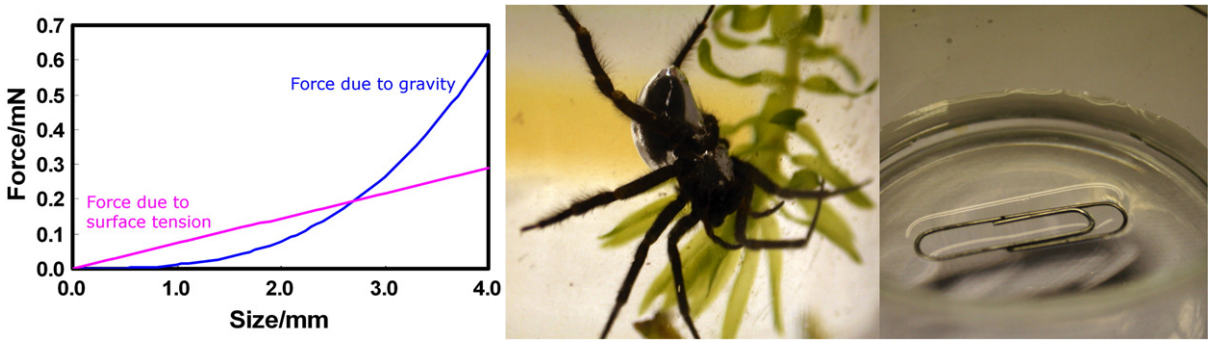

Fig. 1. Effects of surface tension. Surface tension plotted against gravity for water on Earth: a water spider *Argyroneta aquatica* with an air film on it and a paper-clip suspended on water.

Fig. 2. Nasturtium, Ladies mantle and Lupin leaves with water droplets on them.

droplet to have any contact whatsoever and this corresponds to $\theta_e = 180°$. All droplets that have finite contact angles between these two values are therefore partially wetting. The change in sign of Eq. (2) can be used to separate the intrinsic behaviour of a surface for a given liquid. If $\gamma_{SV} < \gamma_{SL}$, the contact angle will be less than 90° and the surface is conventionally described as hydrophilic, whereas, if $\gamma_{SV} > \gamma_{SL}$, the contact angle will be greater than 90° and the surface is conventionally described as hydrophobic. It could be argued, however, that if a droplet attaches to a surface there is a level of absolute hydrophilicity and larger contact angles, including those above 90°, simply indicate relatively less hydrophilicity of the surface [104,105]. As there is always an attraction between a solid and a liquid, due to van der Waals interactions, all surfaces would be hydrophilic under this interpretation. The opposite terminology, where all surfaces with non-zero contact angles with water are considered hydrophobic has also been used and signifies $\gamma_{LV} = \gamma_{SV} - \gamma_{SL}$ from Eq. (2) which means it is the threshold above which it is energetically unfavourable to make the surface completely wet (i.e. replace the vapour interface by a liquid one). The $\gamma_{SV} = \gamma_{SL}$ threshold (contact angle 90°) remains useful as it is the threshold where capillaries with uniform cross-section along their lengths fill, is significant for slightly rough surfaces as will be shown shortly and some important properties depend upon the cosine of the contact angle, which also changes sign at 90°. At this point, as $\gamma_{SV} = \gamma_{SL}$, there is no change in energy on wetting the surface (it is the threshold where putting a solid into a liquid without changing the liquid air interface goes from releasing energy to costing energy) so the liquid forms a shape to minimize the liquid vapour area, i.e. a half sphere.

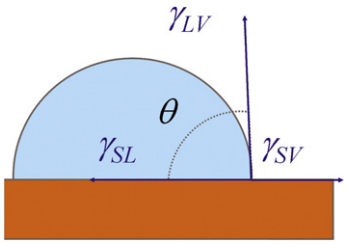

Fig. 3. Diagram showing the forces at the three-phase contact line of a liquid droplet on a solid.

Surfaces with hydrophobic tendencies can be enhanced to super-hydrophobicity by the addition of roughness or, more accurately, a certain type of topography. This can be viewed as a physical amplification of the chemistry of the surface [9]. It can increase the contact angle well beyond that possible by chemistry alone and can approach 180° in some cases. It can also decrease the contact angle towards 0° more than might be expected from the chemistry alone. The amplification effects of surface topography can be understood in the same manner as in deriving the Young equation.

1.3. Young's equation, force balance and surface free energy arguments

One way of looking at the Young equation is that it represents a force balance at the contact line between the three interfaces (solid—liquid—vapour). In a two-dimensional model the horizontal components of the interfacial forces have magnitudes γ_{SV}, γ_{SL} and $\gamma_{LV}\cos\theta$, where θ is the instantaneous (dynamic) contact angle. The balance of interfacial forces at the contact line is $\gamma_{SV} - \gamma_{SL} - \gamma_{LV}\cos\theta$. At equilibrium, the contact line is static and this force must vanish so that,

$$\gamma_{SL} + \gamma_{LV}\cos\theta_e = \gamma_{SV} \tag{3}$$

and this leads directly to Young's equation, (Eq. (2)).

This approach works well with a flat surface, but is less easy to understand when considering a rough surface which has sharp spikes on which resolving forces and angles is less obvious. In the 2D model in Fig. 3 the contact line advancing and receding over the surface would take on different local contact angles as it advanced around the curves of the roughness and the surface could have points at which a slope is multi-valued [10,11].

An alternative approach that inherently involves averaging over a small area is to consider surface free energy changes for perturbations of the contact line (Fig. 4). As the contact line advances along the surface by

a small distance, ΔA, it replaces the solid–vapour interface by a solid–liquid one, thus causing a change in surface free energy of $(\gamma_{SL}-\gamma_{SV})\Delta A$. However, the liquid–vapour interface also gains in length by an amount $\gamma_{LV}\cos\theta$, where we have assumed that any change in the contact angle is a second order effect. The total change in surface free energy, ΔF, accompanying an advance of the contact line is therefore,

$$\Delta F = (\gamma_{SL}-\gamma_{SV})\Delta A + \gamma_{LV}\cos\theta\Delta A \quad (4)$$

Since local equilibrium corresponds to the minimum of surface free energy with a zero gradient, the change in free energy for a small movement of the contact line will necessarily be zero. Thus, we can set ΔF to zero and on rearranging the equation we recover the original Young's equation.

The surface free energy argument is a simple one that relies on a contact line being able to freely explore changes in the energy landscape by making infinitesimal advances and retreats from its existing position. It therefore assumes vanishing contact angle hysteresis and it only guarantees a local equilibrium based upon the surface properties of the area in the vicinity of the local contact line; areas deep within the droplet contact area or well outside of it are irrelevant [12,13]. As presented, the argument describes a 2-dimensional model rather than the 3-dimensional world. However, provided axial symmetry is maintained the argument can be applied to any radial segment. If extended to 3 dimensions a surface free energy argument can also be applied to local contact line changes of drops of complex shapes on complex surfaces.

1.3.1. Rough surfaces and surface free energy arguments

There are two extreme cases that can occur at a rough, hydrophobic surface when a water droplet is applied. One possibility is that the droplet could maintain contact with the entirety of the rough surface (the Wenzel case), thus increasing the interfacial contact area (Fig. 5) [14,15]. Alternatively, the droplet could skip between the peaks of the roughness (the Cassie case), thus leaving a patchwork of solid–liquid and liquid–vapour interfaces below it [16–18].

The surface energy argument can be used again in both cases. In the Wenzel case, the surface areas of both the solid–liquid and the solid–vapour interfaces associated with the advance of the contact line are increased by a factor r, the specific surface area of the rough surface at the contact line (how many times more surface there is than if it were flat). This leads to a surface free energy change,

$$\Delta F = (\gamma_{SL}-\gamma_{SV})r\Delta A + \gamma_{LV}\cos\theta\Delta A \quad (5)$$

which for local equilibrium, $\Delta F = 0$, gives,

$$\cos\theta_W = \frac{r(\gamma_{SV}-\gamma_{SL})}{\gamma_{LV}} \quad (6)$$

This can be substituted with Young's equation, Eq. (2), to give,

$$\cos\theta_W = r\cos\theta_e \quad (7)$$

This is known as the Wenzel equation, as it was first formulated by Wenzel [14]. In Wenzel's equation, the roughness factor, r, acts as an amplification of the effect of the surface chemistry determined term, $\cos\theta_e$; small changes in θ_e become larger changes in θ_W, provided complete contact is retained between the liquid and the solid. The importance of $\theta_e = 90°$ is the changeover in sign of the cosine term. When $\theta_e < 90°$, the effect of increasing roughness r is to further reduce the Wenzel contact angle towards 0°, but when $\theta_e > 90°$, the effect of increasing roughness is to further increase the Wenzel contact angle towards 180°. Thus, Wenzel roughness emphasizes the intrinsic tendency of a surface towards either complete wetting or complete non-wetting [9].

An alternative possibility is that as roughness increases, the liquid no longer retains complete contact with the solid at all points below the droplet. In this other extreme, the liquid bridges between surface features and no longer penetrates between the spaces separating them; a simplified example using flat-topped surface features is shown in Fig. 6. In this simple example we are assuming that the liquid only contacts the flat parts of the surface and that the meniscus below the drop is flat, implying that the gaps between the features are much smaller than the curvature of the meniscus due to the liquid's weight and the pressure exerted by the top meniscus.

As the contact line advances by ΔA, only a fraction $f_s\Delta A$ of the solid is contacted by the liquid and the remainder $(1-f_s)\ \Delta A$ is then the area bridged between surface features; this remainder involves the creation of a liquid–vapour interface. The surface free energy change is then,

$$\Delta F = (\gamma_{SL}-\gamma_{SV})f_s\Delta A + (1-f_s)\Delta A\gamma_{LV} + \gamma_{LV}\cos\theta\Delta A \quad (8)$$

At equilibrium this can be simplified to,

$$\cos\theta_{CB} = \frac{f_s(\gamma_{SV}-\gamma_{SL})}{\gamma_{LV}} - (1-f_s) \quad (9)$$

or, using Eq. (2),

$$\cos\theta_{CB} = f_s\cos\theta_e - (1-f_s) \quad (10)$$

Eq. (10) is known as the Cassie–Baxter formula, or Cassie and Baxter's formula [16]. In contrast to the Wenzel case, small changes in θ_e became smaller changes in θ_{CB} although the absolute value of θ_{CB} is larger than θ_e. Whilst the surface is topographically structured, and one may even say it is rough, the roughness factor, r, does not directly enter into the Cassie–Baxter formula. Indirectly roughness does matter because the balance between roughness and solid surface fraction determines the threshold Young's equation contact angle at which the Cassie–Baxter state becomes the more energetically stable

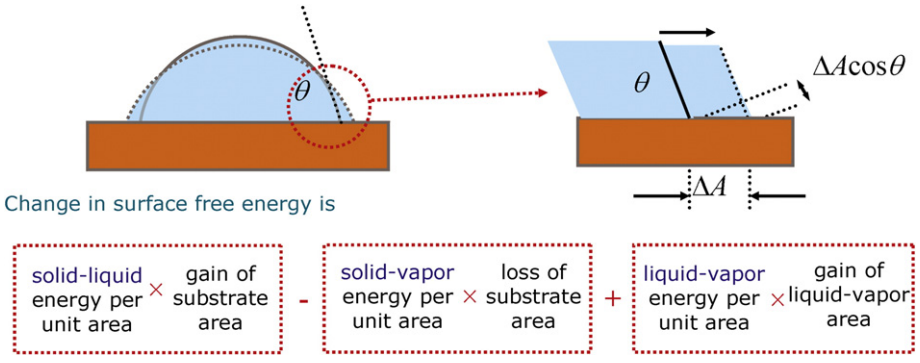

Fig. 4. Contact angle and surface free energy.

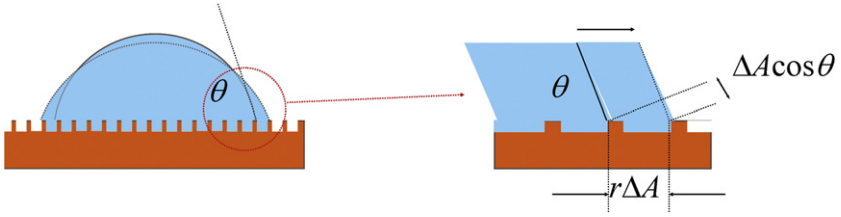

Fig. 5. Contact angle on rough surface using Wenzel equation.

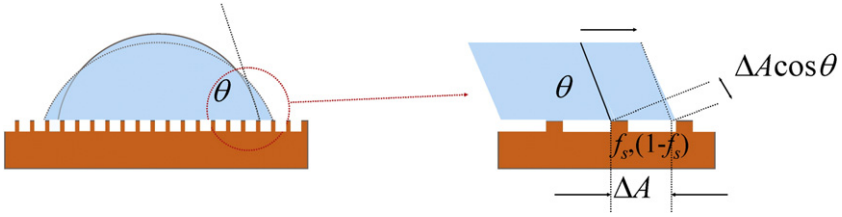

Fig. 6. Contact angle on rough surface using Cassie–Baxter formula.

compared to the Wenzel state; a point examined in detail by Bico et al. [19].

The Cassie–Baxter equation (Eq. (10)) can also be viewed as a weighted mean (by interfacial fraction at the contact line) of the Young's equation contact angle and a contact angle against the vapour (180° and so cos 180° = −1). This way of thinking also reveals that if the pores in the surface are prefilled with the liquid the contact angle there will be 0° and the central negative sign will change to positive, indicating a reduction in observed contact angle [20]. This alternative case is not superhydrophobicity, but can occur on otherwise superhydrophobic surfaces with the right (or wrong) preparation.

1.4. How the suspended state stays suspended

The Cassie and Baxter state with the liquid only wetting the tops of the surface structure can seem strange and this often leads to the use of the terminology "air trapping"; a misleading terminology because the lack of liquid penetration is not a consequence of an inability of air to escape. A useful analogy is that of a bed of nails (a *Fakir's carpet* [21]), where if someone sat on a single upturned nail they would receive a puncture wound, but if they lie carefully across many nails close together their weight is spread across a reasonable area and the local pressure at any one nail is not sufficient to cause injury.[2] In no way is the air beneath trapped and it does not help support the person at all. Indeed in Fig. 7 we can see that small objects (apples) thrown against a bed of nails are impaled, but that a larger object (a person) is not, even when they are also supporting the weight of a second person. Whilst this is only an analogy, the idea of skin effect due to surface tension and the existence of a natural length scale for objects to be able to bridge asperities are useful in considering superhydrophobic surfaces. Whether a liquid penetrates or not is determined by the cost in surface free energy for wetting down the surface structure [22–24].

1.5. Important considerations when using Wenzel and Cassie–Baxter equations

As with all equations it is important to remember how these equations were derived when using them.

Using Young's equation introduces the assumption that we are investigating equilibrium contact angles. This is important, because in practice the Young angle relates to an idealized concept of a contact angle that is not always observable, particularly on roughened or heterogeneous surfaces because the contact line can become locally pinned on sharp points or local heterogeneities.

Whilst the spacing of features below the entirety of the droplet determines whether penetration into the surface structure occurs, it is the spacing and feature shape at the contact line that determines the observed contact angle. Moreover, the predicted Cassie–Baxter (or Wenzel) contact angle assumes a change in ΔA that samples the contact line over a length that is completely characteristic of the surface. For a completely random surface structure, this may be reasonable on average around the entirety of the contact line. However, when the surface has a characteristic symmetry in its surface features or their arrangement on the surface this assumption becomes less certain. One suggested criteria is that if axial symmetry is observed, then these equations will be reasonable approximations [13]. This would not be the case if the surface structure had strong symmetry, such as in the form of parallel grooves. In this situation, the contact angle would be different parallel and perpendicular to the grooves and the droplet would become distorted from an axially symmetric shape. Similarly, if the scale of the roughness is too great the contact line will become locally distorted and an average contact angle will be difficult to measure.

The use of small changes in the contact line to calculate the local equilibrium state has significant implications. In particular, it means that parts of the surface inside or outside a small region close to the contact line do not affect the local equilibrium state. It also means that large scale variations in the surface, including roughness, can only be considered locally. As an example, if the surface consists of two concentric regions concentrically with the outer area having a lower Young's equation contact angle and a droplet of suitable volume is placed centred in the middle, there will be two stable contact angles dependent upon the wetted area at the initial deposition. The first is one with the droplet fully on the inner region with the contact angle of the inner region. The second is with the droplet fully on the outer region, but with the lower contact angle. This can be seen in Fig. 8. In this situation, it would be incorrect to use the Cassie–Baxter equation because for either state, small changes of the contact line of the droplet only sample one type of surface.

Similarly, if the regions are made thinner and packed in a concentric series it is still not possible to use an average of the two surface as the contact line will always be wholly on one surface or the other provided the droplet remains centred on the structure. In the limit the drop will always be on a hydrophilic region but projecting over a hydrophobic region, allowing it to assume any angle between

[2] For a video of a person on a bed of nails see: http://www.naturesraincoats.com/Introduction.html.

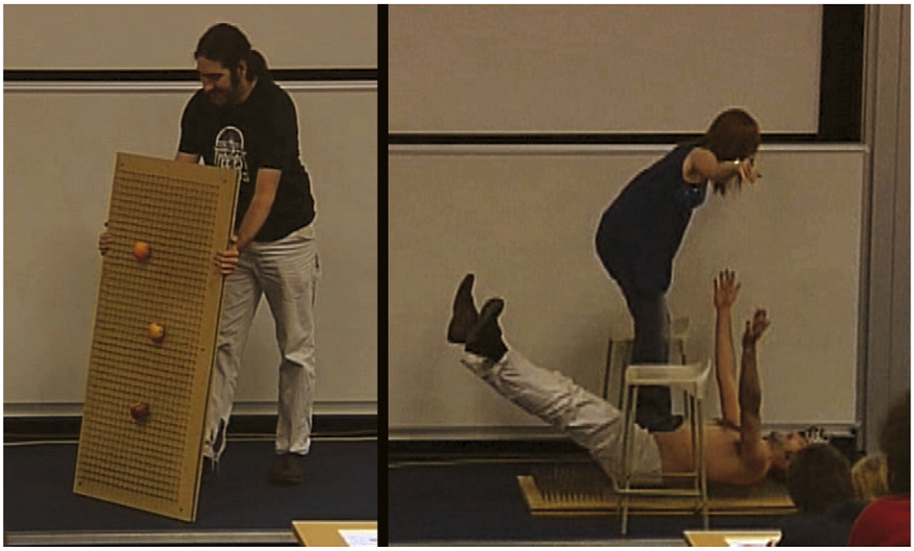

Fig. 7. Dr. James Hind and Laurice Fretwell (NTU) demonstrating a bed of nails, with thanks to them for allowing use of these pictures.

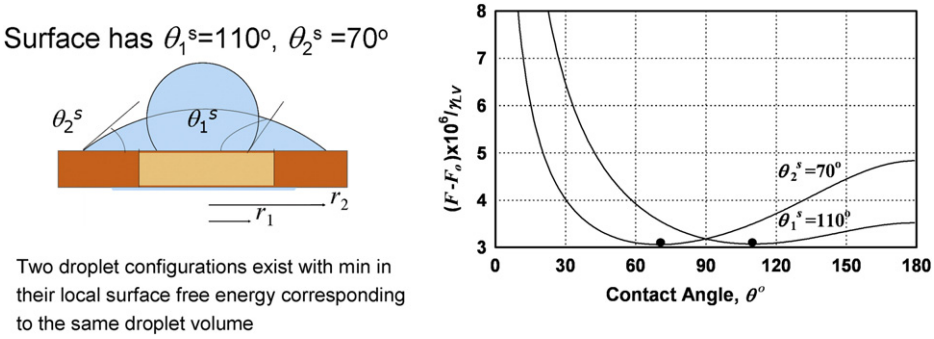

Fig. 8. Multiple stable contact angles for concentric surfaces, reproduced with permission from McHale [13]. Copyright American Chemical Society 2007.

the values of the hydrophobic and the hydrophilic regions. The consideration of surface free energy change that was used to calculate both Wenzel's and Cassie and Baxter's equations requires that an average of the pattern is sampled by the (approximately circular) contact line. Implicit in this is the requirement of a randomly mixed surface with a small feature size or of changes by the liquid on the surface that average out preferred directions due to any symmetry in the surface pattern (Fig. 9).

If the surface pattern beneath the contact line varies with location it is not possible to use global averages of roughness or solid surface fraction in Eqs. (7) and (10) although values local to the contact line may be used. In terms of wetting, the roughness and solid surface fraction properties are not one's of the surface itself, but of the surface sampled locally by the contact line of the liquid. This variation in pattern with position can be used to produce a pattern of surface wettability with variation of the local contact angle from one side of a droplet to the other and so create a driving force to direct the motion of a droplet [9,25–27]. Whether motion occurs depends on droplet size and the contact angle hysteresis. This situation is shown in Fig. 10.

This can be realised in various ways, a fractal copper surface was used in one of our studies [25], causing water to move in a chosen direction.

1.6. More complex topography

Often the structure of a naturally occurring surface is more complex than the models of simple flat-topped surface protrusions. In these cases, it is often difficult to measure the roughness factor r and/or the solid surface fraction f_s, that a droplet experiences. It is also possible that neither a pure Wenzel nor a pure Cassie state will occur. Some of the roughness can be wetted and some can be bridged and the balance between these two can change with the type of liquid.

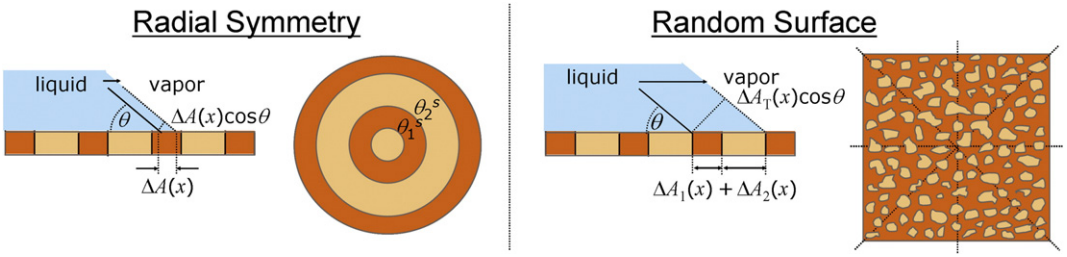

Fig. 9. Concentric surface and random surface, only the random surface will follow Cassie and Baxter's equation. Reproduced with permission from McHale [13]. Copyright American Chemical Society 2007.

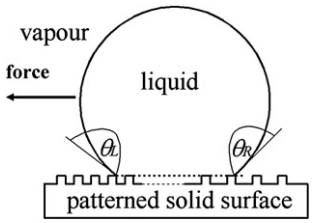

Fig. 10. A patterned surface with changing pattern, giving rise to a lateral force on a drop placed on it. Reproduced with permission from McHale et al. [25].

One approach to dealing with this is to consider each level of roughness as consecutive transformations of the droplet-surface system. For example, for pillars possessing rough tops there are several possibilities, two of which are shown in Fig. 11. In the first case, the small scale structure at the top of pillars is in a Wenzel state, but the large scale structure is in a Cassie state. Mathematically, the Young's equation contact angle, θ_e, for the surface is first transformed using the Wenzel equation and the roughness factor for the small scale structure, r_{small}, to get a Wenzel contact angle, $\theta_W(r_{small}, \theta_e)$. Subsequently, this Wenzel contact angle is transformed using the Cassie–Baxter equation with a solid-surface fraction for the larger scale structure, f_s^{large}, to obtain the final contact angle (i.e. $\theta_{CB}(f_s^{large}\theta_W(r_{small}, \theta_e))$ [28]. In the second case in Fig. 11, the Cassie–Baxter equation is used twice, first with the solid fraction for the small scale structure and then with the solid fraction for the large scale structure. This type of approach can be extended to other combinations of surface types.

A classic example of a combined Wenzel and Cassie–Baxter surface is a set of parallel fibres. In this case, a liquid will wet down the sides of the fibre until its local contact angle on the fibre is the same as Young's equation. Whilst the approach used in Fig. 11 remains valid, the difference is that both the roughness factor, r, and solid surface fraction. f_s, themselves become dependent on the type of liquid (through θ_e). In principle a curved structure, such as a fibre or a "ball-on-a-stick" can suspend a liquid even when its Young's equation contact angle is substantially less than 90°, even down to 0° (Fig. 12) [29–31]. This is particularly important in constructing oil repellent surfaces, where surfaces with intrinsic contact angles greater 90° may not exist; the importance of an inward curve to create a re-entrant surface has been emphasized by Tuteja *et al.* [31,32]. In these cases involving curvature, both the roughness factor r and the solid surface fraction f_s are dependent upon the contact angle, θ_e, as well as the pattern shape as the liquid wets different sections of the curvature depending on the local contact angle (Fig. 12). This has consequences for the extent to which droplets on these surfaces can freely move (i.e. "sticky" versus "slippy" surfaces) since although a bridging state is produced it also involves more extensive contact between the liquid and solid at those points where contact is maintained.

Complex topography is often more effective at generating high contact angles and low hysteresis than simpler surfaces. It has been shown that multiple overlaid scales of roughness are more effective than the sum of the parts, increasing how easy it is to generate a bridging state, how easy it is to maintain and its effectiveness. This has been shown theoretically [32] and experimentally [33,34], an example is shown in Fig. 13.

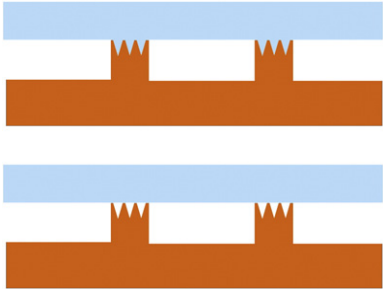

Fig. 11. Multiple scales of roughness can be treated separately and still produce a valid contact angle prediction. Liquid filled case: Create Wenzel angle and use in Cassie–Baxter equation. Non-filled case: Create Cassie–Baxter angle for top and use in Cassie–Baxter for large scale structure.

2. Consequences of superhydrophobicity

2.1. Amplification and attenuation of contact angle changes

If we plot the expected contact angles on a rough surface against those on a smooth surface for different initial contact angles we find that the Cassie–Baxter contact angle changes little as the contact angle of the equivalent flat surface changes, while the Wenzel contact angle does, although it saturates at 0° and 180° [9] (Fig. 14).

This implies that the Wenzel state amplifies the effects of any change in the chemistry of the surface, whilst the Cassie–Baxter state attenuates it. In practice the wetting tends to cross-over from fully wetting Wenzel at low contact angles to non-wetting Cassie–Baxter at higher ones [35]. This is shown experimentally in Fig. 15 [9]. The liquid was changed in this case while keeping the surface constant, but changes in surface chemistry with the same liquid would be equivalent. The response changes through saturation, amplification and attenuation as the wetting state changes from wetting to bridging.

Several liquids that have a low contact angle on a flat surface have a zero contact angle on the rough surface. This raises the question of the definition of a superhydrophilic (or superwetting) surface, since roughness is not required to create film-forming surfaces even for water. However, creating a film where one would not otherwise be created could be regarded as super-wetting. Moreover, whilst a rough surface may have many liquids which on it display a non-zero contact angle, this does not make them all equivalent; the rate at which they approach a final state is affected by the flat surface contact angle and the roughness (i.e. superspreading). It has been shown that the rate at which a droplet spreads is different on a textured surface than on a flat one [36].

2.2. Bridging-to-penetrating transition

Some complex undercut (overhanging) topographies, such as the "ball-on-a-stick" or fibres mentioned earlier go into a bridging mode unless the advancing liquid has a low enough contact angle with the

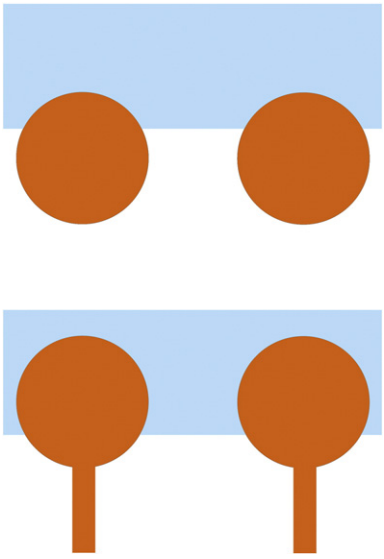

Fig. 12. Top: curved pillars require both Cassie–Baxter and Wenzel equations and the factors depend on the contact angle as well as the pattern geometry. Bottom: re-entrant surfaces can support a bridging state for low contact angles.

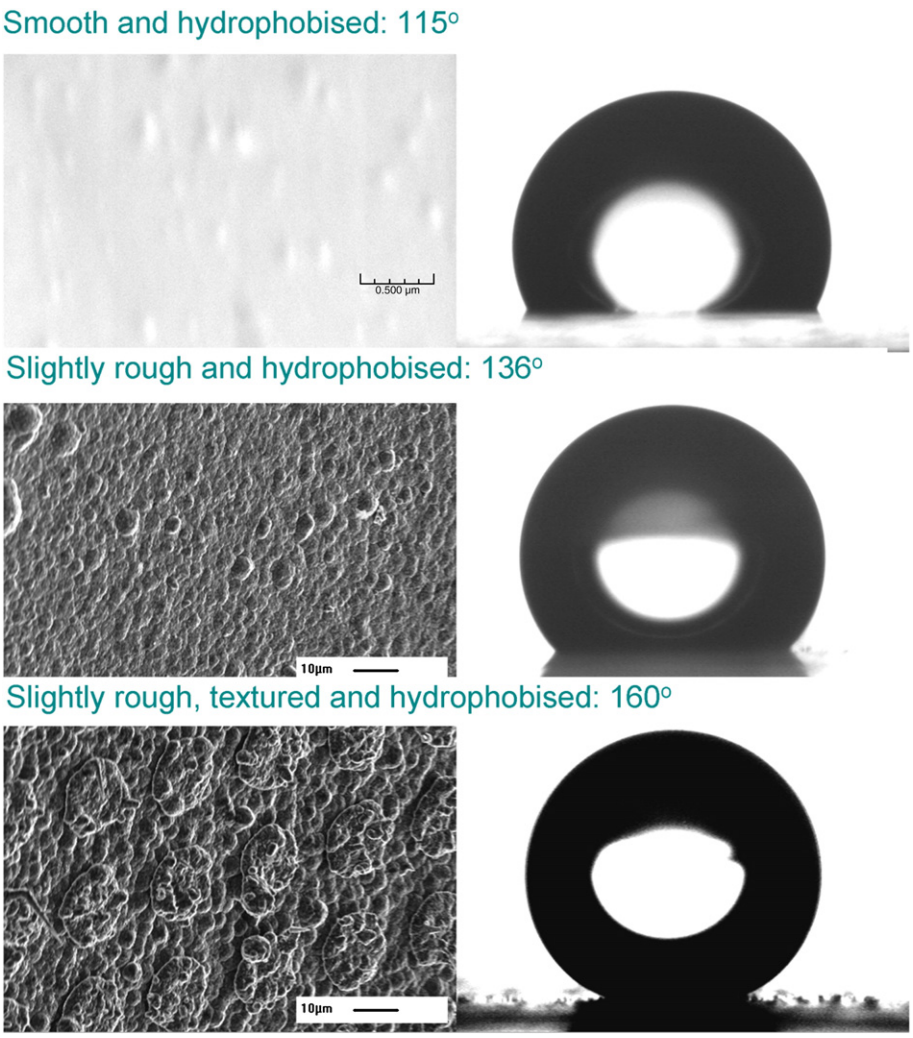

Fig. 13. A surface with two levels of roughness can be considerably more hydrophobic than one with one even when each roughness has little effect on its own. Reproduced with permission from Shirtcliffe et al. [34]. Copyright Wiley-VCH Verlag GmbH & Co. KGaA.

surface to get round the cusp of the structure. This idea was discussed by Herminghaus [37].

Another consideration is how far the meniscus bulges down and ripples naturally. This has been considered recently by Tuteja et al., who has defined some characteristic numbers to estimate when a meniscus should touch the bottom of a given pattern [38]. Previous studies have calculated the energy barrier between Wenzel and Cassie–Baxter states [39]. Fig. 16 shows how varying the height of a pillar pattern affects the

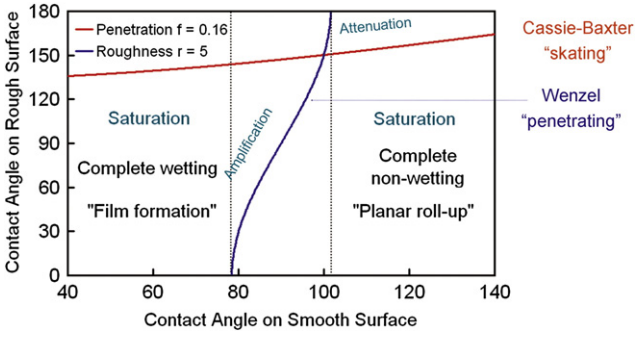

Fig. 14. Contact angles on a rough surface against those on a smooth surface for different initial contact angles for both Wenzel (penetrating) and Cassie–Baxter (bridging) states. Reproduced with permission from G. McHale and M.I. Newton, Colloids and Surfaces A206 (103) (SI) (2002) 193–201, Copyright Elsevier.

contact angle of a drop of water placed on top [40]. Increasing height causes an abrupt change from Wenzel wetting to Cassie–Baxter at an aspect ratio slightly below 1 for small drops carefully placed on top. Transition to the Wenzel state can be induced by shaking, allowing the drop to fall from a height or other ways of applying pressure.

As can be seen the changeover is far from sharp. These pillars were evenly spaced round pillars and had diameters of 15 micrometers so the changeover occurs at an aspect ratio slightly below 1.

One simple way to estimate the point at which the Cassie–Baxter bridging state becomes stable is to calculate the contact angles of the wetting Wenzel state and the bridging state and compare them [41].

An example would be the pillars shown in Fig. 17 (of height h). For a given pattern the values of roughness and solid surface fraction for any height h, pillar diameter, D, and lattice periodicity, L, can be calculated for a given equilibrium angle and plotted against each-other.

$$r = 1 + \frac{\pi D h}{L^2}, \quad f_s = \frac{\pi D^2}{4L^2} \tag{11}$$

The curves in Fig. 17 show that for the 15 µm pattern the Cassie–Baxter state will be stable once the height exceeds 21 µm. This is somewhat greater than the values measured experimentally shown in Fig. 16, but the treatment does not allow for roughness of the sidewalls or projecting edges, which can be seen in the micrograph of the structures and, which can contribute to the creation of metastable

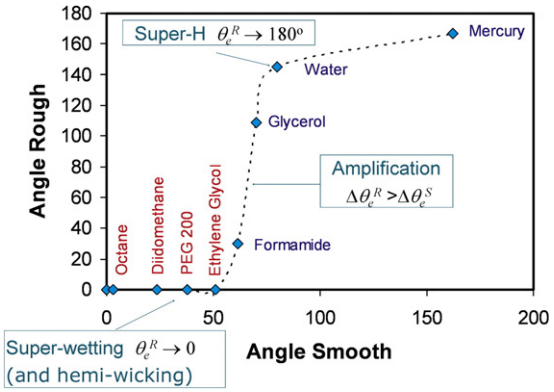

Fig. 15. Experimental data showing saturation of Wenzel wetting at low angle (liquids with contact angles on flat below 50° all go to 0° on the rough surface); amplification at medium angles (the difference between formamide and glycerol is around 15° on a flat surface, 55° on the rough one); and attenuation at higher angles (the difference between water and mercury is lower on the rough surface than the flat one). Reproduced with permission from McHale et al. [9] Copyright Royal Society of Chemistry.

states as overhanging structures with effective pinning points will be produced.

The other reason that this treatment differs from measured values is that there is an energy barrier between the two states, making one of them stable and the other metastable. On many surfaces this energy barrier is large enough that a drop of water will tend to stay in the state that it is put in (the Cassie–Baxter bridging state for a drop applied from the top) unless forced into the other state. A condensing liquid will always form in contact with the surface so droplets forming this way often begin in the Wenzel state and can be trapped there by the energy barrier in the same way that droplets deposited gently onto the surface will start in the Cassie–Baxter state [42]. The way that water condenses on superhydrophobic materials is of particular interest, because of its potential use in condensers [43,44]. Surfaces with overhanging structures enhance the energy barrier between the states, making the thermodynamically unstable state kinetically stable.

2.3. Contact angle hysteresis

As mentioned at the beginning of this article, one of the characteristics often associated with superhydrophobic surfaces is the tendency for droplets of water to roll or slide on them very easily. This is connected with contact angle hysteresis, which is where a contact interface can take a range of angles without moving. Young's equation suggests that there is only one stable contact angle, but on real surfaces there are a range of stable angles. It is common to observe a droplet of water sitting on a tilted surface with a different contact angle at the front and rear edges. Similarly, if water is steadily added or removed from a droplet, initially the contact line remains static and the contact angle increases or decreases. The highest contact angle before movement is known as the advancing angle and the smallest as the receding angle, defining the range of possible angles. Although an infinitely slow rate of movement is theoretically required to get the real values practical equivalents are relatively easy to measure for low viscosity liquids. These angles can be measured by placing a drop on a surface and varying the volume until the contact line moves or by tilting the substrate until the drop begins to move (Fig. 18). There is no theoretical proof that the advancing and receding contact angles measured by these two different methods will be the same, but both give an estimate of contact angle hysteresis and droplet mobility [45].

In particular, for a sliding droplet the angles are influenced by its size. This means that results from different methods do not always agree and the method used to estimate droplet mobility or contact angle hysteresis should always be reported. The angle that a plate must be tilted to get a droplet to slide depends upon the size of the drop and the difference between the cosines of the advancing and receding angles [46]. This angle can be easier to measure than the angles themselves and can be useful, as it describes the observable differences between surfaces. However, a strong dependence upon droplet volume and sensitivity to vibration can make it difficult to compare results between laboratories.

Some flat surfaces have very low contact angle hysteresis and, a clean piece of glass (only possible in a laboratory) can have an advancing contact angle of 0° so must logically have no hysteresis. This means that any water reaching the surface forms a film and then drains off easily, droplets are never formed. This does mean that care must be taken when describing surfaces to provide both contact angle and hysteresis information. A low contact angle surface can be a surface that more easily sheds a liquid than a high contact angle one depending on the relative magnitudes of their contact angle hysteresis.

2.3.1. Superhydrophobicity and contact angle hysteresis

Experimentally it has been observed that hysteresis increases for a Wenzel surface and decreases for a surface with bridging type Cassie–Baxter wetting. There are a few models that have been proposed to explain this [47–49].

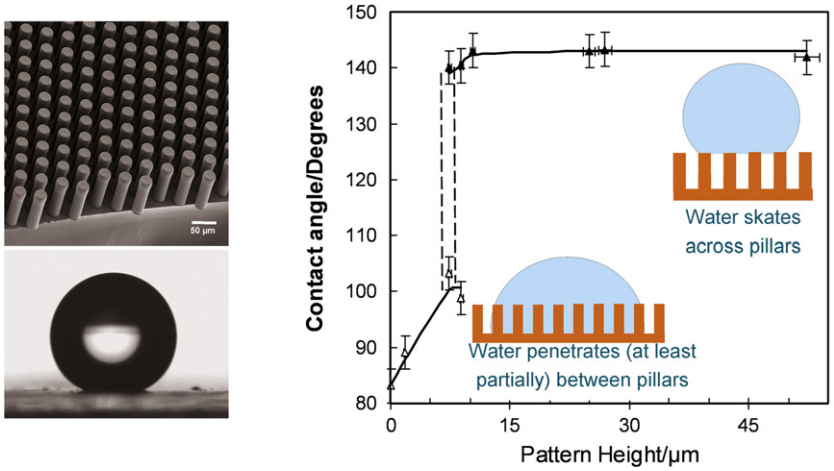

Fig. 16. As the height of polymer pillars are increased the contact angle of water drops placed on them increases and then suddenly jumps to a more or less constant value. This is consistent with a change from Wenzel wetting where changes in height will affect *r* to Cassie–Baxter bridging where the distance to the base is irrelevant. Reproduced with permission from Shirtcliffe et al. [40]. Copyright Institute of Physics.

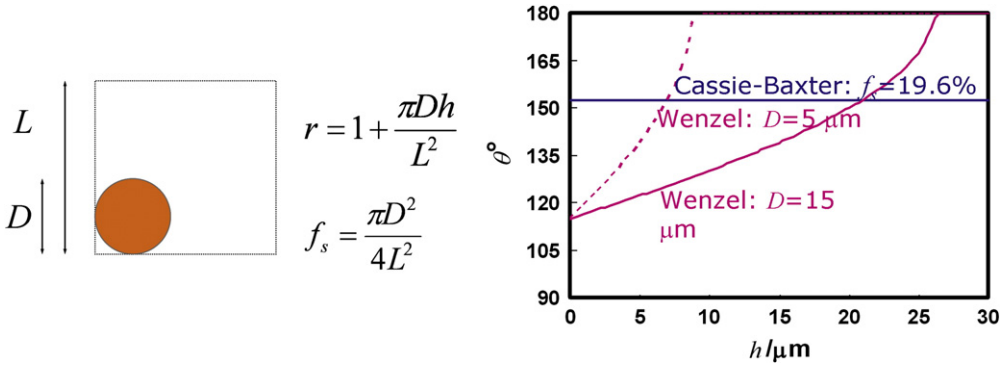

Fig. 17. An example of calculated angles for a square array of pillars showing where the two possible configurations are equivalent.

In the 2D force diagram of a rough surface a drop in the Wenzel state can become pinned by the corners of roughness. However one would expect that the hysteresis of a bridging drop would also increase as the drop must advance round the corner of the pillar to jump to the next and it would recede at around the same angle as on a flat surface.

In 3D this is more complex because the contact line sits on a combination of pillars and holes at any time, meaning that the contact angle must only locally go down to the receding value. It is difficult to rationalise this as a 2D model as the weightings will depend on geometry.

A simpler way to look at the situation is to consider a surface to have intrinsic advancing and receding angles and to average out effects under the contact line by using the surface energy approach used earlier and therefore the Cassie–Baxter and Wenzel equations. As described before, the amplification effect of the Wenzel state then increases the difference between these values and increases hysteresis while the attenuation effect of the Cassie–Baxter bridging state reduces the difference between the values and therefore the hysteresis [47].

There is evidence that defects, contact line perimeter and sharp points induce hysteresis [48,49]. Indeed one of the main theories for the existence of hysteresis of any sort is the presence of areas of different contact angle within the surface of a sample caused by local slope or chemistry, suggesting that a perfect single crystal could have very low hysteresis. This does not, however, lead to simple conclusions about how to increase or decrease hysteresis on a rough surface. As an example, McCarthy et al. [50] showed that posts with different shapes but similar areas showed different hysteresis depending upon their shape with star shapes increasing hysteresis and circular pillars showing lower hysteresis. We showed that for circular pillars in a square lattice arrangement fabricated in SU-8, reducing the size and increasing the density to keep the global surface area fraction constant and therefore increasing the contact line perimeter had no discernible effect on the contact angle or hysteresis [40].

3. Methods for producing superhydrophobic surfaces

Generally a superhydrophobic surface only needs to be hydrophobic and rough on a scale much less than the capillary length (<273 μm for water). This leaves a huge scope for the actual chemistry and topography, and for topology. Additional constraints can be added to improve the properties of the material such as:

- Low solid surface fraction will improve sliding or rolling
- Tall, sharp, features increase the chance of inducing a bridging state, but weaken the surface against abrasion
- Pillars tend to form more “slippy” surfaces than holes, but are again weaker against abrasion
- Multiple length scales improve the effect, higher contact angles and more stable superhydrophobicity are produced than with a single scale roughness
- But a single, small, length scale considerably less than the wavelength of visible light is good for optical transparency
- The base material can be chosen for its properties and then coated to render it hydrophobic if necessary

A recent review focused on materials methods can be found in *Soft Matter* [51].

3.1. Textiles and fibres

Some of the first artificial superhydrophobic surfaces were textiles. Woven and non-woven fibrous materials possess high roughness and fibres lying horizontally have an undercut topography ideal for converting to superhydrophobicity and sometimes oleophobicity. Natural fibres are of the order of micrometers and artificial ones can be made much smaller, the fibres themselves can be roughened to enhance the effect. Some research has been carried out on improving the roughness and hydrophobicity of woven textiles to generate a stronger effect and non-woven mats of electrospun fibres have been found to be highly effective superhydrophobic surfaces and can be produced with very small fibre diameters [52–55].

3.2. Lithography

The two methods mostly used to produce superhydrophobic surfaces are photolithography, where a layer is illuminated through a

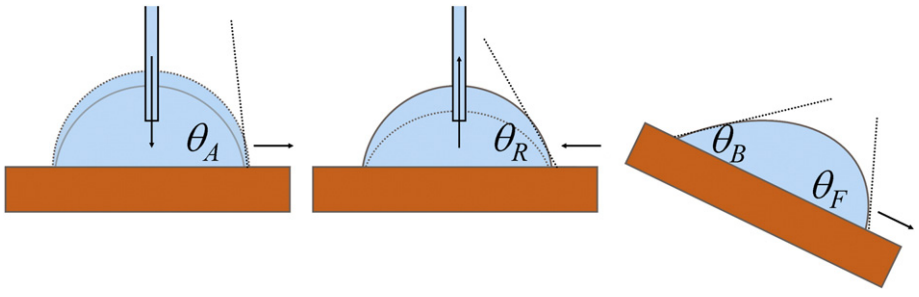

Fig. 18. Measuring advancing, receding and sliding angles.

patterned mask to activate areas and soft lithography, which is the small scale version of contact printing. A relatively high cost method that produces well-defined surfaces and can make many copies of the same thing. These have mostly been used to investigate the theories of wetting and in layered designs, such as microfluidics and electrowetting on complex electrodes. The advantage for theorists is that the r and f_s values of patterns and their symmetry can be varied to investigate the effects of these changes on the physical properties of the surfaces. The other advantage of photolithography is that it is a standard micro-engineering process that can easily be integrated into device fabrication [40,56–60].

3.3. Particles

Colloidal particles are often used to generate the roughness as they can be prepared in large amounts and can self arrange or form random surfaces. Superhydrophobic products, such as paint, are usually supplied in the form of particles in a binder that can be applied to a surface and allowed to set. More organised structures can be formed if the particles are aggregated under control and multiple particle sizes can be used to improve the effect. Several products are on the market that consist of particles suspended in a dilute matrix to produce a superhydrophobic paint [61–63].

3.4. Templating

A copy of any rough surface can be made by filling it with a soft or liquid material, hardening it and removing the original. This can be used to copy large areas of structure and has been used to make superhydrophobic surfaces by copying natural surfaces, such as leaves and insect wings and originals made by the other techniques mentioned here. The advantage is that the original can often be reused and that the material of the copy can be chosen to a certain extent [64–68].

3.5. Phase separation

When a mixture begins to separate into its components it often forms an intermediate structure where the two phases interpenetrate. These structures can be frozen out if one of the separating phases solidifies before separation is complete. The structure can then be converted into a porous solid by removing one phase. This method has been used for some time to generate filters and stationary phases for chromatography, it is also very effective for generating superhydrophobic structures as the solid material is stable, overhangs and is often a polymer so can be hydrophobic on its own right. The size of the roughness can be varied by varying the system parameters and large surfaces can be prepared [69–72].

3.6. Etching

Etching often increases the roughness of a surface and can be used to generate superhydrophobic surfaces. Any type of etching that increases roughness can be used, including acid etching of metals, plasma etching of polymers and laser etching of inorganic materials. Many combinations are possible and the technique is often combined with another roughness generation method to create multiple roughness scales [73–76].

3.7. Crystal growth

The growth of crystals can generate rough surfaces, particularly if needle-like crystals can be produced. Nano-fibres can also be grown on surfaces using catalyst particles to direct growth. This produces surfaces with very high roughness and small size, important for the investigation of some extreme effects [77–80].

3.8. Diffusion limited growth

This is the natural growth pattern when deposition occurs with no surface transport. It can occur in electrochemical growth and in gas phase deposition. The usual deposit looks much like a cauliflower head and has a fractal morphology with a very high surface area. Such surfaces are cheap to make on relatively small scale and can be made in a variety of materials [81–84].

A selection of superhydrophobic surfaces is shown in Fig. 19, showing the diversity in form that the roughness can take.

4. Beyond simple hydrophobicity

4.1. Leidenfrost effect

The ideal superhydrophobic surface would be one whereby the solid surface fraction vanished (i.e. $f_s = 0$). Whilst this may seem impractical to construct, it is known that when a droplet is placed on a surface at the Leidenfrost temperature, a temperature well above the boiling point of the liquid, a boundary layer of vapour be created [85,86]. The layer of vapour reduces the heat transfer from the substrate and the rate of evaporation of the droplet is low, thus allowing it to persist. In this state, the droplet slides freely across the surface (Fig. 20). This is effectively a Cassie–Baxter surface where the solid-surface fraction is zero, making the contact angle very high and the “slippyness” of the surface extremely high [87]. Similarly reduced evaporation has also been observed on superhydrophobic surfaces when the interfacial contact area determines the transfer of heat to the drop [88].

4.2. Super water repellent soil

As can be seen in the picture in Fig. 21, sand is a rough material, often with a grain size smaller than the capillary length of water. Under some conditions the surface of the grains can become hydrophobic and then the sand becomes repellent to water. This usually requires the presence of hydrophobic compounds coating the soil grains; these can be produced by plants, generated in a fire or spilled by man [31,32].

If the grains are adhered to a surface the behaviour is much like that of a superhydrophobic surface, which is a problem because water does not penetrate very well and plants cannot grow as a result. In extreme cases water just persists on the surface, eventually evaporating or building into a flood. In most cases soaking the soil for a long period allows water to penetrate. Once the pores are filled with water the alternative Cassie–Baxter state is reached where the contact angle is reduced. If the soil dries it often reverts to superhydrophobicity. The problem is often remedied by adding surfactants to wet the soil or by adding a high surface area material such as clay to mop up the repellent chemicals.

4.3. Liquid marbles

If the grains are not fixed they adhere to the water droplet and eventually coat it; they are unlikely to escape unless their contact angle is very low or extremely high. In this way even PTFE spheres adhere strongly to the surface of water. The coated drop can then be moved onto a flat surface and will roll around on it as if the surface were superhydrophobic. Water liquid marbles with highly hydrophobic particles can even be placed onto water, where they will sit as long as they are undisturbed, but will merge with the water below if pricked. The situation can be likened to a superhydrophobic surface where the roughness is attached to the droplet [89–92].

Work on liquid marbles shows that these coated droplets bounce off flat surfaces and roll rapidly downhill. They barely interact with the surface, allowing them to behave like a soft solid. Their evaporation is

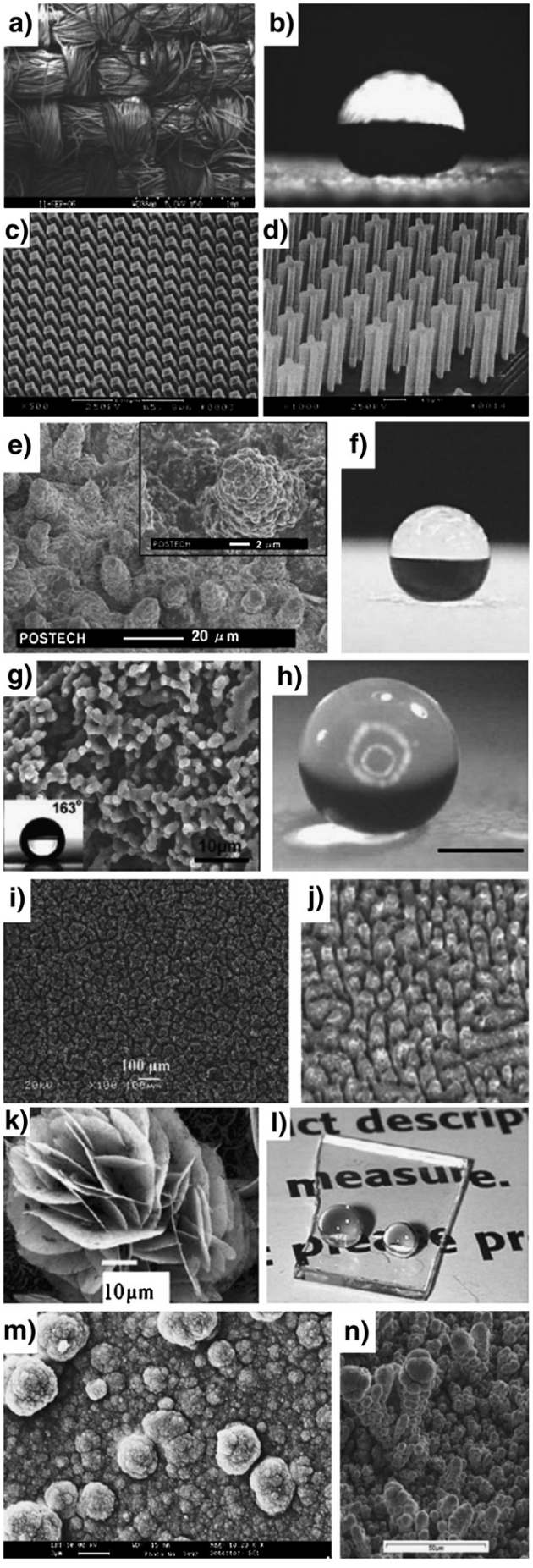

Fig. 20. Leidenfrost drop; water on a heated surface, Reproduced with permission from Biance et al. [87]. Copyright American Institute of Physics.

much reduced as much of the air–liquid interface is replaced with solid–liquid interface.

4.4. Plastron respiration

One of the methods insects and arachnids, such as the spider in Fig. 1, use to breathe underwater is to carry a layer of air inside a superhydrophobic surface on their bodies and to breathe the gas in this layer. This layer, known as a plastron, differs from a bubble in that it cannot shrink, because the gas–water interface is maintained through capillary forces on a superhydrophobic structure. In a plastron, oxygen and carbon dioxide are continually exchanged between the film of air and the surrounding water [93–95]. Indeed some insects can remain underwater indefinitely because the air layer is continually replenished with oxygen. As the gas dissolves into the water an inwardly curved interface is produced. This supports a pressure difference so that the partial pressures of gases in the gas phase can be lower than those in the water thus causing a diffusion of gases across the gas–water interface. In contrast, a simple bubble always has an outwardly curved interface, ensuring that the gas in the bubble will eventually dissolve into the water. We have tested this by placing a fuel cell inside a superhydrophobic block and immersing it in oxygenated water [94]. Although the partial pressure of oxygen dropped it reached a constant value, effectively making an external gill (Fig. 22).

4.5. Digital switching

As shown in Fig. 14 superhydrophobicity acts like an amplifier of contact angle. If the roughness of a surface is extreme enough the amplification effect will become very sharp and a small change in conditions will then cause a switch from non-wetting to fully wetting [11]. This principle is similar to that used in many detection devices and would allow a simple visual test. A suitable type of surface for this is a material with porous-type structure as the effective roughness can be very large.

In Fig. 23 a porous-structure hydrophobic material is heated to cause a small decrease in hydrophobicity (intrinsic contact angle), which causes a change from superhydrophobicity to wicking [20,96].

Fig. 19. Superhydrophobic surfaces prepared in different ways, highlighting the various topographies possible a), b), textile superhydrophobic surfaces; c), d) Lithographic patterns; e), f) Templating; g) h), phase separation; i) j), Etching; k), l), crystal growth; m), n) diffusion limited growth. Reproduced with permission from. a) and b), Michielsen and Lee [52], c) and d) Oner and McCarthy [56], e) Lee and Kwon [67], f), Bormashenko et al. [68], g), Han et al. [71], h) Yamanaka et al. [72] ,i) Guo et al. [73], j) Baldacchini et al. [74], k), A. C. Chen, X. S. Peng, K. Koczkur, B. Miller, *Chem. Commun.*, 2004, 17, 1964–1965, l), T. Ishizaki, N. Saito, Y. Inoue, M. Bekke, O. Takai, *J. Phys. D.*, 2007, 40, 1, 192–197, m), Satyaprasad et al. [81], n) Shirtcliffe et al. [28]. Copyrights a, b, c, d, f, g, j, n, American Chemical Society, e, l, Institute of Physics, h, k, Royal Society of Chemistry, i, m, Elsevier.

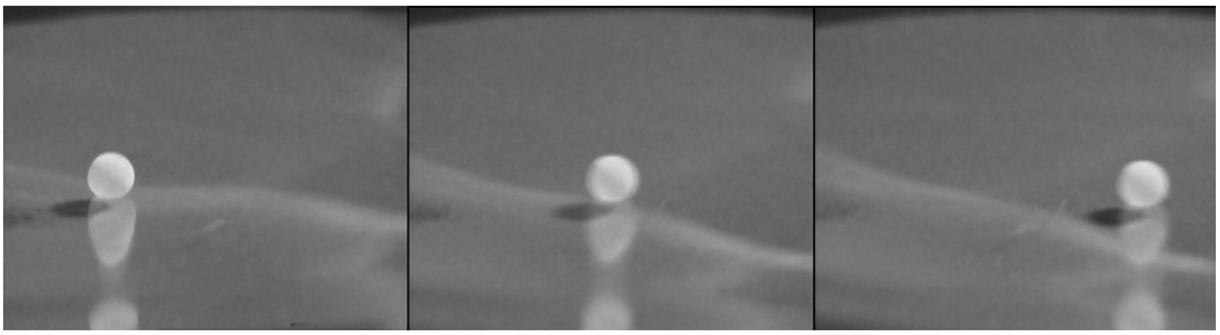

Fig. 21. A liquid marble of water with hydrophobised lycopodium powder rolling across a Petri dish.

4.6. Superspreading

As mentioned earlier in this article, a droplet wetting a rough surface will often exhibit a zero contact angle, but the rate at which it approaches this state is different to that on a flat surface with a zero contact angle. A droplet on a surface spreads until its contact angle, θ, reaches a stable value. On a smooth and flat surface, the driving force, F_d, for this is the out-of-balance component of the capillary force parallel to the surface,

$$F_d \propto \gamma_{LV}(\cos\theta_e - \cos\theta) \tag{12}$$

When the dynamic contact angle is small, the driving force can be approximated by,

$$F_d \propto \gamma_{LV}(\theta^2 - \theta_e^2) \tag{13}$$

In most cases the largest opposing force is viscous dissipation, which can be calculated for a liquid wedge shape assuming the wedge moves forward due to Poiseuille flow and a no-slip boundary condition is obeyed as the liquid–solid interface [97]. This results in dissipation inversely proportional to the tangent of the wedge angle. If the angle is small this is equivalent to being proportional to inverse θ. The edge speed (i.e. rate of change of contact radius), v_E, is then given by,

$$v_E \propto \gamma_{LV}\theta(\theta^2 - \theta_e^2) \tag{14}$$

which is the Hoffmann-Tanner-de Gennes law [97–99]. In the limit of a complete wetting surface (i.e. $\theta_e = 0°$) the edge speed varies with the cube of the dynamic contact angle.

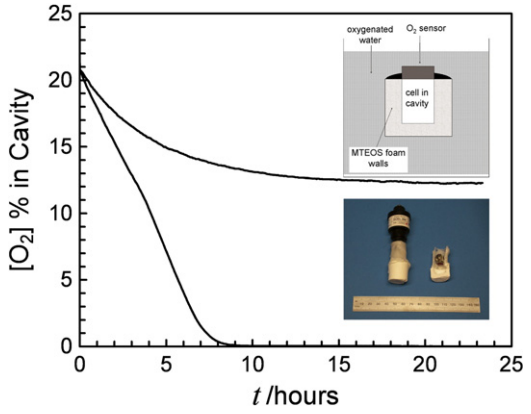

Fig. 22. An artificial plastron constructed from a porous, superhydrophobic material; a fuel cell uses up the oxygen in the cavity and in an equivalent solid walled cavity showing the level of oxygen reaches a steady state as it diffuses in from the water into the gas phase. Reproduced with permission from Shirtcliffe et al. [94]. Copyright American Institute of Physics.

The driving force for spreading is changed for a droplet spreading in the Wenzel mode on a rough surface due to the increased surface area for interaction [100]. On a rough surface a wetting liquid will be in Wenzel mode so the equation becomes modified to

$$F_d \propto \gamma_{LV}(r\cos\theta_e - \cos\theta) \tag{15}$$

In this case, the constant terms in the small angle expansions of the cosines do not cancel, which means that the edge speed has both linear and cubic dependencies,

$$v_E \propto \gamma_{LV}\theta\left[(r-1) + \frac{1}{2}(\theta^2 - \theta_e^2)\right] \tag{16}$$

This also means that the edge speed will not slow as rapidly with decreasing contact angle as in the flat case and information about the surface roughness is encoded into the rate of spreading.

Spreading experiments using droplets of non-volatile polydimethylsiloxane (PDMS) on pillar surfaces with $\theta_e = 0°$ have been used to examine Eq. (16) [100]. In the initial stages of spreading droplet volume was approximately maintained and the spreading droplet engulfed successive pillars. In later stages of spreading a film spread between pillars in advance of the droplet. The initial stages of spreading demonstrated a stick–slip pattern reflecting the pillar structure and an average slope consistent with a power law for $v_E \propto \theta^p$ with p between 1 and 3. When a series of patterns of increasing height were treated in the same manner the exponent changed from 3 down towards 1 as the height increased (Fig. 24).

4.7. Wetting and hemiwicking

In the previous section, the theory assumed that a droplet spread, but always upon a dry surface. Another possibility is that a liquid is imbibed by a surface pattern, spreading within the structure, but leaving the tops of the surface features dry. This is what happens after the initial spreading in the previous section. This situation has been called hemiwicking and has been described by Quéré et al. among others [101,102]. In droplet experiments, a wetting film can sometimes be seen to break away from the droplet and spread within the surface structure, generating a fried egg type pattern. As the liquid spreads within the surface structure, facets can be generated as its rate of spreading in different symmetry directions can be different. The shape of the wetted area may evolve with time as different facets advance at different rates. Fig. 25 shows the development of facets that grow and merge like crystal planes as the wetting front escapes the drop edge [103].

5. Summary and conclusions

Superhydrophobicity in its simplest form is reasonably well understood and most surfaces follow some combination of Wenzel

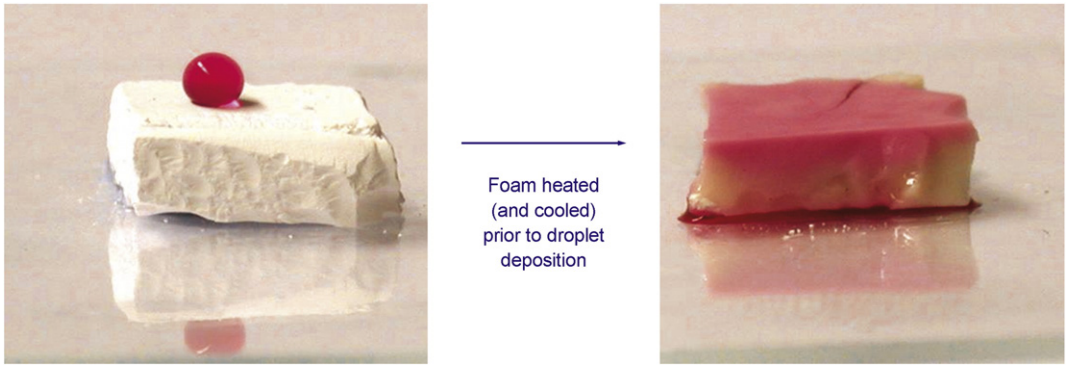

Fig. 23. A porous foam is superhydrophobic. Heat treatment reduces its flat contact angle by a few degrees, but the extremely high roughness causes the material to switch to absorbing the liquid. Reproduced with permission from Shirtcliffe et al. [20]. Copyright Royal Society of Chemistry.

and Cassie–Baxter's equations, which can be understood as solutions for surface free energy minima that can have an energy barrier between them. Contact angle hysteresis is an important property of surfaces and how liquids move on them and is not directly linked with contact angle. For liquid shedding purposes a low contact angle hysteresis is more important than a high contact angle; fortunately Cassie–Baxter bridging superhydrophobic surfaces can provide both. When using these equations it is important to remember the principles upon which they are based and the assumptions used and which therefore define their validity. In many cases surfaces will not simply follow one or the other and it is often difficult to measure enough properties of the surfaces to allow combinations of the two equations to be used. The method by which liquids are deposited or condensed onto the surfaces can have a significant influence on the observed state. The increased interaction area of the Wenzel penetrating state and decreased interaction area of the Cassie bridging state can manifest themselves as amplification and attenuation of wetting and in the contact angle hysteresis and liquid spreading.

The shape of the topography and how many scales that it is rough over as well as the geometrical roughness and the contact angle of the chosen liquid on the chosen material all affect wetting and de-wetting. Wenzel's equation predicts that contact angles below 90° can be decreased by roughness and higher angles are increased, but the effect of bridging allows some surfaces with lower intrinsic contact angles to show increases in contact angle with roughness. The shape of the roughness is critical here to induce bridging. These factors allow extensive scope when designing a material for a particular purpose. Many methods can be used to generate superhydrophobic surfaces.

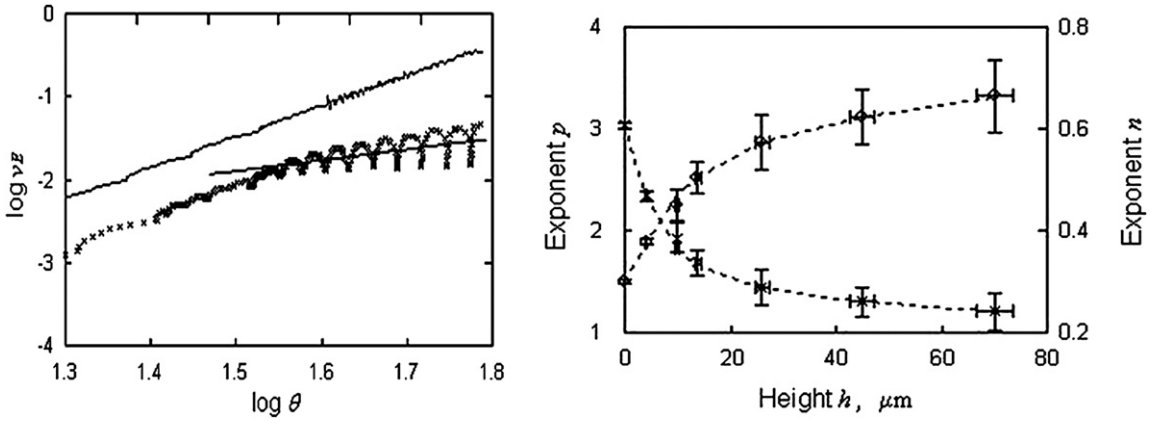

Fig. 24. Left: a comparison of with log (edge speed) against log (contact angle) between a rough surface (lower curve) and a smooth one (upper curve) showing the rough surface has a region similar to the flat surface and one that is different. Right: The change in fitted exponent as the pattern is gradually increased in aspect ratio; exponent p changes from 3 towards 1, the change from a cubic towards a linear law, equally the exponent n linking contact angle and time changes from 0.3 towards 0.75. Reproduced with permission from McHale et al. [36]. Copyright American Physical Society.

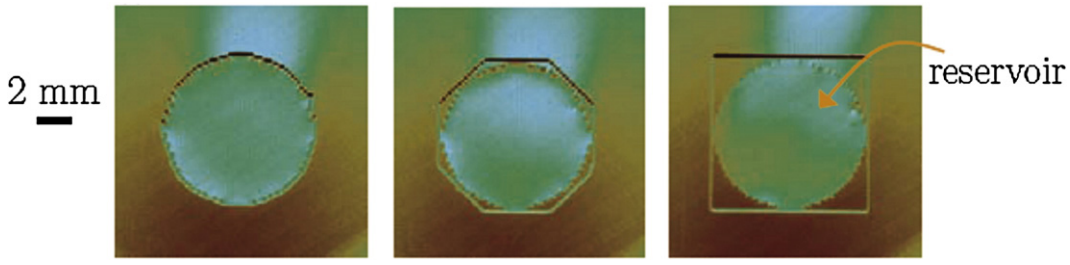

Fig. 25. The progression of a drop from a circle to a square on the top of a square array of pillars. Reproduced with permission from Courbin et al. [103]. Copyright Nature Publishing Group.

All that are needed are sufficiently high intrinsic contact angle and surface roughness (or topography).

Many systems not considered before to be linked can be interpreted as a form of superhydrophobicity; soil hydrophobicity, insect plastron breathing and liquid marbles are some examples. Superhydrophobicity is one example of how topography interacts with surface chemistry to alter wetting properties. However, with a surface chemistry favouring wetting, topography also has an important interaction leading to superspreading, superwetting and other effects on rough surfaces.

There has been considerable research both recent and less recent into different aspects of superhydrophobicity and the areas are gradually being linked. Theory has advanced somewhat and more complicated aspects can often be simulated. A few applications have emerged, but superhydrophobic surfaces tend to make other liquids spread on them and the high aspect ratio roughness is fragile and easily damaged. The more successful applications lie so far in surfaces that do not encounter much oil or abrasion.

References

[1] Adamson AW, Gast AP. Physical chemistry of surfaces. Wiley Blackwell; 1997.
[2] Denny MW. Air and water: the biology and physics of life's media. Princeton University Press; 1993.
[3] Turner JS. The extended organism: the physiology of animal-built structures. Harvard University Press; 2000.
[4] de Gennes PG. Rev Mod Phys 1985;57:827.
[5] Léger L, Joanny JF. Rep Prog Phys 1992;55:431.
[6] McHale G, Käb NA, Newton MI, Rowan SM. J Colloid Interface Sci 1997;186:453.
[7] Barthlott W, Neinhuis C. Planta 1997;202:1.
[8] Neinhuis C, Barthlott W. Ann Bot 1997;79:667.
[9] McHale G, Shirtcliffe NJ, Newton MI. Analyst 2004;129:284.
[10] de Gennes PG, Brochard-Wyart F, Quéré D. Capillarity and wetting phenomena: drops, bubbles, pearls, waves. Springer; 2003.
[11] Quéré D. Annu Rev Mater Res 2008;38:71.
[12] Gao LC, McCarthy TJ. Langmuir 2007;23:3762.
[13] McHale G. Langmuir 2007;23:8200.
[14] Wenzel RN. Ind Eng Chem 1936;28:988.
[15] Wenzel RN. J Phys Colloid Chem 1949;53:1466.
[16] Cassie ABD, Baxter S. Trans Faraday Soc 1944;40:546.
[17] Cassie ABD. Discuss Faraday Soc 1948;3:11.
[18] Johnson RE, Dettre RH. In: Gould RF, editor. Contact angle, wettability and adhesion: advances in chemistry series, vol. 43. Am. Chem. Soc.; 1964. p. 112–35.
[19] Bico J, Thiele U, Quéré D. Colloids Surf A 2002;206:41.
[20] Shirtcliffe N, McHale G, Newton M, Perry C, Roach P. Chem Commun 2005;25:3135.
[21] Quéré D. Nature Mater 2002;1:14.
[22] Patankar N. Langmuir 2004;20:7097.
[23] Reyssat M, Yeomans J, Quéré D. Europhys Lett 2008;81 art. 26006.
[24] Kusumaatmaja H, Blow M, Dupuis A, Yeomans JM. Lett Europhys 2008;81 art. 36003.
[25] McHale G, Elliott SJ, Newton MI, Shirtcliffe NJ. In: Mittal KL, editor. Superhydrophobicity: Localized parameters and gradient surfaces, vol. 6. 'Contact Angle, Wettability and Adhesion', Koninklijke Brill NV; 2009. p. 219–33.
[26] Shastry A, Case MJ, Böhringer KF. Langmuir 2006;22:6161.
[27] Sun C, Zhao XW, Han YH, Gu ZZ. Thin Solid Films 2008;516:4059.
[28] Shirtcliffe N, McHale G, Newton M, Perry C. Langmuir 2005;21(3):937–43.
[29] McHale G, Newton MI, Shirtcliffe NJ. Eur J Soil Sci 2005;56:445.
[30] Bachmann J, McHale G. Eur J Soil Sci 2009;60:420.
[31] Tuteja A, Choi W, Ma ML, Mabry JM, Mazzella SA, Rutledge GC, et al. Science 2007;318:1618.
[32] Nosonovsky M. Langmuir 2007;23(6):3157–61.
[33] Chen CH, Cai QJ, Tsai CL, Chen CL, Xiong GY, Yu Y, et al. Appl Phys Lett 2007;90(17):173108.
[34] Shirtcliffe N, McHale G, Newton M, Chabrol G, Perry C. Adv Mater 2004;16:1929.
[35] Patankar N. Langmuir 2004;20(17):7097–102.
[36] McHale G, Shirtcliffe N, Aqil S, Perry C, Newton M. Phys Rev Lett 2004;93 art. 036102.
[37] Herminghaus S. Europhys Lett 2000;52(2):165–70.
[38] Tuteja A, Choi W, Ma M, Mabry J, Mazzella S, Rutledge G, et al. Science 2007;318(5856):1618–22.
[39] Patankar NA. Langmuir 2004;20:8209–13.
[40] Shirtcliffe N, Aqil S, Evans C, McHale G, Newton M, Perry C, et al. J Micromech Microeng 2004;14(10):1384–9.
[41] Ishino C, Okumura K, Quere D. Europhys Lett 2004;68(3):419–25.
[42] Dorrer C, Ruhe J. Langmuir 2007;23(7):3820–4.
[43] Cheng YT, Rodak DE, Angelopoulos A, Gacek T. Appl Phys Lett 2005;86 art. 194112.
[44] Wier K, McCarthy T. Langmuir 2006;22:2433.
[45] Krasovitski B, Marmur A. Langmuir 2005;21(9):3881–5.
[46] Miwa M, Nakajima A, Fujishima A, Hashimoto K, Watanabe T. Langmuir 2000;16:5754.
[47] McHale G, Shirtcliffe N, Newton M. Langmuir 2004;20:10146.
[48] Gao LC, McCarthy TJ. Langmuir 2006;22:6234.
[49] Reyssat M, Quéré D. J Phys Chem B 2009;113:3906.
[50] Chen W, Fadeev A, Hsieh M, Oner D, Youngblood J, McCarthy T. Langmuir 1999;15(10):3395–9.
[51] Roach P, Shirtcliffe NJ, Newton MI. Soft Matter 2008;4:224.
[52] Michielsen S, Lee HJ. Langmuir 2007;23(11):6004–10.
[53] Liu YY, Wang RH, Lu HF, Li L, Kong YY, Qi KH, et al. J Mater Chem 2007;17(11):1071–8.
[54] Wang T, Hu X, Dong S. Chem Commun 2007:1849–51.
[55] Ma M, Gupta M, Li Z, Zhai L, Gleason KK, Cohen RE. Adv Mater 2007;19:255–9.
[56] Oner D, McCarthy TJ. Langmuir 2000;16(20):7777–82.
[57] Yoshimitsu Z, Nakajima A, Watanabe T, Hashimoto K. Langmuir 2002;18(15):5818–22.
[58] Zhu L, Feng YY, Ye XY, Zhou ZY. Sens Actuators A 2006;130:595–600.
[59] Choi CH, Kim CJ. Nanotechnology 2006;17(21):5326–33.
[60] Wagterveld RM, Berendsen CWJ, Bouaidat S, Jonsmann J. Langmuir 2006;22(26):10904–8.
[61] Li Y, Huang XJ, Heo SH, Li CC, Choi YK, Cai WP, et al. Langmuir 2007;23(4):2169–74.
[62] Sun C, Ge LQ, Gu ZZ. Thin Solid Films 2007;515(11):4686–90.
[63] Patents, e.g CN1919938 (A) and US2004081818 (A1).
[64] Bico J, Marzolin C, Quere D. Europhys Lett 1999;47(2):220–6.
[65] Singh RA, Yoon ES, Kim HJ, Kim J, Jeong HE, Suh KY. Mater Sci Eng C 2007;27(4):875–9.
[66] Li J, Fu J, Cong Y, Wu Y, Xue LJ, Han YC. Appl Surf Sci 2006;252(6):2229–34.
[67] Lee S-M, Kwon TH. J Micromech Microeng 2007;17:687–92.
[68] Bormashenko E, Stein T, Whyman G, Bormashenko Y, Pogreb R. Langmuir 2006;22(24):9982–5.
[69] Shirtcliffe NJ, McHale G, Newton MI, Perry CC, Roach P. Mater Chem Phys 2007;103(1):112–7.
[70] Li X, Chen G, Ma Y, Feng L, Zhao H. Polymer 2006;47:506–9.
[71] Han JT, Xu XR, Cho KW. Langmuir 2005;21(15):6662–5.
[72] Yamanaka M, Sada K, Miyata M, Hanabusa K, Nakano K. Chem Commun 2006;21:2248–50.
[73] Guo Z, Zhou F, Hao J, Liu W. J Colloid Interface Sci 2006;303:298–305.
[74] Baldacchini T, Carey JE, Zhou M, Mazur E. Langmuir 2006;22:4917–9.
[75] Lacroix LM, Lejeune M, Ceriotti L, Kormunda M, Meziani T, Colpo P, et al. Surf Sci 2005;592(1–3):182–8.
[76] Lacroix LM, Lejeune M, Ceriotti L, Kormunda M, Meziani T, Colpo P, et al. Surf Sci 2005;592(1–3):182–8.
[77] Onda T, Shibuichi S, Satoh N, Tsujii K. Langmuir 1996;12:2125.
[78] Wu XD, Zheng LJ, Wu D. Langmuir 2005;21:2665–7.
[79] Lau KKS, Bico J, Teo KBK, Chhowalla M, Amaratunga GAJ, Milne WI, et al. Nano Lett 2003;3:1701–5.
[80] Liu H, Jiang L. Soft Matter 2006;2:811–21.
[81] Satyaprasad S, Jain V, Nema SK. Appl Surf Sci 2007;253(12):5462–6.
[82] Shirtcliffe NJ, McHale G, Newton MI, Perry CC. Langmuir 2005;21(3):937–43.
[83] Karuppuchamy S, Jeong JM. Mater Chem Phys 2005;93:251–4.
[84] Shirtcliffe NJ, Thiemann P, Stratmann M, Grundmeier G. Surf Coat Tech 2001;142:1121–8.
[85] Leidenfrost J. *De Aquae Communis Nonnullis Qualitatibus Tractatus*; 1756.
[86] Gottfried B. Int J Heat Mass Transfer 1966;9:1167.
[87] Biance A, Clanet C, Quéré D. Phys Fluids 2003;15:1632.
[88] Takata Y. Proc. 4th International Conference on Nanochannels, Microchannnels, and Minichannels, Pts A and B; 2006. p. 1333–41.
[89] Aussillous P, Quere D. Nature 2001;411(6840):924–7.
[90] Dorvee J, Derfus A, Bhatia S, Sailor M. Nat Mater 2004;3(12):896–9.
[91] McHale G, Shirtcliffe N, Newton M, Pyatt F, Doerr S. Appl Phys Lett 2007;90(5):054110.
[92] Pike N, Richard D, Foster W, Mahadevan L. Proc Royal Soc London B 2002;269(1497):1211–5.
[93] Thorpe WH. Biol Rev 1950;25:344–90.
[94] Shirtcliffe N, McHale G, Newton M, Perry C, Pyatt F. Appl Phys Lett 2006;89 art. 104106.
[95] Bush J, Hu D, Prakash M. Adv Insect Physiol 2008;34:117–92.
[96] Shirtcliffe N, McHale G, Newton M, Perry C, Roach P. Maters Chem Phys 2007;103:112.
[97] De Gennes PG. Rev Mod Phys 1985;57:827.
[98] Hoffman RA. J Colloid Interface Sci 1975;50:p228.
[99] 22Tanner LH. J Phys D 1978;12:1473.
[100] McHale G, Shirtcliffe N, Aqil S, Perry C, Newton M. Phys Rev Lett 2004;93(3):036102.
[101] Ishino C, Reyssat M, Reyssat E, Okumura K, Quere D. Europhys Lett 2007;79(5):56005.
[102] Starov V, Zhdanov S, Kosvintsev S, Sobolev V, Velarde M. Adv Coll Interf Sci 2003;104:123–58.
[103] Courbin L, Denieul E, Dressaire E, Roper M, Ajdari A, Stone HA. Nat Mater 2007;6:661.
[104] Gao L, McCarthy TJ. Langmuir 2008;24:9183.
[105] McHale G. Langmuir 2009;25:7185.